

Instabilities in Elastic and Magneto-Elastic Beams and Shells: from Shell Buckling to the Design of a Programmable Braille Reader

Présentée le 8 février 2024

Faculté des sciences et techniques de l'ingénieur
Laboratoire des Structures Flexibles
Programme doctoral en mécanique

pour l'obtention du grade de Docteur ès Sciences

par

Arefeh ABBASI

Acceptée sur proposition du jury

Prof. M. S. Sakar, président du jury
Prof. P. M. Nunes Pereira de Almeida Reis, directeur de thèse
Prof. K. Danas, rapporteur
Prof. J. W. Hutchinson, rapporteur
Prof. T. Schneider, rapporteur

Shell structures teach us that strength is not always about rigidity,
but often about finding harmony in curves and contours.

To my family ...
and brave women of my homeland who are fighting for their rights

Acknowledgements

I am sincerely thankful to my advisor, Pedro, for providing me with this wonderful opportunity and trust over four years ago. His consistent support, encouragement, and valuable advice have been crucial in this important journey. I am deeply indebted for his unwavering help, continuous motivation, and priceless guidance. This accomplishment would not have been possible without his guidance. I would like to thank my thesis committee, Prof. John Hutchinson, Prof. Kostas Danas, and Prof. Tobias Schnider, for having accepted to evaluate this thesis. My gratitude also goes to Prof. Selman Sakar for accepting the jury's presidency.

I am also grateful to everyone who I met and collaborated with at the FlexLab. I am so grateful to Dong, who taught me the alphabet of shell and MRE projects specifically at the beginning of my way, in addition to his priceless help with the papers we published together. I will thank Tim, Tomohiko, and Matteo for their invaluable input and expertise; working with you was such a great pleasure. I would like to thank Luna for all her support, help, and patiently listening to my concerns, especially in the past challenging months. I thank Michael for being such a great office mate, in addition to his valuable, deep mathematical input when I had a problem. I thank Fani for her collaborative efforts in composing shell papers, in addition to the great times we had together. I will thank all my friends whom I met at Flexlab and EPFL for the unforgettable moments we had together and their support during my Ph.D. studies, especially Sam, Paul Johanns, Paul Grandgeorge, Eduardo, Bastien, Gilad, Javi, Mrudhula, and Sahar. I would also like to express my gratitude to Noelia for her precious support and unconditional help during my presence at the Flexlab. Additionally, thanks to Petra for her administrative help in the past few months.

Most importantly, I want to thank my mom, dad, and brother in Iran for their unlimited love, support, and motivation during this journey far from home. I couldn't visit them enough during the past five years, but I always had their encouragement throughout my life and studies. Last but not least, I want to say a big thanks to my best friend, partner in crime, and my husband, Reza. Throughout this journey, his unwavering support,

understanding, and encouragement have been my rock and greatest strength, in addition to the wonderful times we spent in Switzerland and Italy. I am truly blessed to have him by my side, cheering me on every step of the way. We embarked on this journey together, and there are still numerous exciting challenges ahead for us to conquer as a team. Thank you very much, everyone!

Lausanne, 31 Octobre 2023

Arefeh Abbasi

Abstract

In this thesis, we conduct a comprehensive investigation into structural instabilities of both elastic and magneto-elastic beams and shells, resulting in a creative proposal to design a programmable braille reader. Methodologically, we combine numerical simulations using the finite element method, precision model experiments, and theoretical modeling. Through our studies, we enhance the understanding of fundamental aspects of the longstanding problem of imperfection-sensitive shell buckling. We also show the potential for groundbreaking applications in functional magneto-active structures.

First, we examine the effect of defect geometry on the buckling strength of pressurized spherical shells. A comparative study between dimpled and bumpy Gaussian defects reveals that shells with the latter exhibit higher knockdown factors than their dimpled counterparts. An interpretation based on curvature profiles adds support to the findings. Second, we address the importance of imperfection sensitivity in predicting the buckling of spherical shells, a canonical challenge in structural mechanics. We focus on the mechanical response of pressurized spherical shells containing a single defect to a point probe. We quantify the nonlinear force-indentation response of these shells under indentation, seeking to predict their critical buckling capacity non-destructively. We examine systematically how the location of the indentation affects the probing efficacy. We show that non-destructive prediction of the onset of buckling is only attainable when the probe is close to the defect.

Third, we present preliminary results from an ongoing investigation into the probing of spherical shells containing a random distribution of defects. Following a probabilistic approach using a large data set obtained from finite element simulations, we analyze the indentation of shells with stochastically located defects. Our findings reveal that the accuracy of the extrapolated (non-destructive) outcomes, including the prediction of the actual knockdown factor, depends strongly on the chosen extrapolation method. Nevertheless, we find that adopting a conservative extrapolation threshold yields a safe lower bound for the knockdown factor, even if these predictions are overly conservative.

Fourth, we turn to bistable, hard-magnetic, elastic beams, combining experiments, finite element modeling, and a reduced-order theory to examine their response under combined mechanical and magnetic loading. The beam, with antiparallel magnetization, exhibits reversible snapping between two stable states. Critical field strengths and high-order deformation modes are characterized using a numerical framework that is first validated against experiments. Additionally, we explore the interplay of magnetic loading and a poking force, providing an understanding of these magneto-elastic structural elements. Finally, we tackle the computational design of programmable braille readers. Leveraging bistable shell buckling, magnetic actuation, and pneumatic loading, a building block, the "dot", is conceptualized. The design process is guided by finite element simulations, which are first validated through experiments on a scaled-up model. The results show the feasibility of selecting design parameters that fulfill geometric and force requirements imposed by Braille standards. The proposed bistability and rapid switching capabilities promise to advance accessibility to tactile information.

Key words: Mechanics of shells, spherical shells, shell buckling, non-destructive probing technique, probabilistic shell buckling, Magneto-rheological elastomer, bistable structures, snap buckling, braille reader

Résumé

Dans cette thèse, nous menons une étude approfondie sur les instabilités structurelles des poutres et des coques élastiques et magnéto-élastiques, qui débouche sur une proposition créative de conception d'un lecteur de braille programmable. Sur le plan méthodologique, nous combinons des simulations numériques utilisant la méthode des éléments finis, des expériences modèles et une modélisation théorique. Grâce à nos études, nous améliorons la compréhension des aspects fondamentaux du problème de longue date du flambage des coques sensible aux imperfections. Nous montrons également le potentiel d'applications dans les structures magnéto-actives fonctionnelles.

Tout d'abord, nous examinons l'effet de la géométrie des défauts sur la résistance au flambage des coques sphériques pressurisées. Une étude comparative entre les défauts gaussiens à fossettes et les défauts gaussiens bosselés révèle que les coques avec ces derniers présentent des facteurs de déformation plus élevés que leurs homologues à fossettes. Une interprétation basée sur les profils de courbure vient étayer les résultats.

Deuxièmement, nous abordons l'importance de la sensibilité aux imperfections dans la prévision du flambage des coques sphériques, un défi canonique en mécanique structurelle. Nous nous concentrons sur la réponse mécanique de coques sphériques pressurisées contenant un seul défaut à une sonde ponctuelle. Nous quantifions la réponse non linéaire de ces coques sous indentation, en cherchant à prédire leur capacité critique de flambage de manière non destructive. Nous examinons systématiquement comment l'emplacement de l'indentation affecte l'efficacité du sondage. Nous montrons que la prédiction non destructive du début du flambage n'est possible que lorsque la sonde est proche du défaut.

Troisièmement, nous présentons les résultats préliminaires d'une étude en cours sur le sondage de coquilles sphériques contenant une distribution aléatoire de défauts. En suivant une approche probabiliste utilisant un large ensemble de données obtenues à partir de simulations par éléments finis, nous analysons l'indentation de coquilles avec des défauts localisés de manière stochastique. Nos résultats révèlent que la précision des résultats extrapolés (non destructifs), y compris la prédiction du facteur d'enfoncement réel, dépend fortement de la méthode d'extrapolation choisie. Néanmoins, nous constatons que

l'adoption d'un seuil d'extrapolation conservateur permet d'obtenir une limite inférieure sûre pour le facteur d'abattage, même si ces prédictions sont trop conservatrices.

Quatrièmement, nous nous intéressons aux poutres élastiques bistables, dures et magnétiques, en combinant des expériences, une modélisation par éléments finis et une théorie d'ordre réduit pour examiner leur réponse sous une charge mécanique et magnétique combinée. La poutre, avec une magnétisation antiparallèle, présente claquage ; une transition de flambage, discontinue et réversible, entre deux états stables entre deux états stables. Les intensités de champ critiques et les modes de déformation d'ordre élevé sont caractérisés à l'aide d'un cadre numérique qui est d'abord validé par rapport aux expériences. En outre, nous explorons l'interaction de la charge magnétique et d'une force d'indentation, ce qui permet de comprendre ces éléments structurels magnéto-élastiques. Enfin, nous nous attaquons à la conception computationnelle de lecteurs de braille programmables. En s'appuyant sur le flambage bistable de la coque, l'actionnement magnétique et une charge pneumatique, un brique de base, le "point", est conceptualisé. Le processus de conception est guidé par des simulations par éléments finis, qui sont d'abord validées par des expériences sur un modèle à échelle réduite. Les résultats montrent qu'il est possible de sélectionner des paramètres de conception qui répondent aux exigences géométriques et de force imposées par les normes Braille. La bistabilité proposée et les capacités de commutation rapide promettent de faire progresser l'accessibilité à l'information tactile.

Zusammenfassung

In dieser Arbeit führen wir eine umfassende Untersuchung der strukturellen Instabilitäten von elastischen und magnetoelastischen Balken und Schalen durch, die in einem kreativen Vorschlag zur Entwicklung eines programmierbaren Braille-Lesegeräts mündet. Methodisch kombinieren wir numerische Simulationen mit der Finite-Elemente-Methode, Präzisionsmodellexperimente und theoretische Modellierung. Durch unsere Studien verbessern wir das Verständnis grundlegender Aspekte des seit langem bestehenden Problems des imperfektionsempfindlichen Schalenknickens. Wir zeigen auch das Potenzial für bahnbrechende Anwendungen in funktionalen magneto-aktiven Strukturen.

Zunächst untersuchen wir die Auswirkung der Defektgeometrie auf die Knickfestigkeit von unter Druck stehenden Kugelschalen. Eine vergleichende Studie zwischen vertieften und genoppten Gauß-Defekten zeigt, dass Schalen mit letzteren höhere Knickfaktoren aufweisen als ihre genoppten Gegenstücke. Eine Interpretation auf der Grundlage von Krümmungsprofilen untermauert die Ergebnisse.

Zweitens befassen wir uns mit der Bedeutung der Empfindlichkeit von Defekten bei der Vorhersage des Knickens von Kugelschalen, einer klassischen Herausforderung in der Strukturmechanik. Wir konzentrieren uns auf die mechanische Reaktion von unter Druck stehenden Kugelschalen, die einen einzelnen Defekt enthalten, auf eine Punktsonde. Wir quantifizieren die nichtlineare Kraft-Eindruck-Reaktion dieser Schalen unter Eindrücken und versuchen, ihre kritische Knickkapazität zerstörungsfrei vorherzusagen. Wir untersuchen systematisch, wie sich der Ort der Einkerbung auf die Wirksamkeit der Prüfung auswirkt. Wir zeigen, dass eine zerstörungsfreie Vorhersage des Knickbeginns nur möglich ist, wenn sich die Sonde nahe am Defekt befindet.

Drittens stellen wir vorläufige Ergebnisse einer laufenden Untersuchung der Sondierung von Kugelschalen mit einer zufälligen Verteilung von Defekten vor. Mit Hilfe eines probabilistischen Ansatzes und eines großen Datensatzes, der aus Finite-Elemente-Simulationen stammt, analysieren wir die Vertiefung von Schalen mit stochastisch verteilten Defekten. Unsere Ergebnisse zeigen, dass die Genauigkeit der extrapolierten (zerstörungsfreien)

Ergebnisse, einschließlich der Vorhersage des tatsächlichen Abschlagfaktors, stark von der gewählten Extrapolationsmethode abhängt. Wir stellen jedoch fest, dass die Annahme einer konservativen Extrapolationsschwelle eine sichere untere Grenze für den Knockdown-Faktor ergibt, selbst wenn diese Vorhersagen zu konservativ sind.

Viertens wenden wir uns bistabilen, hartmagnetischen, elastischen Balken zu, wobei wir Experimente, Finite-Elemente-Modellierung und eine Theorie reduzierter Ordnung kombinieren, um ihre Reaktion unter kombinierter mechanischer und magnetischer Belastung zu untersuchen. Der Balken mit antiparalleler Magnetisierung zeigt ein reversibles Einschnappen zwischen zwei stabilen Zuständen. Kritische Feldstärken und Verformungsmoden höherer Ordnung werden mithilfe eines numerischen Rahmens charakterisiert, der zunächst anhand von Experimenten validiert wird. Darüber hinaus wird das Zusammenspiel von magnetischer Belastung und einer Stoßkraft untersucht, um ein Verständnis für diese magnetoelastischen Strukturelemente zu gewinnen.

Schließlich befassen wir uns mit dem rechnerischen Entwurf von programmierbaren Braille-Lesegeräten. Mit Hilfe von bistabiler Schalenverformung, magnetischer Auslösung und pneumatischer Belastung wird ein Baustein, der "Punkt", konzipiert. Der Entwurfsprozess wird durch Finite-Elemente-Simulationen geleitet, die zunächst durch Experimente an einem vergrößerten Modell validiert werden. Die Ergebnisse zeigen die Machbarkeit der Auswahl von Designparametern, die die geometrischen und Kraftanforderungen der Braille-Normen erfüllen. Die vorgeschlagene Bistabilität und die schnellen Umschaltmöglichkeiten versprechen, die Zugänglichkeit zu taktilen Informationen zu verbessern.

Contents

Acknowledgements	i
Abstract (English/Français/Deutsch)	iii
1 Introduction	1
1.1 Shells Structures and Their Application	4
1.2 Shell Buckling and the Imperfection Sensitivity	6
1.3 Non-Destructive Probing Technique for Shell Structures	14
1.4 Magneto-Rheological Elastomers and Their Applications	17
1.5 Modeling of Magneto-Rheological Elastomers	22
1.5.1 Does the Stretching of MREs Affect the Magnetization?	27
1.5.2 Slender Magneto-Active Structures and Dimensional Reduction	29
1.6 Research Niche and Overall Goal of the Thesis	33
1.7 Outline of the Thesis	35
2 Buckling of Spherical Shells with Dimpled and Bumpy Defects	39
2.1 Literature Review and Motivation	40
2.2 Finite Element Simulations	41
2.3 Knockdown Factor of Bumpy versus Dimpled Shells	44
2.4 Why are Bumpy Shells Stronger than Dimpled Shells?	49
2.5 Summary and Outlook	52
3 Probing the Buckling of Spherical Shells	55
3.1 Literature Review and Motivation	56
3.2 Problem Definition: Non-Destructive Probing of Spherical Shells	58
3.3 Experimental Methods	59
3.3.1 Fabrication of the Imperfect Shell Specimens	60
3.3.2 Predicting the Thickness of the Shell Obtained from Fabrication	61
3.3.3 Characterization of the Shell Geometry	63
3.3.4 Experimental Apparatus and Protocol for the Probing Technique	66
3.4 Numerical Simulations Using the Finite Element Method	68

3.5	Results on Indentation of Pressurized Imperfect Spherical Shells	69
3.5.1	Probing the Shell at the Center of the Defect	69
3.5.2	Can We Probe the Buckling of Spherical Shells Using Indentation?	71
3.5.3	Localized Deformation of Pressurized Spherical Shells under Indentation	74
3.5.4	Characteristic Length of Indentation in Spherical Shells	75
3.6	Summary and Outlook	80
4	Probabilistic Non-Destructive Probing of Spherical Shells	83
4.1	Literature Review and Motivation	84
4.2	Definition of the Problem	85
4.3	Finite Element Simulations	89
4.4	Case I: The Shell Configuration as the Random Variable	90
4.4.1	Effects of Defect Amplitude and Extrapolation Method on Poking Predictions	98
4.5	Case II: the Indentation Location as the Random Variable	102
4.6	Summary and Outlook	106
5	Snap Buckling of Bistable Magnetic Beams	109
5.1	Literature Review and Motivation	110
5.2	Problem Definition: Snap Buckling of Bistable Magnetic Beams	112
5.3	Experimental Methods through Snap Buckling Process	114
5.3.1	Fabrication of the Beam Specimens	115
5.3.2	Preparation of the MRE	115
5.3.3	Fabrication and Magnetization of Beam Specimens	116
5.3.4	Experimental Apparatus	116
5.3.5	Experimental Protocols	119
5.4	Numerical Simulations Using FEM	120
5.4.1	User Element for Riks Analysis	120
5.4.2	Simulation Procedure	122
5.5	A reduced-Order Model for the Snapping of Magnetic Beams	123
5.5.1	Linearized Theory with $\epsilon \ll 1$ and $ \theta \ll 1$	126
5.6	Snapping under Poking Force	128
5.7	Snapping under Magnetic Loading	129
5.8	Snapping under Combined Poking Force and Magnetic Loading	131
5.9	Summary and Outlook	134
6	Snapping of Bistable Magnetic Shells for Braille Reader Design	137
6.1	Literature Review and Motivation	138
6.2	Problem Definition: Braille Reader Design Concept	139

6.3	Experiments with the Scaled-up System	142
6.4	Finite Element Modeling Simulations	145
6.5	Validation of the FEM Simulations Against Experiments	147
6.6	Design of Braille Dots at the Real Scale	150
6.7	Design Improvement Using a Pneumatic System	152
6.8	Expected Challenges to Fabricate at-Scale Braille Dots	154
6.9	Designing a Solenoid for a Braille Reader	154
6.10	Summary and Outlook	157
7	Conclusion and Perspectives	159
7.1	Summary of Findings	159
7.2	Opportunities for Future Work	163
7.3	Final Remarks	164
A	Appendix: Defect-Defect Interactions in Spherical Shells	167
A.1	Problem Definition	168
A.2	Methodology: FEM Simulations	171
A.3	Hypothesis for the Defect-Defect Interaction Regime	172
A.4	Interactions between Two Identical Defects	173
A.5	Interactions between Two Different Defects	177
A.6	Summary and Outlook	179
	Bibliography	210
	Curriculum Vitae	

1 Introduction

From the early days of Euler Bernoulli’s foundational work on structural mechanics to the groundbreaking contributions of Germain, Navier, Kirchhoff, and Von Kármán, the study of slender structures during the past few decades has experienced a significant revival across various fields of engineering and physics [1]. Slender structures are characterized by at least one dimension with a length scale significantly smaller than the others, exhibiting unique mechanical behaviors that are strongly rooted in nonlinear geometry and different from their bulk counterparts [2]. Understanding the behavior of this class of structures is crucial for designing and analyzing a wide range of systems, from bridges and aerospace structures to nanoscale devices [3, 4, 5, 6, 7, 8, 9]. The mechanics of slender structures encompass a diverse range of phenomena, including their deformation, (in)stability, and response to external loads [10]. Of particular interest are the buckling phenomena, where a slender structure undergoes sudden and catastrophic failure due to compressive loads [1, 11]. The buckling of slender structures is influenced by various factors such as geometry, geometric imperfections, material properties, and boundary conditions [12]. Therefore, rationalizing these factors is crucial for designing and optimizing performance and reliability [1]. In this thesis, we delve into the mechanics of slender structures, particularly thin shell structures (see Figure 1.1). Our main focus is on understanding their buckling instability from a fundamental point of view. We also exploit the mechanical instabilities of slender structures as opportunities for scalable, reversible, and robust functional mechanisms that can first be predictively understood and then harnessed for function.

A shell is a slender structure comprising a solid bulk material bounded by two curved surfaces, with the distance between them (the shell thickness, h) being small compared to all other length scales of the structure (*e.g.*, the radius, R , for spherical shells) [16]. Shell structures are critical components in nature and engineering across a wide range of

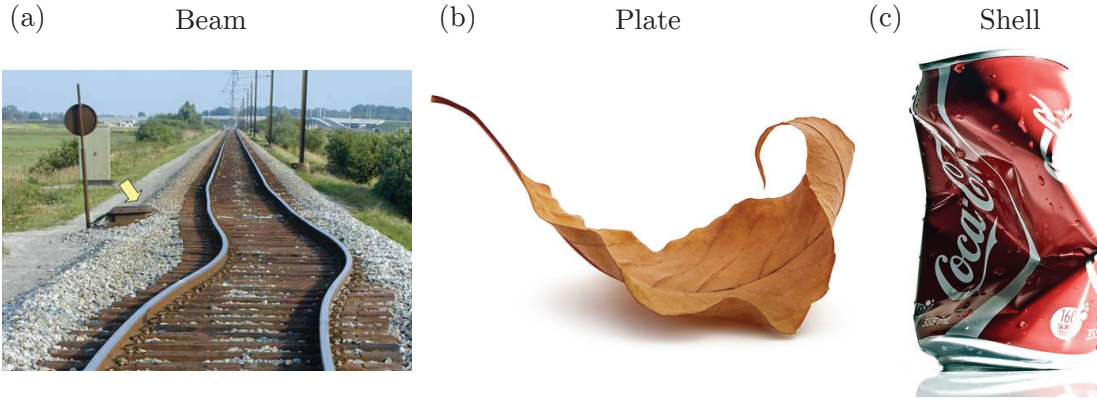


Figure 1.1: **Instability of slender structures.** Sample of one- (a), two- (b), and three-dimensional (c) slender structures. (a) Large lateral misalignments result in catastrophic derailments in the continuous welded rail (CWR) track. Image adapted from Ref. [13]. (b) Cell changes cause buckling of dead leaves due to compression. Image adapted from Ref. [14]. (c) The axial compression on a Coke Can causes it to buckle. Image adapted from Ref. [15].

length scales [17]. The majority of them play a critical role in protecting their contents, making them an essential aspect of structural design [18], where their failure is often undesirable. Shell buckling, as a mode of failure, has long been a canonical problem in the structural mechanics community that can severely compromise the mechanical integrity of the entire system [11]. Hence, it is necessary to address the shortcomings of shell buckling to improve the efficiency and reliability of these structures, which, despite many decades of research, still calls for further, much-needed investigations.

In recent years, there has been a growing interest in exploring the interaction between internal degrees of freedom of the structures and material strains, opening up opportunities for exploring novel structural instabilities within the fields of engineering design and advanced functional materials [19, 20]. Mastering the mechanisms underlying instability could lead to the conception of novel mechanical systems that harvest instability as a route to new functionalities [21]. The elastic buckling of slender structures is a promising way to achieve large, reversible, and out-of-plane deformations to generate advanced functionality [21]. Therefore, it is essential to note that taking full advantage of the buckling and post-buckling regime requires new fundamental approaches for numerical, experimental, and theoretical analysis. Snap-through instabilities are another intriguing aspect of this class of structures [22], which enables rapid deformations. When an elastic object reaches a critical criterion, an elastic object rapidly jumps from one state to another, paving the way for various applications [23, 24, 25]. This snap-through instability presents a unique opportunity to explore a different structural behavior, which complements the more gradual deformations associated with elastic buckling.

Combining slender structures with active materials and non-mechanical stimuli has emerged as a fascinating field of research with diverse applications [26, 27, 28, 29]. Although the mechanical stimuli can cause significant bulk deformation, the time scales for the actuation processes can be relatively long, which might not be optimal in scenarios where rapid actuation is necessary [30, 31]. In contrast, the interplay between external stimuli and elasticity offers a valuable pathway for achieving remote and controllable actuation, with magnetism being a common example [32, 33, 34]. More specifically, magneto-active slender structures made of magneto-rheological elastomers (MREs) have emerged as an active and exciting research area [35]. MREs are smart composite materials that exhibit changes in their mechanical behavior under the influence of an external magnetic field [32]. These structures possess the unique ability to dynamically alter their mechanical properties in response to an external magnetic field, making them highly versatile and controllable for a wide range of applications, from soft robotics [36, 37, 38] to biomedical devices [39]. Thus, rationalizing the mechanics of these structures is crucial for unlocking their full potential.

Drawing upon insights acquired through exploring structural instabilities and their potential for new functionality, this thesis embarks on a comprehensive investigation into the intriguing domain of instability of slender structures. In particular, we will revisit the imperfection sensitivity in shell buckling and explore a non-destructive testing method for probing their (in)stability with modern research tools, including numerical simulations and precision experiments, to rationalize the fundamentals of shell buckling. Our findings will contribute to developing more accurate and predictive models for shell stability, paving the way for the design of safer and more practical structures. Furthermore, we harness the mechanical instabilities of bistable slender structures as opportunities for novel modes of functionality –*Buckliphilia*– instead of the more traditional view of instabilities as the first route for damage or failure –*Buckliphobia* [21]. Subsequently, we will turn to coupling magnetism and elasticity to study magneto-active slender structures. Through a thorough analysis of magnetically induced buckling phenomena, this thesis study aims to contribute to the fundamental understanding and practical implementation of magneto-active slender structures.

This introductory chapter is organized as follows. In Section 1.1, we first provide a brief overview of the literature on the mechanics of spherical shells, their applications, and failure mechanisms. Section 1.2, is dedicated to the important aspect of imperfection sensitivity of shell buckling. Then, in Section 1.3, we describe recent advances on a non-destructive probing technique to estimate the buckling capacity of shell structures. We review recent studies on magneto-rheological elastomers (MREs) and their characteristics and applications in Section 1.4. In Section 1.5, we discuss the history of numerical

modeling and finite element simulation for analyzing structures made of these MRE materials. We also focus on the actuation of MRE slender structures (shells, plates, and beams) and investigate their (in) stability and modes of deformation. In Section 1.6, we describe our research niche and the research questions that will be addressed through the thesis. Finally, in Section 1.7, we present the thesis outline.

1.1 Shells Structures and Their Application

In the field of structural engineering, shells constitute a remarkable category of structures designed to distribute loads and stresses efficiently through their curved surfaces while maintaining a lightweight construction due to their slim profile [40], making them highly desirable for a wide range of applications. The mechanism underlying the load-bearing capacity exhibited by shells confers significant benefits compared to other classes of structural elements, such as beams, trusses, or plates [11]. These advantages include exhibiting high stiffness and geometry-induced rigidity [41], possessing significant strength and structural integrity, effective load-carrying capacity, offering a high strength-to-weight ratio, and providing space containment [42].

Shells are a versatile structural type found countlessly throughout nature and engineering since antiquity [43, 44]. In Figure 1.2, we present several examples of shells across length scales, characterized into two distinct categories: natural shells and engineered shells. In nature (Figures 1.2a, b, c), small-scale shell structures such as pollens play a vital role in facilitating the reproductive process in flowering plants [43]. These tiny structures have evolved to aid in pollination [45] (Figure 1.2a). Nature showcases sub-meter scale shells in various living forms (Figure 1.2b). For instance, animals that possess shells, like pangolin [46], exhibit natural shells in the animal domain. Among living organisms, human skulls [47] is another remarkable example of natural shell structures that encapsulate and protect the vital brain within the human anatomy. Other examples include eggshells [48] and coconut shells [49], which possess protective and structural qualities (Figure 1.2b). Nature also exhibits shell structures at much larger scales. One remarkable example is the Algarve cave [50] (Figure 1.2c), a natural formation that showcases the magnitude and beauty of shell-like structures on a grand scale.

Throughout history, humans have accumulated knowledge and expertise in harnessing the utility of shells for both individual and societal benefits, encompassing primitive and purposeful approaches [42]. Engineered shell structures find applications in various fields at different length scales (see Figures 1.2d, e, f, g, h, and i). In the pharmaceutical industry, centimeter-scale shell structures are used in the form of capsules [51] (Figure 1.2d). These capsules act as protective shells for medications, ensuring their stability and controlled



Figure 1.2: **Exploring shell structures across length scales: in nature (a, b, c) and engineering (d, e, f).** In nature, shells can be observed at (a) small-scale, *e.g.* pollen grains, (b) at a sub-meter scale, such as animal shells, human skulls, eggshells, and coconut shells, and (c) spanning hundreds of meters like the Algarve cave. In engineering, shells can find their application in (d) pharmaceuticals, notably in capsules at a small scale, (e) the hand-made pottery at the sub-meter scale. The engineered shell structures at the hundreds of meters scale can be found in (f) the civil structures and (g) aerospace structures such as the airplanes, (h) space shuttles and (i) satellites. These images in (a), (b), (c), (d), (e), (g), (h), and (i) were adopted from Refs. [45], ([46], [47], [48], [49]), [50], [51], [52], [53], [54], and [55], respectively.

release. Looking back through history, we find that skilled artisans have created beautiful designs and textures in handmade pottery, drawing inspiration from the intricate patterns in natural shells. This centuries-old tradition highlights the enduring appeal and artistic expression that shells have offered [52] (Figure 1.2e). Engineering shell structures are also commonly employed in civil engineering, spanning hundreds of meters. These structures construct visually striking and structurally efficient buildings while serving as architectural wonders that blend aesthetics and engineering principles to create captivating structures such as the masterpiece Duomo Santa Maria del Fiore in Florence (Figure 1.2f).

One of the main applications of engineered shell structures in the 20th century at hundreds

of meters was in the aerospace industry [56]. Shells have played a pivotal role in designing and constructing critical engineering components of aerospace vehicles, including airplanes (Figure 1.2g), space shuttles (Figure 1.2h), and satellites (Figure 1.2i). In aviation, aircraft designers have harnessed the structural efficiency of shell structures to create lightweight yet robust fuselages, wings, and control surfaces [57]. These aerodynamic shells contribute to reduced drag and improved fuel efficiency and ensure the structural integrity required for safe and reliable flight [58]. In space exploration, the development of space rockets and shuttles relied on shell structures to withstand the extreme conditions of launch and re-entry and provide habitable environments for astronauts during missions [59]. The unique combination of strength and low weight inherent in shell structures proved invaluable for the success of space programs [59]. Shell structures have also been employed in designing and constructing satellites, where their lightweight and space-efficient properties are crucial for placing payloads into orbit [60]. By exploring the application of shell mechanics in these aerospace contexts, researchers have not only pushed the boundaries of engineering but have also contributed to the advancement of space exploration and air travel [61].

These three-dimensional curved structures can be classified into two categories: singly curved (shows curvature in one direction) and doubly curved (shows curvature in two directions) surfaces, exemplified by cylindrical and spherical shells, respectively [62]. A spherical shell, which can be seen as an extension of an annulus into three dimensions, represents the region of a ball confined by two concentric spheres of varying radii [63]. A cylindrical shell is a three-dimensional region enclosed by two circular cylinders sharing the same axis and featuring two parallel annular bases perpendicular to the common axis [64]. Understanding the fundamental characteristics of these shell structures is pivotal, as it forms the basis for optimizing their performance and ensuring structural integrity. Specifically, this thesis focuses on exploring the mechanics and harvesting functionality through the instability of spherical shells. We will delve into their buckling behavior and stability landscape under various loading conditions. By gaining deeper insights into the mechanics of spherical shells, this research aims to pave the way for engineering advancements, offering innovative solutions for developing robust and efficient shell structures suitable for diverse applications in the modern world.

1.2 Shell Buckling and the Imperfection Sensitivity

The history of research on the mechanics of shells reflects a captivating journey through engineering and mathematics [65]. Beginning in the 15th century, the polymath Leonardo da Vinci explored the principles of thin structures amongst a myriad of other topics

and set the stage for centuries of exploration in this class of systems [66]. Da Vinci's keen observations and sketches laid the groundwork for understanding the behavior of curved structures under various loading conditions [66]. Advancing into the 17th century, Galileo Galilei's experiments on the strength of materials, coupled with his investigations of the strength and deformation of shells, contributed essential insights into the field and provided valuable empirical knowledge [67], and the study of shell mechanics gained further momentum [67]. In the 18th century, the Swiss mathematician Leonhard Euler made groundbreaking contributions to the theory of elasticity and the mathematical understanding of shell structures, which laid the foundation for subsequent mathematical developments in shell theory [68]. At the start of the 19th century, researchers such as Cauchy and Gauss further advanced the mathematical underpinnings of shell mechanics. Their work in differential geometry and the theory of surfaces significantly contributed to the theoretical framework for understanding curved structures [69, 70].

However, it was not until the 20th century that the field truly matured, thanks to the groundbreaking contributions and the key advancements of eminent figures such as Love, who developed the theory of elasticity for thin shells [71], Mindlin, who introduced the concept of transverse shear deformation in shells [72], Donnell [73] who provided a simplified approach to analyzing of moderately thick shells, Reissner [74] who brought about the modern understanding of shell behavior, and Koiter, Sander, and Budiansky [75, 76, 11] who made an influential contribution to the development of shell theories. These developments intertwined theories of elasticity, plasticity, and geometry, leading to the design innovations of remarkable shell structures today [61].

We can infer important implications for the mechanical behavior of shells by examining the fundamental differences between shells and plates when they are in their original, unstressed forms. Unlike a plate structure, which is flat at rest, a shell structure exhibits curvature in its undeformed configuration (Figure 1.3a). This fundamental difference holds significant importance for the mechanical behavior of shells [77]. The deformation of plates primarily involves bending energy, with stretching energy often being negligible. In contrast, in shells, due to the existence of curvature and their particular geometry, bending and stretching energies are intrinsically coupled and of the same order of magnitude in resistance to external loads, evenly distributing the forces across their surfaces [77]. This distinction between shell and plate structures forms the basis for understanding the mechanical properties and design considerations associated with these structural elements, making them ideal for applications with more complex loading conditions [77].

This difference between the mechanical response of plate and shell structures can also be demonstrated by comparing the critical buckling stress. Considering a shell of radius R and thickness h under external radial compression loading and a circular plate with

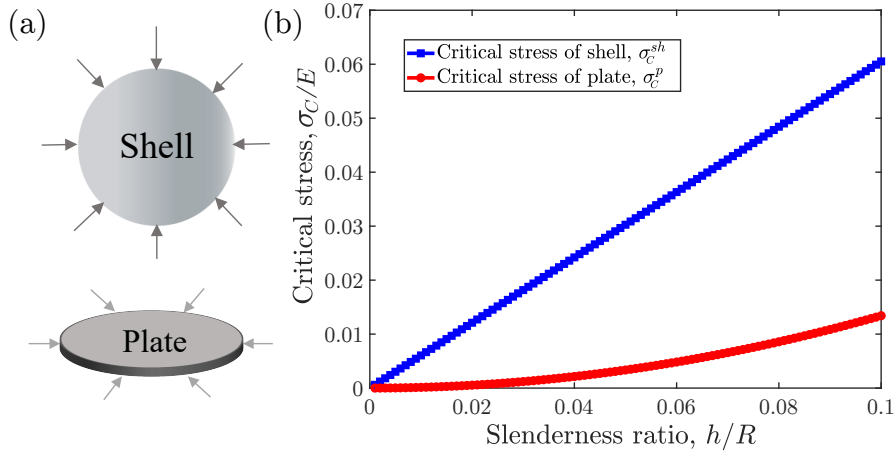


Figure 1.3: **Shell versus plate structures.** The normalized critical buckling stress of shell, σ_C^{sh}/E , and plate, σ_C^p/E , structures versus their slenderness ratio h/R , with fixed Poisson ratio of $\nu = 0.3$.

the same radius of R and thickness of h under radial in-plane compression, the critical buckling stress can be written for a spherical shell as,

$$\sigma_C^{sh} = 2 \frac{\sqrt{DS}}{Rh} = \frac{E}{\sqrt{3(1-\nu^2)}} \frac{h}{R}, \quad (1.1)$$

and for a circular plate as,

$$\sigma_C^p = 14.6 \frac{D}{R^2 h} = 1.22 \frac{E}{(1-\nu^2)} \left(\frac{h}{R} \right)^2, \quad (1.2)$$

where E and ν are the Young's modulus, and Poisson's ratio and $D = Eh^3/12(1-\nu^2)$, and $S = Eh$, are the bending stiffness and the stretching stiffness of the shell and plate structures. Figure 1.3(b) shows an illustrative plot of the critical stress of a shell, σ_C^{sh}/E (Equation 1.1), and a plate, σ_C^p/E (Equation 1.2), as a function of their slenderness ratio, h/R . Considering the same slenderness ratio in both structures, shell structures can carry significantly higher loads prior to buckling compared to their plate counterparts due to the shell effect [2].

The buckling of thin shells has long been a research subject in the structural mechanics community [78, 79, 80], and the prediction of critical loads is at the basis of their design [81, 6]. Thin shells come in various geometries, each with its own unique characteristics and challenges in mechanical design. As already mentioned above, two common types of shells are spherical shells and cylindrical shells. For a spherical shell, one of the most commonly used geometries in engineering structures, the critical load under a uniform pressure loading was first proposed by Zoelly [82] in 1915, based on a linear buckling

analysis,

$$p_c = \frac{2E}{\sqrt{3(1-\nu^2)}} (\eta)^{-2}, \quad (1.3)$$

where $\eta = R/h$ is the slenderness ratio of the shell. Notwithstanding, subsequent studies [83, 84, 85, 86, 87, 88] evidenced that this prediction, p_c , was in systematic disagreement with experimental measures of the buckling pressure, p_{\max} , consistently yielding overestimates. Trying to bring together these two elements has been a fundamental aspect of structural mechanics [80]. The ratio between p_{\max} and p_c is classically referred to as the *knockdown factor*,

$$\kappa = \frac{p_{\max}}{p_c}, \quad (1.4)$$

which can be as low as 0.2 in practical structures (i.e., 80% lower than the value predicted by theory; Equation 1.3) [89]. In reverse, $\kappa = 1$ for a perfect spherical shell.

This inconsistency between classical theoretical predictions and measurements was explored by the survey of classical and new experimental measurements of the knockdown factor as a function of radius to thickness ratio (plotted in Figure 1.4) for shells under compression. In these historical experimental studies, for the radius to thickness range of $76 \leq \eta \leq 2834$, the knockdown factor spread in the range $0.17 \leq \kappa \leq 0.9$, and by increasing η , κ decreases with a large spread. The shells made by low precision fabrication techniques such as metal spinning [84, 85], or plastic vacuum drawing [86] had low values of knockdown factor ($0.17 \leq \kappa \leq 0.8$) due to the defects imparted onto a shell during fabrication or operational usage. However, shell structures made through high-precision fabrication techniques, such as machining aluminium [87] and electrodeposition [88], had higher knockdown factors ($0.45 \leq \kappa \leq 0.9$), even if still with considerable scatter. This discrepancy between theory and experiment was eventually attributed to the high imperfection sensitivity of shells, meaning that the load at which a shell buckle depends strongly on defects in the geometry and material heterogeneities [11, 90, 91].

The highly sensitive nature of shells to imperfections required a reliable prediction of the critical buckling load. Early attempts to rationalize the origin of sub-unity knockdown factors were mostly unsuccessful [92, 93, 94, 83]. In 1945, Koiter [11] carried out a breakthrough theoretical work by developing a general theory of stability for elastic systems subject to conservative loading. Following this seminal development, a vast series of studies were subsequently performed to study the fundamental bases of imperfection sensitivity. The defects were identified in geometry [90, 91], loading [95], pre-buckling deformations [96] or boundary conditions [97] as the culprits of the below-unity knockdown

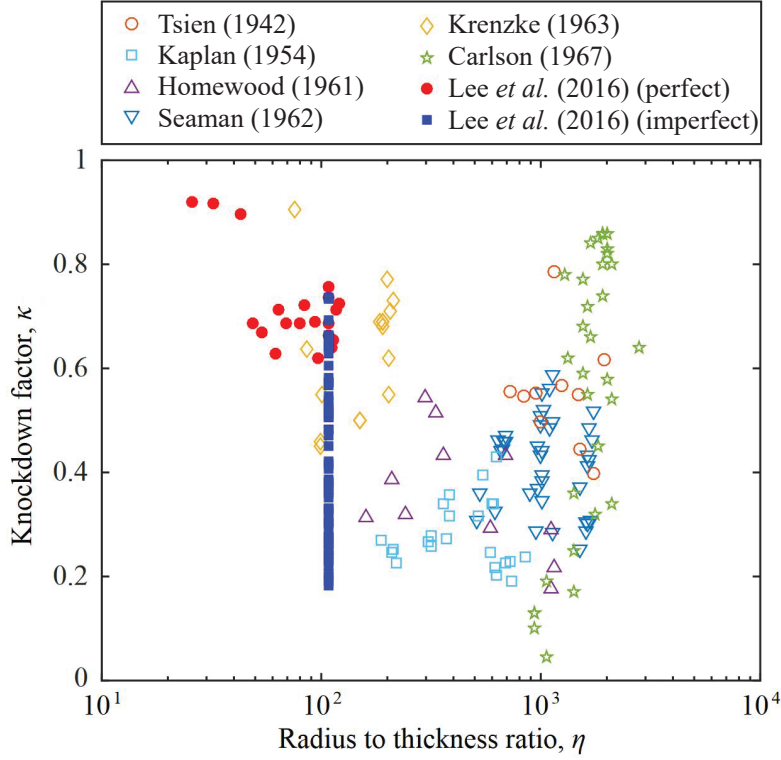


Figure 1.4: **Experimental survey on the knockdown factor of spherical shells.** Knockdown factor, κ , against the radius to thickness ratio, R/t , of spherical shells under pressure. The Figure is adapted from Ref. [89].

factor, $\kappa < 1$. Despite the extensive theoretical and computational studies since Koiter, practical knowledge of shell buckling has remained primarily qualitative, with a striking difficulty in mapping the characterization of the imperfections of a realistic shell into a concrete prediction for its buckling load. Experimental research on shell buckling has long lagged behind the theory and computation [98, 78, 86, 90]. It has become evident that the gap in understanding between theory and practice has been mostly due to a misalignment in the type, quality, and volume of experimental data that was available to provide the necessary physical insight required to construct appropriate models and their validation.

Consequently, for decades, engineers have relied primarily on acquired experience, *ad hoc* guidelines, and over-conservative engineering codes [44]. As part of NASA's endeavor for large shell structures, traditional empirical factors used in design codes were replaced with a new method, which involved initially assessing the manufacturing-specific imperfection signatures and determining the knockdown factors [44, 99]. Given the undeniable importance of the design of engineering shell structures against buckling, which can lead to global failure, the field begs for comprehensive, systematic, and generalizable tools

rooted in a predictive mechanics-based framework that can accurately capture knockdown factors. Early experiments on shells were done on spherical caps fabricated by metal spinning [84, 85], plastic vacuum drawing [86], and machining aluminum [87]. In the 1960s, Thompson [100] and Carlson *et al.* [88] fabricated complete spherical shells by electro-forming, thereby dramatically improving the quality of specimens. However, this technique had drawbacks; the distribution of imperfections could not be systematically varied, and the fabrication process were cumbersome and time-consuming. As such, there was a need for an experimental technique that enabled the fabrication of shells with precision-engineered imperfections of known geometry, which also being sufficiently fast to yield large experimental data sets with a systematic variation of parameters.

Recently, to fill the gap between theory and experiment, Lee *et al.* [101] have revived the experimental research in shell buckling by introducing a rapid, robust, versatile, and precise coating technique to prototype thin spherical shells in a laboratory setting. This fabrication of hemispherical elastic shells was based on the gravity-driven coating of a curved surface with a viscous polymer solution, yielding a nearly uniform shell upon polymerization of the resulting thin film. This technique was later modified to produce a precisely engineered defect of controllable geometry in the shell [89, 102, 103, 104]. Considering the precise defect geometry, for the first time, quantitative relationships between the critical pressure and the geometry of imperfection were obtained by manipulating the defect amplitude, δ [89]. This was achieved through the measurement of the knockdown factor, as illustrated in Figure 1.5. The authors showed that as the amplitude of a single dimple-like defect increases, the knockdown factor decreases until it reaches a plateau, which occurs when the defect amplitude is approximately equal to the shell thickness. A detailed study of the knockdown factor's dependence on geometric parameters of the defect and shell has been conducted [105]. These experimental advances have played an essential role in the revival of the interest in the buckling of both perfect and imperfect shells [106, 107, 108, 109, 105, 110]. However, detailed prior knowledge of the imperfections is still necessary for theoretical or numerical tools to predict the onset of buckling.

Even with the notable progress discussed earlier in the theoretical, experimental, and computational analysis of shells with one defect, numerous unresolved issues persist when considering the more realistic and important scenario of shell buckling caused by multiple imperfections and the possibility of interactions among these defects. The investigation conducted by Wullschleger [111] using nonlinear buckling analysis focused on examining cylindrical shells with two identical dimple imperfections positioned at different distances. The normalized critical buckling load as a function of the circumferential separation for the case of two defects without axial separation (Figure 1.6a) and with

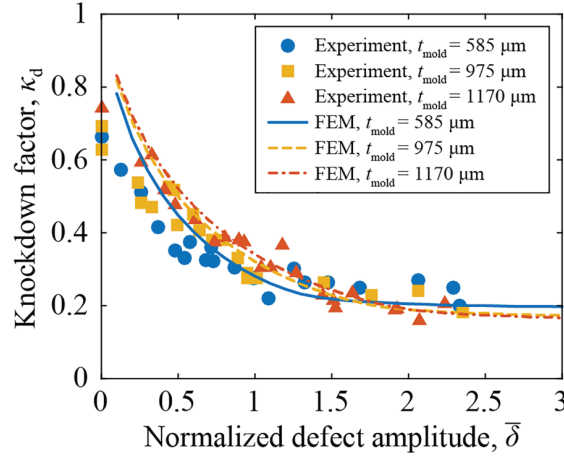


Figure 1.5: **The knockdown factor characterization.** Results obtained from finite element simulations (lines) and experiments (data points) on the relation between the knockdown factor, κ , and the defect geometry. The image is adapted from Ref. [89].

axial separation (Figure 1.6b) was examined. The study by Wullschleger [111] revealed that the interactions between the defects become important when they are near each other and decrease when far apart; at a specific separation, the shell even has a higher buckling capacity than a single defect case. Recently, the impact of defect-defect interactions on the pressure-induced buckling of thin spherical shells containing two dimpled imperfections was investigated [112]; the present author of the thesis collaborated in this reported study (more details are provided in Appendix A). The parameter space, including the angular separation between the defects, the defect geometry, and the radius-to-thickness ratio of the shell, were explored systematically. In Figure 1.6(c) and (d), we plot representative examples of the knockdown factor as a function of the angular separation for the cases of two identical and two different defects, respectively [112]. Qualitatively similar results were observed compared to cylindrical shells with two defects. It was found that the onset of the defect-defect separation for them to interact is set by the critical buckling wavelength reported in the classic shell-buckling literature [113]. Beyond this separation threshold, within the plateau regime, the buckling behavior of the shell is dictated by the largest defect. Additionally, the interaction between two neighboring defects could either reinforce or weaken the shell, depending on the distance between the defects, compared to a single-defect scenario (see Appendix A).

Beyond considering scenarios with only two defects, probabilistic approaches have been suggested to forecast the knockdown factor of cylindrical and spherical shells with a distribution of imperfections. An early study conducted by Amazigo [114] focused on examining cylindrical shells containing axisymmetric defects. They employed a modified truncated hierarchy approach and determined that the spectral density of the random

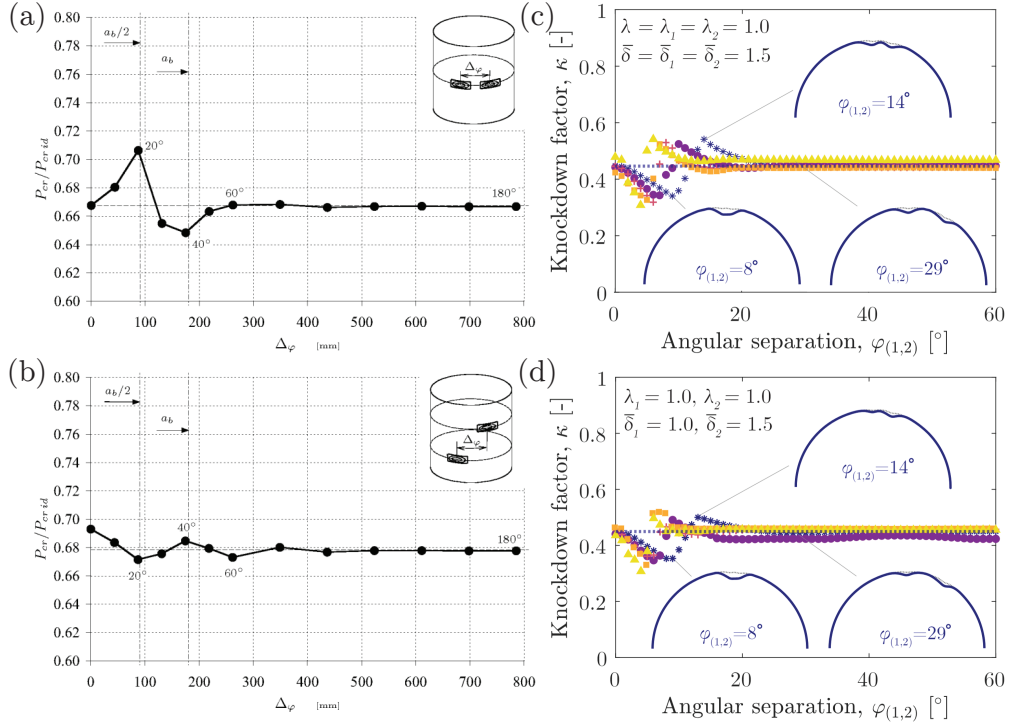


Figure 1.6: **Cylindrical and spherical shells containing two defects.** The normalized buckling load as a function defect separation for a cylindrical shell containing two identical defects (a) without axial distance and (b) with axial distance. The plots are adopted from Ref. [111]. (c) The knockdown factor as a function of angular separation for spherical shells with (c) identical and (d) different defects. The plots are adopted from Ref. [112] which are described in detail in Appendix A.

imperfections influences the ability of the shell to withstand buckling. In a similar investigation on the behavior of imperfect cylindrical shells under axial compression, the Monte Carlo method has been used to statistically study shells containing symmetrical [115] or asymmetrical [116] defects. The investigation showed that probabilistic methods emerged superior to deterministic approaches when evaluating design standards for cylindrical shells. Elishakoff [117] comprehensively examined different probabilistic methods applicable to shell buckling. Recently, Derveni *et al.* [118] examined the realistic case of spherical shells with numerous randomly distributed geometric imperfections on the surface of the shells. These authors discovered that when the amplitude of the defects follows a log-normal distribution, the resulting knockdown factor can be described using a 3-parameter Weibull distribution. This observation categorizes shell buckling as part of a broader group of statistical phenomena known as extreme-value statistics [119, 120, 121, 122, 123, 124].

1.3 Non-Destructive Probing Technique for Shell Structures

As discussed in the previous section, defects significantly impact the ability of thin-walled structures to withstand compression. This finding presents a challenge toward accurately predicting the critical loads at which buckling may occur, as it requires detailed knowledge about the specific characteristics of the defects. Unfortunately, in practice, these defects are often unidentified and can be difficult to detect, which raises the following question: Is there an alternative approach to assessing the stability of shells and categorizing defects non-destructively?

Recently, there have been promising advancements toward developing a general framework to characterize the stability of shells. Therefore, using non-destructive probing techniques or poking from the side to estimate the resistance of shells against buckling loads was proposed [125, 126, 127]. The concept of "probing" can also be linked to the influential study conducted by Eßlinger and Geier in 1972 [128], who explored the effects of tapping cylinders at various levels of axial compression using a finger. While the concept of probing loaded shell structures has been around for some decades [129, 130, 131], it was only in recent years that employing probing as a systematic approach to investigate stability gained traction [127]. This approach was introduced to delve deeper into the exploration of stability landscape in shell structures and to uncover valuable insights into their stability through a low dimensional description and a natural phase-space [130, 125].

The basis of this non-destructive probing approach is to measure the nonlinear force displacement response of the shell to a point probe (Figure 1.7a). Figure 1.7 demonstrate the poking of a compressed cylindrical shell from the side transversely with a controlled displacement. The nonlinear probing response is measured at different levels of compression, and the area under load-displacement curves gives the energy barrier that must be overcome by any static or dynamic lateral disturbances to buckle the shell [130, 125, 132] (see Figure 1.7a). The force-displacement relationship measured by systematically varying the compression level is then used to construct the stability landscape (Figure 1.7b). This novel non-destructive probing technique has been first applied to axially compressed cylindrical shells [130, 125, 126, 127, 133]. Viro *et al.* [127] built an experimental setup to exert a point probe on a cylindrical shell under axial compression (Figure 1.7b). The authors provided experimental evidence that the hyper-dimensional landscape fully characterizes the complex stability of perfect and imperfect cylindrical shells by reducing it to a three-dimensional phase space description that can be analyzed using modern experimental and computational research tools. The ridge can be characterized as the path traced by the peak points of the poker force. Consequently, tracking the ridge down to zero poking force guides spontaneous buckling, and the knockdown factor of cylindrical

shells could be extrapolated correctly.

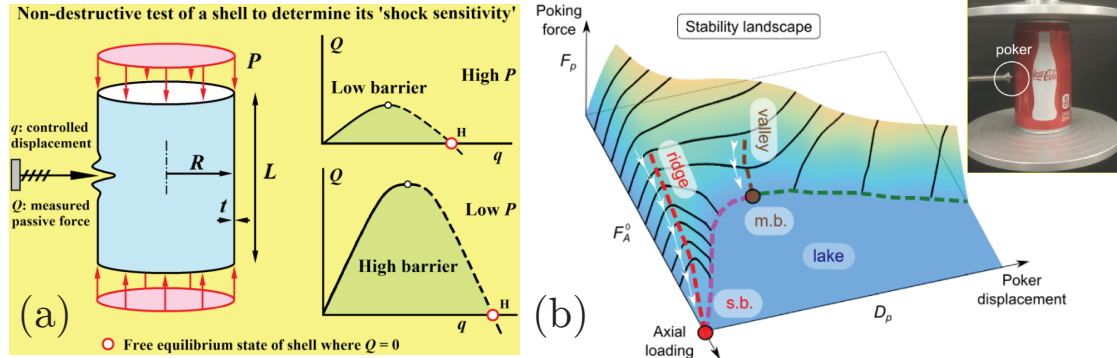


Figure 1.7: **The probing technique for cylindrical shells** (a) Schematic illustration of the proposed probing technique on a cylindrical shell adopted from Ref. [125]. The probing force diagrams are determined at compression levels less than their critical value. (b) An experimental force landscape was created by testing an axially compressed Coke Can specimen by Viot *et al.* [127]. The picture is adopted from Ref. [127].

Horák *et al.* [129] conducted numerical investigations into the energy landscape of cylindrical shells. They investigated various loading conditions of the system along with their associated energy levels. By employing a 'mountain pass' algorithm [129], which is used in the calculus of variations and in finding solutions to nonlinear PDEs, they successfully identified the path of least energy leading to buckling. Interestingly, this path involved a localized equilibrium mode, which differs from the global modes typically obtained through linear stability analysis [1, 134]. Moreover, a new numerical solution was recently proposed, where instead of considering the linear instability of a shell with defects, a finite, nonlinear destabilizing perturbation was imposed on an otherwise perfect shell [133]. In this study, the elastic response of the shell was captured by the Donnell–Mushtari–Vlasov (DMV) theory. The fully nonlinear equilibrium states on the boundary of the unbuckled state's basin of attraction for an axially loaded cylindrical shell were identified. It was shown that, for changes in the applied compression, a single dimple undergoes circumferential snaking, resulting in the circumference being filled with a ring of buckles.

In the series of studies mentioned in the previous paragraph, the non-destructive probing technique was applied to cylindrical thin shells containing local dimple-like imperfections, both computationally [135, 136] and experimentally [127, 137]. The influence of background imperfections and the location of probing relative to the imperfections were considered by examining the robustness of the technique. Abramian *et al.* [138] applied this probing technique to commercial cylinders containing a hole and showed that when the location where buckling nucleates was known, the buckling load of each shell could

be accurately predicted. Ankalhope and Jose [139] showed that the buckling event could be avoided when extrapolating the true buckling load of an imperfect cylinder, but the precision of ridge tracking in evaluating the load-carrying capacity significantly relies on the position of measurement and the distribution of imperfections. The inherent difficulty with this approach was that the resistance to probing would only reach zero if the deformation caused by probing aligns precisely with the natural buckling mode of the cylinder. Therefore, if probing is not performed in a location where the dimple is located (particularly the location of the dominant imperfection [140, 141]), ridge tracking will overestimate the buckling load [137]. Cuccia *et al.* [142] investigated the elastic buckling of thin-shell soda cans with intentional dents, which already possess inherent background imperfections, causing them to buckle at loads well below those of a perfect cylinder. The authors revealed that to identify the most likely initiation site and associated buckling load, the investigation must be conducted with sufficient resolution.

However, despite the body of research summarized above, it remained inconclusive whether the probing technique could serve as an effective way of assessing the stability of *spherical* shells, which parallels the successful case of cylindrical shells in the early studies mentioned above [127]. The response of perfect spherical shells subjected to external uniform pressure with and without a probing force was recently investigated by [107, 108] based on a small-strain and moderate-rotation shell theory formulation, both under prescribed pressure and prescribed volume change. Thompson *et al.* [126] addressed the testing of compressed shell structures using the concept of probing by a controlled lateral displacement to gain quantitative insight into their buckling behavior and to measure the energy barrier against buckling, providing design information about a structure's stiffness and robustness against buckling in terms of energy and force landscapes.

The first experimental study on probing of imperfect spherical shells was carried out by Marthelot *et al.* [102]. They investigated the buckling strength and energy barrier of shells containing a geometric defect subjected to a simultaneous combination of pressure loading and a probing force, demonstrating that the probing strategy applied to the defect successfully assesses the stability of spherical shells. However, considering a point load located off-axis from the defect, the energy barrier measured from the probe was similar to that of a perfect shell but dramatically jumped to zero when buckling occurred. However, these experiments were only conducted in limiting cases; the probe was either located exactly at the center of the defect or far away from the defect. Therefore, there is a need to more systematically explore the response of the spherical shell loaded by a probe located in between the two extreme locations. This timely data would show the limitations and range of applicability of the probing technique in identifying the critical buckling conditions and encoding the characteristics of the stability of spherical shells.

It is within this context that we have performed a thorough investigation into how the response of an imperfect spherical shell is affected by the location(angle) of indentation with respect to the location of the defect; Chapter 3 is dedicated to this research problem.

1.4 Magneto-Rheological Elastomers and Their Applications

In the previous section, we reviewed relevant past literature on the mechanics of shell structures and their buckling phenomena within the domain of linearly elastic materials. We focused on the understanding of the fundamental principles governing the behavior of shells under various loading conditions. As we transition to the next section, our focus shifts towards soft active materials, especially the unique properties of magneto-rheological elastomers (MREs) and active structures harnessing them. Unlike their passive counterparts, MREs can actively adapt and respond to external stimuli, allowing for adaptive and controllable mechanics. This chapter aims to merge the insights gained from the mechanics of slender structures with the potential of active soft materials as we tackle an understanding of linearly elastic and magnetically responsive systems. Eventually, later in this thesis, in Chapter 6, you will combine the mechanics of shells with the active response of MREs.

The general class of soft active materials, distinguished by their mechanical flexibility and capacity to undergo substantial deformations in response to external stimuli, offers the opportunity for creating smart structures and systems across various applications. These applications span diverse fields, from developing sensors [143] and high-performance actuators [28] to tissue engineering [144] and efficient energy harvesting [145, 146]. Various subtypes within this category of materials stand out for their unique capabilities, including photo-activated polymers, which respond to light stimuli [147, 148], shape-memory polymers capable of recovering their original configuration after deformation [149, 150], magnetorheological elastomers (MREs) exhibiting magnetic-field-driven mechanical changes [151, 29, 145], and thermally activated polymers, exhibiting controlled responses to temperature variations [152, 153].

Despite a diverse array of soft active materials, our attention now narrows to a particular subset: magneto-rheological elastomers (MREs). There has been a burgeoning interest in MREs, distinguished by their ability to undergo substantial mechanical deformations under an external magnetic field [32]. MREs offer a unique blend of mechanical flexibility and tunability. The precise control over their mechanical and physical properties through external magnetic fields makes them an enticing subject of study for designing intelligent structures and systems, with a distinctive capacity to respond swiftly and robustly to applied fields, further emphasizing their potential for the design of cutting-edge engineering

solutions [34].

MREs are active composite materials typically consisting of magnetically permeable micron-sized particles homogeneously embedded into a soft polymeric matrix (see Figure 1.8). This unique combination of their structure allows them to possess magnetic properties and the ability to undergo large mechanical deformation. The particles form ordered structures that result in performance enhancements under the influence of a magnetic field. They exhibit a mechanical response that can be adjusted under an external magnetic field [154, 155]. When a magnetic field is applied, it exerts torques and/or forces on the particles within the soft matrix, leading to deformation in the composite material. These materials typically exhibit short response times, enabling them not only to modify their viscoelastic properties and stiffness in response to external magnetic fields but also to undergo substantial deformations.

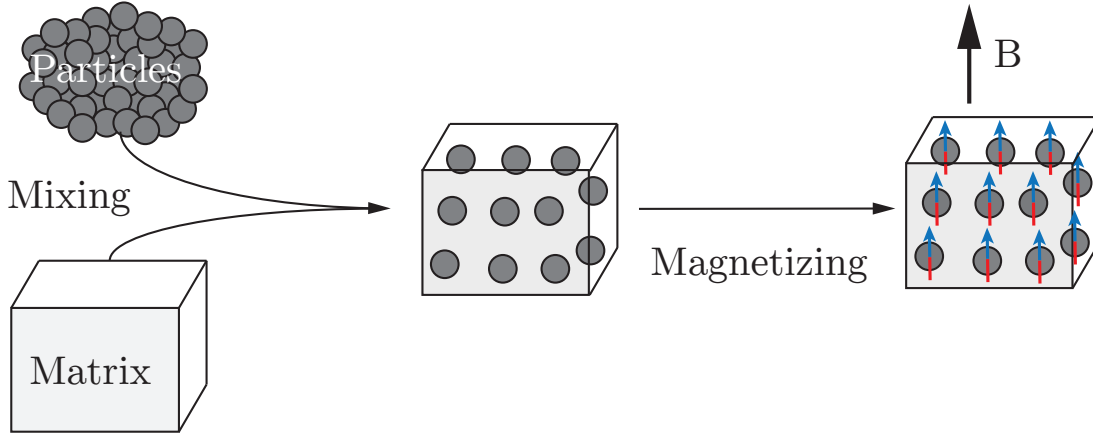


Figure 1.8: **Magneto-rheological elastomer.** The magneto-rheological elastomers are composite materials containing a homogeneous suspension of magnetic particles in a polymeric matrix and exposed to a strong magnetic field in order to align the particles in the direction of the magnetic field and acquire magnetic characteristics.

Over the past few years, MREs have gained significant attention due to their remarkable ability to offer fast, reversible, and remotely controlled shape-shifting behavior [27, 26, 156, 28, 151, 36, 29, 157, 158, 145]. The relationship between mechanics and magnetism in MREs has been utilized in recent studies to create practical devices for a range of applications [26, 27, 28, 29]. Additionally, the latest advancements in materials engineering, simulation, and manufacturing methods of magnetic soft materials, along with the progress in magnetic actuation platforms, have significantly expanded their potential applications in various fields, and we list a number of them below.

MREs have attracted particular attention for their possible applications in soft-robotics [159, 161, 162, 163, 164, 34, 36, 39, 165, 160] (Figure 1.9a, b). For example, using hard-magnetic

composites, magnetic soft robots can swim, walk, and roll in fluid or solid environments, as well as deliver cargo through spatiotemporal control of the magnetic field activation [36] (Figure 1.9a). In Figure 1.9(b), a microswimmer has been developed using a magnetic hydrogel that imitates the helical propulsion of bacterial flagella when subjected to rotating magnetic fields [166]. In soft robotics, MREs have also been applied to the design of many different types of actuators, ranging from undulating [167] to multimodal swimming robots [36] or guided wires [39].

Besides soft-robotics, MREs find applications in other fields, including origami and metamaterials [151, 157, 168, 169, 151, 170, 171, 172] (Figure 1.9c, d). In Figure 1.9(c), a 2D lattice structure was illustrated by assembling hard-magnetic composites manually, with the composites connected by bendable joints. This structure displays varying torque-driven auxetic behavior, which depends on the direction of the applied magnetic field and displays magnetically tunable acoustic properties [173]. A hard-magnetic soft composite Miura-ori fold was created by incorporating alternating oblique patterns of magnetic polarities in Figure 1.9(d). This 3D-printed structure exhibits auxetic properties with negative Poisson's ratios [39]. Additionally, MREs find application in programmable and reconfigurable surfaces [174, 175, 176, 177, 178, 179, 180, 181, 182], such as fluids containing hard magnetic particles propelled through the use of traveling metachronal waves when subjected to rotating magnetic fields [181, 182] (Figure 1.9e). Figure 1.9(f) presents an example of MREs in soft and flexible electronic devices [183, 184, 185, 186, 187, 19]; hard-magnetic composite with electroplated flexible circuits [183]. In the domain of bio-medical devices [39, 188, 189, 190, 191, 192], MREs are used, for example, in magnetic guided wires utilizing hard magnetic-soft composite materials to navigate intricate neurovascular pathways [39] (Figure 1.9g).

Based on the magnetic response of the embedded particles to applied magnetic fields, MREs are classified into two groups: soft-MREs (s-MREs) and hard-MREs (h-MREs). These two classes of magnetic materials differ qualitatively according to the characteristics of their magnetization hysteresis curves: magnetization, \mathbf{M} , versus applied field, \mathbf{H} (Figure 1.10). Two quantities are particularly important in these curves: the remanence (or remanent magnetization), \mathbf{M}_r , and the coercivity (or coercive field), \mathbf{H}_c . The remanence denotes the magnetization that remains in the material once it gets magnetically saturated and after an external magnetic field is removed. The coercivity measures the strength of the magnetic field required to remove the remanent magnetization in the material.

S-MREs contain soft-ferromagnetic particles, which are often iron or iron oxide, and they can reach a high level of saturation magnetization, \mathbf{M}_s (see Figure 1.10). However, the external magnetic field [193] modifies the magnetization of particles, which is changed significantly when the external field is removed, meaning they have a low coercivity. In

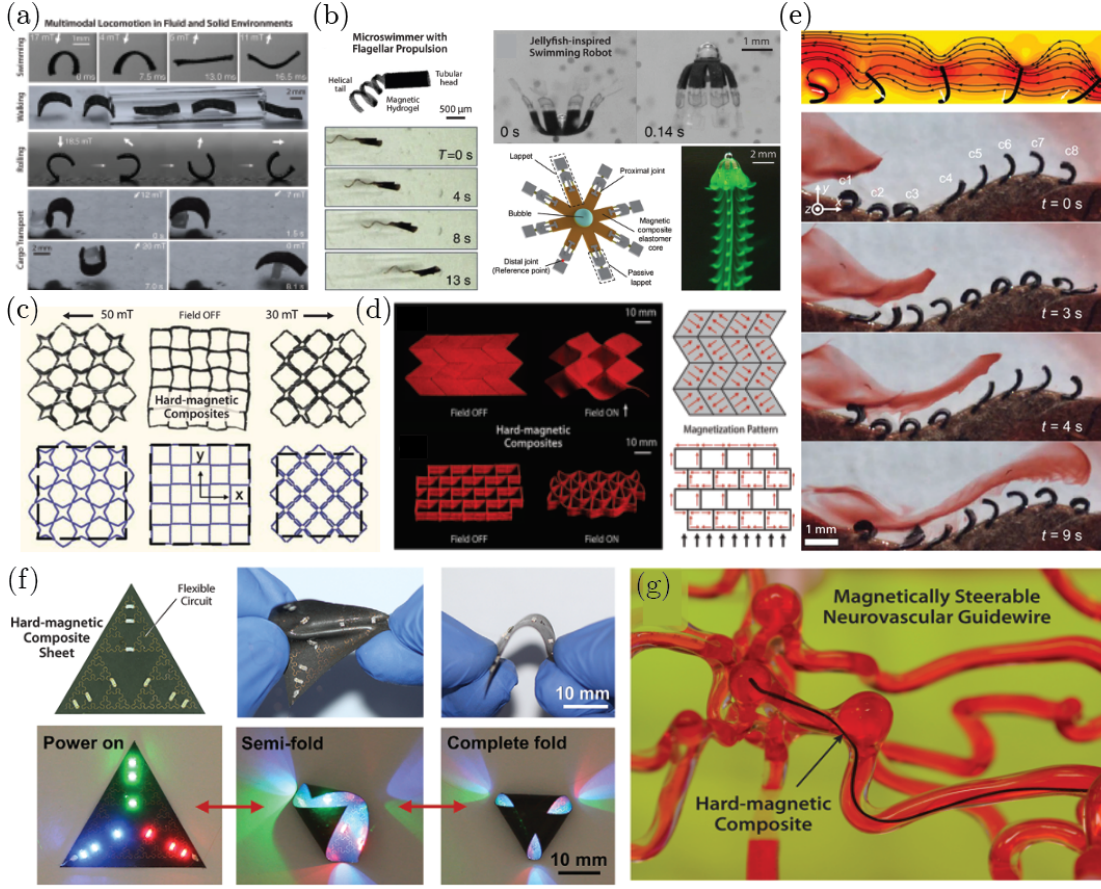


Figure 1.9: **Application of magnetic soft materials.** The magneto-rheological elastomers find various applications in (a, b) soft robotics, (c,d) origamis and metamaterials, (e) programmable and reconfigurable surfaces, (f) soft and flexible electronic devices, and (g) biomedical devices. The pictures in Figures (a), (b), (c), (d), (e), (f), and (g) are adopted from Refs [36], [166], [173], [39], [181, 182], [183], and [39], respectively.

s-MREs, when the particles are embedded in a compliant elastomeric matrix, due to dipole-dipole interactions, they tend to form chains along the field direction [194, 155]. The displacements of the constituent micro-scale particles within the matrix result in macro-scale deformations and changes in the elastic properties of the composite [195, 196, 155]. This class of s-MREs has attracted significant attention. For example, by applying a field gradient to actuate the large deflection of structures made of s-MREs, the rearrangement of the particles inside the matrix causes large deformations and a variation in elastic properties [197, 194]. This actuation have been often used to devise tunable vibration absorbers [198, 199, 200], microfluidic pumps [201, 202]), and force sensors [19] or strain sensors [203]. In devices made of s-MREs, the deformation is induced by the formation of particle chains along the magnetic field (magneto-striction), and these materials often find applications involving compression/elongation motions [161, 204].

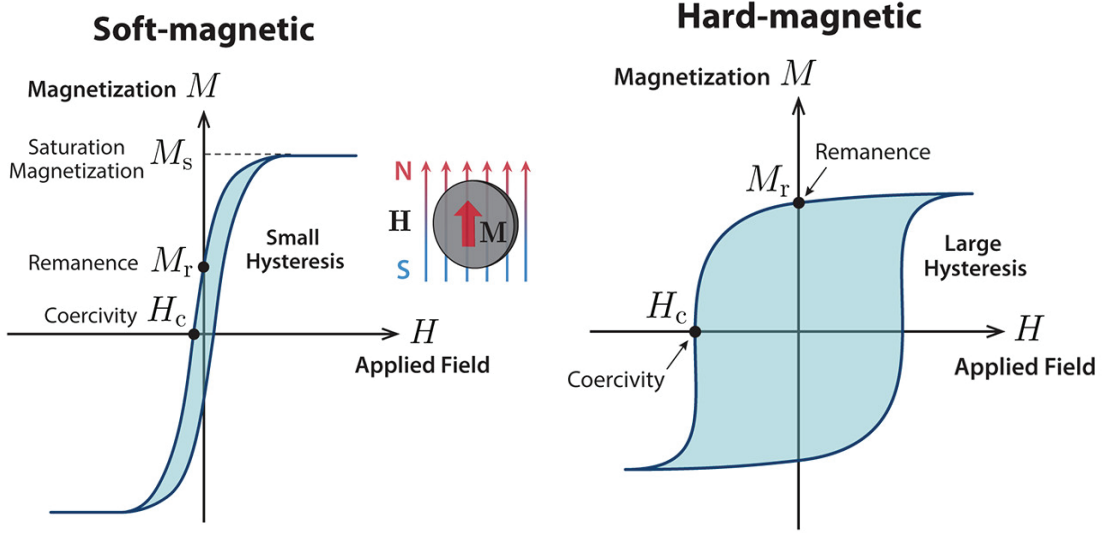


Figure 1.10: **Soft- versus hard-MREs.** The magnetic hysteresis loops (M - H curves) of soft-magnetic and hard-magnetic materials. Unlike hard magnetic materials, soft magnetic materials cannot retain a high magnetization level despite acquiring a higher magnetization due to low coercivity. The figure is adapted from Ref. [145]

By contrast, in h-MREs, which are the focus of this thesis, the hard-ferromagnetic particles such as neodymium-iron-boron (NdFeB) are embedded in the elastomeric matrix. These particles possess a sufficiently high coercivity, H^c compared to s-MREs (see the hysteresis curves in Figure 1.10) and resist the demagnetization by external fields after field saturation [193, 29]. Consequently, the remnant magnetization of h-MRE can be retained during actuation. In particular, flexible slender structures made of h-MREs are capable of significant shape changes, driven by the magnetic body torques induced by the interaction between the intrinsic magnetization of the material and the applied field [34, 151]. While complex motions are challenging to achieve with s-MREs, h-MREs are adapted to more complex 3D deformations, particularly rotational motion, due to the possibility of inducing magnetic torques. The magnetization profile of h-MRE structures can be (inverse) designed and programmed by the local orientation of the magnetized particles to generate complex 3D-shape transformations and optimize the shape-shifting modes for specific applications [34, 151, 205, 206, 207, 158, 38]. This class of MREs shows the rapid, reversible, and controllable ability to change shape, which introduced innovative capabilities in soft robotics [36, 37, 208], biomedicine [39], and meta materials [157, 172], and micro-machines [38].

To harness the full potential of MREs, it is essential to develop accurate and predictive models that can capture their complex mechanical behavior under various magnetic fields and loading conditions. These mechanics-based models play a crucial role in

designing innovative MRE-based devices and structures. As a result, MREs' properties and behaviors are investigated, advancing material science and engineering to create more responsive and versatile structures. For a better understanding of magneto-mechanical effects in MREs, many theoretical, numerical, and experimental research integrating electromagnetism and mechanics have been conducted, which we will elaborate on in the next section.

1.5 Modeling of Magneto-Rheological Elastomers

Significant theoretical, numerical, and experimental research has been conducted on developing predictive models for MREs to rationally design magneto-active systems. These studies aimed to investigate the behavior of MREs when subjected to mainly magnetic actuation [209, 210, 211, 212]. Next, we provide an overview of some of the main concepts regarding the modeling of MREs that will be needed later in this thesis.

The origins of the research on MREs can be traced back to the last century when the theoretical groundwork for the field was established within the domains of continuum mechanics, thermodynamics, and electrodynamics to study their response under magnetic actuation [209, 210, 211, 212]. These initial theoretical advancements in the field of magneto(electro)mechanics preceded the earliest recognized experimental investigations into MRE, which was conducted by Jolly *et al.* in 1996 [213]. In this work, a quasistatic dipolar model was developed to explain the modulus change of an MRE, and experimental testing was conducted to examine the material properties of a composite material comprising an elastomer embedded with ferrous particles under a magnetic field. Following these foundational works, several magneto-mechanical models were then developed, both for soft and hard MREs [35, 214, 215, 216, 32, 217], taking into account, for instance, their anisotropy [197], viscoelasticity [218], and magnetic hysteresis [219]. Additionally, experimental studies were conducted in order to evaluate the developed models [210, 32, 197]. Particularly, Zhao *et al.* [32] developed a simple model based on 3D-printed heterogeneous magnetization profiles for h-MREs, building on past work conducted on the equilibrium of deformable solids under magnetic torques and forces [210, 211] and validated the model with 2D and 3D structures.

Dorfman and Ogden [35, 214, 215] revisited and modernized the modeling of MREs and established the fundamental principles in this area by presenting a framework that combines Maxwell's equations, mechanical balance laws, and thermodynamic equations for a deformable 3D material. They further adapted this general theory specifically for magneto-sensitive elastomers, simplifying the constitutive relations based on the incompressibility and hyperelasticity of the elastomer. Voropaieff *et al.* [220] proposed an

approach based on a continuum description to characterize the constitutive behavior of MREs [216, 197]. For this purpose, they numerically implemented MREs in 3D finite element modeling (FEM) and validated their model by comparing it with experimental data. Using this approach, the MRE structure design could be improved based on an entire overview of the coupled behavior.

Lately, in a pioneering work, Zhao *et al.* [32] introduced a constitutive model to describe the response of h-MREs under the magnetic field. This torque-based theoretical framework took into account the macroscopic behavior, and the authors made several key assumptions in their study. Firstly, they assumed that the h-MRE was pre-magnetized with a known magnetization profile and had a relative permeability close to unity, meaning that the permeability of the MRE is approximately equal to vacuum or air. Secondly, they assumed that the magnetic field within the entire domain was equal to the externally applied field in a vacuum, neglecting the influence of the magnetization of MREs. As a result of these assumptions, the problem was simplified into a mechanical problem under magnetic loading, where the deformation gradient and displacement field served as the only independent variables, eliminating the need to solve the fully coupled magneto-mechanical equations. Next, we provide a concise overview of the fundamental theoretical framework.

The torque-based model proposed by Zhao *et al.* [32] considered magneto-active materials as a homogenized continuum body with a physical behavior given by the Helmholtz free energy configuration. The combined total Helmholtz free energy density of the ideal hard-magnetic soft material per unit volume composed of elastic strain energy density per unit volume, U^e , and magnetic energy density, U^m , concerning the initial configuration as:

$$U = U^e + U^m. \quad (1.5)$$

The magnetic part of the strain energy density is defined as the potential of the magnetic body torque, $\mathbf{T} = \mathbf{m} \times \mathbf{B}^a$, imposed by the magnetic flux density, \mathbf{B}^a as

$$U^m = -J\mathbf{m} \cdot \mathbf{B}^a, \quad (1.6)$$

where \mathbf{m} is the magnetization of the deformed h-MRE body. This magnetization is related to its undeformed magnetization configuration \mathbf{M} as

$$\mathbf{m} = J^{-1}\mathbf{F}\mathbf{M}, \quad (1.7)$$

where \mathbf{F} is the deformation gradient, and $J = \det(\mathbf{F})$ measures the relative volume change.

Therefore, the magnetic potential density with respect to the initial configuration is written as

$$U^m(\mathbf{F}) = -\mathbf{F}\mathbf{M}\cdot\mathbf{B}^a. \quad (1.8)$$

This magnetic energy density couples the magnetic actuation and the elastic deformation. Regarding the magnetic part of the magnetic energy potential, based on ideal hard-magnetic soft material, they assumed a linear relationship between the applied magnetic field \mathbf{H} and the magnetic flux density \mathbf{B} (linear regime of the hysteresis curve in Figure 1.10). This assumption is valid as long as the applied field \mathbf{H} is far below the coercivity \mathbf{H}^c . More precisely, they assume the slope of this relationship to be the vacuum permeability, μ_0 as:

$$\mathbf{H} = \frac{1}{\mu_0}(\mathbf{B} - \mathbf{B}^r), \quad (1.9)$$

where \mathbf{B}^r , the residual magnetic flux density (in the current configuration) corresponds to the magnetic flux density that the material can maintain in the absence of any applied exterior field. The free magnetic energy density (per unit volume) in the current configuration can be derived as the energy to realign this magnetic moment with the applied magnetic flux density [221]. Zhao *et al.* [32] implemented the equilibrium equation of a hard-magnetic body under a uniform field, along with the constitutive law, into 3D finite element modeling (FEM) through a user-defined element subroutine (UEL) developed in the commercial finite element software package Abaqus/Standard. The inputs of the simulation are the global shear and bulk moduli, G and K , respectively, the applied magnetic flux density vector \mathbf{B}^a and the residual flux density vector in the reference configuration \mathbf{B}^r . The torque-based model underwent validation through various test cases involving thin-walled structures subjected to pure magnetic loading [151, 32], soft active robots [39], and morphing architectures [222].

This model predicted the magnetic-activated shape-change of structures fabricated with this hard-magnetic soft material. In Figure 1.11(a), we reproduce a figure adapted from the work of Zhao *et al.* [32] comparing their model-based simulation with the experimental results for the printed 2D and 3D structures. The authors showed programmed shape changes due to the inscribed magnetic domains, observing a good agreement between the experiment and simulations. They also validated their model with experiments in the magnetically actuated bending of the beam with large and extreme deformation (up to 180°), respectively (see Figure 1.11b and c).

In a subsequent study, Garcia-Gonzalez [223] expanded this torque-based model to incorporate viscous contributions to account for relaxation and dissipation effects in the

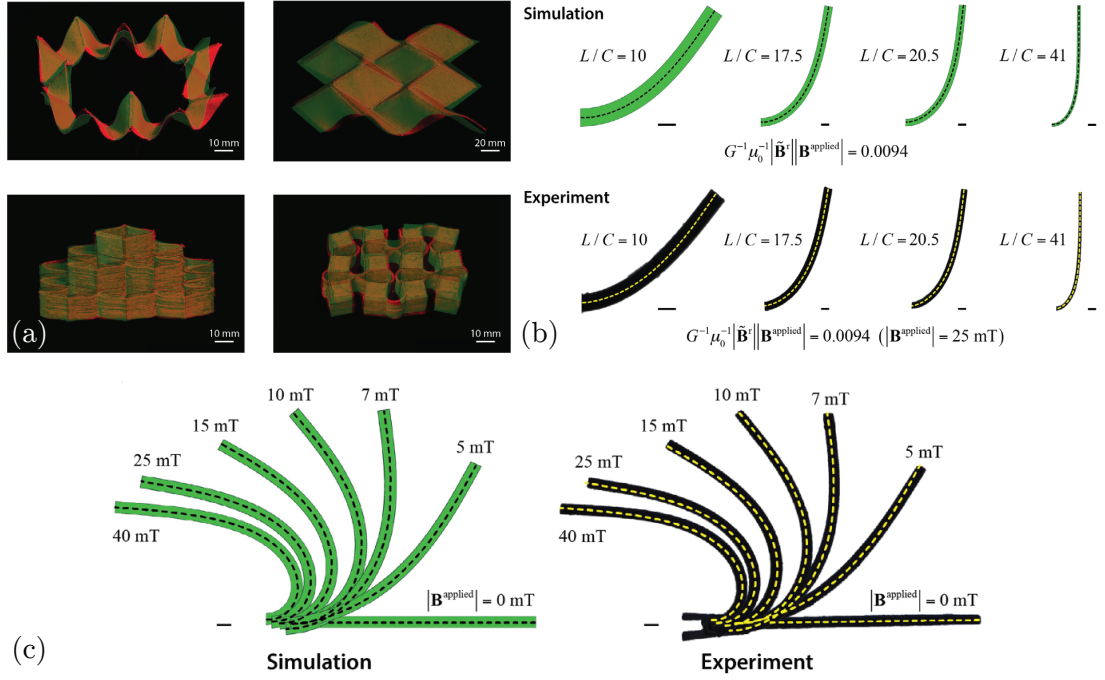


Figure 1.11: **Validation of continuum torque-based model with experiments.** FEM modeling with implemented UEL subroutine for the magnetically actuated (a) 2D and 3D structures with programmed magnetic domains, (b) beam bending with magnetic field perpendicular, and (c) in the opposite direction to the magnetization profile. The pictures are adopted from Ref. [32].

deformation process of these materials when subjected to external magnetic fields and/or mechanical loading. Then, based on this torque-based model, Zhang *et al.* [224] considered the interactions between the magnetic particles and the soft matrix and explored the impact of these interactions on actuation efficiency by employing a micromechanics approach in representative volume element simulations. Their findings demonstrated that particle rotations significantly influence the actuation efficiency, specifically regarding the efficiency of torque transmission.

More recently, coupled constitutive models for MREs with iron particles have been proposed [217]. In this model, an augmented variational principle is developed and used to properly evaluate the homogenized response of MREs. The analytical models are compared with full-field numerical FE simulations of random polydisperse representative volume elements. Following their previous work, Mukherjee *et al.* [219] introduced a fully-coupled modeling framework for incompressible h-MREs through microstructural guidance. The constitutive formulation was established with a strong focus on thermodynamic consistency, and the model parameters were determined through homogenization techniques (see Figure 1.12). In this homogenization technique, each point of the macro-

continuum (Figure 1.12a) is assumed to be described by a representative volume element (RVE) comprising two phases of particle and matrix (Figure 1.12c). A slowly varying microstructure was also considered such that the microstructure can be assumed to be (locally) periodic (Figure 1.12c), resulting in periodic boundary conditions applied on a single RVE (Figure 1.12b).

This novel framework could account for the self-field generated by the MRE and the interactions between microscopic magnetic particles. In contrast to previous studies, the model of Mukhreje *et al.* [225] takes magnetic hysteresis into account in the constitutive relations, enabling it to represent the nonlinear behavior under intense magnetic actuation, even beyond the coercivity of the particles and during particle magnetization, contradicting the observation of the previous torque-based model presented by Zhao *et al.* [32], which considered the effect of stretching deformation of matrix on magnetization. Utilizing this model, the authors analyzed the deformation of an inhomogeneously magnetized cantilever beam, considering cases where neglecting the self-field was not applicable. Moreover, their homogenization simulations demonstrated that the magnetization of a bulk pre-magnetized incompressible hard-MRE with a moderately soft matrix remained unaffected by stretching deformations; a more extended discussion on this point will be presented below, in Section 1.5.1.

Following previous studies, Garcia-Gonzalez and Hossain [226] presented a microstructural model to examine the impact of dipole-dipole interactions on the deformation of h-MREs. The model solely focuses on the rotation of rigid particles to derive the potentials associated with the mutual interactions among the particles and the interactions between the external field and the particles. Then, Rambašek *et al.* [218] conducted a detailed

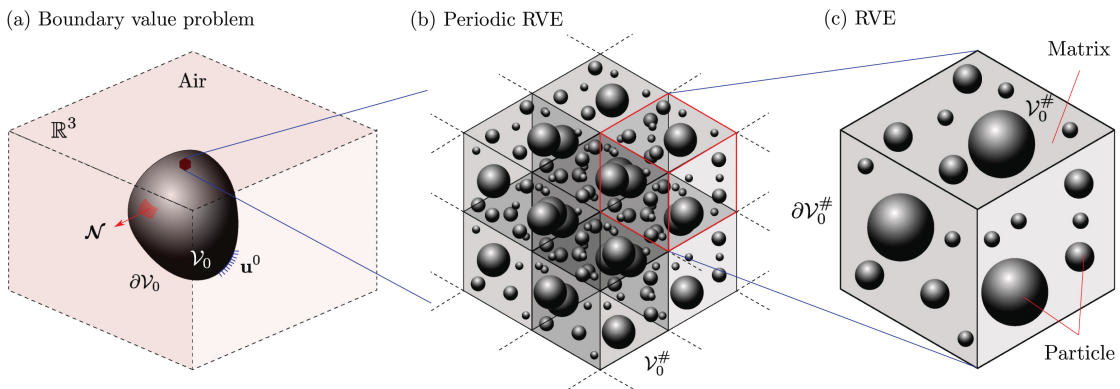


Figure 1.12: **Schematic diagram of homogenization of MREs.** (a) Macroscopic boundary value problem of MRE in the air with the (b) periodic representative volume elements (RVEs), and (c) an RVE occupying a reference volume. The pictures are adopted from Ref. [219].

investigation into the interaction between the viscoelastic properties of the polymeric matrix and the ferromagnetic hysteresis of the particles in h-MREs. They developed a more thorough theoretical and numerical framework that allows for modeling finite strain MREs comprising mechanically soft nonlinear elastic-viscoelastic polymer phases and magnetically hard or soft magnetic phases.

Additionally, numerous research efforts have studied the interaction between particles in h-MREs at the microstructural level. These studies aim to understand how such micro-interactions affect the magnetization and deformation behavior of the composite material. For example, for h-MREs with an extremely soft matrix, dipole-dipole interactions and asymmetric rotations of particles may play an important role in their macroscopic properties and response, as has been recently demonstrated in the literature [227, 228, 229, 224, 226]. In more complex settings, Psarra *et al.* [230] and Sano [231] studied magnetic dissipation and self-interactions using a complete full-field theory, respectively.

1.5.1 Does the Stretching of MREs Affect the Magnetization?

Following the examination of the modeling frameworks for MREs discussed above, this section reviews, as a comparative analysis, the recently introduced 3D continuum theories considering and neglecting the effect of stretching deformation on the magnetization of h-MREs anointed as " *\mathbf{R} -based*" and " *\mathbf{F} -based*", respectively. We seek to clarify the distinctions and limitations of these recent theoretical developments.

In the recent study by Mukherjee *et al.* [217] as discussed above, it was shown that the magnetization of the bulk pre-magnetized incompressible h-MREs with a moderately soft matrix is independent of the stretching deformation. Their homogenization simulations performed on representative volume elements (RVEs) demonstrated that when the h-MRE is under uniaxial tension, and the loading is perpendicular to the pre-magnetization vector, the magnetization remains constant because the matrix is much more compliant to the stretching than the magnetic particles, which remain approximately, undeformed. According to this observation, the authors conclude that the magnetization of h-MRE only depends on its rotation [219, 226], in contrast to the continuum torque-based model proposed by Zhao *et al.* [32] for the magnetization of deformed h-MRE. This latter model is not able to yield accurate predictions when significant stretching deformation is present due to the incorrect description of magnetization.

Subsequently, in an even more recent study, Yan *et al.* [232] studied thin magnetic plates made of h-MREs and found disagreement between the experimental results and the prediction from the \mathbf{F} -based model for the cases where the magnetic field was parallel

to the magnetization profile of the plate. Then, they were motivated by the prior demonstration of the stretch-independence of the magnetization of bulk h-MREs [219]. They expected that using the 3D continuum torque-based model proposed in Ref. [32] may lead to error in the magnetic part of the Cauchy stress tensor due to the inaccurate description of magnetization, leading to the unreliable prediction of deformation of MREs. As an alternative, Yan *et al.* [232] proposed a model derived through dimensional reduction of a 3D continuum theory, adapting the torque-based theory of h-MREs [32]. Considering the composite nature of the MREs with magnetization emerging from the magnetized particles, the magnetization of the h-MREs in its deformed configuration is determined by the deformation gradient \mathbf{F} defined as

$$\mathbf{F} = \mathbf{R}\mathbf{U}, \quad (1.10)$$

composed of the rotation, \mathbf{R} , and the stretch, \mathbf{U} , tensors. However, this continuum description contradicts the findings by Mukherjee *et al.* [219] concerning incompressible h-MREs, which indicates that the effective magnetization of the deformed MRE primarily relies on rotation, regardless of stretching, as individual particles exhibit significant stiffness in contrast to the matrix. Therefore, Yan *et al.* [232] proposed a rotation-based (\mathbf{R} -based) theory by replacing the deformation gradient, \mathbf{F} , with the rotation tensor in Equation 6.1 as

$$\mathbf{m} = J^{-1}\mathbf{R}\mathbf{M} = J^{-1}(\mathbf{F}\mathbf{U}^{-1})\mathbf{M}. \quad (1.11)$$

The authors considered the assumption that the matrix is moderately soft [219], and the rotations of the microscopic particles and the macroscopic MRE remain the same [227, 229, 224]. As a result, the magnetic potential in Equation 1.8 was revised as

$$U_R^m(\mathbf{F}) = -\mathbf{R}\mathbf{M}\cdot\mathbf{B}^a. \quad (1.12)$$

The proposed model was labeled the " \mathbf{R} -based" 3D continuum theory while Equation 1.8 was named the " \mathbf{F} -based" 3D continuum theory. In this \mathbf{R} -based theory, a connection between the magnetizations in both the initial and deformed configurations is established by solely employing the rotation tensor \mathbf{R} , decomposed from the deformation gradient \mathbf{F} . The subsequent experiments by Yan *et al.* [232] showed that the \mathbf{R} -based model is necessary for modeling plate structures subjected to non-negligible stretching deformation under an applied field parallel to the initial magnetization, and the \mathbf{F} -based model introduced errors due to the incorrect description of the magnetization of the structure.

In summary, the two 3D continuum theories, \mathbf{R} -based and \mathbf{F} -based, presented earlier yield consistent results in scenarios where stretching can be neglected. This condition

aligns with the specific problem addressed in this thesis: the snap buckling of bistable magneto-active beams. As a result, the \mathbf{F} -based 3D continuum theory proposed by Zhao *et al.* [32] will be the primary framework employed throughout this thesis.

1.5.2 Slender Magneto-Active Structures and Dimensional Reduction

Using the models highlighted above, the mechanics of magnetic slender structural elements such as beams and rods, plates, and shells have been investigated through a dimensional reduction in various studies to improve the functionality of hard-MRE structures through geometry [233, 234, 232]. Dimensional reduction involves simplifying the mathematical representation of these structures while preserving their essential mechanical behavior [2]. This approach leverages the inherent symmetries and geometry of the system to reduce the number of variables and degrees of freedom, which can obtain effective reduced-order models that capture the dominant features of the original system. Next, we elaborate on some of the main recent findings in this domain.

Flexible and highly deformable structural elements with magnetic properties, such as beams and rods, have been widely employed in various magneto-mechanical systems, allowing for significant deflections in three-dimensional space [34, 203, 39, 37, 208, 158]. In many cases of structural design, employing an extensive 3D continuum theory can be excessive and lead to complex analysis. Therefore, it is preferable to use simplified structural theories to comprehend the magnetic impact and better pinpoint the essential system parameters. The simple shape of these one-dimensional elements simplifies their modeling, design, and fabrication. In parallel with the development of the continuum theories for h-MREs presented in Section 1.5, many research studies have examined how thin beams behave when subjected to magnetic actuation. These investigations have involved a combination of theoretical, computational, and experimental approaches [34, 33, 206, 207, 235, 236, 237].

Based on the 3D continuum model of Ref. [32], and using dimensional reduction, theories for inextensible, hard-magnetic elastica were derived and validated against experiments under either a uniform [158, 34, 233] or constant-gradient [233] magnetic fields. Lum *et al.* [34] introduced a geometrically nonlinear and inextensible beam model developed through the equilibrium of forces and torques along the beam centerline, which was confirmed through experimental validation [203]. The authors subsequently applied the model to optimize the magnetization of the beam to achieve a specific deformation under both uniform and gradient magnetic fields (Figure 1.13a). Using the torque-based continuum model, Wang *et al.* [33] presented a nonlinear inextensible model for hard-magnetic elastica capable of predicting the large deformation of slender beams under

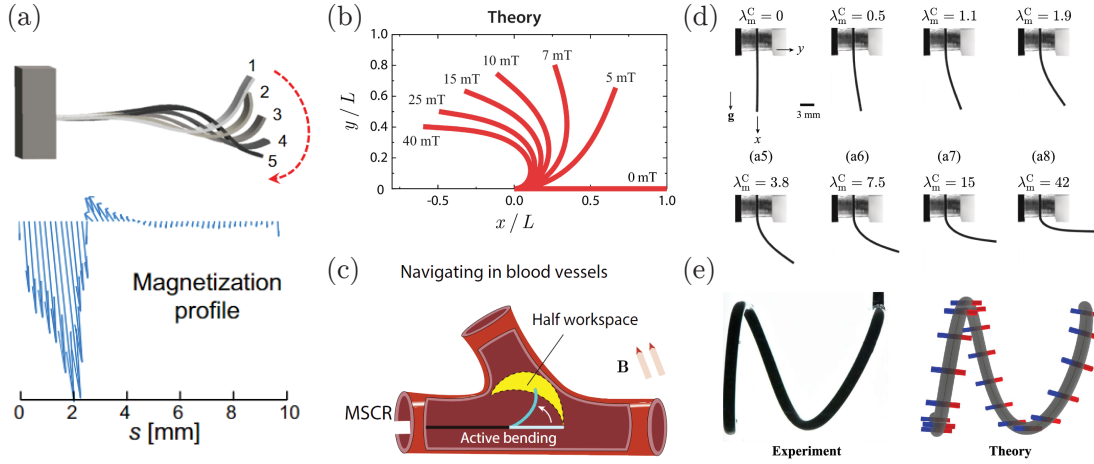


Figure 1.13: **Magnetic beam structures.** (a) A nonlinear inextensible magnetic beam model with the optimized magnetization profile and (b) large deformation, which was used (c) for the design of soft robots. The reduced order model was then used (d) elastic for magnetic beam and (e) Kirchhoff-like theory for magnetic rods. Panels in (a), (b), (c), (d), and (e) are adapted from Refs. [34], [33], [158], [233], and [234], respectively.

a uniform magnetic field (Figure 1.13b). This model was then used to design 1D soft continuum robots [158] (Figure 1.13c).

Yan *et al.* [233] presented a model combining reduced order modeling, 3D finite element simulation, and experiments to investigate the actuation of h-MRE beams under magnetic field with a focus on non-uniform external fields with a constant gradient (Figure 1.13d). Although theoretical concepts for planar deformations of one-dimensional hard magnetic slender structures (such as beams and elastica) were already well-established by the time of their study, there remained a gap in modeling 3D deformations for hard magnetic rods with inherent curvatures. Therefore, considering the 1D structural elements under both bending and twisting, Sano *et al.* [234, 231] developed a similar dimensional reduction and derived a Kirchhoff-like theory for describing the 3D deformation of hard-magnetic rods and investigated the instability of straight and helical rods under the uniform and gradient magnetic actuation (Figure 1.13e).

To account for the extensibility and stretch of the centerline, a geometrically exact beam model incorporating precise geometric nonlinearity was formulated and applied to anticipate the deformation of cantilever beams in uniform fields [237, 206, 207, 235], albeit finding negligible differences with the inextensible model. Also, considerable attention has been dedicated to the (reverse) engineering of beam magnetization profiles, aiming to enhance shape modifications for diverse applications through the utilization of the inextensible and geometrically precise beam model [34, 205, 206, 207, 158, 238].

Even if there have been several studies on modeling the deformation of magneto-active 1D structures, their instability and, more specifically, the snap-through phenomenon under magnetic actuation remained an ongoing research topic, the elastic counterparts of which have been studied extensively [239, 240, 241, 242]. Tan *et al.* [243] investigated the dynamic response and the snap-through instability of a hard magneto-active beam. They focused on the snap-through dynamics of magneto-active bistable beams and proposed a dynamic model using the Euler-Lagrange equations and considering the damped oscillations to predict the dynamic snap-through instability through experiment and theory. Later, Stewart and Anand [244] proposed a \mathbf{R} -based continuum finite-deformation theory for predicting the magneto-viscoelasticity of hard magneto-rheological materials and describing the snap-through dynamics of bistable h-MRE arches. Using finite element simulation, they showed that their theory could reproduce the results of several magnetically induced snap-through experiments on bistable arches in Ref. [243]. Their model accounted for the magneto-elastic coupling with large deformation viscoelasticity, near-incompressibility of the material, and inertial effects.

While significant focus has been directed toward magneto-active 1D structures, there has been comparatively less emphasis on 2D (plates) and 3D (shells) configurations, which form integral components of these structures and have garnered relatively less attention in the existing body of research. We proceed by highlighting noteworthy recent advancements within this domain. Psarra *et al.* [230] examined the stability and post-bifurcation phenomena of an MRE film adhered to a passive elastomer substrate, combining experimental and numerical approaches. The film-substrate system underwent controlled uniaxial mechanical pre-compression loads, enabling an in-depth analysis of pattern formation and its subsequent evolution under large magnetic fields and pre-compression conditions. Yan *et al.* [232] developed a reduced-order model for thin plates made of h-MREs based on a new rotation-based (\mathbf{R} -based; see Section 1.5.1) magnetic potential, an alternative to existing torque-based 3D continuum theory (see Figure 1.14a). This model showed that the rotation-based model is necessary for plates subjected to non-negligible stretching deformation under an applied field parallel to the initial magnetization, supporting the findings of Mukherjee *et al.* [225].

While addressing shell structures, it becomes evident that theoretical models that incorporate non-axisymmetric deformations of magneto-active shells have yet to receive substantial attention. Previous efforts in this direction have primarily been limited to shallow shells, as exemplified by works like those of Seffen *et al.* [245] and Loukaides *et al.* [246]. However, understanding the complex interplay between magnetism and mechanics remained a challenge. In the research conducted by Yan *et al.* [104], a theoretical framework was established to describe the axisymmetric deformation and geometrically

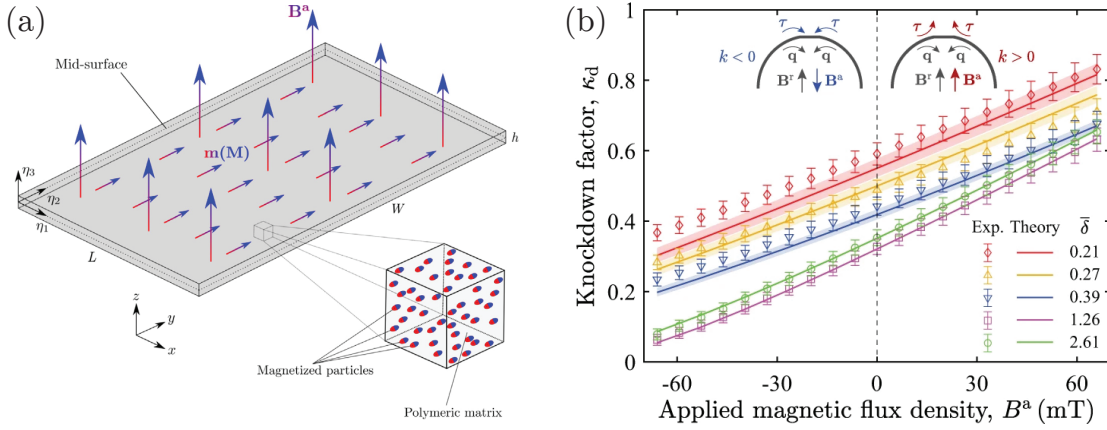


Figure 1.14: **Magnetic plate and shell structures.** (a) A thin plate made of a h-MRE in its initial configuration, subjected to an external magnetic field, \mathbf{B}^a . (b) Knockdown factor versus flux density of the applied field for magnetic shells containing the defects using experimental results and theoretical predictions. The panels (a) and (b) are adapted from Refs. [232] and [104], respectively.

exact strain measures of thin magnetic elastic shells, effectively explaining the fundamental mechanism of elasto-magnetic thin shells and showcasing a good agreement between their modeling and experiments. Using the magnetic field, it was found that it is possible to tune the critical buckling pressure of spherical shells [90, 109]. Figure 1.14(b) shows the knockdown factor of the magnetic shell as a function of the applied magnetic field, which can be increased or decreased depending on the polarity of the field. The authors also identified a dimensionless magneto-elastic buckling number as

$$\Lambda_m = \frac{B^r B^a}{\mu_0 E} \left(\frac{R}{h} \right) \quad (1.13)$$

which is a critical factor that integrates the geometric, mechanical, and magnetic properties of the system under both magnetic field and external pressure. Subsequently, Pezzulla *et al.* [247] formulated a framework for analyzing slender, elastic, magnetic shells employing geometrically exact strain measures [78, 248, 249], broadening the scope of the model by Yan *et al.* [104], which was restricted to axisymmetric shells experiencing axisymmetric deformations. Recently, to showcase the versatility and practicality of the theory, which was developed to predict the snap-through dynamics of bistable arcs, Stewart and Anand [244] employed fully 3D FEM simulations to replicate intricate geometric transformations of the magnetically driven eversion and reversion of a hemispherical shell.

While there have been notable advancements in magneto-active materials and structures, several questions still need to be answered, including the investigation of buckling and snap-through instability in these structures under the influence of a magnetic field.

Addressing these questions is essential for advancing toward the predictive design of magneto-elastic structures. For instance, it remains a subject of great interest to explore how the instability and buckling behavior of these components can be harnessed to enable a wide range of future functionalities. Potential applications span actuators, robotics, MEMS (Micro-Electro-Mechanical Systems), programmable devices, metamaterials, and energy harvesting devices. Furthermore, it is crucial to study how these structures respond dynamically to various external stimuli and interact with other physical phenomena.

1.6 Research Niche and Overall Goal of the Thesis

The research objective of this thesis is to leverage the stability and instability of shells coupled with magneto-rheological elastomers to design a new class of tactile braille readers whose displayed patterns can be changed on demand by applying a magnetic field. We will harvest the buckling of magnetic shells to design active structures that can actively morph under an external magnetic field. Subsequently, we define the research questions and expand on the potential content toward the ultimate research question.

To address this goal, we will need to gain fundamental insight into the mechanics of thin spherical shells, including the multi-stability behavior of shallow shell sections. First, we will study their imperfection sensitivity, the principal factor in their failure mechanism. We will compare the effect of different types of geometric imperfections and their impacts on the buckling capacity of spherical shells. Then, we will characterize their stability landscape through modern research tools, modeling, and experiments. Knowing that defects strongly reduce the buckling resistance of thin shell structures and predicting the critical buckling loads is challenging for a shell structure, we will investigate the recently proposed non-destructive probing technique to predict the critical loading conditions of imperfect spherical shells containing one imperfection. We will also identify the limiting conditions; *e.g.*, the poking location plays a crucial role in the efficacy of prediction. However, the defects are generally unknown and often difficult to identify. As a result, the probing technique will be evaluated on a shell with a realistic defect scenario (imperfect shells with a random distribution of defects) from a statistical point of view, which can inform the design rules of thin-walled structures. In summary, through Part I of this thesis, which includes Chapters 2, 3 and 4, we will tackle the following research questions:

- How does defect geometry (bumpy and dimpled Gaussian defect) influence the critical buckling conditions of spherical shells under external pressure loading?
- What are the non-destructive probing technique limitations for spherical shells, and how does this contribute to mapping the stability landscape of spherical shells?

- Can the proposed poking technique accurately predict the buckling capacity of imperfect spherical shells with a random distribution of imperfections, and what insights can be gained from the probabilistic characterization of stability?

The second direction toward the proposed goal of the thesis is to study the mechanics of active structures made out of magneto-rheological elastomers that can be actuated in the presence of an external magnetic field. We first aim to study the magnetic-driven buckling instability of a simple case of magnetic slender structures (a magnetic beam) under both poking and magnetic actuation. The instability and, more specifically, the snap-through phenomenon of the bistable structure under magnetic and mechanical actuation were studied to identify the rationale between the onset of snapping and the geometry of the beam. The experimental, theoretical, and computational tools needed to predict the critical conditions and snap-through response of magneto-active bistable structures will be developed, which would be valuable for the predictive and rational design of bistable magneto-elastic shells. In summary, in Part II of this thesis, which includes Chapter 5, we will tackle the following research questions:

- How does the magnetization profile of the structure affect the triggering of snap buckling under a magnetic field?
- What critical field strength is required for the onset of snapping in the h-MRE bistable beam?
- How does the reduced-order beam theory rationalize the observed magneto-elastic response in the bistable magnetic beam?
- How does the magnetic field affect the poking-induced snapping of bistable beams?

Finally, considering buckling as a mode of functionality and the knowledge acquired from the first direction of the research, studying the mechanics of shell structures (Part I: Chapter 2, 3, and 4), and the second direction of the research, actuation mechanism of magneto-active materials and structures (Part II: Chapter 5), we propose a novel mechanical design concept for braille dots, the building block of a new class of programmable braille readers. Our design leverages the buckling and (in)stability of bistable thin shell structures and magnetically responsive MREs (Chapter 6). For the final objective of the thesis, we addressed the following research questions:

- How can we create a braille reader actuator using a magnetic shell that can resist buckling under fingertip indentation while easily snapped on-demand with an external magnetic field?

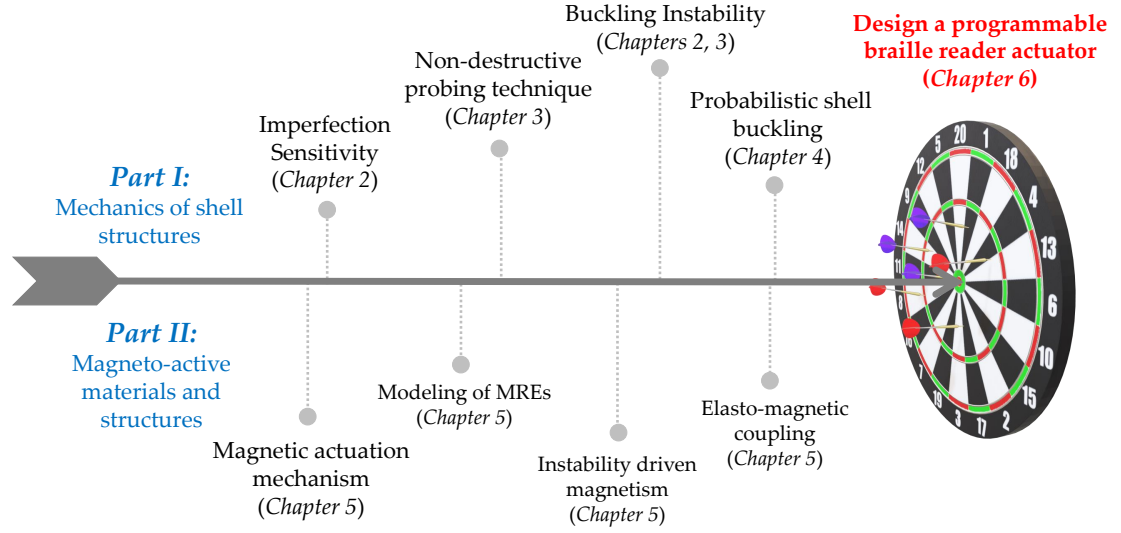


Figure 1.15: **Schematic diagram of the objective of the thesis.** By combining the two lines of mechanics of shell structures and magneto-active materials, we aim to address the final research goal.

- What design parameters are feasible for adhering to standardized geometric and physical specifications of braille systems?
- How to expand the design possibilities while maintaining the required geometry for braille standards?
- What advantages does this design offer over existing solutions of refreshable braille readers?

1.7 Outline of the Thesis

The overall outline of the research goal is presented in Figure 1.15. This thesis is divided into two parts aligned with the two lines of research. Part I is dedicated to the mechanics of thin shell structures and spherical shell buckling (Chapters 2, 3, and 4). In Part II, we focus on the magneto-active materials and structures (Chapters 5). The final goal of the thesis is also the main focus of Chapter 6.

In **Chapter 2**, we revisit the buckling of spherical shells by investigating the effect of defect geometry in dictating the sensitivity of the critical buckling conditions of the shells under external pressure loading. Specifically, we perform a comparative study between shells containing Gaussian defects that are either dimpled (inward) or bumpy (outward).

We employ FEM simulations to compute the knockdown factors for the two cases while systematically exploring the parameter space of the defect geometry. This work has led to the following publication: Arefeh Abbasi, Fani Derveni, and Pedro M. Reis, “Comparing the Buckling Strength of Spherical Shells With Dimpled Versus Bumpy Defects”, *Journal of Applied Mechanics*, 90(6), 061008 (2023).

In **Chapter 3**, we focus on predicting the critical buckling conditions of shell structures. We study the mechanical response of pressurized spherical shells containing a single dimple-like defect to a point probe. Combining experiments, FEM simulations, and existing results from classic shell theory, we characterize the nonlinear force-indentation response of imperfect shells at different pressurization levels, and we seek to identify the critical buckling pressure of the shell. Specifically, the location of the indentation is varied systematically to determine how it affects probing efficiency. This work has led to the following publication: Arefeh Abbasi, Dong Yan, and Pedro M. Reis, “Probing the buckling of pressurized spherical shells”, *Journal of Mechanics and Physics of Solids*, 155, 104545 (2021).

In **Chapter 4**, we investigate the buckling of spherical shells containing a random distribution of defects based on a non-destructive probing technique. Using FEM simulations, we perform a statistical analysis of these imperfect shells in two scenarios: (1) sampling the random variable as the defect distribution and (2) sampling the random variable from the random-chosen poking locations. Such shells are more realistic and practically relevant than the previous single-defect cases. Finally, we compare the predicted knockdown factor statistics using a probing technique with the statistics of the measured knockdown factor.

In **Chapter 5**, we investigate the mechanics of bistable, hard-magnetic, elastic beams, combining experiments, FEM simulations, and a reduced-order theory. This theory is developed in collaboration with Tomohiko Sano. We quantify how the critical field strength required for buckling depends on the imposed end-to-end shortening, the beam geometry, and the material and magnetization properties. A centreline-based theory is developed to rationalize the trade-offs between the various loading and geometric parameters, predicting the conditions for the onset of snapping. We also adapt the FEM for 3D h-MREs to make it amenable to a Riks (arclength) analysis. Additionally, we probe the beam’s load-bearing capacity when the external loading combines a constant magnetic field and poking force. This work has led to the following publication: Arefeh Abbasi, Tomohiko G. Sano, Dong Yan, and Pedro M. Reis, “Snap buckling of bistable beams under combined mechanical and magnetic loading”, *Philosophical Transactions of the Royal Society A*, 381(2244), 20220029 (2023).

In **Chapter 6**, we combine the knowledge of the mechanics of thin shell structures

and magneto-active materials. The objective is to propose a mechanical design concept for the building block, a dot, of programmable braille readers utilizing bistable shell buckling, magnetic actuation, and pneumatic loading. The design process is guided by FEM, which is initially validated through precision experiments conducted on a scaled-up, single-shell model system. Then, the simulations are leveraged to systematically explore the design space, adhering to the standardized geometric and physical specifications of braille systems. Eventually, the geometric design space is proposed for the programmable braille reader actuator, which can be improved through pneumatic loading. This work has led to the following submitted manuscript: Arefeh Abbasi, Tian Chen, Bastien F. G. Aymon, and Pedro M. Reis, “Snap buckling of bistable magnetic shells for a braille reader design”.

In the concluding **Chapter 7**, we summarize the primary findings presented throughout this thesis, providing a comprehensive overview. Furthermore, we identify potential directions for future research that have been inspired by the insights discovered within this study.

2 Buckling of Spherical Shells with Dimpled and Bumpy Defects

In this Chapter, we investigate the effect of defect geometry in dictating the sensitivity of the critical buckling conditions of spherical shells under external pressure loading. Specifically, we perform a comparative study between shells containing dimpled (inward) versus bumpy (outward) Gaussian defects. The former has become the standard shape in many recent shell-buckling studies, whereas the latter has remained mostly unexplored. We employ finite-element simulations, which were validated previously against experiments, to compute the knockdown factors for the two cases while systematically exploring the parameter space of the defect geometry. For the same magnitudes of the amplitude and angular width of the defect, we find that shells containing bumpy defects consistently exhibit significantly higher knockdown factors than shells with the more classic dimpled defects. Furthermore, the relationship of the knockdown as a function of the amplitude and width of the defect is qualitatively different between the two cases, which also exhibit distinct post-buckling behavior. A speculative interpretation of the results is provided based on the qualitative differences in the mean curvature profiles of the two cases.

The text and figures in this Chapter are adapted from the published manuscript in Ref. [110]: Arefeh Abbasi, Fani Derveni, and Pedro M. Reis. **"Comparing the buckling strength of spherical shells with dimpled versus bumpy defects."** Journal of Applied Mechanics 90(6), 061008 (2023).

The structure of this Chapter is as follows. The motivation of this study and a brief literature review on the effect of defect geometry on imperfection sensitivity are presented in Section 2.1. In Section 2.2, we detail the finite element modeling (FEM) simulation performed to acquire the result. Then, in Section 2.3, we perform a detailed comparison between the buckling capacity and knockdown factor of spherical shells containing a single dimpled and bumpy defect based on the geometrical properties of the defect. In Section 2.4, we provide an observational discussion regarding the difference in the

knockdown factor for the two types of defect geometry. Furthermore, in Section 2.5, we summarize our findings and provide a perspective for future work.

2.1 Literature Review and Motivation

The mechanical response of thin elastic shells under compression is highly nonlinear [249, 248], with a strong sensitivity to imperfections [250, 251, 11, 252]. Predicting the buckling strength of shells is a longstanding canonical problem in the structural mechanics community [80, 79]. Despite the classic, albeit still challenging, nature of the problem, there has been a recent revival in the interest and research of shell buckling. The study of the critical buckling conditions of spherical shells has been reinvigorated by recent advances in experiments and computation [101, 89, 102, 253, 103, 127, 254, 135, 41].

Most of the recent investigations on spherical-shell buckling are mentioned in Section 1.2 [106, 107, 108, 109, 131, 126] have considered standardized dimpled (Gaussian) defects. Other types of imperfections (*e.g.*, through-thickness defects [253, 90, 255], and dent imperfections [256]) have also been considered, but such cases are sparser. A benefit of focusing on standardized dimples is that they allow for a better contextualization and interpretation of results across different studies. These dimpled imperfections are axisymmetric, localized, and characterized by a radial modulation of the shell mid-surface from a perfect sphere of radius R , by

$$w_I = c\delta e^{-(\beta/\beta_o)^2}, \quad (2.1)$$

where β is the polar angle measured from the north pole (β_o where the center of the defect is located), and the constants β_o and δ control the width and amplitude of the defect (see Figure 2.1). The defect amplitude, which is typically normalized by the thickness of the shell, $\bar{\delta} = \delta/h$, corresponds to the maximum radial deviation at the center of the defect. It is also common to define a geometric parameter [257],

$$\lambda = \{12(1 - \nu^2)\}^{1/4} \eta^{1/2} \beta_o, \quad (2.2)$$

to rescale the defect width, normalizing effects arising from the radius-to-thickness ratio, η , of the shell.

In the existing literature, the prefactor c in Eq. (2.1) has been consistently set to $c = -1$, corresponding to inward-pointing dimples, as shown schematically in Figure 2.1(a). The knockdown factor, κ (see Equation 1.4), of such shells containing dimpled defects, was found in experiments, as well as theoretical and computational analyses, to depend

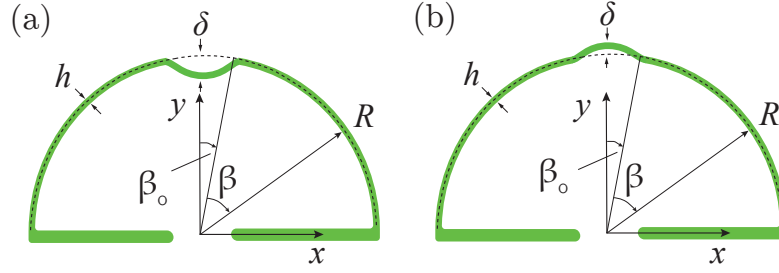


Figure 2.1: **Schematic diagrams of the two types of geometry** considered for our imperfect shells containing (a) a dimpled defect and (b) a bumpy defect, with $c = -1$ and $c = +1$ (cf. Equation 2.1), respectively. In both cases, the hemispherical shells have radius R and thickness h , and the defect is located at the pole (β_0) with a geometry characterized by the amplitude, δ , and half-angular width, β_0 .

strongly on $\bar{\delta}$, dropping sharply from unity for $0 < \bar{\delta} \lesssim 1$ and reaching a plateau for $\bar{\delta} \gtrsim 1$ [89]. Moreover, these results demonstrated that the geometric parameter λ governs the onset and level of the plateau in the $\kappa(\bar{\delta})$ curves, as characterized thoroughly in Ref. [105]. The authors revealed a lower bound of the plateau level that depends solely on η and λ .

Here, we revisit the buckling of a spherical shell containing a single Gaussian defect according to Equation (2.1). We perform a comparative study of the knockdown factor for the previously considered dimpled (inward) defects ($c = -1$; see Figure 2.1a) compared to the symmetric case for bumpy (outward) defects ($c = +1$; see Fig. 2.1b). Recently, Derveni *et al.* [118] have studied the buckling of shells containing a large distribution of defects, validating FEM simulations against experiments using bumpy defects, a choice that was driven by practical experimental constraints; but the difference between dimples and bumps was not explored in detail (see Section 1.2). Otherwise, to the best of our knowledge, bumpy defects have not been investigated systematically to date. We will focus on the following research question: How does the buckling strength compare between single-imperfection shells containing a dimpled versus a bumpy defect?

2.2 Finite Element Simulations

In Figure 2.1, we present schematic diagrams of the two types of geometries for the imperfect hemispherical shells that we will consider, containing either a dimpled defect ($c = -1$ in panel (a)) or a bumpy defect ($c = +1$ in panel (b)). We will focus on hemispherical shells of radius $R = 24.85$ mm, thickness $h = 0.23$ mm, and, thus, $\eta = R/h = 108$ with a single imperfection located at the pole, without loss of generality [106] given the large value of η . This generality assumes there is essentially no dependence of

knockdown factor characterization on η for sufficiently slender shells as long as the defect width is scaled according to Equation (2.2). Each shell is clamped at the equator and (de)pressurized to load it under compression until buckling occurs.

The initial shell geometry considered in the simulations is axisymmetric. As such, the 2D cross-sectional profiles of the imperfect shells presented in Figure 2.2 for different values of $\bar{\delta}$ and λ (see color bar) suffice to fully describe this initial geometry. The perfectly spherical case ($\bar{\delta} = 0$, $\lambda = 0$) is represented by the dashed line. Panels (a, c) and (b, d) represent the shell with dimpled ($c = -1$) and bumpy ($c = +1$) defects, respectively. Representative defects with the same defect width, $\lambda = 2.5$, in a range of amplitudes, $\bar{\delta} \in \{1, 2, 3, 4, 5\}$, are shown in Figures 2.2(a,b). In Figures 2.2(c,d), we present representative shell profiles with the same defect amplitude, $\bar{\delta} = 2.5$, in a range of widths, $\lambda \in \{1, 2, 3, 4, 5\}$. The corresponding lower panels in Figures 2.2 show magnified views of the defect profiles localized at the pole. Beyond these representative cases, our investigation will consider the following ranges for the geometric-parameters space of the defect: $\bar{\delta} \in [0.1, 5]$ in steps of $\Delta\bar{\delta} = 0.1$ for the defect amplitude and $\lambda \in [0.25, 5]$ in steps of $\Delta\lambda = 0.25$ for $\lambda \leq 1$ and $\Delta\lambda = 0.5$ for $\lambda \geq 1$ for the (normalized) defect width; while fixing all other parameters mentioned above. Although these initial geometries are axisymmetric, it is important to anticipate, as our results will evidence, that the post-buckling modes can be asymmetric, especially for shells with bumpy defects.

The material was modeled as a neo-Hookean solid, with Young's modulus of $E = 1.26$ MPa, and a Poisson's ratio of $\nu \approx 0.5$ (assuming incompressibility). These material-specific material properties were chosen to align with the previous experimental studies in Ref. [89, 102, 253, 258, 118], where they were measured directly from experiments and used to validate the finite-element simulations.

The set of geometric and physical parameters mentioned above was chosen to match with Ref. [89] toward enabling a direct comparison with this previous study. However, for the present simulation framework, instead of using the axisymmetry model of Ref. [89, 105], we use a three-dimensional description of the structure using shell elements to capture possible asymmetry buckling behavior. This finite element modeling (FEM) approach has been validated against precision experiments for the specific problem of shell buckling [118, 258]. We followed the FEM methodology to perform simulations with the commercial package Abaqus/Standard.

We employed four-node S4R shell elements with reduced integration points, allowing for finite membrane strains. The hemispherical shell was discretized using sweep meshing, with 300 and 1200 elements in meridional and azimuthal directions, respectively. A mesh convergence study was also conducted in order to ensure that the results were not

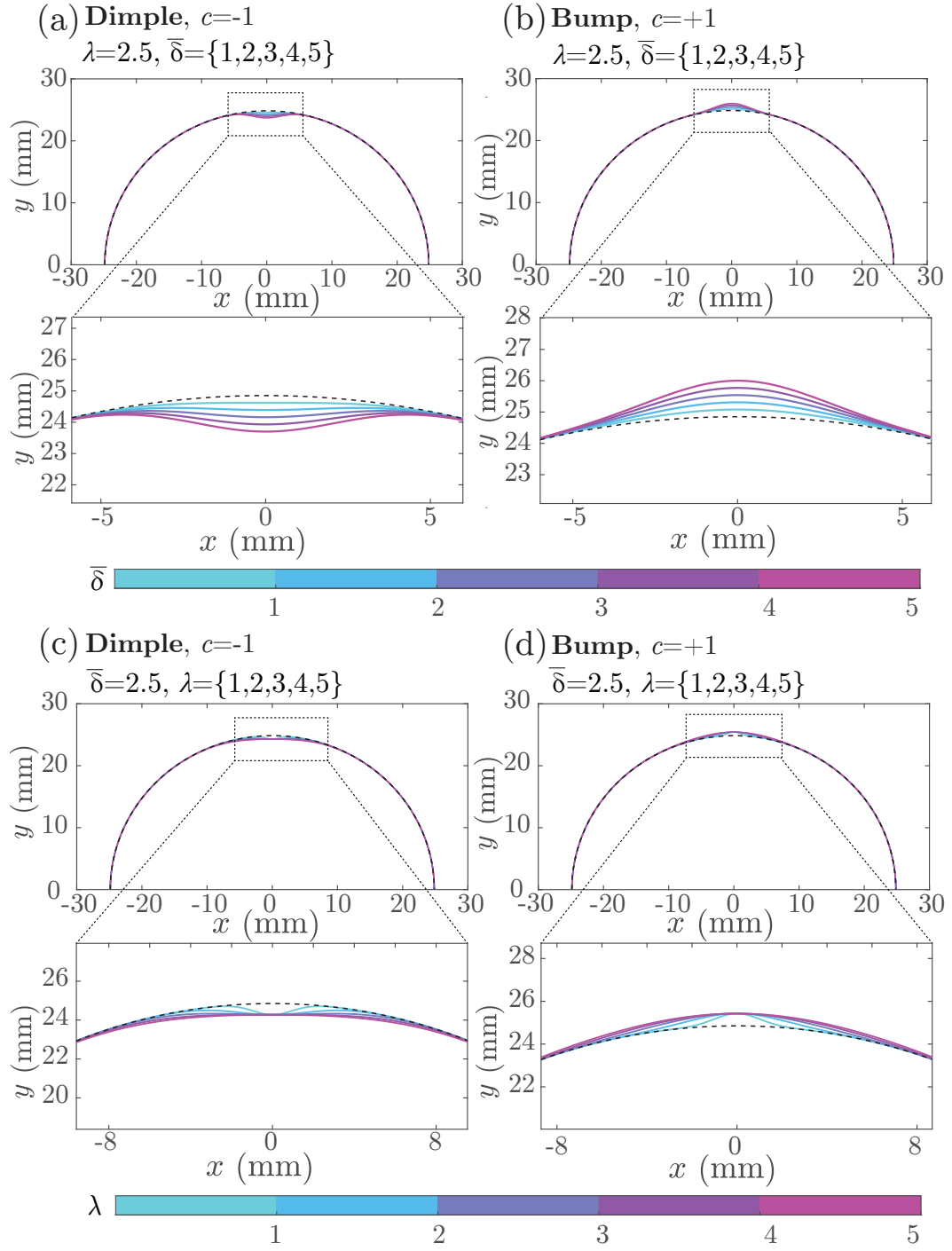


Figure 2.2: **Representative examples of the initial geometric profiles of the imperfect shells considered.** The shells contain defects with (a,b) $\lambda = 2.5$ and $0 \leq \bar{\delta} \leq 5$, and (c,d) $\bar{\delta} = 2.5$ and $0 \leq \lambda \leq 5$. The defects correspond to $c = -1$ in (a,c) and $c = +1$ in (b,d). The lower panels show amplified views near the defects. These geometric profiles serve as input to the FEM simulations.

influenced by mesh size. A Riks solver [259] was used to capture the progress of the simulation along the arc length of the load-displacement curve. We selected an initial arc length of increment of 10^{-1} , with minimum and maximum increment sizes of 10^{-5} and 0.5, respectively. Geometric nonlinearities were considered throughout the study.

In the FEM simulations, each imperfect shell geometry was pressurized until the onset of buckling, at which point the maximum pressure value, p_{\max} , was recorded. Then, the knockdown factor was computed using Equation (1.4). Throughout this Chapter, for ease of comparison, we will refer to the knockdown factor of the imperfect shell with a dimpled defect as κ_D and κ_B for the bumpy defect. The FEM results for the dimpled shells were first verified against Ref. [89] in the previously explored range of parameters and then expanded to a systematic parameter exploration of dimpled and bumpy defects.

2.3 Knockdown Factor of Bumpy versus Dimpled Shells

Following the methodology introduced above, we start our investigation to explore the parameter space of dimpled and bumpy defects. We will characterize and compare the effects of bumps and dimples on the buckling behavior, especially the knockdown factor, of the pressurized imperfect shells.

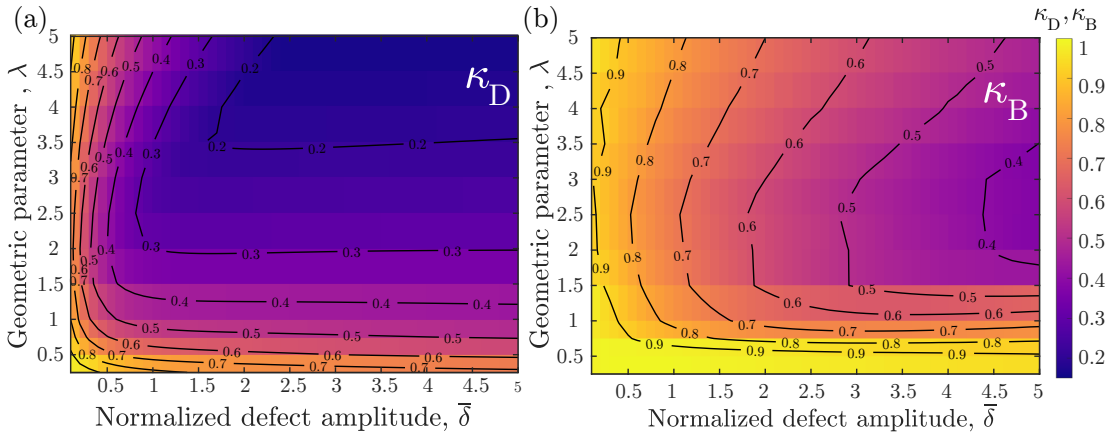


Figure 2.3: **Surface plots of the knockdown factor of shells** containing (a) a dimpled imperfection, κ_D , and (b) a bumpy imperfection, κ_B , for different values of the dimensionless geometric parameter (width), $0.25 \leq \lambda \leq 5$, and normalized defect amplitude, $0.1 \leq \bar{\delta} \leq 5$. Counter lines are superposed for the corresponding values of κ_D and κ_B , in steps of 0.1. The color bar is shared for (a) and (b).

In Figure 2.3, we present surface plots with all the data we obtained from the FEM simulations for the knockdown factor of shells with a dimpled and bumpy imperfection in the whole parameter space $(\bar{\delta}, \lambda)$ specified in Section 2.2: panel (a) for κ_D and panel

(b) for κ_B . Color coding is used to quantify the knockdown factor (see the colorbar). Contour lines for constant values of κ_D and κ_B , in intervals of 0.1, are superposed on the surface plots. For the dimpled shells (Figure 2.3a), the minimum value of the knockdown factor, $\kappa_D \approx 0.15$, is found on the upper extremity of the $(\bar{\delta}, \lambda)$ parameter space. This means that a shell with the deepest and widest defect has the lowest knockdown factor, a fact that is well-established in the literature. By contrast, for bumpy shells (Figure 2.3b), in the explored range, the minimum knockdown factor ($\kappa_B \approx 0.37$) occurs for the defects with the largest amplitude but intermediate width ($2 \lesssim \lambda \lesssim 3$). Overall, the values of κ_B are consistently larger than those of κ_D ; the geometry of dimples plays a more significant role in reducing the knockdown factor of an imperfect shell compared to bumps. These features highlight the first and major qualitative differences between the two cases.

Next, we elaborate on the data presented in Figure 2.3 to more comprehensively describe the impact of the various parameters of the defect geometric on the knockdown factor, κ_D for dimples and κ_B for bumps. For this purpose, we first characterize the dependence of the knockdown factor on the defect amplitude and then on the normalized defect width for both cases. In Figure 2.4, we present κ_D and κ_B as functions of $\bar{\delta}$, each curve corresponding to a different value of λ (see colorbar and marker symbols). The data for shells with dimpled imperfections is shown in panel (a), and those with bumpy imperfections in panel (b).

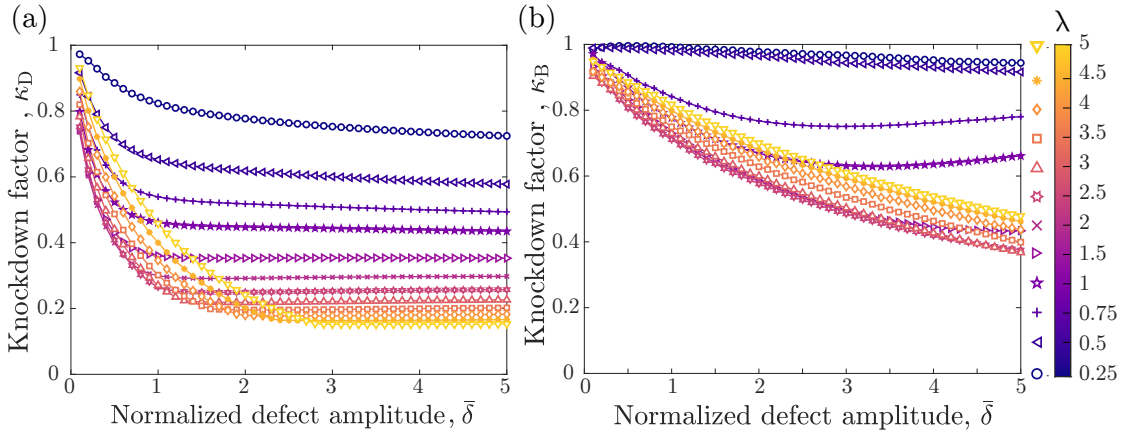


Figure 2.4: **Knockdown factor, κ , as a function of the normalized defect amplitude, $\bar{\delta}$, for imperfect shells with defects in a range of $\lambda \in [0.25, 5]$ (see colorbar and marker symbols).** (a) Knockdown factor, $\kappa_D(\bar{\delta})$, for a shell with a dimpled imperfection; *i.e.*, $c = -1$ in Equation (2.1). (b) Knockdown factor, $\kappa_B(\bar{\delta})$, for a shell with a bumpy imperfection; *i.e.*, $c = +1$ in Equation (2.1).

Note that the $\kappa_D(\bar{\delta})$ data in Figure 2.4(a) are a re-computation of what is already presented in Ref. [89], while the range of geometric parameters for $\lambda < 1$ and $\bar{\delta} > 3$ is further expanded herein. Still, for verification purposes, we selected a specific set of parameters

($\lambda(0 < \bar{\delta} \leq 3) = \{1.5, 5\}$) and confirmed identical results to those in Ref. [89]. We recall that in this previously studied case of dimpled imperfections, κ_D decreases monotonically with $\bar{\delta}$ and eventually reaches a plateau. Both the plateau level and its onset depend on λ , as characterized previously in Ref. [105]. The plateau is less pronounced when $\lambda < 1$ (regime not explored previously). For example, in the extreme case of $\lambda = 0.25$ (the narrowest defects), no plateau is reached; after an initially fast decay, the knockdown factor continues to decrease as the amplitude increases all the way to high-amplitude defects of $\bar{\delta} = 5$. We emphasize that there is little novelty in these results for dimpled shells, which were already presented in Ref. [89] and are presented here for completeness to enable a direct comparison with the case of bumpy imperfections discussed next.

Imperfect shells with bumpy defects exhibit a $\kappa_B(\bar{\delta})$ behavior (Figure 2.4b) that is qualitatively different from the dimpled case discussed above (Figure 2.4a). The main feature is that the values of κ_B tend to be higher overall than κ_D , with smoother decays as a function of $\bar{\delta}$, and non-monotonic behavior in some of the curves. Moreover, the κ_B curves do not exhibit the prominent plateaux observed in κ_D . Three regimes are observed. First, for shells with relatively narrow defects, $\lambda = \{0.25, 0.5\}$, κ_B remains close to unity across the entire range of $\bar{\delta}$; these shells are nearly insensitive to imperfections. Second, for shells with intermediate-width defects, $\lambda = \{0.75, 1\}$, the $\kappa_D(\bar{\delta})$ curves are non-monotonic; κ_B decreases for $0.1 \leq \bar{\delta} \lesssim 3$ and then increases beyond $\bar{\delta} \approx 3$. Third, for $\lambda \geq 1.5$, $\kappa_B(\bar{\delta})$ decreases again monotonically.

In Figure 2.5, to characterize the knockdown factor behavior with respect to the defect width, we present κ_D for dimpled shells (Figure 2.5a), and κ_B for bumpy shells (Figure 2.5b), as functions of λ . The results are qualitatively the same as in Figure 2.5. In the case of dimpled shells (Figure 2.5a), for small defect amplitudes, $\bar{\delta} \leq 3$, the $\kappa_D(\lambda)$ curves are non-monotonic. First, $\kappa_D(\lambda)$ decreases until a threshold defect amplitude and then increases. However, for larger defect amplitudes, $\bar{\delta} \geq 3$, κ_D decreases monotonically. We highlight the fact that the threshold defect amplitude, $\bar{\delta} \approx 3$, corresponds to the largest dimple amplitude before the onset of any of the plateaux for the whole range of λ considered. Past $\bar{\delta} \approx 3$, the $\kappa_D(\lambda)$ curves are monotonic due to the insensitivity of shells to defect amplitude in this regime, for all λ values explored (cf. Figure 2.5a).

Turning to bumpy defects, in Figure 2.5(b), we plot κ_B versus λ , noting that the behavior is different than their dimpled counterpart (Figure 2.5a). We find that $\kappa_B(\lambda)$ is always non-monotonic, decreasing up to $\lambda \lesssim 2.5$, and then increasing for $\lambda \gtrsim 2.5$. By contrast, for the dimpled shells (Figure 2.5a), $\kappa_D(\lambda)$ was only non-monotonic when $\bar{\delta} \leq 3$. This distinguishing feature between bumpy and dimpled shells can be attributed to the fact that, in the dimple case, the plateau region is insensitive to defect amplitude when $\bar{\delta} \geq 3$ for all values of λ ; this behavior does not exist in bumpy shells given the absence of any

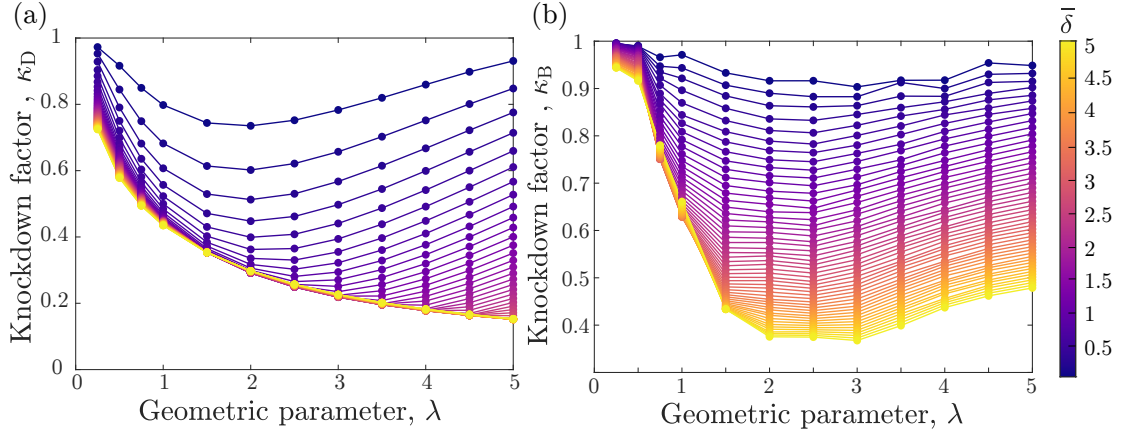


Figure 2.5: **Knockdown factor, κ , as a function of the normalized defect width, λ for imperfect shells with defect amplitudes in a range of $\bar{\delta} \in [0.1, 5]$ (see colorbar).** (a) Knockdown factor, $\kappa_D(\lambda)$, for a shell with a dimpled imperfection; *i.e.*, $c = -1$ in Equation (2.1). (b) Knockdown factor, $\kappa_B(\lambda)$, for a shell with a bumpy imperfection; *i.e.*, $c = +1$ in Equation (2.1).

plateauing.

Representative snapshots of post-buckling configurations obtained in the FEM simulations are shown in Figure 2.6; the color map represents radial displacements. The top (x - y) view of the shells is presented in the top row, and the isometric (x - y - z) view is in the lower row. We refer to the post-buckling configuration as the first stable mode captured along the pressure-volume path [89] immediately after the onset of buckling. By way of example, in Figure 2.6, we consider imperfect shells containing a dimpled defect with $\lambda = 2.5$ and $\bar{\delta} = 1.8$, in panel (A), and bumpy defects with $\lambda = 2.5$ and $\bar{\delta} = \{0.3, 1.3, 2.9, 4.4\}$, in panels (B)-(E), respectively.

The axisymmetric post-buckling configuration in Figure 2.6(A) is representative of all the dimpled imperfect shells within the explored range of parameters: the buckling initiates at the defect location and expands axisymmetrically outwards. The post-buckling configurations are qualitatively distinct for shells with bumpy defects and depend on the value of $\bar{\delta}$; see Figure 2.6(B)-(E). For small defect amplitudes (*e.g.*, $\bar{\delta} = 0.3$, B), the shell buckles with a periodic deformation mode (akin to wrinkling) near the clamped equator, far from the bumpy defect located at the north pole. It is possible these results for small-imperfection shells are dominated by imperfections induced by the clamping conditions or by numerical imperfections (artifacts) caused by the meshing. However, in the experimental observations of Ref. [118], we did find that the buckling location is close to the boundary for small bumpy defects, which would tend to suggest that the periodic deformation mode is not an artifact. For higher values of $\bar{\delta}$, the loci of buckling occur near

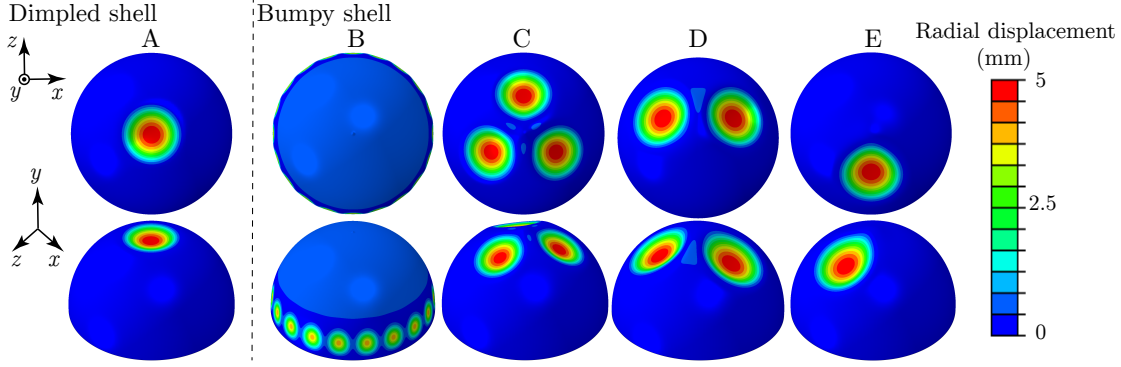


Figure 2.6: **Representative post-buckling configurations.** (A) A dimpled post-buckling configuration is representative of all shells containing a dimpled defect (even if the exact values of the radial displacement may differ). (B, C, D, E) Post-buckling configurations of shells containing a bumpy defect, for the selected cases of $\lambda = 2.5$ and $\bar{\delta} = \{0.3, 1.3, 2.9, 4.4\}$, respectively.

the bumpy defect but non-axisymmetrically to its side. For example, these post-buckling configurations are lobed with three, two, or one inverted-cap region for $\bar{\delta} = 1.3, 2.9$, and 4.4 , respectively. A detailed analysis of these post-buckling configurations for bumpy shells is beyond the scope of the present study.

Finally, for an even more direct comparison between the dimpled and bumpy cases, in Figure 2.7, we convey an alternative representation of the same data reported above by plotting κ_D as a function of κ_B . Each data point corresponds to the same pair of $(\bar{\delta}, \lambda)$ parameters for bumps and dimples. Different marker symbols and colors define various values of λ , while the marker size indicates the variation of $\bar{\delta}$. Beyond the specific quantitative observations uncovered from the data in Figures 2.4 and 2.5, this representation highlights that bumpy shells consistently have a higher buckling strength than dimpled shells, with all of the data lying above the $\kappa_B = \kappa_D$ line (dashed line in Figure 2.7). Three different regimes of behavior are observed, similar to Figure 2.7(b). First, for $\lambda = \{0.25, 0.5\}$, both κ_B and κ_D decrease with increasing defect amplitude, but the reduction in κ_D is more pronounced than κ_B ought to the lower sensitivity of bumps to defect amplitude in this regime. Second, for $\lambda = \{0.75, 1\}$, we observe a non-monotonic behavior; with increasing $\bar{\delta}$, first, both κ_D and κ_B decrease until a specific value of $\bar{\delta}$ after which, κ_B increases, while κ_D continues to decrease. Two distinct regions are obvious in the third and last regime for $\lambda \geq 1.5$. Initially, decreasing κ_D follows a decrease in κ_B until the defect amplitude of the plateau onset [105]. After this onset, κ_B continues to decrease while κ_D remains approximately unchanged (plateau region of insensitivity to defect amplitude).

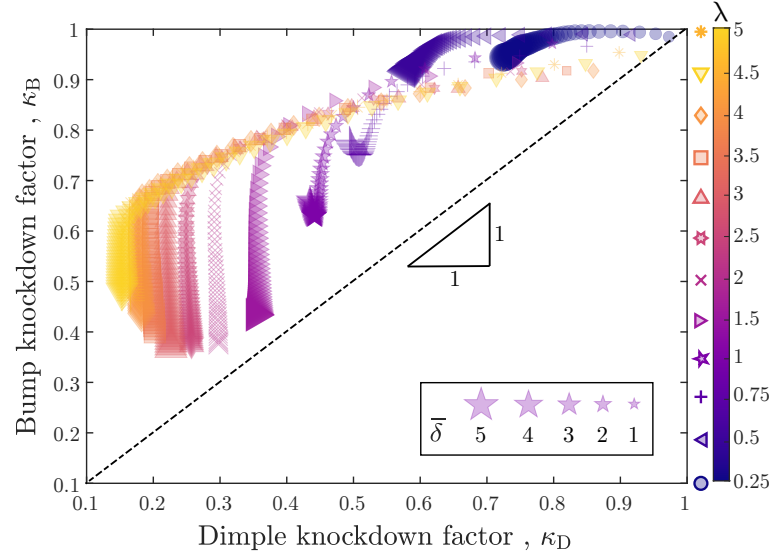


Figure 2.7: **Knockdown factor of bumpy shells, κ_B , versus that of dimpled shells, κ_D** , for a range of dimensionless defect geometric parameters, $0.25 \leq \lambda \leq 5$, and defect amplitudes, $0.1 \leq \bar{\delta} \leq 5$. The values of λ are color-coded (see color bar), and the values of $\bar{\delta}$ are represented by the size of the symbol (see legend). The dashed line represents $\kappa_B = \kappa_D$.

2.4 Why are Bumpy Shells Stronger than Dimpled Shells?

In this section, we provide a discussion that seeks to address, even if speculatively, the following emerging questions: Why are bumps stronger than dimples? Why do bumps show different buckling modes of deformation compared to dimples?

The dimpled and bumpy shells are only distinguishable by their defect region located at the pole, with $c = \pm 1$ in Equation (2.1). We focus on the difference in the geometry of their undeformed (initial) configuration, as measured by the mean and Gaussian curvatures profiles defined, respectively, as

$$\begin{aligned}\mathcal{K}_H(\beta) &= \frac{1}{2}(k_1 + k_2), \\ \mathcal{K}_G(\beta) &= k_1 k_2,\end{aligned}\tag{2.3}$$

where k_1 and k_2 are the two principal (local) curvatures of the shell surface. We have numerically computed \mathcal{K}_H and \mathcal{K}_G with the function `surfature` [260] in *MATLAB*, taking as input the point-cloud data representation of the undeformed surface that input into the FEM simulations. We will add the subscripts D and B to denote the corresponding quantities for dimples and bumps, respectively, *i.e.*, $(\mathcal{K}_{HD}, \mathcal{K}_{HB})$ and $(\mathcal{K}_{GD}, \mathcal{K}_{GB})$.

In Figure 2.8, we plot the mean curvature, \mathcal{K}_H , in panels (a) and (b), and the Gaussian

curvature, \mathcal{K}_G , in panels (c) and (d), as functions of the polar angle, β . The angular width of the defect, β_o , defined in Equation (2.1), is represented by the vertical dashed lines. We restrict our results to the representative case with $\lambda = 2.5$ (where the knockdown factor of bumpy shells is lowest) while varying the defect amplitudes $\bar{\delta} = \{1, 2, 3, 4, 5\}$ (see color bar). The left panels (a) and (c) correspond to the dimpled shells, and the right panels (b) and (d) to the bumpy shells. Qualitatively similar behavior to what we describe next is found for other values of λ , but a detailed quantitative analysis is beyond the scope of the present work and unnecessary to the qualitative interpretation that we will provide.

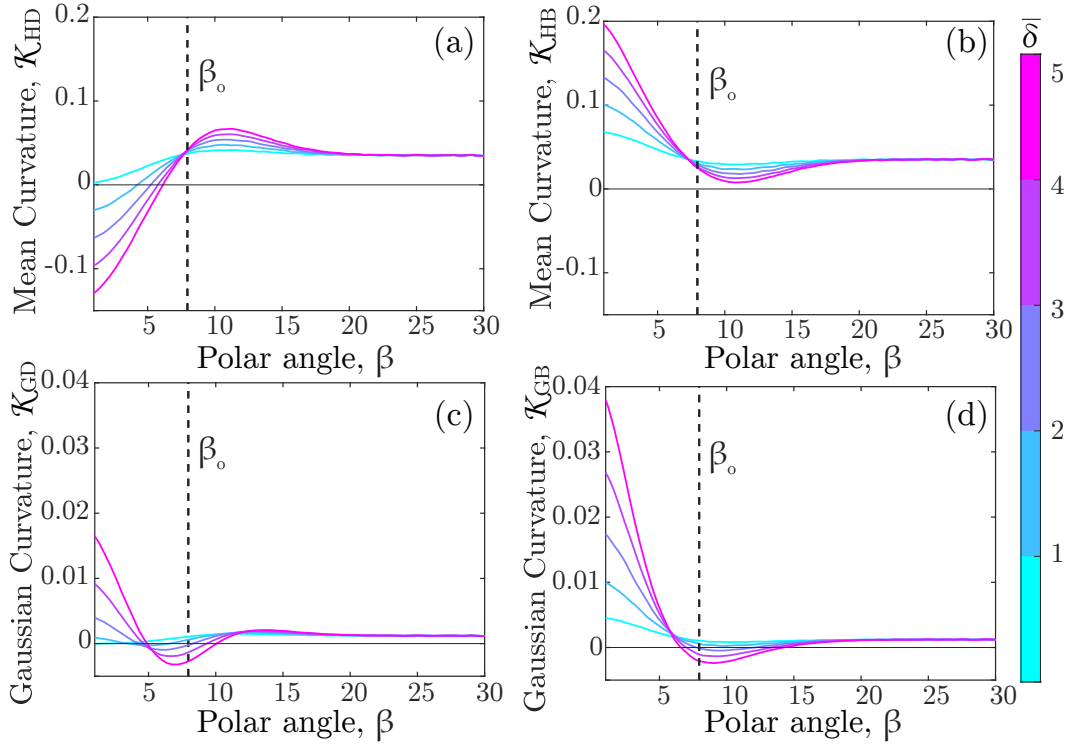


Figure 2.8: **Curvature profiles of the initial geometry of the imperfect shell as a function of the polar angle, β .** Representative cases are chosen with the dimensionless geometric parameter of $\lambda = 2.5$, and amplitudes in a range of $\bar{\delta} \in [1, 5]$ (see color bar). (a) Mean curvature, \mathcal{K}_{HD} , and (c) Gauss curvature, \mathcal{K}_{GD} , for a shell with a dimpled imperfection; *i.e.*, $c = -1$ in Equation (2.1). (b) Mean curvature, \mathcal{K}_{HB} , and (d) Gauss curvature, \mathcal{K}_{GB} , for a shell with a bumpy imperfection; *i.e.*, $c = +1$ in Equation (2.1). The vertical dashed line indicates β_o , the defect opening angle corresponding to $\lambda = 2.5$.

Hereon, we shall refer to the $\beta < \beta_o$ region as the *core* of the defect and to the neighboring region right past the defect, $\beta \gtrsim \beta_o$, as the *rim* of the defect. The mean-curvature curves for dimpled shells, $\mathcal{K}_{HD}(\beta)$ (Figure 2.8a), exhibit a maximum located at the defect rim. Within the defect core, by construction, the dimples have a minimum mean curvature that is typically negative and always lower than that of the nominal spherical shell. By

contrast, for the bumpy shells, all the $\mathcal{K}_{HB}(\beta)$ curves have a minimum located at the defect rim (Figure 2.8b). At the defect core, the bumps have positive mean curvature, always greater than that far away in the shell.

Rewording the above observations, it is important to highlight that the minimum of \mathcal{K}_H occurs at the core for dimples and at the rim for bumps. Conversely, the maximum of \mathcal{K}_H occurs at the rim for dimples and at the core for bumps. As evidenced in Figure 2.6 and studied extensively in the literature, a depressurized imperfect spherical shell exhibits a buckling mode with one (or more) inward-inverted cap, whose mean curvature has the opposite sign of the nominal sphere. It is reasonable to envision that regions of mean curvature lower (or higher) than that of the nominal sphere will serve as weak (or strong) spots, respectively. This reasoning, even if speculative, is compatible with the results in Figure 2.6. For dimples (Figure 2.6A), the post-buckling configuration does indeed occur at the defect core, where \mathcal{K}_H is minimum. For bumps (Figure 2.6B-D), the buckling appears to nucleate at the defect rim, where \mathcal{K}_H is minimum, and repelled by the defect core, which appears to have a stiffening effect. Moreover, the fact that \mathcal{K}_H is always positive in the considered range of $\bar{\delta}$ may be the source of why the knockdown factor of bumpy shells is consistently higher than that of dimpled shells.

Regarding the Gaussian curvature data presented in Figure 2.8(c, d), the results are, as far as we can tell, less insightful. We observe that at the defect core, \mathcal{K}_G is higher for the bumpy than the dimpled shells, which may further contribute to the lower buckling strength of the latter (for the same magnitude of geometric parameters). Otherwise, both cases display Gaussian curvature profiles that are qualitatively similar. All \mathcal{K}_G curves are non-monotonic with a minimum near the defect rim, occurring before (or after) β_0 for dimples (or bumps), respectively. In both cases, this minimum can be negative for defects with larger amplitudes ($\bar{\delta} \gtrsim 1$ for the dimples and $\bar{\delta} \gtrsim 3$ for the bumps) but always positive otherwise. Outside of this region of the minimum neighboring the rim, $\mathcal{K}_G > 0$ in both cases. Overall, we do not see any salient qualitative differences in the \mathcal{K}_G between the dimpled and bumpy cases that correlate to the $\kappa_D > \kappa_B$ reported in Figure 2.7 and earlier plots.

There are similarities between the geometry of the bumpy shells we considered and the classical literature for the Cohn-Vossen shape [261]. Shells with non-constant and sign-changing Gaussian curvature can be a source of an exceptional bending mode on a surface of revolution [2]. It is possible that this behavior can be related to the different buckling modes we observed in our bumpy shells, although we have no formal ground other than reasoning by analogy to support this statement. Future theoretical work will be necessary to further rationalize the present findings, which point to the importance of the detailed curvature profiles of doubly curved imperfect shells, with a special spotlight

on their mean curvature.

2.5 Summary and Outlook

In this Chapter, we used a finite-element simulations approach, which was validated previously against experiments, to study the buckling strength of imperfect shells containing either a dimpled or a bumpy imperfection. Whereas dimpled shells have been studied previously in much detail, bumpy shells have remained largely unexplored. We considered defects with a standard Gaussian profile (cf. Equation 2.1), enabling direct and detailed comparisons across the dimpled ($c = -1$) and bumpy ($c = +1$) cases. Our results evidence that the role of bumps in reducing the buckling strength of the spherical shell is less dramatic than for dimples, at least within the ranges of parameters we explored. The knockdown-factor sensitivity to the detailed defect geometry is also less prominent in bumps. Overall, the knockdown factor of a bumpy shell is always greater than that of a dimpled one, $\kappa_B > \kappa_D$, for the same magnitude of geometric parameters. In both cases, the knockdown factor is not always reduced when the defect is widened.

We attempted to discuss the differences in knockdown factor between dimpled and bumpy shells under the light of their mean and Gaussian curvature profiles. Our interpretation suggests that regions of the imperfect shell with minimal mean curvature serve as weak points for the onset of buckling. These minima occur at the defect core for dimpled shells and at the defect rim for bumpy shells. For the latter, the core appears to have a stiffening effect, which repels the post-buckling inverted caps, making the buckling mode asymmetric and potentially multi-lobed.

We acknowledge that our investigation was mostly descriptive and observational. In the absence of a formal theoretical framework, it is difficult to devise a predictive rationale for these observations. Still, we hope that our thorough comparative study will be valuable in the ongoing revival of shell-buckling studies. A systematic theoretical investigation will be a much-needed next step in rationalizing the current findings. Additionally, it would be interesting to consider other imperfection geometries and establish direct relations between the mean/Gaussian curvature profiles and the resulting critical buckling conditions. Shell buckling is a highly nonlinear and nontrivial phenomenon, and we believe that specific case studies like ours are essential to gaining insight and motivating modeling directions.

From a practical viewpoint, our research is aligned with efforts currently underway by NASA and others interested in large-scale shell structures [99, 44, 262]. These efforts aim to replace the purely-empirical knockdown factors guidelines in design codes of aerospace structures with mechanics-based predictive methods that take manufacturing-based data

on the imperfection distributions as input. Our results demonstrate that different types of defects, even if characterized by similar geometric parameters, can yield quantitatively and qualitatively different reductions of buckling strength. For example, the design of shells containing only bumpy defects can be tackled less conservatively than dimpled shells.

3 Probing the Buckling of Spherical Shells

As elaborated in the Introduction chapter (Section 1.2) The prediction of the critical buckling conditions of shell structures is plagued by imperfection sensitivity. Non-destructive testing through point-load probing has been recently proposed to map the stability landscape of cylindrical shells. However, the counterpart procedure for spherical shells is still debatable. In this Chapter, we focus on the mechanical response of pressurized spherical shells containing a single dimple-like defect to a point probe. Combining experiments, finite element modeling (FEM), and existing results from classic shell theory, we characterize the nonlinear force-indentation response of imperfect shells at different pressurization levels. From these curves, we seek to identify the critical buckling pressure of the shell. In particular, the indentation angle is varied systematically to examine its effect on the probing efficacy. We find that the critical buckling point can be inferred non-destructively by tracking the maxima of the indentation force-displacement curves if the probe is implemented sufficiently close to the defect. When probing further away from the defect, the test fails to predict the onset of buckling since the deformation due to indentation remains localized in the vicinity of the probe. Using FEM simulations and shallow shell theory, we quantify the characteristic length associated with this localized deformation due to indentation, both in linear and nonlinear regimes. Our results demonstrate the limiting conditions of applicability for the usage of probing as a non-destructive technique to assess the stability of spherical shells.

The text and figures in this Chapter are adapted from the published manuscript in Ref. [258]: Arefeh Abbasi, Dong Yan, and Pedro M. Reis. **"Probing the buckling of pressurized spherical shells."** Journal of the Mechanics and Physics of Solids 155, 104545 (2021).

This Chapter is organized as follows. The motivation of this study is presented in Section 3.1, along with a brief literature review on the non-destructive probing technique.

Then, we define the problem at hand in Section 3.2. In Section 3.3, we describe the experimental methodology to fabricate imperfect shells containing a precisely engineered defect, as well as the experimental protocol followed in the probing tests. Details on the FEM simulations are provided in Section 3.4. In Section 3.5.1, we report on experiments and numerical simulations to investigate the response of the fabricated imperfect shell under pressure loading while simultaneously indenting it at the center of the defect. Then, in Section 3.5.2, we vary the indentation angle by incrementally moving the indentation point away from the defect to study its influence on the performance of the probe and to examine the applicability of this technique in predicting the knockdown factor of the shell non-destructively. The FEM is validated by comparing numerical predictions to experimental measurements. In Section 3.5.3, we investigate the localized deformation of pressurized spherical shells under indentation at different locations. Finally, in Section 3.5.4, we use classic shallow shell theory and the validated FEM to rationalize our results. Specifically, we analyze the localized nature of the indentation and characterize the length scale associated with the indentation neighborhood. Eventually, in Section 3.6, we summarize our findings and provide a perspective for future work.

3.1 Literature Review and Motivation

Toward developing a general framework to characterize the stability of shells, a novel non-destructive probing technique has been proposed and successfully applied to axially compressed cylindrical shells as discussed in detail in the Introduction chapter (Section 1.3) [130, 125, 126, 127]. The basis of this approach is to measure the nonlinear response of the shell to a point probe. The force-displacement relationship measured by systematically varying the level of axial compression is used to construct the stability landscape. The area under load-displacement curves gives the energy barrier that must be overcome by any static or dynamic lateral disturbances to buckle the shell [130, 125, 132]. Viro *et al.* [127] built an experimental setup to exert a point probe on cylindrical shells under axial compression. The authors provided experimental evidence that the hyper-dimensional landscape fully characterizes the stability of perfect and imperfect cylindrical shells. The complex stability of shells was reduced to a three-dimensional phase space description that can be analyzed using modern tools from nonlinear dynamics and dynamical systems. By tracking the ridges of force-displacement curves, the knockdown factor of cylindrical shells could be extrapolated correctly.

Recently, Abramian *et al.* [138] applied this probing technique to commercial cylinders containing a hole and showed that when the location where buckling nucleates is known, the buckling load of each individual shell can be accurately predicted. Additionally, a

new numerical solution was recently proposed, where instead of considering the linear instability of a shell with defects, a finite, nonlinear destabilizing perturbation was imposed on an otherwise perfect shell [133]. In this study, the elastic response of the shell was captured by the Donnell–Mushtari–Vlasov (DMV) theory. The fully nonlinear equilibrium states on the boundary of the unbuckled state’s basin of attraction for an axially loaded cylindrical shell were identified. It was shown that, for changes in the applied compression, a single dimple undergoes homoclinic snaking in the circumferential direction until the circumference is completely filled with a ring of buckles.

In a series of related studies, the non-destructive probing technique was recently applied to cylindrical thin shells containing local dimple-like imperfections, both computationally [135, 136] and experimentally [137]. The proposed algorithm based on the probe force-displacement curves was validated on perfect, as well as imperfect, axially loaded cylindrical shells. More importantly, the influence of background imperfections and the location of probing relative to the imperfections were considered to examine the robustness of the technique. The results showed that the probe has to be set close enough to the dominant defect in the shell to ensure a high-fidelity prediction.

To date, it has remained inconclusive whether the probing technique can serve as an effective way of assessing the stability of spherical shells in a way that parallels the successful case of cylindrical shells mentioned above. The response of perfect spherical shells subjected to external uniform pressure with and without a probing force was recently investigated by Hutchinson *et al.* [107, 108] based on a small-strain and moderate-rotation shell theory formulation, both under prescribed pressure and prescribed volume change. Thompson *et al.* [126] addressed the testing of compressed shell structures using the concept of probing by a controlled lateral displacement to gain quantitative insight into their buckling behavior and to measure the energy barrier against buckling, providing design information about a structure’s stiffness and robustness against buckling in terms of energy and force landscapes.

The first experimental study on probing of imperfect spherical shells was carried out by Marthelot *et al.* [102]. They investigated the buckling strength and energy barrier of shells containing a geometric defect subjected to a simultaneous combination of pressure loading and a probing force. They showed that the probing strategy applied to the defect is a successful way to assess the stability of spherical shells. In contrast, by considering a point load located off-axis from the defect, it was found that the energy barrier measured from the probe was similar to that of a perfect shell but dramatically jumped down to zero when buckling occurred. However, these experiments were only conducted in limiting cases; the probe was either located exactly at the center of the defect or far away from the defect. Therefore, there is a need to more systematically explore the response

of the spherical shell loaded by a probe located in between the two extreme locations. This timely data would indicate the limitations and range of applicability of the probing technique in the context of identifying the critical buckling conditions and encoding the characteristics of the stability of spherical shells.

3.2 Problem Definition: Non-Destructive Probing of Spherical Shells

We have performed a thorough investigation on how the response of an imperfect spherical shell is affected by the location (angle) of indentation with respect to the location of the defect. By analyzing the indentation force-displacement curves measured by a probe positioned at different locations, which are systematically varied, we seek to estimate the critical point and contrast this value with the direct measurement obtained from the buckling test. Using shell theory and experimentally validated finite element modeling (FEM), we then describe how the localized nature of indentation of spherical shells dominates the performance of probing and obstructs its usage as a non-destructive technique to predict the buckling conditions of spherical shells.

We consider a thin, elastic, hemispherical shell of radius, R , and constant thickness, h , containing a geometric defect at its north pole; see the schematic diagram in Figure 3.1(a). As a representative example of a thin shell, in both experiments and simulation, we will focus on a value of the radius-to-thickness ratio of $R/h = 78$, unless otherwise stated (specifically in Section 3.5.4 where we systematically vary h , and hence, also R/h). The shell is clamped at its equator. The amplitude of the defect, δ , corresponds to the maximum radial deviation of the shell from a perfect hemisphere. Defining β as the polar angle measured from the north pole (where $\beta = 0$), the axisymmetric dimple-like defect extends over the region $0 \leq \beta \leq \beta_o$, with β_o being its half angular width (*i.e.*, the angular amplitude).

The shell is first loaded under uniform pressure, which is set at a prescribed value, p_o . The shell is then indented by a point load applied on its outer surface, along its radial direction, while imposing the indentation displacement, ξ . This indentation is performed by a rigid circular indenter of radius a (see schematic in Figure 3.1b). The resulting reaction force of the indenter is referred to as the probe force, F . Each indentation test is performed at different pressure levels (p_o) to obtain the corresponding probe force-displacement curves, $F(\xi)$.

In Figure 3.1(c), we show a sketch of a representative $F(\xi)$ curve at a set pressure level (the actual data will be presented in Figure 3.7). The probing force first increases with

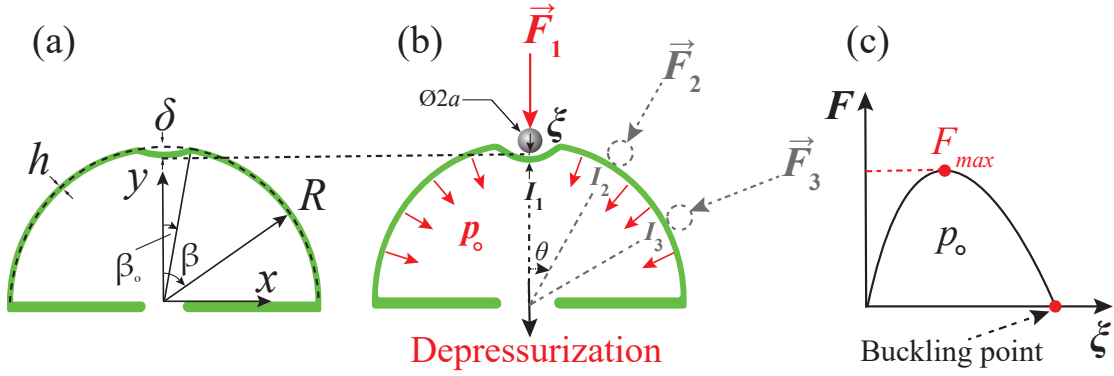


Figure 3.1: **Definition of the problem.** (a) A spherical shell of radius, R , and thickness, h , contains a dimple-like geometric defect at the north pole. The geometry of the defect is characterized by its amplitude, δ , and half-angular width, β_o . (b) The shell is simultaneously depressurized to a preset pressure level p_o and then indented radially by a circular rigid indenter of radius, a , inducing a deflection ξ at the contact point I . The action line of the force, F , is set at an angle θ with respect to the (vertical) axis of symmetry of the defect. To change the probe angle, the indentation is applied at different locations (I_1, I_2, I_3, \dots). (c) Sketch of a typical probe force versus displacement curve, $F(\xi)$, at the constant preset pressure level of p_o .

probe displacement to a maximum value (F_{max}), after which F decreases and eventually reaches zero when the shell collapses. If the prescribed pressure is increased to a level such that $F_{max} = 0$, the shell is loaded at the critical point, and the corresponding pressure is the critical load. From the $F(\xi)$ curves measured before reaching the collapse at $F_{max} = 0$, and motivated by recent work on cylindrical shells [127, 108, 130, 125, 126], one may expect that extrapolating the $F_{max}(p_o)$ curve to zero would provide access to the critical buckling pressure of our spherical shells in a non-destructive manner. We also seek to examine the robustness of this non-destructive technique in testing imperfect spherical shells. Specifically, we focus on the effect of positioning the probe with respect to the location of the defect. To do so, we will systematically vary the angle, θ , between the line of action of the probe force and the axis of symmetry of the defect. We will analyze the nonlinear force-displacement response of indentation exerted at different positions in order to attest its ability to predict the critical point without prior knowledge of defect distribution.

3.3 Experimental Methods

In this section, we first present the rapid prototyping technique that we used to fabricate shell specimens containing a precisely engineered imperfection. We then calibrate the thickness and characterize the geometry of defects using optical profilometry. This

fabrication technique was developed in collaboration with Dong Yan. Finally, we detail the apparatus and the experimental protocol that was developed to exert indentation on pressurized imperfect shells.

3.3.1 Fabrication of the Imperfect Shell Specimens

We fabricated imperfect hemispherical shells containing a precisely engineered geometric defect following a customized coating protocol proposed for the first time in our recent work [104], which itself was built upon a previously developed coating technique [101, 89], with some important modifications. Next, we detail the basis of the fabrication protocol. The protocol contains 2 steps – (I) Fabrication of the mold and (II) Fabrication of the shell.

(I) Fabrication of the mold: First, we manufactured an elastic mold as the negative of a rigid hemisphere (stainless steel ball, radius 25.4 mm, TIS-GmbH, Germany) using a silicone-based vinylpolysiloxane (VPS) polymer (Elite Double 32, Zhermack, Italy), base to catalyst ratio of 1:1 in weight, fully mixed for 10 s at 2000 rpm (clockwise), and then degassed for 10 s at 2200 rpm (counterclockwise) using a centrifugal mixer (ARE-250, Thinky Corporation, Japan). The liquid VPS was poured into a boxed-shaped container with the hemisphere placed on its bottom side (Figure 3.2a). A cylindrical pillar (radius 4.41 mm) was 3D-printed and positioned at a distance of ≈ 0.5 mm above the north pole of the steel ball. As a result, the mold contained a circular thin region of half angular width 10° and thickness 0.5 mm at the pole. When the VPS was cured, the mold was detached from the ball and the pillar (Figure 3.2b). Next, we activated the mold surface utilizing air plasma generated by a plasma cleaner (PDC-002-HPCE, Harrick Plasma) for 2 minutes and then treated with TMCS (Trimethylchlorosilane, Sigma-Aldrich) in a vacuum chamber for 1 hour. The purpose of this treatment was to reduce the adhesion strength between the mold and the MRE so that shell specimens could be easily demolded.

(II) Fabrication of the shell: The shell specimen was then fabricated by coating the concave inner surface of the mold with the VPS solution (Figure 3.2c and 3.2d). The polymer mixture was prepared and poured into the mold by waiting for a set time $t_w = 210$ s upon preparation, thereby raising the viscosity [101] to target the desired value of the shell thickness ($h = 0.327$ mm); more details in Section 3.3.2. The gravity-driven viscous flow yielded a thin layer of VPS on the mold by facing the spherical surface down (Figure 3.2d). To produce a geometric defect in the shell before the polymer was cured, we applied constant negative pressure to the mold to a set pressure level $q = 1.2$ kPa by extracting the air inside using a syringe pump (Figure 3.2e). Under this depressurization, the soft spot (plate-like thin region) of the mold deformed inwards, and the associated

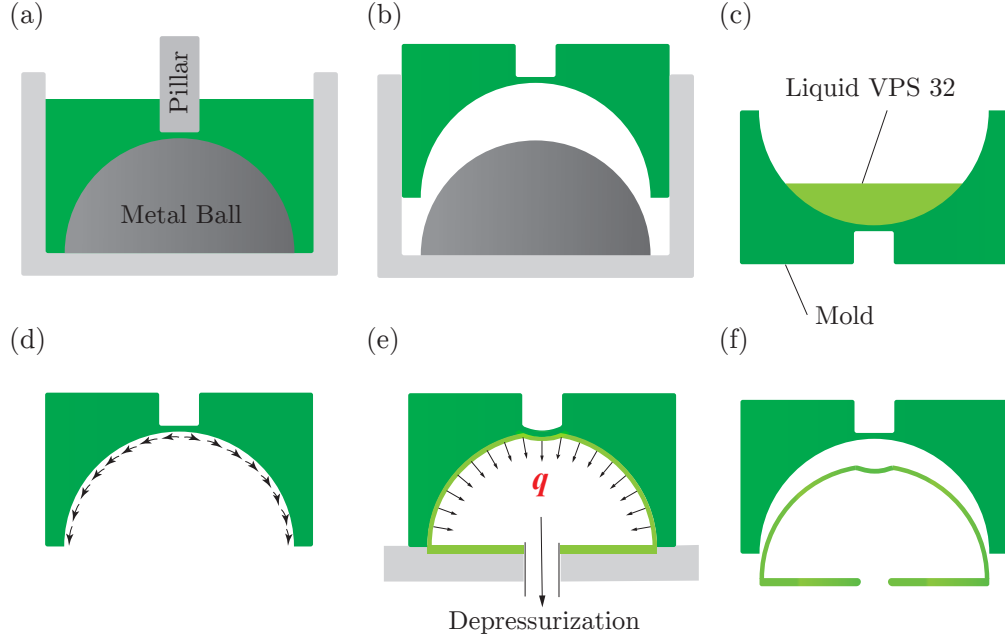


Figure 3.2: **Schematic diagrams of the experimental protocol employed in the fabrication of thin hemispherical shells containing a geometric defect.** (a) First, A metal hemisphere (radius $R=25.4$ mm) and a 3D-printed cylindrical pillar are used to fabricate a mold. (b) The mold is detached from the metal ball after it is cured. (c) A negative spherical mold with a thin region at the pole was filled with liquid VPS. (d) The mold is turned upside-down, leading to the mold then being coated by the gravity-driven viscous flow of VPS, yielding a thin film on the mold. (e) During the curing of the polymer solution, the elastic mold was depressurized to deflect the thin region, thus producing a geometric defect in the shell. (f) Finally, upon curing, the shell was peeled off from the mold.

deflections eventually produced the axisymmetric dimple-like geometric defect at the pole upon curing. During this depressurization stage, the bulk regions of the mold (other than the soft spot) exhibited negligible deformation. Finally, the thin, elastic, imperfect shell was peeled off from the mold (Figure 3.2f). Using this technique, we were able to vary the geometry of the defect on demand, namely its amplitude δ and half angular width β_0 , by setting the applied pressure and the width of the thin region of the mold, respectively. Additional details of the protocol can be found in Ref. [104].

3.3.2 Predicting the Thickness of the Shell Obtained from Fabrication

In this Section, we report the result from the calibration of the thickness and setting the waiting time for the shell fabrication protocol. As shown by Lee *et al.* [101], the final

thickness of the shell is given by

$$h \sim \sqrt{\frac{\mu_0 R}{\rho g \tau_c}} \quad (3.1)$$

where μ_0 and ρ are the viscosity and the density of the polymer solution, respectively, R is the radius of the mold, and τ_c is the characteristic curing time. Therefore, the thickness of the shell can be systematically increased, on-demand, by increasing the waiting time. To characterize and calibrate the thickness of the shell, h , we fabricated a series of shells with different values of waiting time while keeping the radius constant. Then, we cut a narrow strip from the shell along the meridian to measure the thickness of this strip at five different locations using a microscope (VHX-5000, Keyence Corporation, Japan). The values for three different specimens with the same waiting time were averaged. In Figure 3.3, we plot the thickness of the shell, h , as a function of the waiting time, t_w . We observe that the thickness of the shell increased significantly due to the increase in t_w , which is consistent with the previous results in Ref. [101]. Given this calibration for a desired thickness value, the shell fabrication was done based on the respective t_w . The waiting time chosen and fixed for the following results is 210 s, which gives us a shell with a thickness of $h = 327 \pm 11 \mu\text{m}$. The corresponding radius-to-thickness ratio is $R/h = 78$.

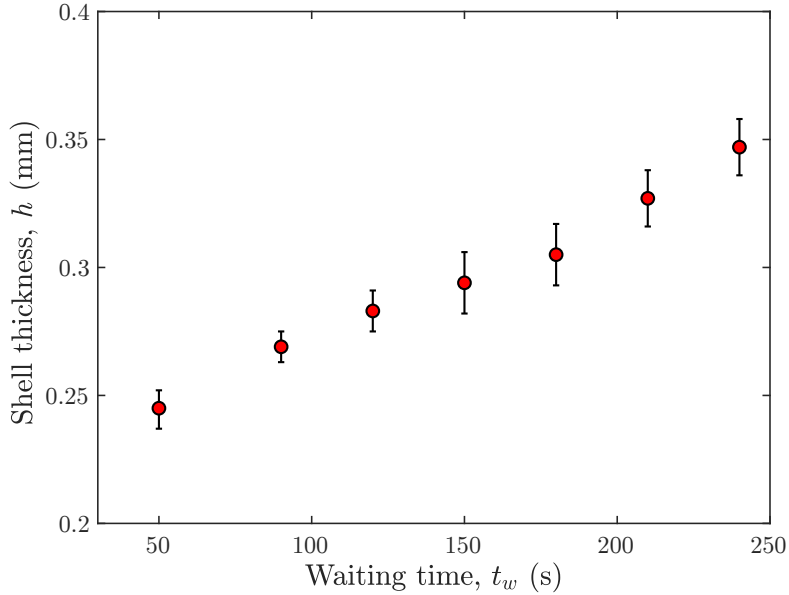


Figure 3.3: **Shell thickness calibration.** Experimental data for the thickness change of the elastic shell ($R=25.4\text{mm}$), h , as a function of waiting time, t_w . As the waiting time increases, the thickness of the shell increases due to the change in viscosity.

3.3.3 Characterization of the Shell Geometry

Following the protocol presented above, we fabricated shell specimens of radius $R = 25.4 \text{ mm}$ and thickness $h = 327 \pm 11 \mu\text{m}$, yielding a radius-to-thickness ratio of $R/h = 78$. As stated in Section 3.2, we will fix this value of R/h throughout this Chapter as representative of a thin shell, except for Section 3.5.4, where h , and hence R/h , will be varied systematically. Following a procedure developed in our previous study [104], we characterized the geometry of the fabricated defect through profilometry by measuring the 3D profile of the shell (outer surface) using an optical profilometer (VR-3200, Keyence Corporation). The defect profile is represented by the radial deviation of the outer surface of the shell with respect to a fitted perfect sphere (in the region away from the defect located at the pole of the shell), w_I , which was averaged latitude-wise due to axisymmetry condition of the shell. The defect geometry can then be described analytically on the basis of the deformation of the elastic mold during shell fabrication [104]. To ensure comprehensive coverage, we will now elaborate further on the technique next.

A plate model to describe the generated defect geometry: The fabrication technique presented in Section 3.3.1 enables us to systematically set the defect geometry. The angular width of the defect can be set by changing the diameter of the pillar during the manufacturing of the mold itself. On the other hand, the amplitude of the defect, δ , can be tuned by varying the level of depressurization of the mold and be described analytically on the basis of the deformation of the elastic mold during shell fabrication [104]. In order to provide an analytical description of the defect geometry, we used a simple plate model. In contrast to the soft spot, the bulk region outside the soft spot exhibits negligible deformation during pressurization. Moreover, the sphere of this soft spot has a sufficiently small radius of curvature (compared to the radius of curvature of the shell) that can be considered almost a flat plate. Therefore, the idea is to simplify the thin circular region of the mold as a flat plate clamped at its boundary and describe its deflection under uniform pressure loading by Kirchhoff-Love plate theory [1]. This plate's deflection under pressure determines the defect profile. We found that despite the flexible bulk region constraining the boundary of the thin region, the measured profiles can be represented by the solution corresponding to a clamped boundary condition (see Figure 3.5). Nevertheless, the width and amplitude of the defect should be defined by fitting, the details of which will be described below.

For an isotropic and homogeneous plate under pure bending, the classic Kirchhoff-Love plate theory yields the following governing equation [1]

$$\frac{\partial^4 w_I}{\partial x^4} + 2 \frac{\partial^4 w_I}{\partial x^2 \partial y^2} + \frac{\partial^4 w_I}{\partial y^4} = 0 \quad (3.2)$$

where w_I is the out-of-plane displacement of the plate, and x and y are the two in-plane coordinates. Solving Equation 3.2 for the specific case of a circular plate under uniform pressure loading and clamped boundary conditions yields the following expression for the out-of-plane deflection:

$$w_I(r) = -\frac{qA^4}{64D} \left(\frac{r^2}{A^2} - 1 \right)^2, \quad (3.3)$$

where q is the applied pressure, $D = Eh^3/12(1 - \nu^2)$ is the bending rigidity of the plate, $r = \sqrt{x^2 + y^2}$ is the distance from the center of the plate, and A is the radius of the circular plate. In Figure 3.4, the normalized defect amplitude, $\bar{\delta}$, is plotted as a function of depressurization (see Figure 3.2e), q , after demolding, which shows a linear function. The slope of this line is based on Kirchoff-Love plate theoretical prediction (Equation 3.3), which depends on the bending stiffness of the thin region of the mold. The presence of a non-zero intercept on the horizontal axis is attributed to the inherent deflection of the thin region. This deflection could arise from the pre-existing stresses generated in the mold during the polymer curing process of VPS.

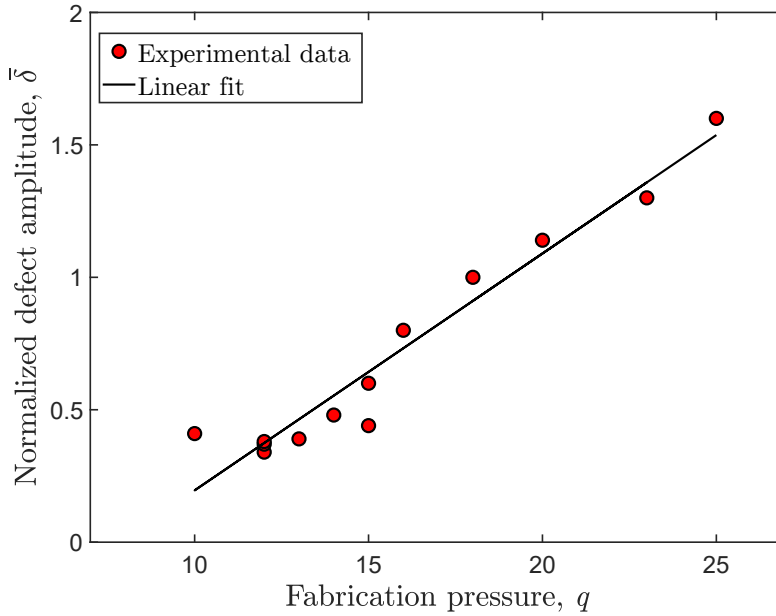


Figure 3.4: **Normalized defect amplitude, $\bar{\delta}$, as a function of depressurization, q .** The defect amplitude can be easily tuned just by changing the pressure. A linear function is fitted on the fabrication pressure as a function of the defect amplitude.

We consider that the deflection at the center of the circular plate, $w(0) = -\frac{qA^4}{64D}$, is equal to the defect amplitude, δ , and r/A is approximately equal to β/β_0 based on the geometry. Finally, the profile of the dimple-like defect ($\beta \leq \beta_0$), which originates from

the deformation of the plate-like region in the mold, can then be written as

$$\frac{w_I(\beta)}{h} = \frac{\delta}{h} \left(1 - \frac{\beta^2}{\beta_o^2}\right)^2. \quad (3.4)$$

We note that this description is only valid in the region of the defect. Away from the defect, the shell is spherical: $w_I(\beta)/h = 0$ for $\beta > \beta_o$.

In Figure 3.5, we present a typical example of a defect profile of the shell specimen that will be used in the subsequent indentation tests. We have fitted Equation (3.4) to the experimentally measured profile, taking the amplitude, δ , and half angular width, β_o , of the defect as fitting parameters, finding excellent agreement between the two (see Figure 3.5).

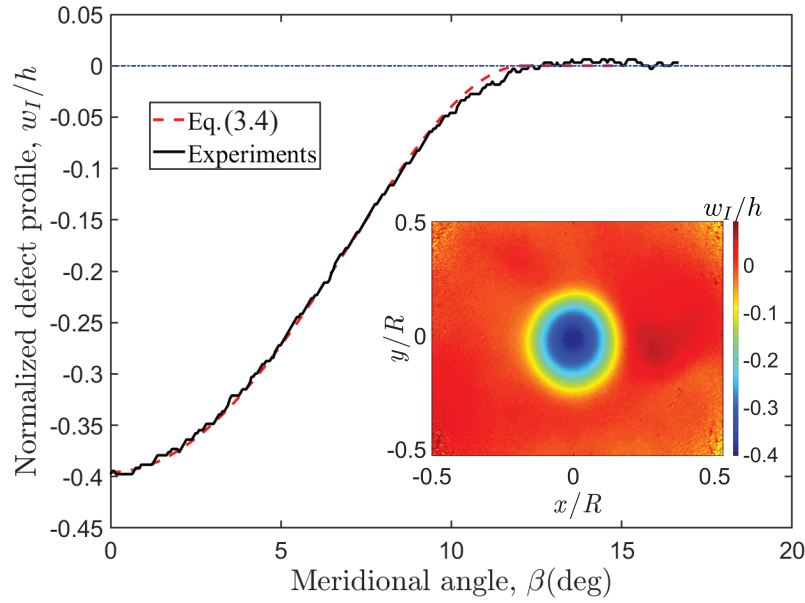


Figure 3.5: **Characterization of the defect geometry.** Two-dimensional profile (solid line) of the dimple-like defect w_I , normalized by shell thickness h , versus meridional angle β , obtained by averaging the measured 3D defect profile, latitude-wise, using an optical profilometer (see the inset). The dashed line represents the analytical description of Equation (3.4). These results correspond to a representative shell containing a defect that was measured to have a normalized amplitude of $\bar{\delta} = 0.4 \pm 0.02$ and a half angular width of $\beta_o = 11.7^\circ \pm 0.05^\circ$. The results from a systematic exploration of shells with other design parameters will be presented later in this Chapter.

For the particular defect taken as a representative example (see Section 3.4), we obtained $\bar{\delta} = \delta/h = 0.4 \pm 0.02$ and $\beta_o = 11.7^\circ \pm 0.05^\circ$ from the fitting procedure. The knockdown factor for this shell was measured experimentally to be $\kappa = 0.42 \pm 0.01$ using a standard

buckling test [89], in good agreement with the FEM prediction of 0.43. This difference is due to the uncontrollable imperfections intrinsic to the fabrication technique. Additional information on our numerical simulations will also be provided in Section 3.4. In Section 3.5, we will present the results of indentation tests on this shell specimen.

3.3.4 Experimental Apparatus and Protocol for the Probing Technique

In Figure 6.5, we present a photograph of the experimental apparatus used to perform the probing tests on our imperfect shells, based on earlier experiments developed by Marthelot *et al.* [102]. The to-be-tested hemispherical shell was mounted onto an acrylic plate. The clamped boundary condition at the equator was ensured by the thick band at the bottom of the shell (approximately 5 mm thick) formed by the drainage of the excess polymer during fabrication. The gap between the rim of the specimen and the acrylic plate was sealed by VPS polymer poured around the thick band to ensure air tightness. The acrylic plate was then fixed onto a high-precision multi-angle mount (Arca-Swiss C1 Cube Geared Head, France), adapted to adjust the position and direction of indentation. The shell was connected to a syringe pump (NE-1000, New Era Pump Systems Inc., Farmingdale, NY), which extracted air from inside the shell, through the pneumatic circuit, at a rate of 0.1 mL/min to generate a negative pressure on the shell. A pressure sensor (MPXV7002, NXP Semiconductors, The Netherlands) monitored the pressure differential between the inside and the outside of the shell, p_o , at an acquisition rate of 1 Hz. The pneumatic circuit also contained a tank with a large volume of air ($V = 120$ L), serving as a buffer to ensure prescribed pressure conditions and minimize spurious variations of pressure during the indentation procedure. The level of fluctuations of p_o during the indentation test was kept below 3% for larger pressures (above 30 Pa) and below 15% for lower pressures (below 30 Pa).

In each experimental run, we first loaded the shell to a preset pressure level, p_o , using the syringe pump. Once the desired pressure value was reached, the shell was indented by a rigid spherical Rockwell C diamond indenter (tip radius $a = 200 \mu\text{m}$, CSM) mounted onto a universal testing machine (5943, Instron, Norwood, MA). This point-indentation force was consistently applied in the radial direction (perpendicular to the shell surface), either at the shell pole (where the defect is located) or at an angle between the direction of the indentation force and the radial line perpendicularly concentric to the defect. The latter is defined as the probe angle, θ . The indentation displacement ξ was imposed by the testing machine (rigid probe) at a constant velocity of 0.06 mm/s. The reaction force of the indenter (indentation force), F , was measured by a load cell (2530-5N, Instron). During data processing, the zero point of the indentation displacement was set at the moment of contact between the indenter and the shell, after which the reaction force

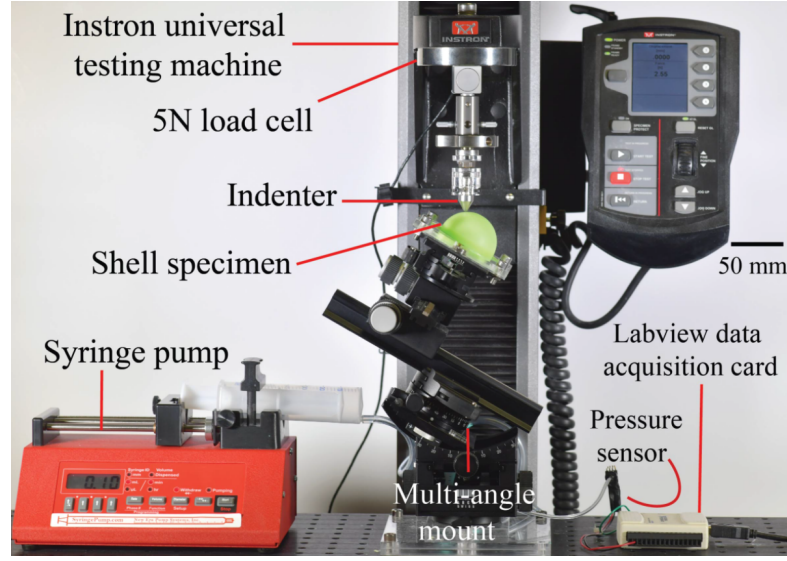


Figure 3.6: **Photograph of the experimental apparatus used for the indentation tests.** In each experimental run, the shell was first depressurized to a prescribed pressure level and then indented under imposed displacement conditions by a universal testing machine. A high-precision multi-angle mount allowed for the indentation to be performed at different locations of the shell.

increased continuously.

Following previous studies [108, 102], we non-dimensionalize the indentation deflection as

$$\bar{\xi} = \sqrt{1 - \nu^2} \frac{\xi}{h}. \quad (3.5)$$

and the probe force as

$$\bar{F} = \frac{FR}{2\pi D}, \quad (3.6)$$

where $D = Eh^3/12(1 - \nu^2)$ is the bending modulus of the shell. Moreover, the prescribed pressure level, p_o , at which the indentation test was performed, is normalized by the classic buckling pressure, p_c from Equation (1.4), as

$$\bar{p} = \frac{p_o}{p_c}. \quad (3.7)$$

The buckling of thin spherical shells is dominated by the local region near the defect [109], which, in our study, is located at the north pole, away from the equator. The deformation caused by indentation is also localized near the indenter set in the vicinity of the north pole, which will be elaborated in Section 3.5.3. As such, the effect of boundary conditions at the equator on critical buckling pressure and indentation behavior should be negligible [106].

We can expect the results presented in this work on hemispherical shells clamped at the equator should be equally applicable to full spherical shells as buckling is confined to the vicinity of the pole such that, if the shell is not shallow, the buckling thresholds are not strongly dependent on the location of the clamping boundary [263].

For the indentation tests, we used the shell fabricated and characterized following the procedures described in Sections 3.3.1 and 3.3.3, respectively. Prior to indentation, the shell was preset at prescribed pressure levels, which were varied systematically in the range $0 \leq \bar{p} < p_{\max}/p_c$ (recalling that p_{\max} is the critical buckling pressure measured in a standard buckling test). From the recorded indentation force-displacement curves, $\bar{F}(\bar{\xi})$, we attempted to assess the stability of the shell. The results for the case of indentation at the pole of the shell ($\theta = 0^\circ$) will be provided in Section 3.5.1. Non-axisymmetric cases will be considered in Section 3.5.2, for indentation tests conducted at the following values of the probe angle: $\theta = \{5^\circ, 10^\circ, 12^\circ, 15^\circ, 30^\circ\}$.

3.4 Numerical Simulations Using the Finite Element Method

In parallel to the experiments, we performed FEM simulations using the commercial package Abaqus/Standard. The goal of these simulations was to predict the response of imperfect spherical shells under simultaneous pressure loading and indentation, as well as to explore parameters more systematically than those available through experiments.

Toward reducing computational costs, we exploited the symmetry of the system and only considered one-half of the hemispherical shell (hence, a quarter of the shell), with symmetric boundary conditions applied on the plane of symmetry. The equator of the shell was set as a clamped boundary. A geometric defect (with the profile described by Equation 3.4 and the amplitude and width characterized in Section 3.3.3) was introduced into the initial shell geometry. The VPS polymer was modeled as an incompressible Neo-Hookean material, with Young's modulus of $E = 1.26 \pm 0.01$ MPa measured from standard tensile tests on dog-bone specimens, and the Poisson's ratio was assumed to be $\nu \approx 0.5$.

The shell was discretized by four-node shell elements S4R with a structured mesh scheme, with 300 and 600 elements in the meridional and azimuthal directions, respectively. The element S4R is able to describe the finite membrane strains and arbitrarily large rotations of shells. A mesh convergence study was also implemented to ensure that the results were independent of the mesh size. We modeled a rigid indenter discretized by R3D4 rigid elements to apply the indentation under imposed displacements. A hard and frictionless contact was assigned between the indenter and the shell. Geometric nonlinearities were

taken into account throughout the simulations.

The simulations were implemented in two steps:

- (i) **Depressurising:** First, the shell was loaded by a uniform live pressure, \bar{p} , applied on its outer surface;
- (ii) **Indentation:** While maintaining the pressure \bar{p} set in step (i), the indentation displacement ($\bar{\xi}$) was then imposed onto the shell at a probe angle θ . The indentation force \bar{F} was computed from equilibrium.

For each pressure level explored, we obtained the probe force-displacement curve and the full displacement field of the shell.

3.5 Results on Indentation of Pressurized Imperfect Spherical Shells

We shall start our investigation by reporting, in Section 3.5.1, results on the response of depressurized spherical shells subjected to an indentation applied at the center of the dimple-like defect. Upon validating our FEM procedure by contrasting the numerical results against experiments, in Section 3.5.2, we perform probing measurements and simulations at different probe angles. From the results, we seek to analyze the effect of the probe angle on predicting the critical buckling conditions of the shell and examine the efficacy of indentation as a technique to assess shell stability. Finally, in Sections 3.5.3 and 3.5.4, we study the localized deformation of spherical shells resulting from indentation. Furthermore, adapting well-established results from classic shallow shell theory, we quantify the characteristic length of this deformation. The shallow shell equations are applicable to this case (and to deep shells), as long as the loads and the resulting stresses are restricted to shallow regions, where the indentation-induced dimple is localized in the neighborhood of the indenter [108]. Moreover, outside of this region, the stresses and strains due to indentation and depressurization are sufficiently small compared to those in the dimple, such that the predictions of shallow shell theory remain relevant.

3.5.1 Probing the Shell at the Center of the Defect

In Figure 3.7, we present a set of experimental results for the response of the probe force versus the displacement of the indenter applied onto the shell. For now, the indentation point located at the center of the dimple-like defect ($\theta = 0^\circ$; cases with $\theta > 0^\circ$ will be

explored in Section 3.5.2). The prescribed depressurization was systematically varied at 11 values, ranging from $\bar{p} = 0$ to $\bar{p} = 0.38$. The maximum imposed displacement of the indentation was $\bar{\xi} = 8$. At each value of \bar{p} , in order to enhance the signal-to-noise ratio, 6 independent, but otherwise identical, experimental runs were conducted, and the measured indentation forces were averaged to yield the $\bar{F}(\bar{\xi})$ curve presented in Figure 3.7. The corresponding shaded region is the standard deviation of these 6 measurements.

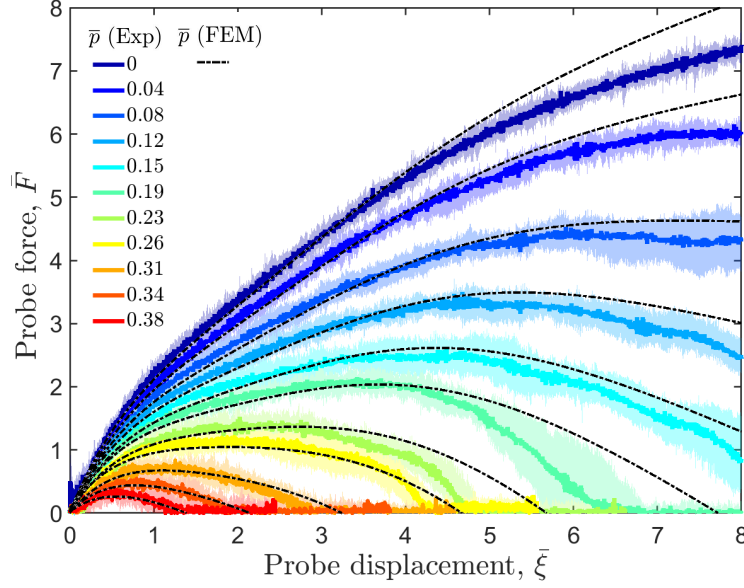


Figure 3.7: **Force-displacement curves for the indentation of the hemispherical shell.** The normalized probe force, $\bar{F} = FR/(2\pi D)$, is plotted as a function of the normalized indentation displacement, $\bar{\xi} = \sqrt{1 - \nu^2}\xi/h$. The indentation was applied at the center of the defect ($\theta = 0^\circ$): experiments (solid lines) and FEM simulations (dashed lines). The indentation tests were performed at 11 levels of depressurization (see legend). Each solid line was obtained by averaging the results from 6 independent experimental runs under identical conditions. The corresponding shaded region associated with each curve represents the standard deviation of these 6 identical measurements. The dashed lines are predictions from the FEM simulations associated with the respective experimental curves, with no fitting parameters; all quantities were measured from the experiments.

From the results shown in Figure 3.7, as previously described by Marthelot *et al.* [102], we notice that, without pressure loading ($\bar{p}=0$), the indentation process is always stable and the probe force increases monotonically with displacement. Each response at lower values of the pressure loading ($\bar{p} < 0.08$) can be divided into the following two distinct regimes:

1. **Small indentations ($\xi \lesssim h$):** In this regime, the indentation displacement remains

smaller than the shell thickness. The force-displacement relationship is linear, as described by Reissner's theory for spherical shells under point load indentation [264, 265];

2. **Large indentations ($\xi \gtrsim h$):** In this regime, the indentation displacement is larger than the shell thickness. The force-displacement relationship is nonlinear, as first studied by Pogorelov [266].

For intermediate levels of depressurization ($0.12 \leq \bar{p} \leq 0.19$), the indentation curve is non-monotonic; the probe force increases initially, reaches a maximum value \bar{F}_{\max} , and then decreases with increasing probe displacement. For levels of depressurization above $\bar{p} \geq 0.19$, the probe force can eventually reach zero within the indentation displacement range of the experiments. At this point, the shell becomes unstable (critical buckling point) and snaps to a collapsed state. The work done by the probe force is equal to the energy barrier that needs to be overcome to attain the buckled state. Also, it is important to mention that, compared to a perfect shell [108, 102], the load-carrying capacity and energy barrier of this imperfect shell are significantly reduced due to the presence of the dimple-like defect.

Following the computational methodology described in Section 5.4, we have used FEM to predict the behavior of this shell under indentation, and the obtained force-displacement curves at different pressure levels are also presented in Figure 3.7, juxtaposed onto the corresponding experimental curves. Excellent agreement is found between experiments and simulations, thereby serving as a validation of the FEM. We note that all the parameters used in the simulations were measured independently from the experiments, with no fitting parameters. Having validated the FEM against experiments, we will further explore the indentation problem by performing systematic computations in Sections 3.5.2 and 3.5.3.

3.5.2 Can We Probe the Buckling of Spherical Shells Using Indentation?

In this section, we will assess the relevance of the non-destructive probing technique to predict the critical load of pressurized spherical shells, which was originally proposed and applied on cylindrical shells [136, 137, 127, 133, 130, 108, 125, 126]. We seek to determine the required proximity of the probe to the defect without the foreknowledge on the location and size of imperfections. In particular, we will apply the probe at various locations on the shell by moving the indentation point away from the center of the defect and quantifying the resulting response, both experimentally and numerically.

In Figure 3.8(a), we present the FEM results for the indentation at $\theta = 0^\circ$ (from

Figure 3.7) in the $(\bar{p}, \bar{\xi}, \bar{F})$ space. The maximum probe force, $\bar{F}_{\max} = F_{\max}R/2\pi D$, provides a measure of the largest load that the shell can sustain prior to collapse, which can be tracked at increasing pressure levels (green circles on each curve in Figure 3.8a). It is anticipated that the characteristics of shell stability, such as the critical load, are encoded in the variation of \bar{F}_{\max} [127]. More precisely, the energy barrier, which measures the shock-sensitivity of the pressurized shell against disturbances at the pre-buckling state, is equal to the work done by the probe to reach the unstable post-buckling state ([125]). Once this work tends to vanish, the shell is loaded close to the buckling capacity. By sequentially increasing the prescribed pressure until $\bar{F}_{\max} = 0$, the pressure level reached at this stage corresponds to the critical buckling load of the shell. However, in practice, we should always ensure that \bar{F}_{\max} is larger than zero to avoid the catastrophic collapse of the tested shell. Therefore, we identify the critical point by numerically extrapolating the experimental measured \bar{F}_{\max} to zero, using a third-order polynomial extrapolation.

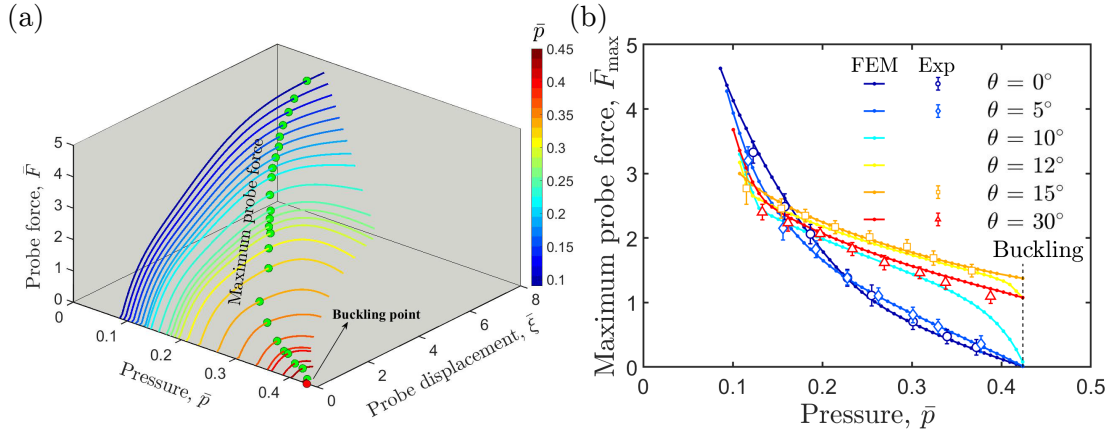


Figure 3.8: **2D and 3D indentation curves.** (a) 3D representation of the indentation curves shown in Figure 3.7, in the $(\bar{p}, \bar{\xi}, \bar{F})$ space. The peak values of the probe force, \bar{F}_{\max} , are represented by the circles on each curve. The indentation was performed at the center of the defect ($\theta = 0^\circ$). (b) Normalized maximum probe force, \bar{F}_{\max} , versus the prescribed pressure, \bar{p} , at different probe angles: $\theta = \{0^\circ, 5^\circ, 10^\circ, 12^\circ, 15^\circ, 30^\circ\}$. The data points represent the experimental measurements, and the solid lines are the predictions from the FEM simulations. The knockdown factor of this shell measured through an independent buckling test is $\kappa = 0.42$.

In Figure 3.8(b), we plot \bar{F}_{\max} versus \bar{p} while probing the shell at the center of the defect ($\theta = 0^\circ$). The experimental force-displacement signals were filtered and smoothed with a 50-point moving average filter in order to facilitate the definition and extraction of the maximum probe force. We find that \bar{F}_{\max} decreases sharply (by 80%) as \bar{p} is increased from 0.1 to 0.43. The extrapolation in the limit of $\bar{F}_{\max} \rightarrow 0$ indicates that $\kappa = 0.44$, which is in good agreement with the value $\kappa = 0.42$ measured from an independent

experimental buckling test. In this case of indentation at the center of the defect, the probing serves successfully as a non-destructive technique to estimate the critical buckling conditions of the spherical shell. We note that, based on the FEM data, we systematically set an upper limit on the pressure applied for probing, p_{lim} , and extrapolated the critical point from the maximum probe forces obtained below this limit. This allowed us to determine a threshold $p_{\text{lim}}/p_c = 0.36$, above which the extrapolated buckling load is excellent, approaching the measured value with less than 2% relative error. This pressure threshold is still in the safe region (far from $\kappa = 0.43$) to avoid the collapse of the shell caused by the probe.

To assess the ability of the probing technique when the indentation is exerted at various locations, we systematically varied the probe angle: $\theta = \{5^\circ, 10^\circ, 12^\circ, 15^\circ, 30^\circ\}$. Consequently, the indentation point was moved away from the center of the defect. First, we indented the shell at $\theta = 5^\circ$, the results of which are shown in Figure 3.8(b). The probing force follows a path that only slightly deviates from that of the $\theta = 0^\circ$ case while still showing a similar trend and decreasing to zero as the prescribed pressure reaches the critical load of the shell. In this case, the knockdown factor can still be accurately inferred.

Next, we increase the probe angle to $\theta = 10^\circ$. Initially, with increasing \bar{p} , the maximum probe force evolves by following an entirely distinct path from the previous two cases ($\theta = 0^\circ$ and $\theta = 5^\circ$). However, closer to the load-carrying capacity of the shell, the path rapidly turns and drops to the critical point. Again, in this case, the correct knockdown factor can be inferred from the probing. However, the extrapolation must be performed based on the data in the nonlinear vicinity of the critical point, with the eminent risk of buckling. We highlight that this extrapolation cannot be done from the beginning of the $\bar{F}_{\text{max}}(\bar{p})$ path. The sudden change of the maximum force-pressure path and the sharp decrease in \bar{F}_{max} for larger pressure values in the cases of $\theta = 10^\circ$ and $\theta = 12^\circ$ (half angular width of the defect $= 11.7^\circ$) is presumably due to the nonlinear interaction between the probe and the edge of the defect.

Further increasing the distance of the probing point from the defect ($\theta = 15^\circ$ and $\theta = 30^\circ$), we observed no visible trace of the defect in the force signal until \bar{p} approaches the critical pressure with the sudden collapse of the shell. In these two cases, the buckling point and the corresponding knockdown factor are unpredictable by tracking the maximum probe force and extrapolating it in the limit $\bar{F}_{\text{max}} \rightarrow 0$. The probe for these indentations, away from the defect, appears to be insensitive to the defect and misrecognizes the imperfect shell as if it was perfect.

An interesting result, which was also alluded to by Marthelot *et al.* [102], was observed

when the indentation was applied at $\theta = 12^\circ$ and $\theta = 15^\circ$. There is an unexpected increase in the maximum indentation force that the shell can sustain, compared to that at $\theta = 30^\circ$. In this regime, the probe is set at the edge of the defect, and the coupling between the localized deformation associated with the dimple-like defect and the probe force is more complex; the indentation deforms the shell locally in a way that weakens the influence of the initial imperfection on the response of the shell. This observation highlights the high degree of nonlinearity in shell mechanics problems.

We highlight that the experimental data and FEM results plotted in Figure 3.8(b), at different probe angles, are in remarkably good quantitative agreement. In summary, the results presented above demonstrate some potential limitations in using probing as a non-destructive technique to assess the stability of imperfect spherical shells since the probe has to be performed in the near vicinity of the most serious defect in the shell, whose location would be most likely unknown *a priori* in any situation of practical relevance. Indeed, performing such a positionally targeted test would require previous knowledge of the distribution of imperfections, in which case the behavior of the shell could be more easily and accurately predicted numerically by taking the full shell geometry into account [89, 253, 267]. The mechanism underlying these observations stems from the fact that the deformation due to the probe force is localized in spherical shells, as we study in detail in the next section. The interaction between the localized probe and the defect is limited, which affects the detectability of the defect.

3.5.3 Localized Deformation of Pressurized Spherical Shells under Indentation

Thus far, we provided experimental and numerical evidence that the mechanical response of pressurized spherical shells under point indentation differs strongly depending on the location of the probing with respect to the most vulnerable (imperfect) region. In this section, we will relate this finding to the deformation profiles of the imperfect shells due to indentation.

In Figure 3.9, we plot the FEM-simulated profile of the imperfect shell tested in Sections 3.5.1 and 3.5.2, at $\bar{p} = 0.25$, before and after imposing an indentation displacement of $\bar{\xi} = 3$. This probing is applied at the following different angles $\theta = \{0^\circ, 5^\circ, 15^\circ, 30^\circ\}$. We find that when the shell is indented at or close to the center of the defect ($\theta = \{0^\circ, 5^\circ\}$), the localized region of deformation overlaps almost entirely with the dimple-like defect. Consequently, the defect significantly influences the response of the shell due to the indentation, thereby ensuring that the critical point can be captured by the probe. By contrast, when the probing is performed further away from the defect (*e.g.*, $\theta \leq 15^\circ$),

there is little or no overlap between the deformed region and the existing defect, and the probe misses the detection of the critical buckling point. As a result, for these cases of indentation away from the defect, the corresponding $\bar{F}(\bar{p})$ curves (Figure 3.8b) show little difference with respect to those of a perfect shell, even if the probed shell is intrinsically imperfect. In these cases, the lack of interaction between the defect and the probe precludes access to the stability landscape of the imperfect shell.

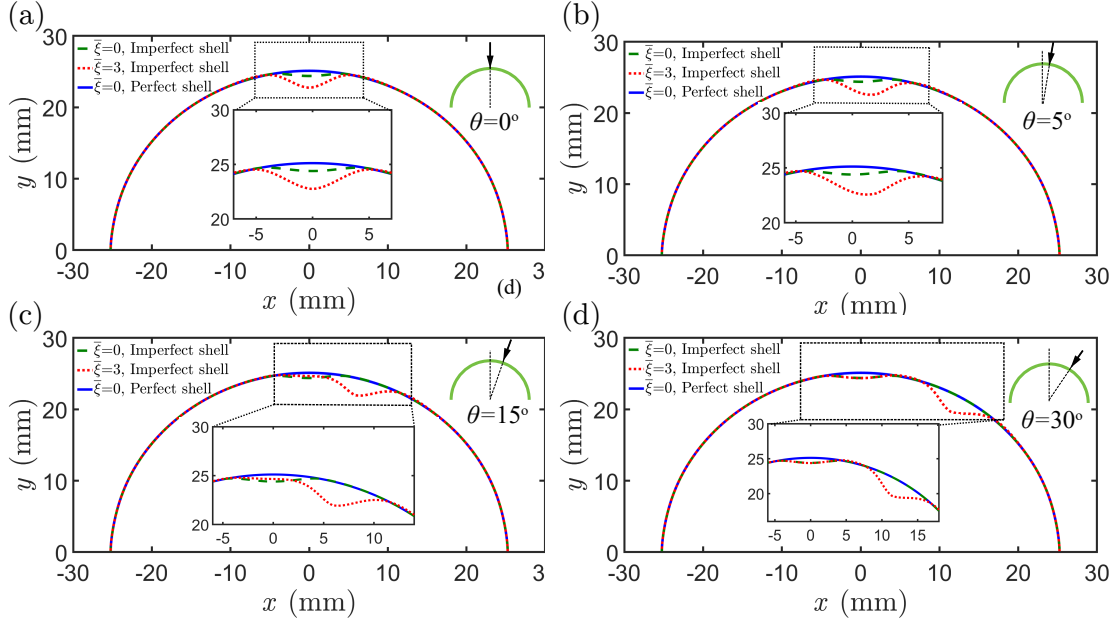


Figure 3.9: **Deformation profiles of the imperfect shell**, pressurized at $\bar{p} = 0.25$, in its initial configuration ($\bar{\xi} = 0$, dashed line) and deformed configuration (at $\bar{\xi} = 3$, dotted line), computed through FEM. The indentation is applied at (a) $\theta = 0^\circ$, (b) $\theta = 5^\circ$, (c) $\theta = 15^\circ$, and (d) $\theta = 30^\circ$. To aid visualization, the deformation profiles of the indented imperfect shell are represented by the associated radial displacement from a perfect spherical shell pressurized at the same level (solid line) and magnified by a factor of 4. Insets: Zoomed-in profiles at the vicinity of the defect and indentation region.

3.5.4 Characteristic Length of Indentation in Spherical Shells

Having observed that the deformed neighborhood of the indentation plays an important role in the interaction between the probe and the defect, we proceed by quantifying the characteristic length scale of the deformation of the indented shells. In this section, we shall focus exclusively on perfect shells so as to investigate their mechanical response to indentation independently of any interactions with geometric defects. The experimental shell specimen used in this section was fabricated without intentionally introducing a defect so that it is as nearly ‘*perfect*’ as they can be in practice. Naturally, there may still be small-scale imperfections intrinsic to the fabrication procedure (*e.g.*, roughness

of the otherwise spherical mold or heterogeneities in the polymer mixture). In fact, the knockdown factor of these nearly perfect shells is $\kappa = 0.91$ (instead $\kappa = 1$ for a perfect shell), which, nonetheless, does not affect the findings reported in this section. The FEM simulations are performed with a truly spherical shell.

We will contrast our experimental and FEM data with classic analytical solutions obtained by Reissner [264, 265] and [266] a segment of a thin, elastic, spherical shell subjected to a concentrated point force. Reissner's solution was obtained from simplified shallow shell equations (relevant for shells with a height-to-diameter ratio lower than approximately 1/8). Such equations are linearized, but some important nonlinear terms related to buckling were preserved. These equations are also applicable to deep shells, as long as the loads and the resulting stresses are restricted to (*i.e.*, localized in) shallow regions. For completeness, we recall the main features of these seminal results on shell indentation:

1. **Linear regime:** When $\xi/h \lesssim 1$, Reissner [264, 265] followed the framework of linear shallow shell theory to propose an analytical solution for the radial displacement:

$$\frac{w_{\text{Reissner}}(r)}{h} = \frac{\sqrt{12(1-\nu^2)} R}{2\pi} \frac{F}{h E h^2} \text{kei}\left(\frac{r}{\ell}\right), \quad (3.8)$$

where r is the horizontal distance from a point on the shell to the point of application of the concentrated point force F , $\text{kei}(\cdot)$ is the imaginary term of the modified Bessel-Kelvin function, and the balance between bending and stretching effects yields the characteristic length scale $\ell = [\sqrt{R h}][12(1-\nu^2)]^{-1/4}$. Therefore, at the indentation point ($r = 0$), the deflection is predicted to be

$$\frac{\xi}{h} = \frac{w_{\text{Reissner}}(0)}{h} = -\frac{\sqrt{3(1-\nu^2)} R}{4} \frac{F}{h E h^2}, \quad (3.9)$$

such that the dependence between the indentation force and displacement is linear ($F \sim \xi$).

2. **Nonlinear regime:** When $\xi/h \gtrsim 1$, Pogorelov [266] made use of geometric arguments and a general variational principle to obtain an analytical solution for the radial displacement at the indentation point, $w_{\text{Pogorelov}}(0)$:

$$\frac{\xi}{h} = \frac{w_{\text{Pogorelov}}(0)}{h} = \frac{1}{9\pi^2 c^2} \left(\frac{R}{h}\right)^2 \left(\frac{F}{E h^2}\right)^2, \quad (3.10)$$

where $c=0.19$ is a numerical coefficient. Equation (3.10) indicates a nonlinear indentation force-displacement relationship of $F \sim \sqrt{\xi}$. Pogorelov developed this approach to describe the behavior of thin spherical shells under point indentation,

with considerable changes in shape, based on the assumption that the shell's middle surface under such a deformation is close to the isometric mapping of the initial surface. The shape of the shell in the transition zone between the undeformed and mirror-reflected parts is determined by minimizing the strain energy in this region due to the smoothing of the edge between the two parts (computed according to the linear membrane and bending strains), under appropriate boundary conditions. The indentation force-displacement relationship of the shell is then obtained from the minimization of the total potential energy of the system.

In Figure 3.10, we plot experimental and FEM results for the dimensionless indentation force, $\bar{F} = F/(Eh^2)$, versus the normalized indentation displacement, ξ/h , for a shell indented at its pole ($\theta = 0^\circ$), in the absence of pressure loading. Linear (when $\xi \lesssim h$) and nonlinear (when $\xi \gtrsim h$) regimes can be clearly identified in this force-displacement curve. The transition from the linear to the nonlinear regimes does indeed happen in the range $0.3 \lesssim \xi/h \lesssim 0.5$, consistently with the classic result of $\xi < h/3$ for the validity of linear shell theory. However, since the transition is smooth, we prefer to stick with the less precise statement that the transition between the two regimes happens when the indentation amplitude is of order h . The results in Figure 3.10 are compatible with the classic regime of validity for the linear theory of shells ($\xi < h/3$).

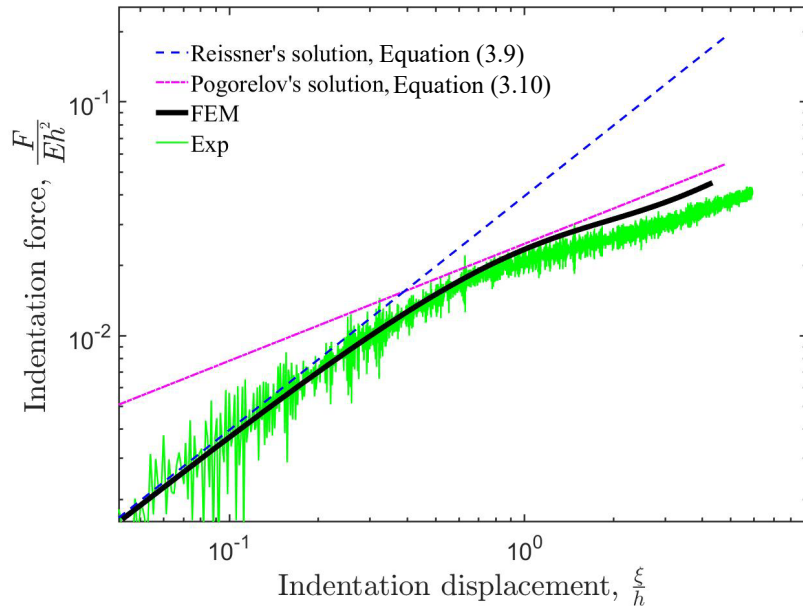


Figure 3.10: **Force-displacement curves for a spherical shell indented at its pole** ($\theta = 0^\circ$): experiments (thin solid curve), FEM simulations (thick solid curve). The predictions from Reissner's theory [265], Equation (3.9), and Pogorelov's theory [266], Equation (3.10), are represented by the dashed and dash-dotted lines, respectively.

The classic analytical predictions of Equation (3.9) and Equation (3.10), for the linear and nonlinear regimes, respectively, are superimposed onto our data. As expected, Reissner's solution yields excellent predictions in the linear range, while the nonlinear range is well described by Pogorelov's solution, in both cases, without any adjustable fitting parameters.

Having thoroughly validated our simulations against experiments (see Figures 3.7, 3.8b, and 3.10), hereon, we shall rely exclusively on the FEM data. We have studied the extent of deformation due to indentation in the linear and nonlinear regimes, from which we observed the deformation is concentrated at the indentation point and decays rapidly away from it. As such, we can focus on the case of indentation at the pole ($\theta = 0^\circ$) and characterize the neighborhood of indentation by the zero crossing distance r_z , which is defined as the distance from the center of indentation to the first point of $w(r_z)/R = 0$. This characteristic length quantifies the localized nature of the indentation of spherical shells.

We study the extent of deformation due to indentation in the linear and nonlinear regimes of indentation deformation while systematically varying the indentation angle $\theta = \{0^\circ, 5^\circ, 15^\circ, 30^\circ\}$. In Figure 3.11, we plot the radial deflection of the shell, w/R , resulting from the indentation as a function of the meridional angle, β . The indentation displacement was increased systematically up to $\xi = 2.7h$ (see the legend of Figure 3.11) across the linear and into the nonlinear regimes. The localized nature of the deflection profiles is evident from the data: The deformation is concentrated at the indentation point and decays rapidly away from it. The spatial extent of the deform region only changes slightly for the different curves ($0 < \xi \leq 2.7h$) but remains independent of the indentation location ($\theta = \{0^\circ, 5^\circ, 15^\circ, 30^\circ\}$ in the respective panels of Figure 3.11).

We focus on the case of indentation at the pole ($\theta = 0^\circ$) and, in Figure 3.12b, plot w/R as a function of meridional distance r , against Reissner's solution from Equation (3.8). It is evident that for displacements smaller than the shell thickness ($\xi \lesssim h$), Equation (3.8) (dashed lines) is in excellent agreement with the FEM data (solid lines). However, deviations occur in the nonlinear regime ($\xi \gtrsim h$).

In the FEM simulations, we considered shells with different radius-to-thickness ratios ($64 \leq R/h \leq 121$) and extracted r_z from their deflection profiles under various indentation displacements. We also obtained a theoretical prediction from Reissner's solution – Equation (3.8) – by setting $w_{\text{Reissner}}(r_z) = 0$, which is satisfied only if $\text{kei}(r_z/\ell) = 0$. Then we numerically determined the first zero-crossing point as

$$r_z = \frac{3.9}{[12(1 - \nu^2)]^{1/4}} \sqrt{Rh}. \quad (3.11)$$

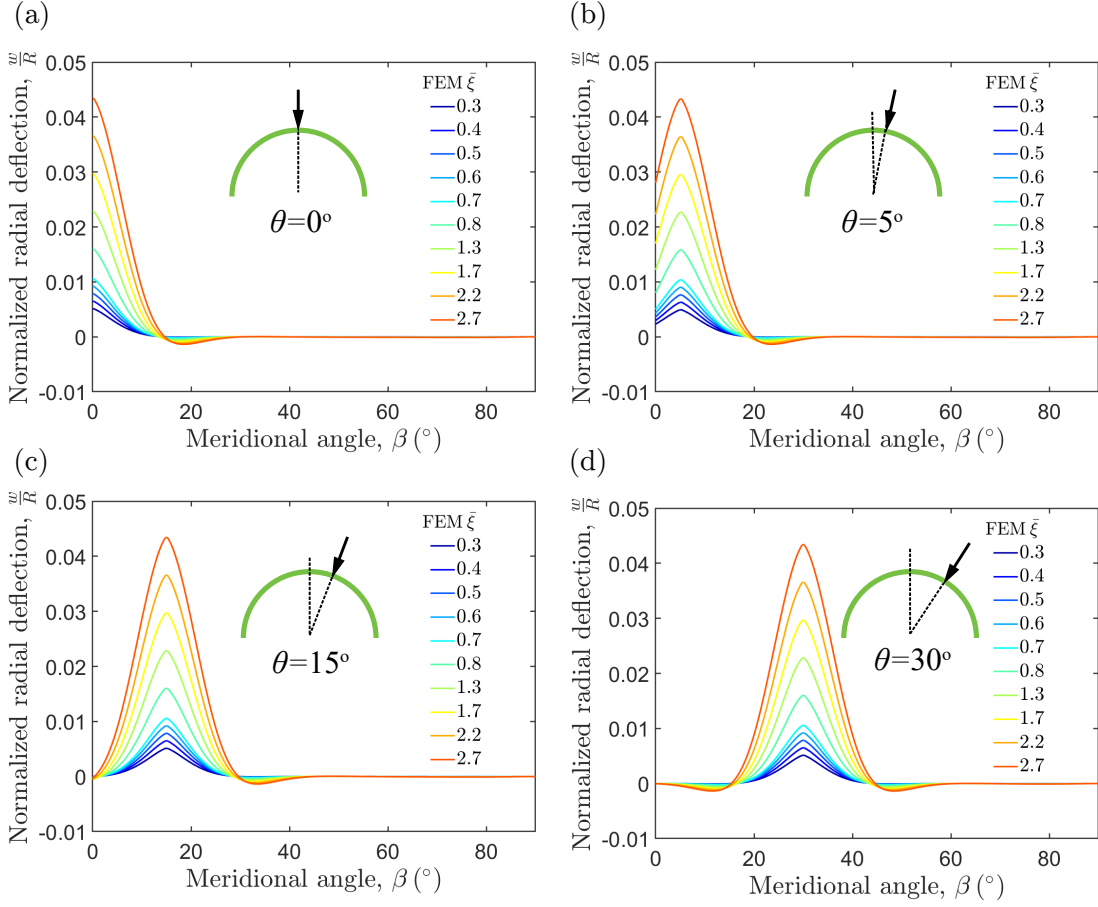


Figure 3.11: **FEM-computed normalized radial deflection, w/R , versus meridional angle, β** , for a perfect shell with $R = 25.4$ mm and $h = 327$ μ m, under different indentation displacements (values detailed in the legends). The probing is applied at the following values of the indentation angle: (a) $\theta = 0^\circ$, (b) $\theta = 5^\circ$, (c) $\theta = 15^\circ$, and (d) $\theta = 30^\circ$. For these data, no pressure loading is applied.

For incompressible materials ($\nu = 0.5$), we have $r_z = 2.25\sqrt{Rh}$. From Equation (3.11), the characteristic length scale of indentation is predicted to scale as $r_z \sim \sqrt{Rh}$, independently of the indentation displacement, ξ .

In Figure 3.13, we plot r_z data obtained by FEM as a function of \sqrt{Rh} , contrasted with Equation (3.11); the line colors refer to the values of the indentation displacement in FEM (as detailed in the legend). For clarity, the data was split for the linear regime ($0 < \xi \lesssim h$, Figure 3.13a) and for the nonlinear regime ($\xi \gtrsim h$, Figure 3.13b). In the linear regime (Figure 3.13a), good agreement is found between FEM and Equation (3.11), validating the linear dependence of characteristic length, $r_z \sim \sqrt{Rh}$, even if there is a slight systematic vertical shift for the FEM data from Reissner's theory that increases with ξ . We anticipate that this discrepancy is most likely due to the simplification of

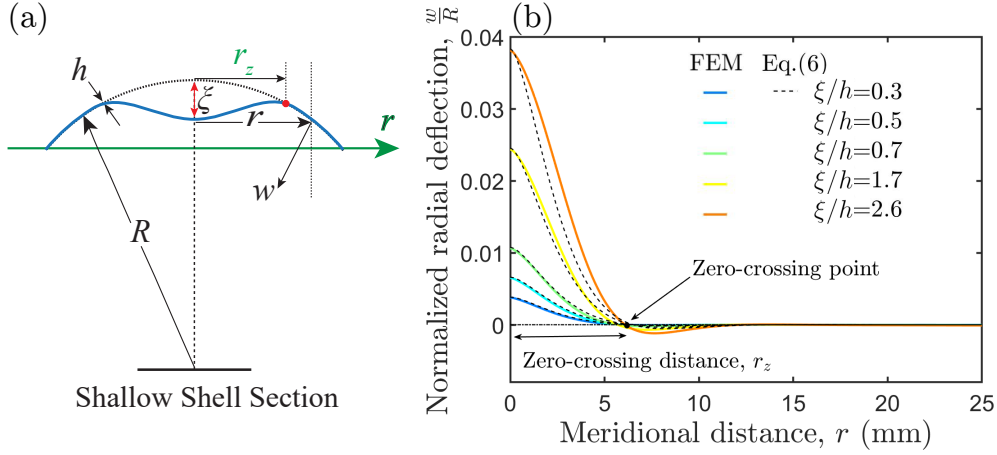


Figure 3.12: **Deformed spherical shell under indentation.** (a) Schematic of a deformed shallow spherical shell of radius R and thickness h under indentation. (b) Normalized radial deflection, w/R , as a function of meridional distance, r , for a shell of $R/h = 78$ at different indentation displacements (as detailed in the legend). The solid lines correspond to FEM data, while dashed lines are predictions by Reissner's solution in Equation (3.8). The zero-crossing distance, r_z , is defined as the distance from the center of indentation to the first point where the deflection crosses zero, $w(r_z)/R = 0$.

linear shallow shells in Reissner's solution. When $\xi \gtrsim h$ (Figure 3.13b), the perturbed region of radius r_z grows more significantly with indentation, but the linear scaling \sqrt{Rh} is maintained. Hence, we find that Reissner's solution is unable to capture our FEM data in the nonlinear regime. Overall, we find that the measured characteristic length of indentation is consistent with the scaling $r_z \sim \sqrt{Rh}$, with a nearly constant prefactor of 2.25 in the linear regime but an indentation-dependent prefactor in the nonlinear regime.

For the shell tested in our experiments, Equation (3.11) yields a characteristic length of indentation $r_z = 6.5$ mm, corresponding to an angle of $\theta_z = 14.8^\circ$. From all the evidence reported above, we speculate that θ_z , together with the half angular width of the defect $\beta_o = 11.7^\circ$, dictates the critical indentation angle, above which the probing test fails to identify the buckling conditions. In future work, it would be valuable to perform a parametric study to more systematically quantify the dependence of the critical indentation angle on both the length scale of indentation and the geometry of defects.

3.6 Summary and Outlook

We have investigated the behavior of imperfect spherical shells subjected to a point indentation, with a focus on the effect of the indentation angle, by combining precision experiments, finite element modeling, and theoretical analysis. When the indentation is

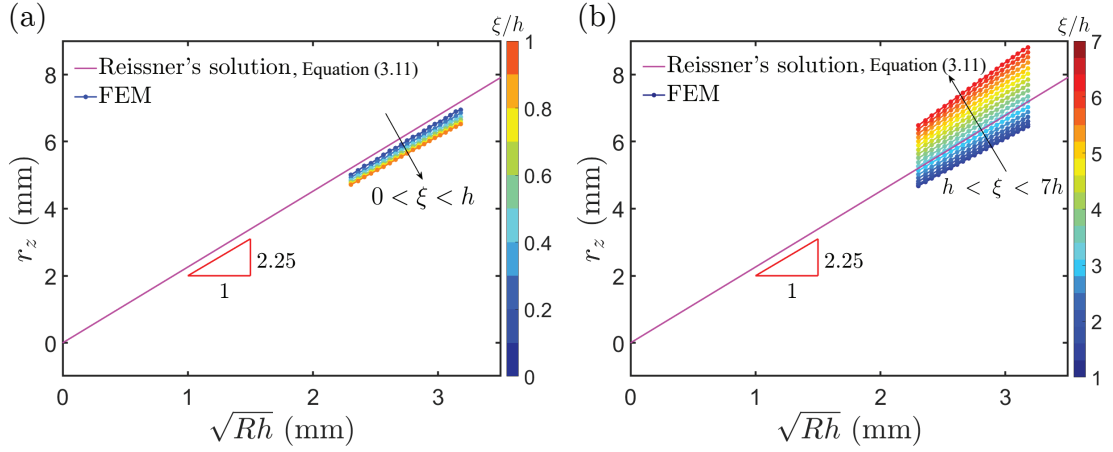


Figure 3.13: **Characteristic length of indentation, r_z , as a function of \sqrt{Rh}** in the (a) linear ($h < \xi < 7h$) and (b) nonlinear ($\xi \gtrsim h$) regimes. The solid lines correspond to the theoretical predictions of Equation (3.11), with a slope of 2.25, and colored circles-lines correspond to the FEM data for different values of the indentation displacement (ξ); see the adjacent color bar.

applied at the center of the defect under imposed displacement conditions, the reaction force shows a non-monotonic relationship with the displacement at relatively larger pressure levels, which first increases to a peak value and then decreases to zero, accompanied by the occurrence of buckling. The knockdown factor of the shell is successfully identified by tracking the peak of the force-displacement curve with increasing prescribed pressure level and extrapolating to the point of maximum force reaching zero. In this case, indentation can be used to probe the stability of the shell. However, as the probe is moved away from the center of the defect above a critical angle, the test fails to identify the buckling point prior to the collapse of the shell. We find that the localized nature of indentation in spherical shells limits the interaction between the defect and the probe. The characteristic length associated with the indentation's neighborhood scales as $r_z \sim \sqrt{Rh}$, in both the linear and nonlinear regimes.

Our findings demonstrate that point-load probing can only be useful as a local strategy to assess the stability of spherical shells as long as the indentation is performed in the close neighborhood of the defect. This limitation comprises broader applications in common engineering settings, where the distribution and magnitude of the imperfections are typically unknown. The counterpart evaluation on cylindrical shells [136, 137] through FEM and experiments also showed that the probing technique over-predicts the buckling load, once the distance between the probe and the defect reaches a critical value. It would be interesting to study the characteristic length of the influence region of indentation in cylindrical shells since, in this Chapter, we have focused solely on spherical shells. As

we have done in our case of spherical shells, we can also expect that this length should determine the detectability of the probe in cylindrical shells.

Future work could consider simultaneously setting multiple probes on one shell or implementing probing in sequence along an effective path, although such indentation-probing approaches would likely be cumbersome. A more viable route to predict the critical buckling conditions may be the mapping of the full 3D geometry of an imperfect shell through X-ray micro-computed tomography coupled with FEM simulations using the measured geometry, as we have recently demonstrated for idealized single-defect imperfections [103, 104]. An appropriate and effective protocol is still to be developed for the non-destructive testing of the critical buckling conditions of imperfect spherical shells in general engineering scenarios.

4 Probabilistic Non-Destructive Probing of Spherical Shells

The buckling capacity of shell structures exhibits a high sensitivity to imperfections, requiring prior knowledge of defects to predict critical buckling conditions accurately. A recent innovative method proposes the prediction of buckling capacity in thin shells through controlled indentation of pre-compressed specimens, providing an estimate of their resistance to buckling. However, this approach underlines the pivotal role of probing location, highlighting that accurate determination of buckling capacity depends on proximity to the most significant defect. Since defect locations are typically unknown and challenging to identify, this study addresses the issue by extending the probing technique to predict the buckling behavior of spherical shells with randomly distributed imperfections. By employing finite element simulations, we conduct a statistical analysis of these realistically imperfect shells, subjecting them to probing either at a specific location or at various random locations. Notably, these shells offer a better representation of practical scenarios than the prior single-defect cases we studied in Chapter 3. With the use of various extrapolation techniques to project the force-displacement response during indentation, it becomes evident that the robustness of the technique heavily relies on the extrapolation method chosen. Consequently, the extrapolated data varies, leading to different predictions. We recognize that our discoveries, focused on the probabilistic assessment of stability in shells with random imperfections through a statistical probing approach, may have limited immediate implications for shaping the design principles of thin-walled structures.

This Chapter is structured as follows. Section 4.1 presents the motivation behind this study, accompanied by a review of the literature on shells with a random distribution of imperfections and their sensitivity to imperfection. Next, in Section 4.2, we define the problem under consideration. Following this, Section 4.3 outlines the details of our numerical simulations, which explore the non-destructive testing of imperfect shells

possessing a distribution of imperfections, with indentation applied either at the pole of the shell or randomly chosen locations. The outcomes of the probabilistic investigation of indentation, while indented at the pole of the hemispherical shell with the random variable sampled from the shell configuration, are discussed in Section 4.4. Moving on to Section 4.5, we explore the probabilistic indentation technique for a single shell configuration while the random variable is sampled from the location of the indentation. Finally, in Section 4.6, we summarize our findings and provide a forward-looking perspective for future research endeavors.

4.1 Literature Review and Motivation

While considerable progress has been achieved in the theoretical, experimental, and computational investigations of shells with single defects, understanding shell buckling in the presence of multiple or distributed imperfections subject to potential defect-defect interactions remains an ongoing inquiry that holds practical relevance and realism. Following the studies on the imperfection sensitivity of shell structures (see Chapter 1 for a detailed review of past work), statistical methodologies were introduced for analyzing shells characterized by a distribution of imperfections. However, these approaches called for a probabilistic understanding of geometry and imperfection distribution, which was challenging to obtain using contemporary tools, thus restricting practical application. Beyond considering scenarios with only two defects [111, 112], the knockdown factor of cylindrical and spherical shells with a distribution of imperfections can be predicted via probabilistic methods. An early study by Amazigo [114] focused on examining cylindrical shells containing axisymmetric defects. According to their findings, the spectral density of random imperfections influences the shell's ability to withstand buckling. Using the Monte Carlo method, a similar investigation was conducted on the behavior of imperfect cylindrical shells under axial compression with symmetrical [115] or asymmetrical [116] defects. It was found that probabilistic methods were superior when evaluating cylindrical shell design standards to deterministic approaches. Elishakoff [117] examined different probabilistic methods applicable to shell buckling. Recently, Derveni *et al.* [118] examined the realistic case of spherical shells with numerous randomly distributed geometric imperfections on the surface of the shells. These authors discovered that when the amplitude of the randomly distributed defects follows a log-normal distribution, the resulting knockdown factor can be described using a 3-parameter Weibull distribution. This observation categorizes shell buckling as part of a broader group of statistical phenomena known as extreme-value statistics [119, 120, 121, 122, 123, 124].

To date, despite previous investigations into the imperfection sensitivity of shell structures

featuring random boundary and geometric imperfection distributions [118, 114, 268, 269, 270, 271, 272, 273], a suitable and efficient protocol for the non-destructive assessment of critical buckling conditions in imperfect spherical shells within general engineering contexts remains unavailable. Additionally, the findings in Chapter 3 demonstrated that the non-destructive probing method could effectively forecast the buckling capacity of spherical shell structures without causing damage, provided that probing is performed at strategically chosen locations. Nevertheless, a key challenge restraining its broader empirical application in engineering shell structures is the absence of an effective strategy for establishing the optimal probe location, particularly when faced with an unknown imperfection distribution.

4.2 Definition of the Problem

In this investigation, we use a statistical framework to analyze the non-destructive probing technique applied to spherical shells featuring a random distribution of imperfections. We conduct systematic sampling of random variables in two distinct cases: firstly (Case I), drawing from the defect distribution, and secondly (Case II), from various indentation locations. This approach enables a comprehensive design space analysis, including these stochastic variables. Through this probabilistic examination, we aim to ascertain how the extrapolated knockdown factor, derived from probing signals and projected towards the buckling threshold, aligns with the statistically derived realistic knockdown factor for shell structures with numerous defects. The protocol for generating these spherical shells with a random distribution of imperfections adhered to the same procedure outlined in Ref. [118].

We consider a thin elastic and hemispherical shell of radius, R , and thickness h containing a random distribution of dimpled geometric imperfections (see Figure 4.1). The number of imperfections exceeds unity ($N > 1$), and each defect is nominated with the index i . The boundary condition is assumed to be clamped for the same reason described in Chapters 2 and 3. Each defect with the index i introduces the radial deviation of w_i from the mid-surface of a spherical shell. Therefore, the generalized form of Equation 2.1 can be written as

$$w_i(\beta) = -\delta_i e^{-(\beta/\beta_0)^2}, \quad (4.1)$$

where the variable β represents the local angular distance from the center of the defect in spherical coordinates. The constants δ_i and β_0 correspond to the amplitude (maximum outward deviation from the mid-surface) and half-angular width of the i th defect, respectively. As illustrated in Figure 4.1(a), the position of the center of each defect on the

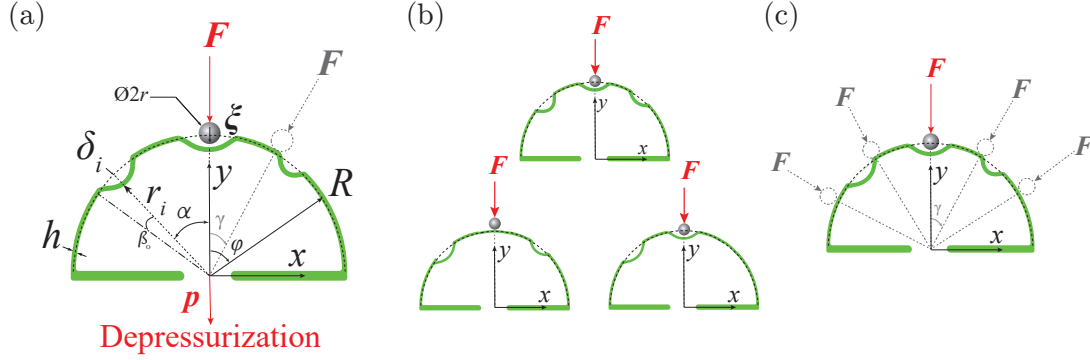


Figure 4.1: **Definition of the problem.** (a) This figure presents a two-dimensional representation of an elastic hemispherical shell featuring a dispersion of dimpled imperfections, subject to two distinct probabilistic indentation scenarios. (b) *Case I*: Different shell configurations with a defined set of parameter values undergo indentation at a consistent pole location, denoted as $\gamma = 0$. (c) *Case II*: In this case, a specific shell characterized by a distribution of imperfections is subjected to indentation at randomly selected locations, γ .

middle surface of the shell ($\beta = 0$) is determined by the radial vector with a unit radial vector:

$$\mathbf{e}_{r_i} = \sin \phi_i \cos \theta_i \mathbf{e}_x + \cos \phi_i \mathbf{e}_y + \sin \phi_i \sin \theta_i \mathbf{e}_z, \quad (4.2)$$

where ϕ_i and θ_i are the zenith and azimuthal coordinates of the i -th defect. Therefore, the exact location of the center of each defect on the mid-surface of the shell is defined by the coordinate (ϕ_i, θ_i) . As a result, the general description for the radial distance of the mid-surface of the shell can be written as

$$r_m(\phi, \theta) = R + \sum_{i=1}^N w_i(\phi, \theta). \quad (4.3)$$

The angular separation between the two neighboring defects with the index i and j , whose centers are located at \mathbf{e}_{r_i} , and \mathbf{e}_{r_j} , also is defined as

$$\alpha_{(i,j)} = \left| \arccos(\mathbf{e}_{r_i} \cdot \mathbf{e}_{r_j}) \right|. \quad (4.4)$$

Our shell is assumed to feature a total of N imperfections distributed randomly across its surface. These imperfections possess varying defect amplitudes, following a lognormal distribution as described in [118], and their positions are determined using a random sequential adsorption algorithm [118]. These designs investigate specific values of the defect's angular width, denoted as β_0 , which consequently affects λ as defined in Equa-

tion 2.2. Consequently, the probability density function (PDF) for the defect amplitude, following a lognormal distribution, can be expressed as follows:

$$f(\bar{\delta}_i) = \frac{1}{\bar{\delta}_i \sigma \sqrt{2\pi}} \exp\left(-\frac{(\ln \bar{\delta}_i - \mu)^2}{2\sigma^2}\right). \quad (4.5)$$

Here, μ and σ are related to the average defect amplitude and the degree of dispersion or spread of these defect amplitudes.

$$\bar{\delta} = \exp\left(\mu + \frac{\sigma^2}{2}\right), \quad (4.6)$$

with the standard deviation of

$$\Delta\bar{\delta} = \{\exp(\sigma^2) - 1\} \exp(2\mu + \sigma^2)^{1/2}. \quad (4.7)$$

The adoption of a lognormal distribution for defect amplitudes implies that when taking natural logarithms of these defect amplitudes, denoted as $\ln(\bar{\delta})$, the resulting values follow a normal distribution characterized by a mean μ and a standard deviation σ . Employing a lognormal Probability Density Function (PDF) to introduce these imperfections confers several advantages. It ensures that we exclusively deal with positive values for δ_i , focusing solely on dimples rather than a mixture of dimples and bumps. Moreover, lognormal distributions of imperfections find widespread use in the analysis of structural reliability [274, 275, 276].

The placement of each defect, as defined by Equation 4.2, is conducted randomly across the shell's surface utilizing a technique called random sequential adsorption [277, 278, 279]. This method is widely employed in generating isotropic porous structures. In this context, we modify the technique to the volumetric domain, randomly distributing the defects on the curved surface of a hemispherical shell. To ensure non-overlapping defects, a minimum angular separation of α_{min} is strictly maintained. The process of introducing defects concludes when the spherical cap, determined by a maximum zenith angle of ϕ_{max} , can no longer accommodate another defect. We chose a ϕ_{max} of 60 degrees to minimize potential boundary interference. Within the hemispherical cap, we designate the angular position of the center of each defect, denoted as (ϕ_i, θ_i) , as the random variable,

$$(\phi_i, \theta_i) = (\arccos(1 - x_\beta(1 - \cos \phi_{max})), 2\pi x_\theta), \quad (4.8)$$

where $x_\phi \in [0, 1]$ and $x_\theta \in [0, 1]$ represent two random variables, each indicating the probability of placing a defect anywhere on the hemisphere cap. This allocation also adheres to the constraint of maintaining a specific angular separation between defects

denoted by indices i and j ,

$$\alpha_{(i,j)} \geq \alpha_{\min}, \quad (4.9)$$

given that $\alpha_{\min} \geq 2\beta_0 = 2 \arcsin(l/R)$ [118], where l represents the opening length of the defect. The following procedure is followed for each fixed l in the shell design. A new defect (indexed as i) is randomly positioned on the shell and assessed against Equation 4.9, taking into account all previously existing defects ($j = 1, \dots, i-1$). If Equation 4.9 is satisfied, a subsequent defect (indexed as $i+1$) is introduced through the same process. However, if Equation 4.9 is not met, the i th defect is removed, and a fresh random location is chosen until a valid condition is met, up to a maximum limit of 10^6 attempts. Upon reaching this threshold, the process of introducing defects concludes, and the final count of defects denoted as N , is determined.

After creating a shell structure with randomly distributed imperfections, we proceed to perform an indentation on the shell. The indentation process varies depending on the specific case under consideration. It involves the use of a rigid spherical indenter with a radius much smaller than the shell's radius, denoted as $r \ll R$ (refer to the schematic in Figure 4.1a). The positioning of the probe is deliberately adjusted, allowing for random alterations in the angle, γ , between the line of action of the probe force and the axis of symmetry of the shell. The shell undergoes a two-step process. Initially, it is subjected to a uniform pressure load set at a predefined value, denoted as p_0 . Subsequently, a point load is applied along the radial direction of the outer surface of the shell, inducing an indentation with a specified displacement, ξ . The resulting reactive force from the indenter is referred to as the probe force, denoted as F . Each indentation test is conducted at varying pressure levels, denoted as p_0 , to generate the corresponding probe force-displacement curves, represented as $F(\xi)$.

We will investigate two distinct scenarios denoted as *Case I* and *Case II*, as depicted in Figure 4.1(b) and (c), respectively. The subsequent sections will outline the process and objectives of each case.

Case I: *Defect amplitude and location as random variables, constant indentation location ($\gamma = 0$):* In this scenario (as depicted in Figure 4.1b), we generated statistical ensembles of imperfect shells, all sharing a statistically equivalent configuration defined by a specific set of parameters $(\bar{\delta}, \Delta\bar{\delta}, \lambda, \alpha_{\min}) = (\{0.2, 0.5, 1, 1.5\}1, 0.3, 1, 10^\circ, 25^\circ)$. This requires producing numerous shell configurations for each set of variables (500 different shell configurations). Each shell configuration was initially subjected to uniform pressure, precisely set at a prescribed value p_0 , as detailed in Chapter 3. Subsequently, it underwent indentation by a point load applied through a rigid indenter, consistently positioned

at $\gamma = 0$, following the procedure outlined in Chapter 3. Throughout the series of depressurizations, we recorded the probe force response, denoted as F . Finally, for each of these configurations, we also recorded the maximum force value, F_{max} , as a function of pressure level, $F_{max}(p_0)$.

Case II: *Single shell configuration with random indentation location (γ):* As depicted in Figure 4.1(c), in this scenario, we draw our random variable from the indentation location, γ . We focus on a single shell with specific parameter values, $(\bar{\delta}, \Delta\bar{\delta}, \lambda, \alpha_{min}) = (1, 0.3, 1, \{10^\circ, 25^\circ\})$. Systematically, we measure the indentation force response, F , at randomly selected locations while varying the level of depressurization. Finally, we extract the maximum indentation force, F_{max} , in relation to the level of depressurization for different random indentation locations.

4.3 Finite Element Simulations

We conducted finite element method (FEM) simulations using the commercially available ABAQUS/Standard software. The shell structure, featuring a random distribution of imperfections with defect amplitudes sampled from a lognormal distribution, was generated following the methodology established by Derveni *et al.*[118]. This approach was initially validated through experimental work. Given the dispersed nature of the imperfections across the shell surface, a fully 3D numerical analysis was crucial for this study. To reduce the computational cost of the study, we utilized S4R shell elements with reduced integration points, allowing for the incorporation of finite membrane strains. The hemispherical shell was discretized into four sections, each comprising 150 elements in both azimuthal and meridional directions, selected after verifying mesh convergence. The material behavior was emulated using a neo-Hookean model, exhibiting properties akin to a nearly incompressible solid with a Poisson's ratio of $\nu = 0.5$. The Young's modulus, determined through experimental data, was found to be $E = 1.25 \pm 0.01$ MPa. These material properties were derived from standard tensile tests conducted on dog-bone specimens, in accordance with prior experiments detailed in Ref. [258].

Following the procedure outlined in Chapter 3, we conduct indentation tests for the two specified cases outlined in the preceding section and detailed below, Case I and II. As a first step, we establish a mesh scheme covering the entire shell. Subsequently, we displace the nodes based on the defined design parameters $(\bar{\delta}, \Delta\bar{\delta}, \lambda, \alpha_{min})$, generating imperfections following Equation 4.1. Since the imperfection layout is specified at the mid-surface of the shell, no adjustments to the reference surface mesh are required. Throughout all simulations involving dimpled shells, we maintain a uniform nodal thickness for each node, set at a fixed value of $R/h = 110$. With the imperfect shell properly configured, we

proceed with the indentation process for Cases I and II, as elaborated in the following sections.

- **Case I:** We analyze 500 unique realizations of shell structures characterized by the same parameter set, $(\bar{\delta}, \Delta\bar{\delta}, \lambda, \alpha_{\min}) = (\{0.2, 0.5, 1, 1.5\}, 0.3, 1, \{10^\circ, 25^\circ\})$. These structures have defects distributed using the random adsorption algorithm, and their defect amplitude follows a lognormal distribution. Initially, each shell undergoes uniform live pressure applied on its outer surface, denoted as $\bar{P} = p_0/p_c$. While maintaining this pressure, we apply an indentation displacement (similar to Section 3.4) onto the shell at a probe angle of $\gamma = 0$. We record the force-displacement response for each pressure set and extract the maximum force value, denoted as $\bar{F}_{max} = F_{max}R/2\pi D$ (similar to Section 3.4).
- **Case II:** In this instance, we focus on a specific shell structure, with the parameter set of $(\bar{\delta}, \Delta\bar{\delta}, \lambda, \alpha_{\min}) = (1, 0.3, 1, \{10^\circ, 25^\circ\})$. The defect distribution in this single shell adheres to the same protocol as in Case I. However, in this scenario, the indentation location is determined randomly, following the algorithm defined for defect placement. After establishing the indentation locations, the shell undergoes loading via a uniform live pressure applied on its outer surface, denoted as \bar{P} . Subsequently, the force-displacement response is recorded for each pressure setting, from which the maximum force signal, $\bar{F}_{max}(\bar{P})$, is extracted.

4.4 Case I: The Shell Configuration as the Random Variable

In this section, we address the first research question (*Case I*) outlined in Section 4.2, which involves examining the efficiency of the probing technique in predicting the buckling behavior and critical conditions of shells containing a significant number of imperfections, each of which has a specific defect amplitude denoted as $\bar{\delta}_i = \delta_i/h$. These amplitudes of imperfections follow a lognormal distribution, characterized by the probability density function (PDF) $f(\bar{\delta}_i)$ in Equation (4.5), with an average magnitude of $\bar{\delta}$ and a standard deviation of $\Delta\bar{\delta}$. The investigated parameter combinations are: $\bar{\delta} = 0.2, 0.5, 1, 1.5$ and $\Delta\bar{\delta} = 0.3$. Additionally, we maintain the defect width $\lambda = 1$ and set the minimum angular separation between any two defects as $\alpha_{\min} = \{10^\circ, 25^\circ\}$. Seeding is confined within a defined spherical cap region, with a maximum angle $\phi_{max} = 60^\circ$ to mitigate boundary interference. For each set of design parameters $(\bar{\delta}, \Delta\bar{\delta}, \lambda, \text{ and } \alpha_{\min})$, we generate 500 statistically equivalent realizations of shell structures, each subjected to 13 levels of depressurization, and then performed indentation, resulting in a total of 52,000 Finite Element Method (FEM) simulations. Specifically, for the data illustrated in Figure 4.2, we produce 500 instances for each shell design to ensure statistical robustness and verify

the independence of ensemble size.

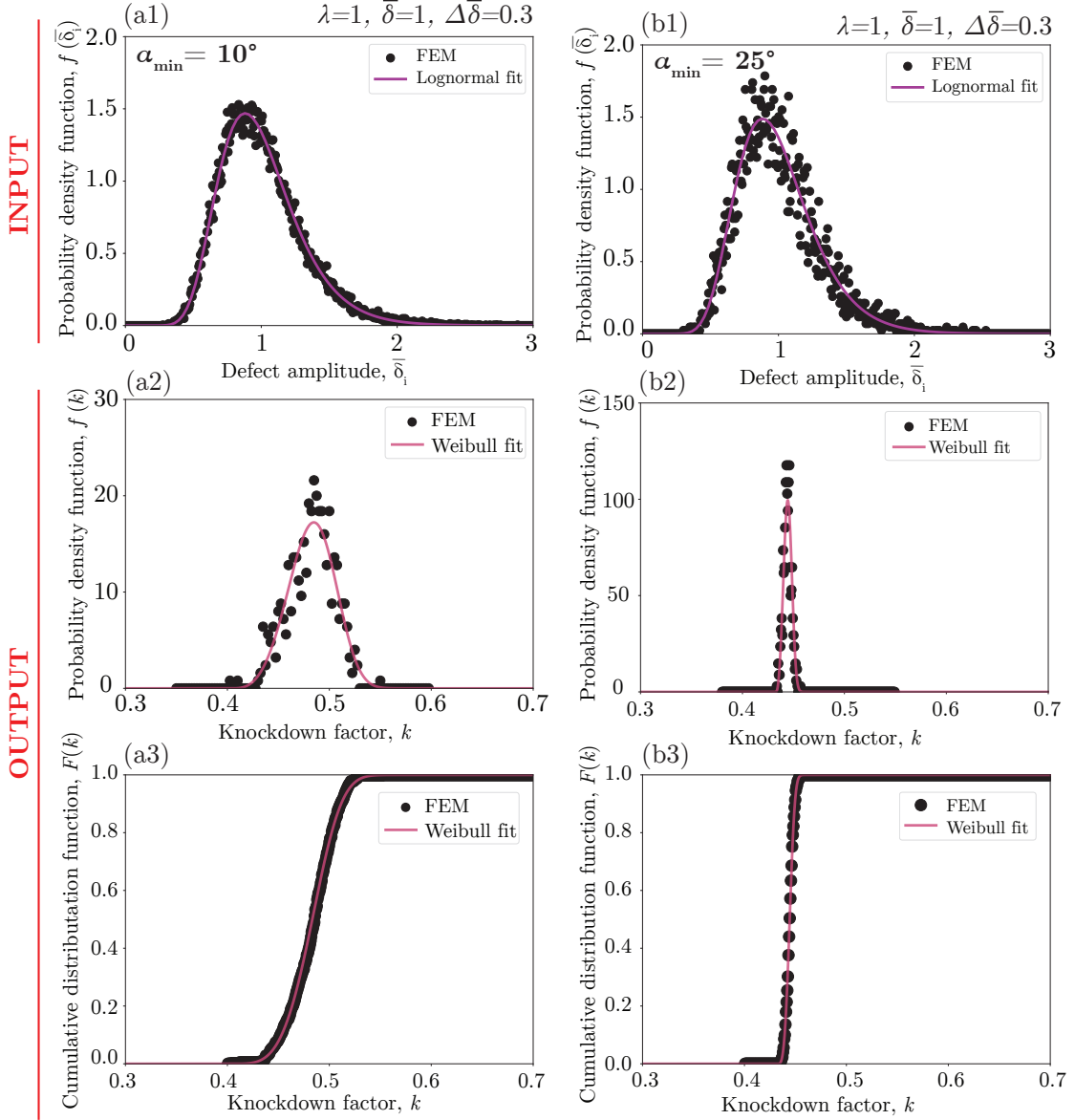


Figure 4.2: Probabilistic evaluation of the knockdown factor in a spherical shell with imperfections. The input Probability Density Function (PDF) of defect amplitudes sharing the same distribution parameters, $\lambda = 1$, $\bar{\delta} = 1$, and $\Delta\bar{\delta} = 0.3$. However, the minimum separation angle between defects varies, with (a1) $\alpha_{min} = 10^\circ$ and (b1) $\alpha_{min} = 25^\circ$. The resulting Probability Density Function and Cumulative Distribution Function, PDF, ($f(k)$) and CDF ($F(k)$) of knockdown factors for shells with $\alpha_{min} = 10^\circ$ are illustrated in (a2) and (a3) respectively. Similarly, (b2) and (b3) depict the PDF, ($f(k)$) and, CDF ($F(k)$) of knockdown factor of shells with $\alpha_{min} = 25^\circ$.

In the first case, illustrated in Figure 4.1(b), we conduct an indentation test on 500

instances of the shell, all indented at the pole ($\gamma = 0$), utilizing the same set of statistical parameters. These structural defects within the shell are randomly dispersed, with their defect amplitudes conforming to a lognormal distribution [118]. According to Derveni *et al.* [118], the knockdown factor for these 500 shells should exhibit statistics following a Weibull distribution. To validate this assertion and gain insights into the statistical characteristics of the real knockdown factor of our shells, we will present and define the input and output statistics of the system in *Case I* (see Figure 4.1b) as follows.

In Figure 4.2(a1), we present an illustration showing the input statistics for a design of shells with numerous defects characterized by parameters $(\bar{\delta}, \Delta\bar{\delta}, \lambda, \alpha_{min}) = (1.0, 0.3, 1, 25^\circ)$. The probability density function of the defect amplitudes, as is obvious from the fit, was sampled from the lognormal distribution (Equation 4.5). We then performed Finite Element Method (FEM) simulations for a group of 500 statistically equivalent designs and measured their respective knockdown factors, denoted as k . Following this, we construct the probability density function (PDF) of the output, referred to as $f(k)$, as shown in Figure 4.2(a2). Our analysis corroborates the assertion made in the recent study by Derveni *et al.* [118] that the histogram, derived from the FEM data of the knockdown factor, can be precisely characterized by a three-parameter Weibull distribution (depicted by the solid line) as

$$f(k) = \frac{m}{\hat{k}} \left(\frac{k - k_{min}}{\hat{k}} \right)^{m-1} \exp \left(- \left(\frac{k - k_{min}}{\hat{k}} \right)^m \right). \quad (4.10)$$

The parameters \hat{k} , m , and k_{min} refer to the scale, shape, and threshold values, respectively. The inclusion of k_{min} as the third parameter is essential to consider the lower limit of k , which corresponds to the plateau observed in the knockdown factor-defect amplitude, $k(\delta)$, curves [118] (see Figure 1.5). In Figure 4.2(b1), another set of shell configuration examples with just a different value of the minimum separation of each two defects, $(\bar{\delta}, \Delta\bar{\delta}, \lambda, \alpha_{min}) = (1.0, 0.3, 1, 10^\circ)$, is presented, which also leads to Weibull statistics for the knockdown factor, as shown in Figure 4.2(b2). The representations of the Weibull distribution in Figure 4.2(a2) and (b2) were generated using three fitting parameters \hat{k} , m , and k_{min} . These parameters were determined through the Maximum Likelihood Estimation technique [118]. With these parameters, we calculated the respective Weibull cumulative distribution functions (CDFs) as:

$$F(k) = 1 - \exp \left(- \left(\frac{k - k_{min}}{\hat{k}} \right)^m \right). \quad (4.11)$$

The Weibull cumulative distribution function (CDF) of the Finite Element Method (FEM) knockdown factor data, as depicted in Figures 4.2(a3) and (b3), aligns remarkably well with the CDF fit of the Weibull function. According to these results, we deduce

that the actual knockdown factor statistics follow a 3-parameter Weibull distribution, which is derived based on extreme value theory. This assumes that the likelihood of failure for a single representative component within a structure adheres to a power-law distribution tail [118]. Consequently, if any component, specifically the weakest link, experiences a breakdown, it results in the overall failure of the entire system, indicating that probabilistic shell buckling belongs to extreme-value phenomena.

Given an understanding of the input characteristics of the shell configurations and the output statistics of the knockdown factor, we aim to establish a connection between the input and output through the nondestructive indentation test outlined in Chapter 3. In this *Case I*, the indentation point is fixed at the pole of the hemispherical shell structure, denoted as $\gamma = 0$, regardless of whether a defect is randomly located at the pole or not. Simultaneously, the random variable is the shell configuration with different designs of imperfections. The prescribed depressurization was systematically varied at 13 levels, ranging from $\bar{P} = 0$ to $\bar{P} = 0.4$. After conducting indentation at each level of depressurization, in Figure 4.3, we display the maximum force, $\bar{F}_{\max} = F_{\max}R/2\pi D$, plotted versus these pressure levels, \bar{P} , for the indentation response of 500 realizations of shells with the statistical parameter set of $(\bar{\delta}, \Delta\bar{\delta}, \lambda, \alpha_{\min}) = (1.0, 0.3, 1, 10^\circ)$ in (a), and $(\bar{\delta}, \Delta\bar{\delta}, \lambda, \alpha_{\min}) = (1.0, 0.3, 1, 25^\circ)$ in (b). The black dashed line represents the mean of the maximum price force at each pressure level.

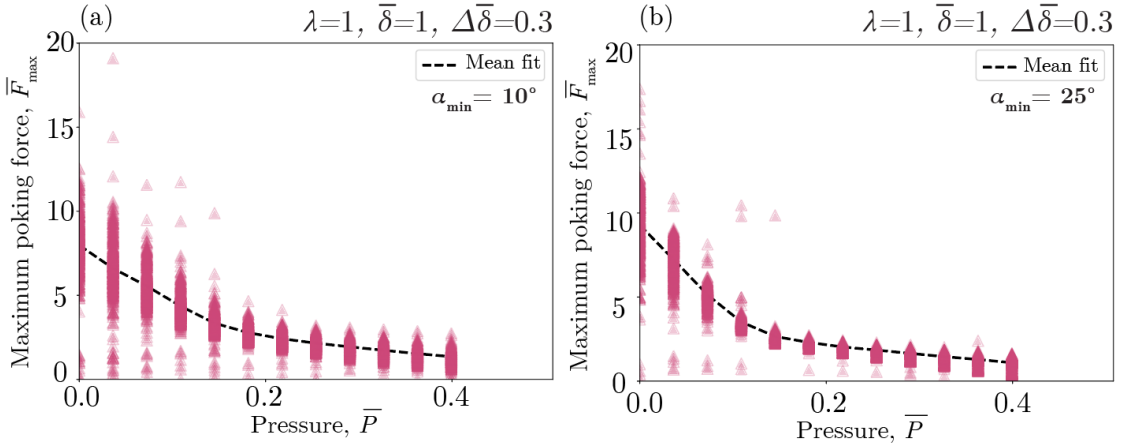


Figure 4.3: **Force-displacement response of shells with a random distribution of imperfections under indentation.** The normalized maximum probe force, $\bar{F}_{\max} = F_{\max}R/2\pi D$, versus the prescribed pressure, \bar{P} , for indentation of 500 shell configurations at the probe angle of $\gamma = 0$ for the minimum angular separation of (a) $\alpha_{\min} = 10^\circ$, and (b) $\alpha_{\min} = 25^\circ$. The data points represent the predictions from the FEM simulations. The dashed line presents the average fit at each pressure level.

From these plots, we first observe that the distribution of the measured maximum

probing force at lower pressure levels is more scattered and has a wider distribution range. This arises from the fact that when the shell is less pressurized, it possesses a larger energy barrier toward buckling, and the defects influence the indentation response. In contrast, at high-pressure levels close to buckling pressure, the energy barrier toward buckling is negligible, and even a small perturbation of the shell results in shell buckling without feeling the defects; hence, a small distribution of maximum indentation force values is observed. Additionally, the maximum force-pressure relation also exhibits a nonlinear trend in both cases of Figure 4.3(a) and (b). Comparatively, the maximum force distribution in Figure 4.3(a) with a larger minimum separation between the defects of $\alpha_{\min} = 10^\circ$ (indicating significant defect-defect interaction) is more scattered than $\alpha_{\min} = 25^\circ$, which shows less defect-defect interactions.

With the maximum indentation force-pressure signals illustrated in Figure 4.3 at hand, we commence our approach, which involves extrapolation towards zero maximum probing force, as elaborated in Chapter 3 and depicted in Figure 6.2. This procedure empowers us to ascertain the critical pressure prediction of spherical shells for various configurations. Our goal is to address two pivotal research inquiries: What do the statistics of the predicted knockdown factors extracted from these extrapolation data indicate, and how do they compare to the actual knockdown factor statistics derived from FEM simulation of 500 distinct realizations of spherical shells with randomly distributed imperfections?

Prior to delving into the impact of various polynomial extrapolation techniques in Section 4.4, we employed Gaussian Process Regression (GPR) on the maximum indentation force-pressure dataset to extrapolate the 500 curves towards zero maximum force. The GPR model was configured with a Matern kernel, which governs the smoothness of the predicted function. The loop iterated through different configurations, fitting the GPR model to each set of data points and generating predictions [280]. This approach provides a versatile and probabilistic framework for modeling the intricate relationship between force and pressure. It proves especially invaluable when dealing with complex and noisy data, enabling the encapsulation of uncertainties in the underlying process and furnishing reliable predictions, even in regions where data may be sparse or absent [280].

We obtained the 500 extrapolated knockdown factors, denoted as k_{ex} , through Gaussian Process Regression (GPR). As shown in Figure 4.4(a) and (b), we generated the probability density function (PDF) for these 500 extrapolated knockdown factors, denoted as $f(k_{ex})$, with the parameter set $(\bar{\delta}, \Delta\bar{\delta}, \lambda, \alpha_{\min}) = (1, 0.3, 1, 25^\circ)$. In Figure 4.4(a), we applied Maximum Likelihood Estimation (MLE) to fit the extrapolated data with a 3-parameter Weibull distribution, while in Figure 4.4(b), we employed the Bayesian technique along with the Markov Chain-Monte Carlo algorithm to fit the Weibull function. Figures 4.4(c) and (d) depict the cumulative density functions (CDFs) of the extrapolated knockdown

factors, $F(k_{ex})$, corresponding to the data illustrated in Figures 4.4(a) and (b), respectively. The symbols represent the extrapolated data points, and the solid lines represent the fitted Weibull distribution. In Figure 4.4(b), the posterior predictive distribution is also illustrated, which makes predictions about future observations based on the posterior distribution of model parameters using the Bayesian approach. Concerning the CDF of the extrapolated knockdown factor in Figure 4.4(d), the gray-shaded region indicates the uncertainty associated with the bandwidth of parameters of the Weibull fit, determined using the Bayesian technique.

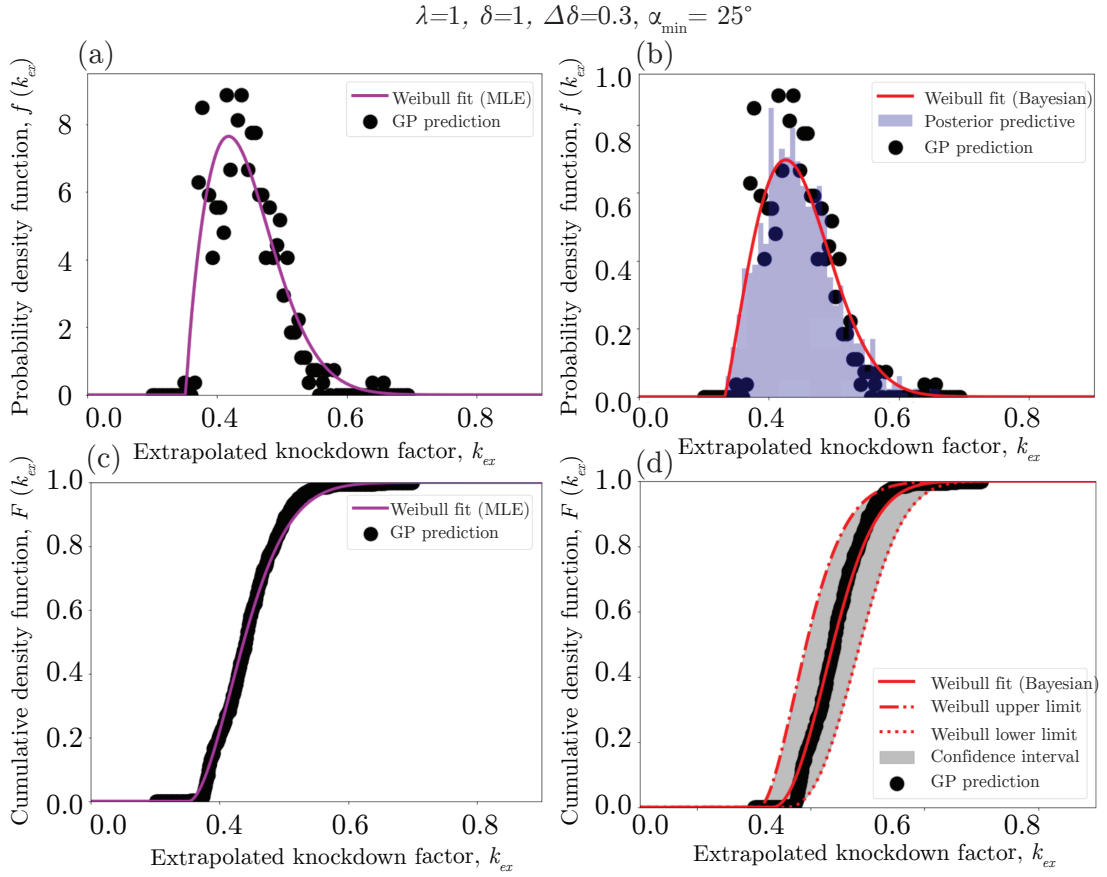


Figure 4.4: **Extrapolated knockdown factor statistics.** (a) The Probability density function (PDF) and (c) Cumulative Density Function (CDF) representation of the extrapolated knockdown factor obtained through Gaussian Process Regression. The solid lines represent the fitted Weibull function using Maximum Likelihood Estimation. (b) The PDF, and (d) CDF of the extrapolated knockdown factor through Gaussian Process Regression. The solid lines represent the fitted Weibull function using the Bayesian method based on the Markov Chain Monte Carlo algorithm. The data in (a), (b), (c), and (d) correspond to the variable sets $(\bar{\delta}, \Delta\bar{\delta}, \lambda, \alpha_{\min}) = (1.0, 0.3, 1, 25^\circ)$.

We have observed that, when employing both Maximum Likelihood Estimation (MLE)

and Bayesian techniques, the extrapolated data derived from Gaussian Process Regression (GPR) correlates quite well with the 3-parameter Weibull distribution fit. This agreement indicates that both methods yield consistent predictions, suggesting that the Weibull distribution, which was a suitable fit for the actual knockdown factor statistics [118], may also serve as an appropriate model for the extrapolated knockdown factor obtained through the indentation technique. Nonetheless, it is imperative to thoroughly investigate the impact of the extrapolation technique (more details in Section 4.4.1). Further elaboration on the distinctions in parameters and the level of certainty associated with each technique (MLE versus Bayesian) will be provided next.

In Table 4.1, we present a comparative analysis of the parameters derived from the Weibull fit applied to the extrapolated knockdown factor data. This analysis employs two distinct methodologies: Maximum Likelihood Estimation (MLE) and the Bayesian approach based on utilizing the Markov Chain Monte Carlo (MCMC) algorithm. Markov Chain Monte Carlo (MCMC) is a popular statistical tool employed for approximating numerical integration and sampling from intricate probability distributions. Its application is particularly valuable in Bayesian statistics and in scenarios where exact solutions are challenging or unattainable [281]. Through the Bayesian approach, we not only obtain estimates for the Weibull parameters, denoted as $(\hat{k}, m, k_{min}) = (2.103, 0.1275, 0.333)$, but also achieve a comprehensive characterization of parameter uncertainty (refer to the range of parameters in Table 4.1). This comprehensive assessment provides a more robust evaluation of model fit compared to the Maximum Likelihood Estimation (MLE) method, which typically yields singular point estimates, denoted as $(\hat{k}, m, k_{min}) = (1.771, 0.104, 0.353)$, without considering the associated uncertainty, but offering simplicity and is straightforward to implement and interpret.

Parameters	MLE	Bayesian
Shape, \hat{k}	1.771	[1.728, 2.477]
Scale, m	0.104	[0.102, 0.153]
Location, k_{min}	0.353	[0.310, 0.355]
KS-test statistics	0.052	0.080
p-value	0.139	0.059

Table 4.1: **Compariosn of MLE versus Bayesian techniques.** Comparison between the parameters of Weibull fit calculated through MLE and Bayesian method and the results of Kolmogorov-Smirnov (KS) test.

In order to evaluate the goodness-of-fit for both the Bayesian method based on Markov Chain Monte Carlo (MCMC) and the Maximum Likelihood Estimation (MLE) technique, The Kolmogorov-Smirnov (KS) test is playing a crucial role. This statistical test [282] serves as a robust tool to determine the significance of differences between the two

datasets. Notably, it operates on a non-parametric basis, implying that it makes no assumptions about the underlying distributions of the data. The KS test accomplishes this by comparing the empirical Cumulative Distribution Function (CDF) of the observed data with the theoretical CDF derived from the fitted models. The outcomes of this test offer crucial insights into how well each method captures the true distribution of the knockdown factor data. This assessment is pivotal in ensuring that the selected modeling approach accurately mirrors the observed data, forming a reliable foundation for making predictions and inferences. The p-values obtained from the KS test, quantitatively measuring the agreement between empirical and theoretical distributions, affirm that both methods, with a good estimation, yield comparable results, attesting to their goodness of fit, strengthening our confidence in the accuracy of the chosen modeling strategies and their ability to represent the underlying extrapolated data effectively. The results of this comparison indicate that the extrapolated knockdown factor data, obtained through GPR with accurate estimation, closely adheres to the Weibull fit using both MLE and Bayesian method, which has been demonstrated to provide an effective description for the knockdown factor statistics of spherical shells [118].

After examining the statistics of the extrapolated knockdown factor, now in Figure 4.5, we overlay the fit of real knockdown factor statistics of the 500 configurations of imperfect shells with the extrapolated data and the fitted Weibull function demonstrated in Figure 4.4. Figure 4.5(a) presents the probability density function for the parameter set $(\bar{\delta}, \Delta\bar{\delta}, \lambda, \alpha_{min}) = (1.0, 0.3, 1, 25^\circ)$, and Figure 4.5(b) presents the parameter set of $(\bar{\delta}, \Delta\bar{\delta}, \lambda, \alpha_{min}) = (1.0, 0.3, 1, 10^\circ)$. The first observation from the results reveals that the distribution of the real knockdown factor has a significantly narrower bandwidth compared to the extrapolated fit bandwidth. This observation arises from the fact that the uncertainty of the extrapolation results in a large scatter of the extrapolated data. Secondly, although the mode of the extrapolated fit and the real data fall within the same range of knockdown factor, approximately 0.45, the magnitude of the PDF at this specific point—indicating the relative likelihood of observing a random variable and a measure of how "dense" the probability is around that point—is much larger in real knockdown factor data compared to the extrapolated fit. This is again a result of the large scatter of the extrapolated data points. However, with all that said, the minimum or threshold of the histogram of the extrapolated knockdown factor fit is much lower than the threshold of the real knockdown factor distribution. , implying that the extrapolation provides a safe prediction for the design of shells. Upon comparing the outcomes presented in Figure 4.5(a) and (b), it is evident that the statistical distribution of the actual knockdown factor for shells with interacting defects ($\alpha_{min} = 10^\circ$) exhibits a broader range in comparison to the scenario with non-interacting defects ($\alpha_{min} = 25^\circ$). This discrepancy arises from the intricate nature of defect interactions, leading to a more

conservative prediction from extrapolation in the non-interacting case.

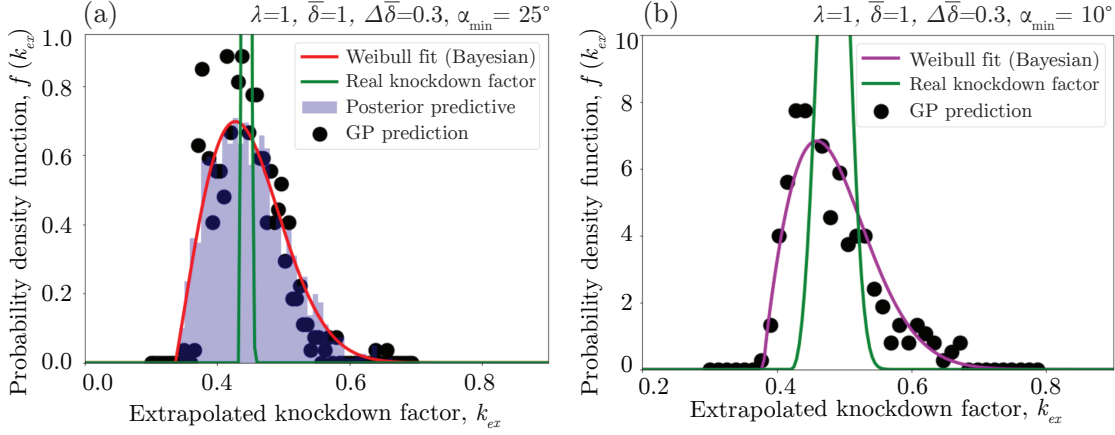


Figure 4.5: **Extrapolated knockdown factor versus the real knockdown factor for Case I.** The PDF of extrapolated knockdown factor, $f(k_{ex})$ (symbols), the fitted knockdown factor (solid lines), and the real knockdown factor (solid green line) are superposed for the variable set of (a) $(\bar{\delta}, \Delta\bar{\delta}, \lambda, \alpha_{min}) = (1.0, 0.3, 1, 25^\circ)$, and (b) $(\bar{\delta}, \Delta\bar{\delta}, \lambda, \alpha_{min}) = (1.0, 0.3, 1, 10^\circ)$.

4.4.1 Effects of Defect Amplitude and Extrapolation Method on Poking Predictions

Having analyzed the extrapolated knockdown factor statistics and compared them with the actual knockdown factor data, we now delve into the impact of the average defect amplitude of the shell, denoted as $\bar{\delta}$, as well as the extrapolation method. This examination aims to assess the effectiveness of the poking technique in predicting the knockdown factor and to offer design guidelines for spherical shells characterized by a random distribution of imperfections.

To explore the impact of defect amplitude on poking statistics, In Figures 4.6(a)-(d), we illustrate the relationship between the maximum indentation force (\bar{F}_{max}) and the pressure level (\bar{P}) across 500 different shell realizations for each parameter set with varying average defect amplitudes defined by $(\Delta\bar{\delta}, \lambda, \delta, \alpha_{min}) = (0.3, 1, \{0.2, 0.5, 1, 1.5\}, 25^\circ)$, respectively. Firstly, a consistent nonlinear response of maximum force-pressure is observed across all levels of defect amplitude. Additionally, all force-pressure signals exhibit a nonlinear behavior with two sublinear regimes. The first regime occurs at low-pressure levels ($\bar{P} < 0.1$), which differs slightly between different levels of average defect amplitude due to the fact that the indenter must penetrate deeply into the shell to reach the buckling point. However, in the second regime, for higher pressure levels ($\bar{P} > 0.1$), the maximum

force-pressure signal shows similar results for all defect amplitudes, which indicates that the indenter cannot distinguish the defect when the shell is highly pressurized and is close to buckling. Moreover, as the pressure increases, the distribution bandwidth of the maximum force narrows due to the shell structure approaching the buckling point. It is noteworthy that the distribution bandwidth of the force is smaller for smaller $\bar{\delta}$ and widens with increasing defect amplitude.

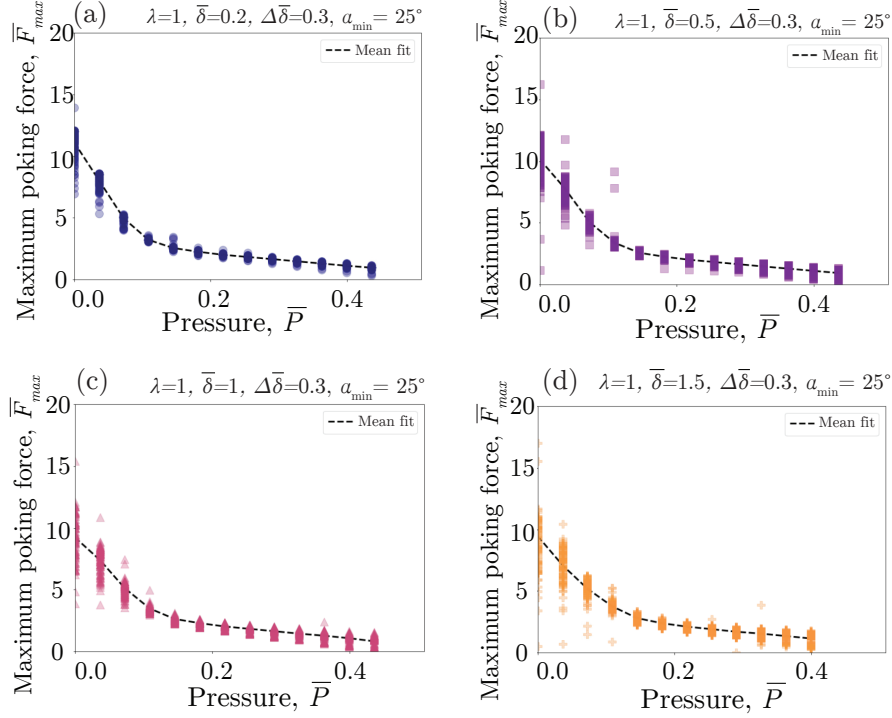


Figure 4.6: **The effect of average defect amplitude on maximum force-pressure response.** The maximum force, \bar{F}_{max} , as a function of the normalized pressure, \bar{P} , for 500 shell realizations of $(\Delta\bar{\delta}, \lambda, \alpha_{min}) = (0.3, 1, 25^\circ)$, for each (a) $\bar{\delta} = 0.2$, (b) $\bar{\delta} = 0.5$, (c) $\bar{\delta} = 1$, and (d) $\bar{\delta} = 1.5$. The symbols are the FEM data, and the dashed lines are the average of the maximum force at each pressure level.

Having noted that the trend in the maximum force-pressure for all defect amplitudes exhibits a consistent pattern, our objective is to investigate the impact of various extrapolation techniques on the extrapolated knockdown factor statistics and their influence on predicting the real knockdown factor. Furthermore, we seek to determine if the insights gained from the extrapolation based on GPR in Section 4.4 can be broadened. This involves investigating how the choice of extrapolation method (various polynomials), along with the average size of the defects, influences the accuracy of knockdown factor predictions using poking technique.

Hence, in Figure 4.7, we present the probability density function (PDF) of the extrapolated

knockdown factor alongside its Weibull fit, juxtaposed with the actual knockdown factor statistics. These are provided for various defect amplitudes and extrapolation methods. The fixed parameter set for this series of figures is $(\Delta\bar{\delta}, \lambda, \alpha_{min}) = (0.3, 1, 25^\circ)$. Specifically, Figures 4.7(a), (b), (c), and (d) correspond to $\bar{\delta} = 0.2$, $\bar{\delta} = 0.5$, $\bar{\delta} = 1$, and $\bar{\delta} = 1.5$, respectively. Furthermore, we employed three distinct polynomial extrapolation methods: linear, cubic, and quintic polynomials corresponding to panels (1), (2), and (3), respectively. The symbols represent the extrapolated data, the dashed line denotes the Weibull fit applied to the extrapolated data, and the solid lines represent the actual knockdown factor statistics.

In Figure 4.7 (a), we observe that for a small defect amplitude of $\bar{\delta} = 0.2$, the extrapolated knockdown factor prediction using the linear polynomial overestimates the knockdown factor. On the other hand, the cubic polynomial provides accurate predictions for both the threshold parameter of the Weibull fit and the magnitude of the PDF, although it slightly underestimates the mode. While successfully predicting the threshold parameter of the Weibull function with good agreement, the quintic polynomial does not yield a conservative estimate. For $\bar{\delta} = 0.5$ (Figure 4.7 b), the linear extrapolation does not provide a good estimation for all the PDF magnitudes, the threshold, and the mode of the histogram. In this case, using the cubic and quintic polynomials yields fairly similar results with a conservative prediction of the threshold. However, the mode and magnitude of the PDF and the mode prediction are not well estimated. As we increase the average defect amplitude to $\bar{\delta} = 1$, we observe that the polynomial extrapolation does not accurately estimate the real knockdown factor statistics. Although the cubic and quintic polynomials can give a reasonable estimation of the lower bound and the threshold of the distribution, as well as a conservative prediction for the mode of the distribution, overall, the prediction deviates significantly from the real knockdown factor data. For the largest defect amplitude considered in this study, $\bar{\delta} = 1.5$, the linear extrapolation does not provide a reliable prediction due to the fact that the predicted data are scattered and do not align well with the Weibull fit. Regarding the cubic and quintic extrapolations, again, they give a conservative prediction for the threshold and the mode of the distribution compared to the real knockdown factor distribution. Still, the extrapolated data is too scattered to be fitted with the Weibull distribution perfectly.

It is crucial to note that the accuracy of the extrapolated data and the alignment between the predictions derived from the poking technique and the actual knockdown factor statistics are highly contingent on the chosen extrapolation method. Upon careful examination of three different polynomial extrapolation techniques, third-order polynomials yield results that are more comparable to knockdown factor statistics in practice. Furthermore, it is worth highlighting that as the parameter $\bar{\delta}$ increases, the alignment between the

extrapolated data and the real knockdown factor diminishes. Interestingly, for $\bar{\delta} = 0.2$, we attain the highest level of agreement. This underscores the significance of this specific parameter in achieving accurate predictions.

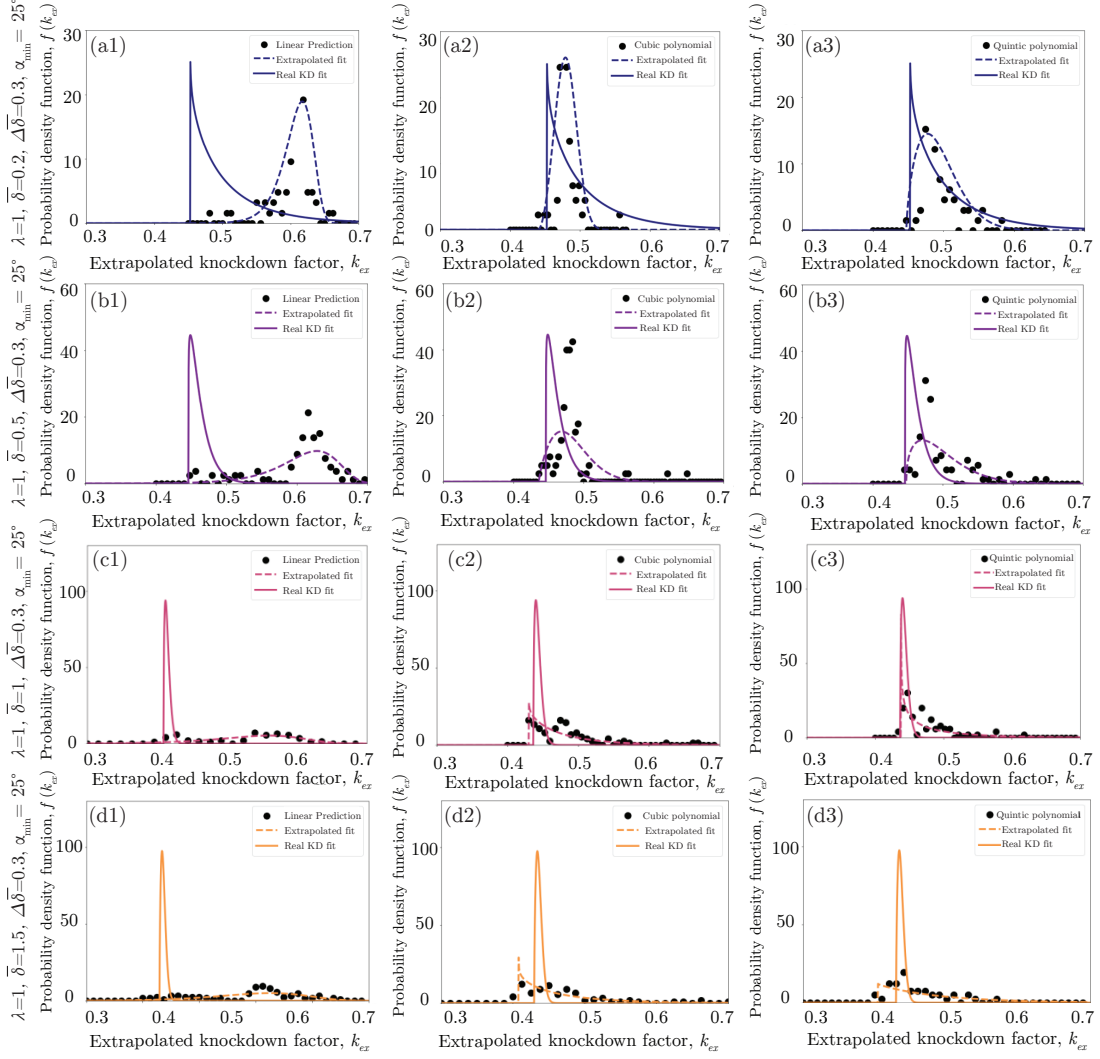


Figure 4.7: **Comparative analysis of extrapolation using different polynomials for various average defect amplitudes.** The probability density function of the extrapolated knockdown factor, $f(k_{ex})$ is presented for the parameter set $(\Delta\bar{\delta}, \lambda, \alpha_{min}) = (0.3, 1, 25^\circ)$ with different average defect amplitudes: (a) $\bar{\delta} = 0.2$, (b) $\bar{\delta} = 0.5$, (c) $\bar{\delta} = 1$, and (d) $\bar{\delta} = 1.5$. For each case, extrapolation is performed using three different polynomial orders: (a1), (b1), (c1), and (d1) represent linear polynomial extrapolation. (a2), (b2), (c2), and (d2) denote cubic polynomial extrapolation. Finally, (a3), (b3), (c3), and (d3) correspond to quintic polynomial extrapolation.

4.5 Case II: the Indentation Location as the Random Variable

In this section, unlike the previous one, we sample the random variable for our probabilistic non-destructive indentation analysis from the indentation location. As depicted earlier in Figure 4.1(c), we focus on a specific single configuration of shell structure and conduct the indentation test at 500 randomly chosen locations of γ . To determine these random indentation points, we employ the random adsorption algorithm, the same method used for locating random defects (as detailed in Section 4.4). The parameter set for the shells under consideration in this section is $(\bar{\delta}, \Delta\bar{\delta}, \lambda, \alpha_{min}) = (1, 0.3, 1, \{10^\circ, 25^\circ\})$. Our objective is to gain insights into how the random placement of indentations influences the effectiveness of the non-destructive probing technique in the design of shell structures.

In Figure 4.8, we present the relation between the maximum force, \bar{F}_{max} , and the pressure level, \bar{P} , for the indentation test conducted at 500 different locations with the parameter set $(\bar{\delta}, \Delta\bar{\delta}, \lambda, \alpha_{min}) = (1, 0.3, 1, 25^\circ)$, with the real knockdown factor value of $k = 0.45$. Each data point represents the maximum force obtained from an indentation at one of these 500 locations during a series of depressurizations. The symbols denote the Finite Element Method (FEM) extracted data, while the dashed line represents the average of the maximum poking forces across all indentation locations at each depressurization level.

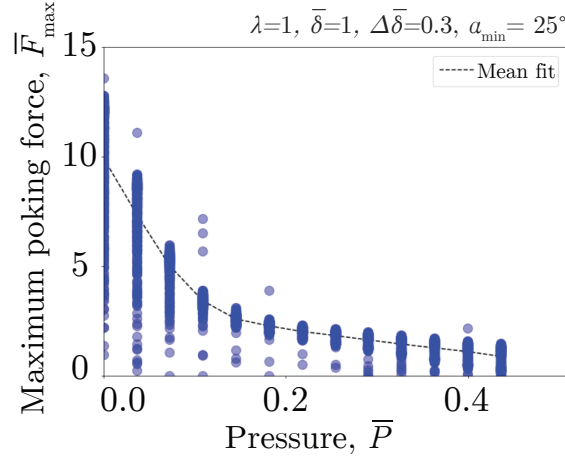


Figure 4.8: **Force-displacement response during indentation at random locations (Case II).** The normalized maximum probe force, $\bar{F}_{max} = \frac{F_{max}R}{2\pi D}$, is plotted against the prescribed pressure, \bar{P} , for indentation at 500 different locations. This analysis pertains to a specific shell configuration characterized by the parameter set $(\bar{\delta}, \Delta\bar{\delta}, \lambda, \alpha_{min}) = (1, 0.3, 1, 25^\circ)$. The symbols represent the Finite Element Method (FEM) data, while the dashed line represents the mean fit at each pressure level.

Similar to the previous section, the maximum force-pressure response exhibits non-linear behavior. At low-pressure levels, the distribution bandwidth of the maximum force is wider due to the substantial energy barrier the shell faces before reaching the buckling point. This results in a more pronounced influence of various defects on the probing force. Additionally, the distribution of the maximum force is reasonably scattered, largely contingent on whether the indenter is positioned over a defect or not. This discrepancy is more pronounced at lower pressure levels and is of particular concern.

In this analysis, we extended the 500 different curves from Figure 4.8 towards zero poking force using Gaussian Process Regression (GPR). This method, which was introduced in Section 4.4, has demonstrated its effectiveness in providing a conservative prediction of the parameters for the actual knockdown factor statistics. In Figures 4.9(a) and (b), we depict the Probability Density Function (PDF) and Cumulative Density Function (CDF) of the extrapolated data, represented by the symbols, respectively. The extrapolated data is then fitted with a 3-parameter Weibull distribution using the Bayesian approach, providing similar results to MLE (see section 4.4). The posterior predictive of the fitted Weibull function is displayed for the PDF of the extrapolated data in Figures 4.9(a), and the region of uncertainty is presented for the CDF of the extrapolated data in Figures 4.9(b). It is evident that, similar to the scenario in Case I, the extrapolated data conforms well to the 3-parameter Weibull fit, which accurately describes the statistics of the actual knockdown factor data. However, this was not the case when the data were extrapolated using polynomials.

In Figure 4.10(a) and (b), we overlay the extrapolated data for two different shells with two sets of parameters: $(\bar{\delta}, \Delta\bar{\delta}, \lambda, \alpha_{min}) = (1, 0.3, 1, 25^\circ)$ and $(\bar{\delta}, \Delta\bar{\delta}, \lambda, \alpha_{min}) = (1, 0.3, 1, 10^\circ)$, with the actual knockdown factor of the shell structure, respectively. This comparison allows us to analyze the impact of the random selection of the indentation location and to compare it with the real knockdown factor data for two distinct shells with varying minimum defect separation angles. For the shell depicted in Figure 4.10(a), the actual knockdown factor is $k = 0.45$, while for the one in Figure 4.10(b), it is $k = 0.51$, both indicated by the green dashed line.

Remarkably, in both cases, we observe qualitatively similar results, with the actual knockdown factor falling within the tail of the distribution. From a practical standpoint, this observation leads us to conclude that the minimum and threshold values of the extrapolated knockdown factor distribution are consistently smaller than the real knockdown factor, $k_{min} < k$. This observation provides a conservative estimate for the design of slender structures. Additionally, the mode of the distribution for the fit of the extrapolated data, representing the most probable knockdown factor, also tends to be smaller than the real knockdown factor data in the case of extrapolation. Again, this

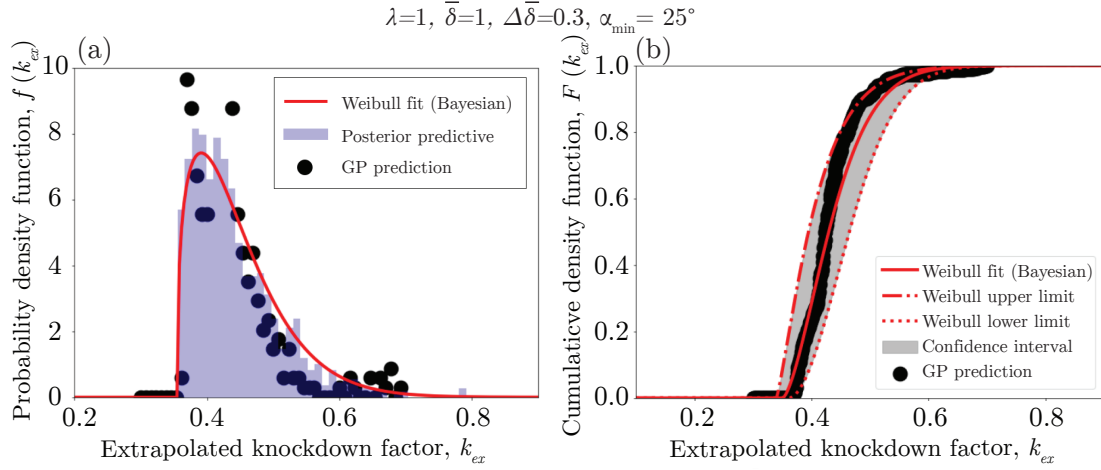


Figure 4.9: **The extrapolated knockdown factor statistics for case II.** (a) The Probability Density Function (PDF), and (b) the Cumulative Distribution Function (CDF) of the extrapolated knockdown factor for a specific single shell with the parameter set of $(\bar{\delta}, \Delta\bar{\delta}, \lambda, \alpha_{min}) = (1, 0.3, 1, 25^\circ)$ and a knockdown factor of $k = 0.45$. The symbols represent the extrapolated knockdown factor, while the solid line depicts the Weibull function fitted using the Bayesian method. The blue region is the posterior predictive, and the gray region is the region of uncertainty of parameters

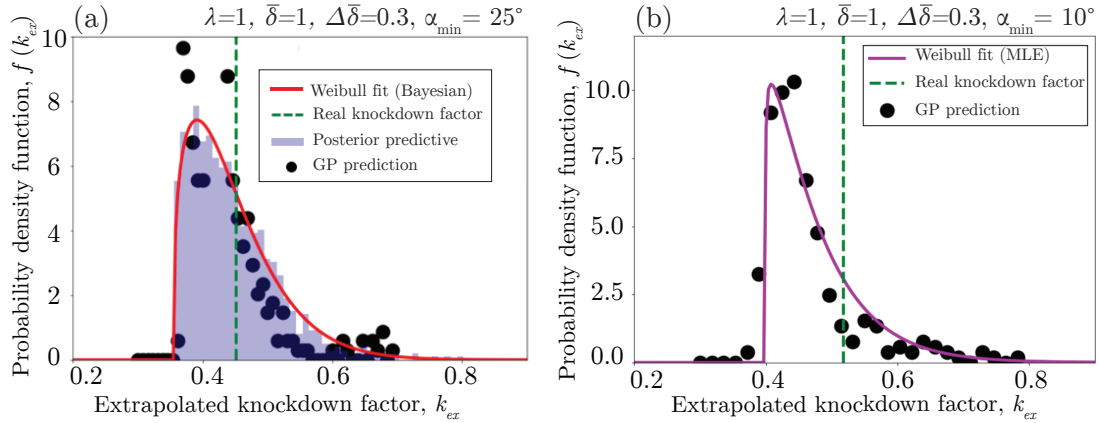


Figure 4.10: **Extrapolated knockdown factor versus the real knockdown factor.** The extrapolated knockdown factor (symbols), the fitted knockdown factor, and the real knockdown factor (green dashed line) are superposed for the variable set of (a) $(\bar{\delta}, \Delta\bar{\delta}, \lambda, \alpha_{min}) = (1.0, 0.3, 1, 25^\circ)$, and (b) $(\bar{\delta}, \Delta\bar{\delta}, \lambda, \alpha_{min}) = (1.0, 0.3, 1, 10^\circ)$ for the shell of Case II. The real knockdown factors for (a) and (b) are 0.45 and 0.51, respectively.

underscores the conservative nature of the prediction from the extrapolated data using the GPR.

To investigate the mismatch between the projected knockdown factors and the actual value and comprehend the underlying causes, we examine three distinct extrapolation

outcomes showcased in Figure 4.11. Our focus zones in on three specific indentation points delineated in Figure 4.10(a): one featuring an extrapolated value surpassing the expected value (configuration A), another below the real knockdown factor (configuration B), and the last hovering close to it (configuration C). Overlaying the maximum force-pressure curve in these three cases with their extrapolations—yielding $\kappa_{ex}=0.0.5$ (above the actual $\kappa = 0.45$), $\kappa_{ex}=0.43$ (below the actual value), and $\kappa_{ex}=0.45$ —reveals a compelling explanation tied to the indentation location (refer to the inset of Figure 4.10).

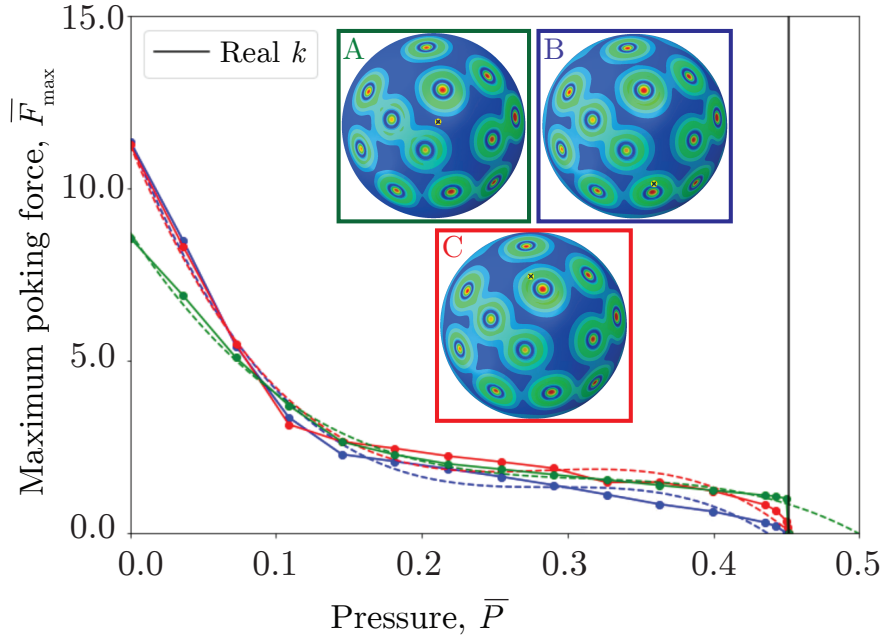


Figure 4.11: **Sensitivity of the knockdown factor extrapolation.** The maximum poking force, \bar{F}_{max} as a function of the depressurization level, \bar{P} , for indentation at a random location on the shell of Figure 4.10(a). The dashed line represents the extrapolation and the vertical solid line shows the real knockdown factor of this specific shell.

Our investigation unravels a trend: continuing the measurement of maximum force at elevated depressurization levels via FEM simulations triggers a force reduction, culminating in zero force at $\kappa = 0.45$. This finding underscores that the efficacy of extrapolation techniques hinges not only on the chosen methodology but also on the selected threshold for conducting extrapolations, as well as the specific indentation location. For instance, when indenting at a location devoid of defects (configuration A), the force-pressure trajectory proceeds without the presence of any defect trace but abruptly descends to zero at the buckling point. Consequently, the extrapolation tends to present a value surpassing the actual one, inching closer to the ideal value. Conversely, when indentation occurs near or at the defect (Configurations B and C), the extrapolation can happen at

the knockdown factor or below the value, depending upon both the extrapolation type and its threshold. The highly nonlinear interaction effect between the defects and the indentation, in addition to these intertwined factors, collectively contribute to a spectrum of predictions, resulting in variations around the factual value of the knockdown factor.

4.6 Summary and Outlook

In this chapter, we presented preliminary findings regarding the statistical analysis of buckling in spherical shells with randomly distributed imperfections. To explore the influence of different random variables (such as defect location and indentation position), we divided our study into two distinct cases, labeled *Case I* and *Case II*. In *Case I*, we sampled random variables from the imperfections (including their location and size), while in *Case II*, we focused on sampling variables from the indentation location. In both cases, we conduct indentation using 500 realizations of these random variables.

In *Case I*, we conducted a comprehensive analysis across various shell parameter sets, including defect amplitude and minimum separation angle of the defects. Additionally, we employed different extrapolation techniques, such as Gaussian Process Regression (GPR) and linear, cubic, and quintic polynomials. These various extrapolation methods each offered unique predictions for knockdown factor statistics and interpretations of the results. Our objective was to compare the extrapolated knockdown factor statistics with real data, which revealed a significant dependency on both the type of extrapolation method and the defect amplitude. Moving on to *Case II*, we focused on comparing extrapolated statistics generated through GPR with the single knockdown factor of the shell. Our analysis demonstrated that, for varying minimum defect separations, the threshold and mode parameters are smaller compared to the actual knockdown factor data.

This chapter provides the information that extrapolating the indentation curves cannot provide direct implications for the behavior of spherical shells with random imperfections when subjected to indentation. Our observations highlight the sensitivity of the extrapolation technique in predicting knockdown factors, which is crucial for practical structural design. Despite our efforts, we discovered that neither Case I nor Case II provided a sufficiently robust framework for accurately and non-destructively predicting the buckling capacity of real shell structures. This is primarily due to the significant influence of various parameters and the uncertainties introduced by the extrapolation technique.

In Chapter 7, we outline several promising avenues for future research. A possible solution involves harnessing machine learning (ML) tools to forecast buckling capacity. Initially,

we plan to employ Graph Neural Networks (GNN) to predict critical buckling conditions. This entails mapping the complete 3D geometry of an imperfect shell, including defect locations, onto graphs, in conjunction with Finite Element Method (FEM) simulations. Subsequently, ML algorithms will be employed to train a model that links imperfect shells with randomly distributed imperfections to predict knockdown factors. Another prospective area of future research entails utilizing the entire maximum force-pressure signal leading up to the point of buckling, as determined through FEM simulations. This signal will form the basis for training a model and linking it to the actual knockdown factor. It is imperative to note that acquiring complete maximum force-displacement data will be essential, as extrapolation may present a challenging aspect in ML methodologies.

We anticipate that integrating these ML prediction tools will facilitate the development of a reliable and efficient protocol for non-destructive testing of critical buckling conditions in imperfect spherical shells across diverse engineering scenarios. Furthermore, we aspire that our current and ongoing work will serve as a catalyst for further exploration in this promising research direction.

5 Snap Buckling of Bistable Magnetic Beams

In this Chapter, we investigate the mechanics of bistable, hard-magnetic, elastic beams, combining experiments, finite element modeling (FEM), and a reduced-order theory. The beam is made of a hard magneto-rheological elastomer, comprising two segments with antiparallel magnetization along the centerline, and is set into a bistable curved configuration by imposing an end-to-end shortening. Reversible snapping is possible between these two stable states. First, we experimentally characterize the critical field strength for the onset of snapping at different levels of end-to-end shortening. Second, we perform 3D FEM simulations using the Riks method to analyze high-order deformation modes during snapping. Third, we develop a reduced-order centerline-based beam theory to rationalize the observed magneto-elastic response. The theory and simulations are validated against experiments with excellent quantitative agreement. Finally, we consider the case of combined magnetic loading and poking force, examining how the applied field affects the bistability and quantifying the maximum load-bearing capacity. Our work provides a set of predictive tools for the rational design of one-dimensional, bistable, magneto-elastic structural elements.

The text and figures in this Chapter are adapted from the published manuscript in Ref. [283]: Arefeh Abbasi, Tomohiko G. Sano, Dong Yan, and Pedro M. Reis. **"Snap buckling of bistable beams under combined mechanical and magnetic loading."** Philosophical Transactions of the Royal Society A, 381(2244), 20220029 (2023).

This chapter is organized as follows. The motivation of this study and a brief literature review on the effect of defect geometry on imperfection sensitivity are presented in Section 5.1. In Section 5.2, we define the problem at hand. In Section 5.3, we present the experimental method to fabricate the h-MRE beam specimens and describe the experimental protocol for snap-buckling tests. The FEM simulations using the Riks method are detailed in Section 5.4. In Section 5.5, we derive a 1D reduced-order model

for bistable magnetic beams. Then, in Sections 5.6-5.8, we report the experimental results and their comparisons with the theoretical and FEM predictions. Finally, our main contributions and an outlook for future work are summarized and discussed in Section 5.9.

5.1 Literature Review and Motivation

Bistable structures are central in the design of many functional devices [284, 285, 286, 287, 288], whose internal energy comprises two minima, separated by a maximum, representing the barrier to a fast transition between two stable states. This snap-through instability can be exploited to cause relatively large displacements, or rotations, with low work for actuation, offering potential applications in several engineering domains, including micro-electromechanical systems [241, 289], robotics [290, 24], energy harvesting [291, 292], actuators [293, 294], origami structures [295, 296], and deployment mechanisms [297]. Bistable beams can be classified into two categories [298]: (i) pre-shaped, which do not possess residual stresses, and (ii) pre-compressed, which are stressed post-production to exhibit the first buckling-mode configuration [299]. The latter has gained much attention due to their manufacturability and versatility [300, 294, 301]. Next, we provide an overview of recent research centered on pre-compressed beams, the type central to our study.

Many past studies on pre-compressed beams have focused on their snap-through characteristics [299, 241, 242, 289, 302]: the critical load and displacement, and the travel distance from the first stable state to the new configuration. These features can be set by design parameters; *e.g.*, the beam geometry, end-to-end shortening [241], actuation loading and position [303, 304, 305, 306, 307, 308, 309, 310], and boundary conditions [311, 305, 306, 301]. A recently emerging trend in the field of bistable beams is the usage of active materials with external stimuli to control the stability during snap-through by inducing local strains from temperature gradients, swelling, or electric/magnetic fields. For example, electrostatic [312, 313], piezoelectric [314], and magnetic [315, 316] actuation have all been used to control the bistability.

More specifically, there has been a burgeoning interest in MREs (details in Chapter 1.8), with a mechanical response that can be tuned under an external magnetic field [154, 155]. Structures made out of MREs offer opportunities for fast, reversible, and remotely controlled shape-shifting behavior [27, 26, 156, 28, 151, 36, 29, 157, 158, 145]. In particular, flexible slender structures made of h-MREs are capable of significant shape changes, driven by the magnetic body torques induced by the interaction between the intrinsic magnetization of the material and the applied field [34, 151]. The magnetization profile of h-MRE structures can be designed by the local orientation of the magnetized

particles to generate complex 3D-shape transformations and optimize the shape-shifting modes for specific applications [34, 151, 205, 206, 207, 158, 38].

Owing to the elasticity-magnetism coupling, together with the underlying geometric nonlinearities, modeling the mechanical behavior of hard-magnetic soft structures is challenging, but there have been recent advances in this direction. A continuum theory has been developed [32] for the finite deformation of 3D (bulk) h-MREs through a nonlinear magneto-mechanical constitutive law. In this framework, the Helmholtz free energy density includes elastic (neo-Hookean) and magneto-elastic terms. A simulation framework by the same authors using FEM was also developed. Subsequently, a full-field 3D continuum model for h-MREs was proposed [219], also incorporating magnetic dissipation, particle-particle interactions, and the surrounding air effects. They validated their model by performing microscopic homogenization simulations applied to macroscopic boundary value problems. Based on the 3D continuum model and using dimensional reduction, theories for inextensible, hard-magnetic elastica were derived and validated against experiments under either a uniform magnetic field [158, 34] or a field with constant gradient [233]. A similar dimensional reduction approach was applied to model the 3D deformation of hard-magnetic rods under uniform and gradient magnetic fields [234, 231]. Considering the extensibility of the centerline, a geometrically exact beam model under uniform fields was developed to predict the deformation of cantilever beams [206, 207, 235], albeit finding negligible differences with the inextensible model. A similar strategy based on dimensional reduction has been employed to capture the behavior of magnetic thin plates [232], and predict the axisymmetric deformation of pressurized hard magnetic shells [104]. This 1D shell model was later generalized in a 3D configuration [247].

Even if there have been several studies on modeling the deformation of magneto-active structures, their instability and, more specifically, the snap-through phenomenon under magnetic actuation remains an ongoing research topic. Important questions to address include predicting how bistable systems switch between stable configurations under a magnetic field and evaluating the contributions of the various buckling modes and energy levels to this transition, the elastic counterparts of which have been studied extensively [239, 240, 241, 242]. Additionally, theoretical and computational tools are needed to predict the critical conditions and snap-through response of magneto-active structures. Such developments would be valuable for the predictive and rational design of bistable magneto-elastic systems.

5.2 Problem Definition: Snap Buckling of Bistable Magnetic Beams

In this Chapter, we study the snap-through of elastic bistable beams under magnetic actuation, combining theory, FEM, and experiments. First, we demonstrate that snap-buckling can be triggered in the presence of an external uniform magnetic field. We quantify how the critical field strength required for buckling depends on the imposed end-to-end shortening (setting the pre-buckled configuration), the beam geometry, and the material and magnetization properties. A centerline-based theory is developed to rationalize the trade-offs between the various loading and geometric parameters, predicting the conditions for the onset of snapping. In parallel, we adapt the finite element method (FEM) for 3D h-MREs proposed in Ref. [32] to make it amenable to Riks (arc-length) analysis. With this enhancement, it is possible to track the stable and unstable branches of the load-displacement curve during snapping. We also probe the beam's load-bearing capacity when the external loading combines a constant magnetic field and poking force.

We seek to investigate the snap buckling of a bistable magneto-active beam under magnetic loading, which may also be combined with a poking force. We consider a hard-magnetic, thin, elastic beam of length L and rectangular cross-section of width b and thickness h (Figure 5.1a). The beam is made of an isotropic and homogeneous h-MRE material that has Young's modulus, E , and Poisson's ratio, ν . The configuration of the beam is described using the Cartesian basis vectors $(\hat{\mathbf{e}}_x, \hat{\mathbf{e}}_y, \hat{\mathbf{e}}_z)$, aligned, respectively, to the length, thickness, and width directions of the originally straight beam (Figure 5.1a). The beam is parameterized using the arc length coordinate, $0 \leq s \leq L$, along its centerline.

The left and right halves of the beam are magnetized permanently in opposite directions, parallel and anti-parallel to $\hat{\mathbf{e}}_x$, respectively, with the absolute residual magnetic flux density of B^r (Figure 5.1a). Given the slenderness of the beam, the residual magnetic flux density is assumed constant across the cross-section but varies along the arc length direction as:

$$\mathbf{B}^r(s) = -B^r \operatorname{sgn}\left(s - \frac{L}{2}\right) \hat{\mathbf{e}}_x. \quad (5.1)$$

Having also compared this magnetization profile with the uniform case, $\mathbf{B}^r = -B^r \hat{\mathbf{e}}_x$, we found that the profile in Equation (5.1) is more effective in inducing snap buckling. Even if we recognize that the present choice is ad hoc, it works, and it is simple; we leave a more systematic exploration of other magnetization profiles for future work. The magnetic loading is exerted on the beam by the application of an external magnetic field, \mathbf{B}^a . Owing to the profile of the residual magnetic flux density vector, \mathbf{B}^r , with respect to

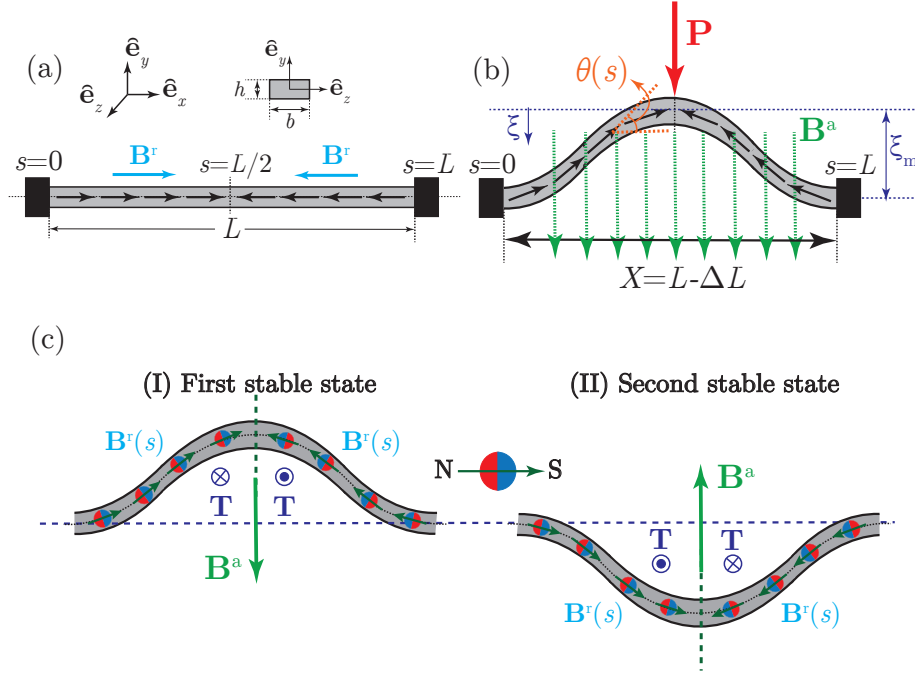


Figure 5.1: **Definition of the problem.** (a) Schematic diagram of the undeformed configuration of a naturally straight beam of initial length L , thickness h , and width b . The beam is composed of two segments with antiparallel magnetization, \mathbf{B}^r , along the centerline according to Equation (5.1). (b) The beam is first pre-loaded by imposing a dimensional end-to-end shortening, ΔL , thereby deforming to a curved, bistable configuration, and then made to snap between the two stable configurations under an applied uniform magnetic field, \mathbf{B}^a , and/or a poking force, \mathbf{P} . (c) The beam exhibits two stable equilibrium states; upon the application of an external magnetic field, the generated torques can switch the beam between configurations (I) and (II).

the direction of the applied magnetic field, \mathbf{B}^a , we will demonstrate that the proposed configuration can induce snap-through buckling of the beam.

The magnetized beam is naturally straight in its initial configuration, with the two ends clamped at $s = 0$ and $s = L$ (Figure 5.1a). To form a buckled (bistable) beam, we then impose a dimensional end-to-end shortening, ΔL , by translating the end at $s = L$ (Figure 5.1b), such that the projected length of the beam becomes $X = L - \Delta L$. The (dimensionless) end-to-end shortening is then defined as $\epsilon = \Delta L/L$. In the initial curved configuration set by ϵ with the first-buckling-mode shape, considering w as the displacement of the beam in the \hat{e}_y direction, the vertical rise of the beam's mid-span along \hat{e}_y , is denoted by ξ_m . Subsequently, the mid-span displacement $w(s = L/2) = \xi \neq \xi_m$ will vary when external loads are applied. The deformed configuration of the beam is described by the angle, $\theta(s)$, between the tangent of the centerline and \hat{e}_x (Figure 5.1b), with clamped boundaries; $\theta(0) = \theta(L) = 0$.

Once pre-loaded into a curved configuration, the beam can undergo a snap-through instability by the application of either a poking force, \mathbf{P} , or a uniform magnetic field, \mathbf{B}^a , or the combination of the two (Figure 5.1b). Specifically, under an external magnetic field, a magnetic body torque, \mathbf{T} , results from the resistance to rotation of the vector of the residual magnetic flux density, \mathbf{B}^r , which tends to align \mathbf{B}^r with the applied magnetic field, \mathbf{B}^a (Figure 5.1c). Hence, snap-buckling is primarily driven by the magnetic body torque [32]

$$\mathbf{T} = \frac{1}{\mu_0} \mathbf{B}^r \times \mathbf{B}^a, \quad (5.2)$$

where μ_0 is the vacuum permeability. Snap buckling can occur under a uniform magnetic field due to the rotation of two halves of the beam in opposite directions. Maximal torque is generated when the magnetic field and the magnetization direction are perpendicular. Thus, the magnetization profile proposed in Equation (5.1) lowers the energy barrier required to reach the second stable state. Experimentally, the simplest and closest layout to this configuration can be produced by mid-folding the beam during magnetization, yielding opposite magnetization vectors in each of its halves after unfolding. After switching from one stable state (Figure 5.2cI) to another (Figure 5.2cII), and removing the exterior magnetic field, the beam stays in the second stable position. The process can be reversed by applying a magnetic field with opposite polarity. In the case of snap buckling under simultaneous mechanical and magnetic loading, the beam is first loaded under a prescribed value of the uniform magnetic field and then indented by a concentrated load applied, $\mathbf{P} = -P\hat{\mathbf{e}}_y$ at its mid-span (Figure 5.1b).

Whereas many previous studies have addressed the critical conditions for the classic problem of snap buckling of elastic bistable beams [241, 317, 289, 318, 305, 306, 319, 316], in this study, we investigate the conditions for snapping of a bistable, hard-magnetic beam under the combined influence of the magnetic loading and a poking force.

5.3 Experimental Methods through Snap Buckling Process

This section presents the experimental methodology, first describing the fabrication of the beam specimens (Section 5.3.1) and, then, detailing the experimental apparatus (Section 5.3.4). Finally, we describe the experimental protocols, parameters, and procedures (Section 5.3.5).

5.3.1 Fabrication of the Beam Specimens

The beam specimens were fabricated using a casting protocol adopted from our recent work [233]. The main modification from our previous work is the process we use to magnetize the specimens, with two symmetric regions of antiparallel magnetization. This specific magnetization profile was chosen to facilitate snapping under magnetic loading. For completeness, we provide an overview of the full fabrication protocol.

5.3.2 Preparation of the MRE

The beam specimens were cast with an h-MRE composite, prepared by mixing NdPrFeB particles (average diameter of $5\mu\text{m}$, mass density of $\rho_{\text{mag}} = 7.61\text{ g/cm}^3$, MQFP-15-7-20065-089, Magnequench) with Vinylpolysiloxane (VPS) polymer (VPS-22, the mass density of $\rho_{\text{vps}} = 1.16\text{ g/cm}^3$, Elite Double, Zhermack). The following three steps were followed to prepare the initial liquid MRE mixture for the fabrication of beam specimens:

- **(i) Mixing:** We added the non-magnetized NdPrFeB particles into the liquid VPS-22 base, with a mass ratio of 2:1. This suspension was mixed using a centrifuge (ARE-250, Thinky Corporation) for 40 s at 2000 rpm (mixing mode) and then 20 s at 2200 rpm (defoaming mode).
- **(ii) Degassing:** We degassed the solution in a vacuum chamber (absolute pressure below 8 mbar) to eliminate air bubbles trapped during the mixing process.
- **(iii) Adding catalyst:** The same amount of VPS-22 catalyst to that of the VPS-22 base was added into the mixture obtained during step (ii). After another mixing step for 20 s at 2000 rpm (mixing mode), followed by 10 s at 2200 rpm (defoaming mode), the liquid MRE was ready to be used for the fabrication of beam specimens, which cured in 15–20 mins.

The fraction of NdPrFeB particles in the h-MRE was 50.0% in mass ($c_v = 13.2\%$ volume fraction). Upon curing the h-MRE, we measured the Young's modulus of MRE through the cantilever tests. We cut off three beams of width $3.36 \pm 0.54\text{ mm}$ from a plate of thickness $2.420 \pm 0.012\text{ mm}$ cast using the previously prepared liquid MRE. Three clamping positions were used in the tests to vary the effective length of each beam between 36 mm and 50 mm. A camera captured the shape of the cantilever beam as it deflected under self-weight at each length. The Young's modulus of the MRE was then determined by minimizing the difference between the deformed beam shape shown by Euler's elastica [2] and that measured in the experiments. The tests on the three specimens at three different lengths for each specimen resulted in the average Young's

modulus of $E = 1.16 \pm 0.04$ MPa. The density of the MRE was $\rho = 2.01 \pm 0.05$ g/cm³ according to the law of mixtures [320], and the Poisson's ratio was assumed to be $\nu \approx 0.5$ (near incompressibility).

5.3.3 Fabrication and Magnetization of Beam Specimens

As shown schematically in Figure 5.2(a), the mold used for the casting of the beam specimens was a sandwich structure consisting of (i) a front cover plate, (ii) a patterned plate, and (iii) a back cover plate. The patterned plate was punched with a narrow channel of dimensions, length, L , and width, w , using the last cutter (Figure 5.2b). The mixed solution was then injected into a sandwich mold using a syringe through the inlet (in the front plate) using a syringe (Figure 5.2c) until it filled up the channel and cast a straight beam. Throughout the fabrication process, the mold was placed vertically so that air inside the channel could be removed through the outlet. Upon curing, the beam was then peeled off from the mold.

To achieve the desired magnetization profile, we folded the beam at mid-span (Figure 5.2c) and placed it inside an impulse magnetizer (IM-K-010020-A, flux density ≈ 4.4 T, Magnet-Physik Dr. Steingroever GmbH). The magnetization of the embedded particles became permanently aligned to the direction of the field generated by the magnetizer (Figure 5.2c). Owing to this folded configuration, after unfolding each half of the beam developed antiparallel magnetization (Figure 5.2d), with the residual magnetic flux density, \mathbf{B}^r , described in Equation (5.1). The saturated particles maintain a remanent flux density of 0.90 T (reported by the supplier). Assuming a uniform dispersion of the particles in the polymer matrix, and no re-arrangements during magnetization, the composite can be considered as a homogeneous continuum solid with a uniform magnetization on each half, whose magnitude was computed as the volume average of the total magnetic moment of the individual particles, $M = 94.1$ kA/m.

After magnetization, two non-magnetic cubes of pure VPS ($8 \times 15 \times 15$ mm³) were mounted onto each of the beam extremities to set clamped boundary conditions (Figure 5.2d). Finally, the end-to-end shortening, $\epsilon = \Delta L/L$, was imposed on the originally straight beam using an acrylic sample holder, exciting in the first buckling mode, with bistability, shown schematically in Figure 5.1.

5.3.4 Experimental Apparatus

With the originally straight beam set in a curved (bistable) configuration, the experiments involved loading the specimen magnetically, mechanically, or both, using the apparatus

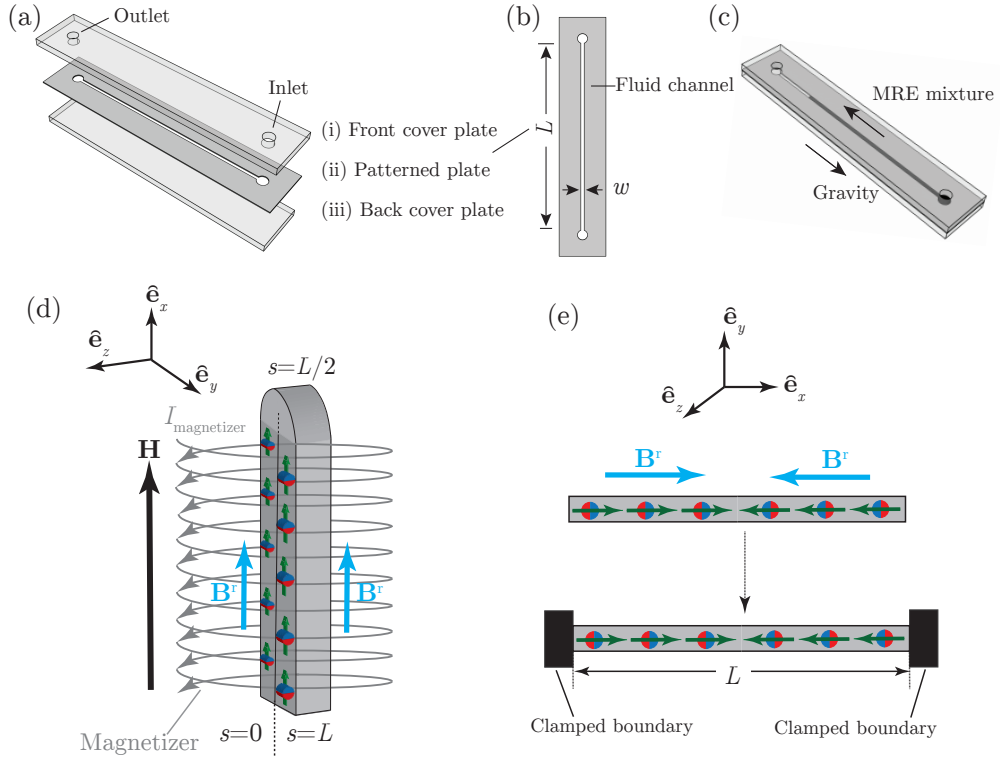


Figure 5.2: **Schematics of the fabrication and magnetization of beam specimens.** (a) The sandwich structure of the mold: (i) a front cover plate, (ii) a patterned thin sheet, and (iii) a back cover plate. (b) Dimensions of the channel laser-cut in the thin sheet to cast the beams. (c) Liquid MRE is injected from the bottom inlet to fill up the mold. (d) The beam was magnetized while folded at the mid-span, $s = L/2$, inside a pulse magnetizer, which generates a strong axial magnetic field, \mathbf{H} . (e) After unfolding, the magnetized specimen exhibited the antiparallel residual magnetic flux density of \mathbf{B}^r described in Equation (5.1). Two non-magnetic cubic blocks attached to the extremities ensured clamped boundary conditions.

shown in Figure 5.3(a). Gravitational effects were minimized by placing the beam with the deflection direction, $\hat{\mathbf{e}}_y$, perpendicular to gravity, $-g\hat{\mathbf{e}}_z$. A digital camera was set underneath the coils for imaging (Figure 5.3a6).

For the magnetic loading tests, we used a pair of identical coaxial coils (different from the impulse magnetizer mentioned above), in a Helmholtz configuration, which generated a steady axial symmetric magnetic flux density, $\mathbf{B}^a(x, y, z)$ [104]. The coils were connected in series and separated axially by a distance equal to the mean radius of each coil ($R = 59.5 \text{ mm}$). In this configuration, the current was made to flow through both coils in the same direction to generate a uniform magnetic field in their central region

(Figure 5.3a),

$$\mathbf{B}^a = B^a \hat{\mathbf{e}}_y. \quad (5.3)$$

Each coil was manufactured by winding an aluminum circular spool with an enameled copper wire (Repelec Moteurs S.A.). The dimensions of the coils were 86 mm for the inner diameter, 152 mm for the outer diameter, and 43 mm in height. A DC power supply powered the coils, providing a maximum power of 1.5 kW (EA-PSI 9200-25T, EA-Elektro-Automatik GmbH). The magnitude of the magnetic field, B^a , was varied by adjusting the current output (0-25 A) from the power supplier.

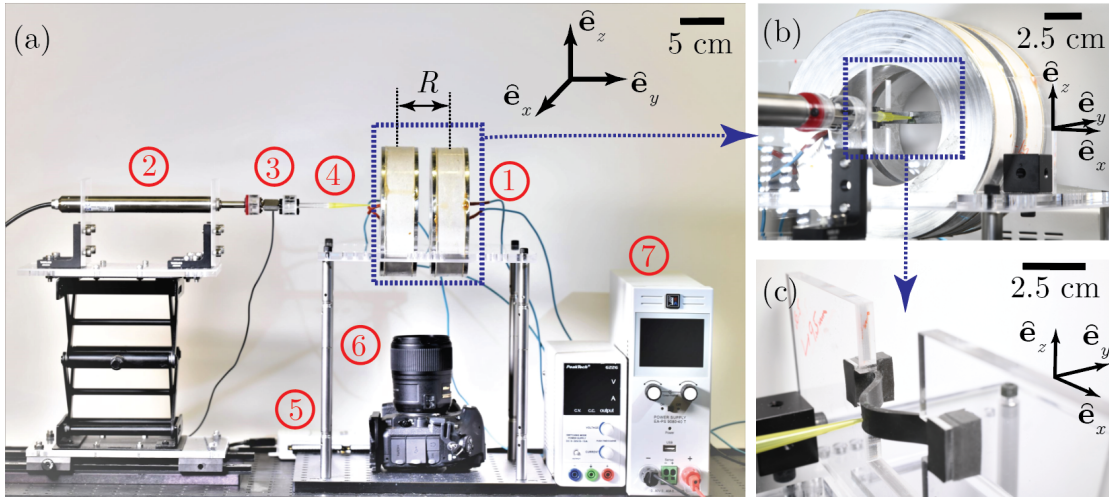


Figure 5.3: Photographs of the experimental apparatus. (a) A magnetic beam is positioned in between a set of Helmholtz coils (1) and loaded by an indenter (4). This indenter is attached to a motorized linear actuator (2), and the reaction force is monitored by a force sensor (3). The force-displacement data is acquired using a LabVIEW data acquisition card (5), and a camera (6) is used to image the beam profile. The coils are driven by the current output of a DC power supplier (7). (b) Zoomed view of the pair of Helmholtz coils. (c) Representative beam specimen positioned inside the coils.

For the mechanical load tests, we indented the beam specimen using a custom-built apparatus and measured the force-displacement curves. The poking device comprised two parts: a high-resolution linear actuator (L-220.50DG, PI, Germany) driven by a 1-axis DC motor controller (C-863 Mercury Servo Controller, PI, Germany, Figure 5.3a2) to impose the displacement, and a force sensor (LRM200, 5lb, JR S-beam load cell, Futek, CA, USA, Figure 5.3a3) to measure the reaction force at an acquisition rate of 1 kHz. The indenter was a plastic (non-magnetic) needle cap (plastic taper tip Luer Lock 20GA \times 1/4" Vita needle, MA), chosen to avoid any magnetic field distortions. This indenter assumed rigid compared to the beam specimen was attached to the tip of the linear actuator, as shown in Figure 5.3(a4). The tip of the indenter was glued to the beam at mid-span

using VPS solution, thereby restraining rotation and translation at the point of contact. This attachment enabled the acquisition of the complete load-displacement during poking, including both stable and unstable paths.

5.3.5 Experimental Protocols

To investigate the snap buckling of bistable hard magnetic beams, we performed three sets of experiments with different loading conditions (i) poking force, (ii) magnetic load, and (iii) combined mechanical and magnetic load using, respectively, the poking apparatus, the coils, or both. The corresponding results from these experiments will be presented in Sections 5.6, 5.7, and 5.8, respectively. Next, we detail the configurations of the fabricated specimens, the range of parameters explored, and the experimental protocols.

We tested three separate, but otherwise identical, beams (length $L = 60.00 \pm 0.10$ mm, width $b = 8.00 \pm 0.04$ mm, and thickness $h = 2.00 \pm 0.06$ mm) to examine the experimental reproducibility and uncertainty. Throughout the experiments, the slenderness ratio was kept constant, $k = L/h = 30$. The end-to-end shortening was varied in the range $0 \leq \epsilon = \Delta L/L \leq 0.6$. Next, we describe each of the experimental tests under the different loading conditions.

(i) *Snap-through under poking force*: In order to capture the stable and unstable portions of the loading path, poking force, in the absence of a magnetic field, was applied along $\hat{\mathbf{e}}_y$, with the indenter glued to the beam at mid-span ($s = L/2$), and at the constant velocity of 0.02 mm/s to ensured quasi-static conditions. For each level of ϵ , the mid-span displacement varied in the range $0 \leq \xi \leq 2\xi_m$.

(ii) *Snap-through under magnetic loading*: In a second set of experiments, the beam specimen was placed within the region of a uniform magnetic field generated by the Helmholtz coils [233]. Two different protocols were followed to measure (ii.a) the critical magnetic field for snapping, B_{cr}^a , and (ii.b) the full load-displacement response, $B^a(\xi)$, as detailed next. (ii.a) To measure B_{cr}^a , we gradually increased the magnitude of the applied magnetic flux density (by increasing the current, I , in the coils; steps of 0.05 A and 10 s) until snap-through occurred. Assuming the snap-through phenomena is nearly instantaneous, and the waiting time between each two steps is larger than the viscous relaxation time [22, 321], we neglected dynamic effects and measured the critical snapping magnetic field at the snapping step. (ii.b) By adopting the above experimental procedure, we characterized the full bistable response, capturing the stable and unstable paths. First, prior to magnetic loading, the poking was performed under displacement-control conditions at the speed of 0.02 mm/s (along $\hat{\mathbf{e}}_y$). The indenter was then stopped at each

step of 0.2 mm, and the magnetic field was increased from zero, in the $-\hat{\mathbf{e}}_y$ direction, to balance the poking force, until a zero-force was measured by the load cell. Assuming the equilibrium of the specimen and the quasi-static experimental conditions, the measured applied magnetic field required for zero force was ensured to lie on the equilibrium curve, $B^a(\xi)$.

(iii) *Snap-through under combined mechanical and magnetic load:* In a third set of experiments, we investigated the effect of magnetic loading on the snap-through response of the beam under simultaneous poking force. In each experimental run, the beam was first loaded under a steady magnetic field and then indented following the same protocol as in (i). We repeated the experiment at eleven different levels of magnetic field strength, in the range $-4.5 \text{ mT} \leq \mathbf{B}^a \leq 53.4 \text{ mT}$, in steps of 6 mT, ensuring that $B_{\text{cr}}^a \leq B^a$. From the measured curves of poking force versus displacement, $P(\xi)$, we characterized the stability of the beam for these combined loading conditions.

5.4 Numerical Simulations Using FEM

In parallel with the experiments, we performed 3D FEM simulations using an existing user-defined element [32] in the commercial software package ABAQUS/Standard 6.14. As detailed in Section 5.4.1, we have modified this user element to enable Riks analysis on hard-magnetic structures. The Riks algorithm allows for the solution of the equilibrium equation of a structure by prescribing the arc length of its loading path so as to track both stable and unstable equilibrium states. We use this technique to study the snapping behavior of our magnetic beam subjected to a uniform magnetic field. The simulation procedure is, then, detailed in Section 5.4.2.

5.4.1 User Element for Riks Analysis

Our FEM approach is based on an existing continuum theory of ideal hard-magnetic soft materials [32] with a permanent magnetization independent of external magnetic fields. As a result, the \mathbf{F} -based 3D continuum theory proposed by Zhao *et al.* [32] will be the primary framework. In this theory, the effect of an applied magnetic field on a magnetized, deformable body is considered through a potential (density) as a function of the deformation gradient (\mathbf{F}), the external field flux density (\mathbf{B}^a) and the magnetization of the material ($\mu_0^{-1}\mathbf{B}^r$):

$$\hat{U}^m = \mu_0^{-1} \mathbf{F} \mathbf{B}^r \cdot \mathbf{B}^a. \quad (5.4)$$

This magnetic potential is added to the total energy of the system. Under this description, distributed magnetic torques imposed by the applied field result in an asymmetric part of the Cauchy stress. The field produced by the magnetic body and the induced self-interactions are neglected.

As we described in detail in Section 1.5.1 of Chapter 1, the two 3D continuum theories, \mathbf{R} -based and \mathbf{F} -based, yield consistent results in scenarios where stretching can be neglected. This condition aligns with the specific problem addressed in this section: the snap buckling of bistable magneto-active beams. While immediate stretching following snapping may be observed, it has been a minor concern due to the absence of a dynamic analysis. However, a recent study by Stewart *et al.* [244] has directed the focus towards an examination of the dynamics and viscoelastic properties associated with the snapping of magnetic bistable beams. It is important to highlight that a recent study on hard-magnetic plates [232] proposed a rotation-based (\mathbf{R} -based) magnetic potential by replacing the deformation gradient, \mathbf{F} [232], with the rotation tensor. This work was, in turn, motivated by an equally recent but prior demonstration of the stretch-independence of the magnetization of bulk h-MREs [219]. Indeed, the subsequent experiments in Ref. [232] showed that the \mathbf{R} -based model is necessary for plates subjected to non-negligible stretching deformation under an applied field parallel to the initial magnetization.

These latest findings bring into question why, in the present Chapter, we decided not to use the \mathbf{R} -based magnetic potential, choosing the \mathbf{F} -based model description instead. Given the assumption of an inextensible centerline made when developing the beam model, together with the orthogonality between the field and the initial magnetization of the configuration considered in this work, the potential in Equation (5.4) is expected to be appropriate for the current problem, as also justified by the excellent agreement between our theory, FEM, and experiments. Also, the Kirchhoff assumptions adopted in the 1D model correct the error from using the potential in Equation (5.4), as pointed out in Ref. [232], given that inextensibility together with the fact that normals do not change length, thereby removing any stretching-induced effects from the \mathbf{F} -based. As a final practical justification, the \mathbf{F} -based model is significantly simpler mathematically than the \mathbf{R} -based one and, therefore, it is preferable in cases where both yield the same results. Still, future efforts should be dedicated to developing \mathbf{R} -based beam and rod models for more general cases where stretching of the centerline may be important.

This \mathbf{F} -based theory has been previously implemented in the commercial FEM software package ABAQUS through a user-defined 8-node solid element [32] while assuming that the elastic behavior of the material is assumed to be neo-Hookean. To capture the unstable equilibrium path of the snapping beam under magnetic actuation, we had to adapt this previously developed user element to make it compatible with the Riks

analysis in ABAQUS. In the Riks analysis, the magnitude of external loads, which is usually prescribed during a simulation, is considered as an unknown and solved simultaneously with displacements from equilibrium. Alternatively, the ‘arc length’ of the static equilibrium path of a system in the load-displacement space is imposed to control the progress of the simulation. In order to implement the Riks analysis in the presence of a uniform magnetic field, we define its magnitude as a loading parameter using the keyword `*DLOAD` in ABAQUS rather than a field variable in the previous work [32]. As such, the field strength can be taken into account as an unknown in the solution domain. This modification on the original user element allows us to simulate both the stable and unstable response of the magnetic beam during snapping, the results of which will be presented in Section 5.7.

5.4.2 Simulation Procedure

We modeled an initially straight clamped-clamped beam as a 3D solid body. Similarly to the experiments (see Figure 5.2), the beam was composed of two halves with antiparallel magnetization vectors. The length and width of the beam were the same as the experimental specimens. The beam was discretized by the user-defined elements introduced in Section 5.4.1, using a structured mesh with 16, 4, and 120 elements seeded, respectively, in the width, thickness, and length directions. The mesh was deemed to be sufficiently fine through a convergence study. The material of the beam was assumed to be incompressible with a shear modulus $G = 0.39$ MPa (paralleling the experiments; see Section 5.3) and a bulk modulus 100 times larger than G . Given the large deflection of the beam during snapping, geometric nonlinearities were taken into account throughout the simulations. We highlight that the simulations employed the material properties characterized in the experiments (see Section 5.3) with no fitting parameters.

For the simulation protocol, we first imposed an end-to-end shortening, ϵ , to buckle the beam and reach the preset bistable state. We then studied the snapping of the beam in three loading cases: (i) poking force, (ii) pure magnetic load, and (iii) combined mechanical and magnetic loads. Each simulation run involved the following two sequential steps:

Step (a) – Buckling: First, ϵ was imposed to the straight beam, causing it to buckle into a curved configuration characterized by the classic sinusoidal Euler mode for a clamped-clamped beam. In this step, we obtained several post-buckled beam configurations by varying the end-to-end shortening $0 \leq \epsilon \leq 0.6$; the same range as in the experiments. To trigger buckling, geometric imperfections with the shape of the first eigenmode and a maximum amplitude of $0.1h$ were injected into the initial straight configuration.

Step (b) – Snapping: For the loading case (i) – (snap-through under poking force) we indented the beam at mid-span by prescribing the displacement, ξ , which was increased step-by-step until the beam reached the other stable configuration. The poking force, P , was computed as a reaction force from equilibrium. From the load-displacement curve, $P(\xi)$, we identified the critical load for snapping at different end-to-end shortenings (Section 5.6). For loading case (ii) – (snap-through under pure magnetic load), we applied a magnetic field on the entire beam with a *Riks* step in order to capture the full loading path during snapping. In the search for the equilibrium state, the strength of the applied field is set as an unknown, which, along with the displacements of the beam, was solved under a prescribed arc length increment of the loading path. We computed the critical field strength, the equilibrium path with stable and unstable branches, and the change of the strain energy during snapping. For the loading case (iii) – (snap-through under combined mechanical and magnetic loads), a magnetic field with a given flux density lower than the critical value to trigger the snapping was first applied on the beam. Under this constant field, in the next step, we indented the beam by applying a displacement load at the mid-span to make it snap to the other stable configuration. We computed the poking force-displacement curve, $P(\xi)$, for different values of the magnetic field. Then, we extracted the critical poking force under the effect of magnetic load at different end-to-end shortenings.

5.5 A reduced-Order Model for the Snapping of Magnetic Beams

We proceed by presenting a centerline-based theory for the problem defined in Section 5.2 (see Figure 5.1b). This theory was developed by Tomohiko G. Sano in collaboration with the author of this thesis. We consider a thin, inextensible, hard-magnetic, and doubly-clamped beam, under Kirchhoff assumptions [322]; *i.e.*, normals to the beam centerline remain normal and unstretched during deformation. Building upon recent developments for hard-magnetic beams [205, 34, 33, 233, 234], we develop a 1D beam model through dimensional reduction [2], taking the 3D Helmholtz free energy for ideal hard-magnetic soft materials from Ref. [32] as a starting point, on top of other classic ingredients. The elastic (bending) energy of the beam is described by Euler’s elastica [2], and the work of poking force was addressed in Ref. [318]. Using the principle of virtual work (PVW), we will show that the derived ordinary differential equation (ODE) for the bending angle, $\theta(s)$, is equivalent to a clamped-clamped elastica under a *redefined* poking force applied at mid-span ($s = L/2$). Hence, the effect of the applied magnetic load on the snap-through buckling is qualitatively identical to that of a poking force at mid-span.

Following classic beam kinematics, we define $0 \leq s \leq L$ to be the arc length of the (inextensible) centerline of a beam, located at $\mathbf{r}(s) = (x(s), y(s))$. We consider a beam clamped both at $s = 0$ and $s = L$, with $\mathbf{r}(0) = (0, 0)$ and $\mathbf{r}(L) = (X, 0)$. The bending angle, $\theta(s)$, is measured from $\hat{\mathbf{e}}_x$, such that the centerline tangent is $\hat{\mathbf{t}} \equiv \mathbf{r}' = (\cos \theta(s), \sin \theta(s))$, where $(\cdot)' = d(\cdot)/ds$ and the corresponding boundary conditions are $\theta(0) = \theta(L) = 0$. The relation between $\theta(s)$ and $\mathbf{r}(s)$ is obtained by integrating $\hat{\mathbf{t}}$:

$$\mathbf{r}(L) = (x(L), y(L)) = \left(\int_0^L \cos \theta(s) ds, \int_0^L \sin \theta(s) ds \right) = (X, 0), \quad (5.5)$$

which acts as a constraint.

Next, we consider first the external virtual work (EVW) and then the internal virtual work (IVW), before invoking the PVW to derive the governing equation for $\theta(s)$.

A reaction force (F_x, F_y) is applied at $s = 0$ and the poking force, $\mathbf{P} = (0, -P)$, at $s = L/2$. Defining $\mathbf{N}(s) = (N_x, N_y)$ as the internal force on the cross section at s , force balance yields

$$\mathbf{N}(s) = (N_x, N_y) = \left(-F_x, -F_y + P\Theta\left(s - \frac{L}{2}\right) \right), \quad (5.6)$$

with the Heaviside step function $\Theta(x) = \{\text{sgn}(x) + 1\}/2$ representing the discontinuity (of magnitude P) in the N_y component at $s = L/2$, due to the applied poking force. The EVW is then computed as

$$\text{EVW} = \int_0^L \left\{ -F_x \cos \theta + \left(-F_y + P\Theta\left(s - \frac{L}{2}\right) \right) \sin \theta \right\} ds. \quad (5.7)$$

The Helmholtz free energy proposed in Ref. [32] for hard-magnetic materials can be decomposed into an elastic part, associated with mechanical deformation, and a magnetic part, arising from the interactions between remanent magnetization and the external field. Based on this decomposition, the total energy of a hard-magnetic beam is the sum of the elastic energy, U^{el} , and the magnetic potential, U^{m} . Assuming a Hookean constitutive

law,

$$U^{\text{el}} = \int_0^L \frac{EI}{2} \theta'^2 ds, \quad (5.8)$$

where EI is the flexural rigidity of the beam of Young's modulus, E , and a second moment of inertia, $I = h^3b/12$.

According to Zhao *et al.* [32], we now make use of the magnetic potential density \hat{U}^{m} in Equation (5.4). Focusing on the geometry of our problem (see Figure 5.1b), we set the applied field to $\mathbf{B}^{\text{a}} = B^{\text{a}}\hat{\mathbf{e}}_y$, and the magnetization vector $\mathbf{M} = \mathbf{B}^{\text{r}}/\mu_0$ exhibiting the specific profile of Equation (5.1); in the deformed configuration, \mathbf{M} is parallel to the tangent vector $\hat{\mathbf{t}}$ for $0 \leq s \leq L/2$ (or anti-parallel for $L/2 \leq s \leq L$). The deformation gradient $\overset{\circ}{\mathbf{F}}$ for thin beams has been derived in [34, 33, 233] as:

$$\overset{\circ}{\mathbf{F}} = \begin{pmatrix} \cos \theta & -\sin \theta \\ \sin \theta & \cos \theta \end{pmatrix}. \quad (5.9)$$

Hence, the magnetic potential for our beam is

$$U^{\text{m}} = - \int_0^L hb \overset{\circ}{\mathbf{F}} \mathbf{M} \cdot \mathbf{B}^{\text{a}} ds = \frac{hbB^{\text{r}}B^{\text{a}}}{\mu_0} \int_0^L \text{sgn} \left(s - \frac{L}{2} \right) \sin \theta(s) ds. \quad (5.10)$$

Invoking the PVW, mechanical equilibrium is assured when the EVW is balanced by the IVW = $\delta U^{\text{el}} + \delta U^{\text{m}}$ yielding

$$EI\theta'' + F_x \sin \theta - \tilde{F}_y \cos \theta = -\frac{1}{2} \left(P - \frac{2hbB^{\text{a}}B^{\text{r}}}{\mu_0} \right) \text{sgn} \left(s - \frac{L}{2} \right) \cos \theta, \quad (5.11)$$

with $\tilde{F}_y \equiv F_y - (P/2)$ and boundary conditions $\theta(0) = \theta(L) = 0$. The two unknowns, F_x and F_y , are the Lagrange multipliers associated with the clamped boundary [2] and can be determined through Equation (5.5). Note that the term in Equation (5.11) involving $2hbB^{\text{a}}B^{\text{r}}/\mu_0$ can be interpreted as a second poking force, in addition to P . Therefore, we can define an effective poking force under the combined mechanical and magnetic loading:

$$P^* \equiv P - \frac{2hbB^{\text{a}}B^{\text{r}}}{\mu_0}. \quad (5.12)$$

Hence, the analysis of snap buckling of the hard-magnetic beam under a uniform magnetic field is simplified by treating the developed magnetic torques as an effective poking force acting at mid-span, noting that these two scenarios share similar boundary conditions. A similar approach was followed in Ref. [33] for the deformation of the tip of an elastica under magnetic loading. Now, we use Equation (5.12) to rewrite Equation (5.11) as

$$EI\theta'' + F_x \sin \theta - \tilde{F}_y \cos \theta = -\frac{P^*}{2} \operatorname{sgn} \left(s - \frac{L}{2} \right) \cos \theta. \quad (5.13)$$

This new ODE is equivalent to a clamped-clamped elastica under poking force P^* applied at $s = L/2$ [241, 318]. Under appropriate boundary conditions, $\theta(0) = \theta(L) = 0$, and the constraint in Equation (5.5), Equation (5.13) defines a boundary value problem that can be solved numerically to predict the classic N-shape snap-through response of a doubly clamped beam [241], but now under combined magnetic loading and poking force. We do so using the solver `bvp5c` in `MATLAB`. Note that all the relevant parameters in this model are characterized experimentally, and there are no fitting parameters. In Sections 5.6–5.8, we will compare the predictions from this magnetic beam model against FEM simulations (detailed in Section 5.4) and experiments (detailed in Section 5.3).

5.5.1 Linearized Theory with $\epsilon \ll 1$ and $|\theta| \ll 1$

For configurations of the bistable beam with small values of end-to-end shortening ($\epsilon \ll 1$), the deformations are small ($|\theta| \ll 1$) at the onset of snapping. In this limit, with $\sin \theta \simeq \theta$ and $\cos \theta \simeq 1 - (\theta^2/2)$, Equation (5.13) simplifies to

$$\theta'' + \bar{F}_x \theta - \bar{\tilde{F}}_y = -\frac{\bar{P}^*}{2} \operatorname{sgn} \left(\bar{s} - \frac{1}{2} \right), \quad (5.14)$$

where we have used the following dimensionless variables: $\bar{s} = s/L$, $\bar{F}_x \equiv F_x L^2/EI$, $\bar{\tilde{F}}_y \equiv \tilde{F}_y L^2/EI$, and $\bar{P}^* \equiv PL^2/EI - (2hbB^a/B^r L^2 EI \mu_0)$. Expanding Equation (5.5) with respect to $|\theta| \ll 1$, the corresponding boundary conditions are

$$\int_0^1 \frac{\theta^2(\bar{s})}{2} d\bar{s} = \epsilon, \quad \text{and} \quad \int_0^1 \theta(\bar{s}) d\bar{s} = 0. \quad (5.15)$$

Employing the method of variation of parameters, the solution of Equation (5.14) is

$$\theta(\bar{s}) = \frac{\bar{\tilde{F}}_y}{\kappa^2} \varphi_1(\bar{s}) + \frac{\bar{P}^*}{\kappa^2} \varphi_2(\bar{s}), \quad (5.16)$$

where we have introduced the wave number $\kappa \equiv \sqrt{\bar{F}_x}$ and the functions φ_1 and φ_2 , which are, respectively, symmetric and asymmetric functions with respect to $s = 1/2$, are

defined next. The two unknown parameters, $\kappa = \sqrt{\bar{F}_x}$ and $\bar{\bar{F}}_y$, are determined using the boundary conditions in Equation (5.15) to arrive at

$$\kappa = 9, \quad \text{and} \quad 2\epsilon = \left(\frac{\bar{\bar{F}}_y}{\kappa^2}\right)^2 c_1 + \left(\frac{\bar{P}^*}{\kappa^2}\right)^2 c_2, \quad (5.17)$$

where $c_1 \equiv \int_0^1 (\varphi_1(\bar{s}))^2 d\bar{s}$ and $c_2 \equiv \int_0^1 (\varphi_2(\bar{s}))^2 d\bar{s}$ are two positive numerical constants as follows next.

Here, we discuss a few details of the solution of Equation (5.14) to arrive at Equation (5.16). The functions, φ_1 and φ_2 , were introduced to solve the linear inhomogeneous ODE with the method of variation of parameters (Section 5.8) and are written as

$$\varphi_1(s) \equiv 1 - \frac{\cos\left(\kappa\left(s - \frac{1}{2}\right)\right)}{\cos(\kappa/2)}, \quad (5.18)$$

and

$$\varphi_2(s) \equiv \frac{1}{2} \left[\operatorname{sgn}\left(s - \frac{1}{2}\right) \left\{ \cos\left(\kappa\left(s - \frac{1}{2}\right)\right) - 1 \right\} + \tan\left(\frac{\kappa}{4}\right) \sin\left(\kappa\left(s - \frac{1}{2}\right)\right) \right], \quad (5.19)$$

where we have used $\tan(\kappa/4) = (1 - \cos(\kappa/2))/\sin(\kappa/2)$. Note that $\varphi_1(s)$ and $\varphi_2(s)$ are, respectively, symmetric and asymmetric function with respect to $s = 1/2$. The two numerical constants in Equation (5.11), c_1 and c_2 , are computed as

$$\begin{aligned} c_1 &\equiv \int_0^1 \varphi_1^2(s) ds = \frac{2\kappa - 3\sin\kappa + \kappa\cos\kappa}{\kappa + \kappa\cos\kappa}, \\ c_2 &\equiv \int_0^1 \varphi_2^2(s) ds = \frac{1}{8} \left(2 + \frac{1}{\cos^2(\kappa/4)} - \frac{12}{\kappa} \tan\left(\frac{\kappa}{4}\right) \right). \end{aligned} \quad (5.20)$$

Using Eqs. (5.11), we can now discuss the critical condition for snap buckling. Given that c_1 , c_2 and ϵ are all positive, $\bar{\bar{F}}_y$ ceases to exist, and the beam snaps, when $(\bar{P}^*/\kappa^2)^2 c_2 \geq 2\epsilon$. Hence, the critical condition for the snap transition is

$$|\bar{P}_{\text{cr}}^*| = \kappa^2 \sqrt{\frac{2}{c_2}} \epsilon = C_0 \sqrt{\epsilon}, \quad (5.21)$$

with the positive constant $C_0 \simeq 130$ [318, 241]. The dimensional version of Equation (5.21), through Equation (5.12), is

$$\left| \frac{bhB^a B^r L^2}{\mu_0 EI} - \frac{P_{\text{cr}} L^2}{2EI} \right| = C_0 \sqrt{\epsilon}. \quad (5.22)$$

For reasons that will become clearer in Section 5.8, we recognize the critical load at which snapping occurs as the maximum load that the beam can support before snap-through, $P_{\text{cr}} = P_{\text{max}}$, and we rewrite Equation (5.22) back in dimensionless form

$$\bar{P}_{\text{max}} = 2(\bar{B}^a + C_0\sqrt{\epsilon}), \quad (5.23)$$

where $\bar{P}_{\text{max}} = P_{\text{max}}L^2/(EI)$ and the applied magnetic field was nondimensionalized as:

$$\bar{B}^a = \frac{bhL^2B_{\text{cr}}^aB^r}{EI\mu_0}, \quad (5.24)$$

characterizing the relative importance of the magnetic load and beam-bending effects. According to Equation (5.23), under the assumption of $\epsilon \ll 1$ and when $\bar{B}^a > 0$ (*i.e.*, \mathbf{B}^a and \mathbf{P} are in the same direction), the maximum poking force that the clamped-clamped magnetic beam can support before snapping is expected to depend linearly on the applied magnetic field \bar{B}^a , with a slope 2 and an offset $2C_0\sqrt{\epsilon}$ set by the end-to-end shortening. This prediction will be tested against experiments and FEM in Figure 5.8 (Section 5.8). In the absence of a magnetic field ($\bar{B}^a = 0$), we recover the standard result, the critical poking force for purely elastic snapping [318], with the scaling $\bar{P}_{\text{max}} \sim \sqrt{\epsilon}$, which will be tested against experiments and FEM in Figure 5.4 (in Section 5.6).

5.6 Snapping under Poking Force

Next, we focus on the classic bistable response when the beam subjected *only* to a poking force ($B^a = 0$) at mid-span. Even if well-established [318], this case serves as a pre-validation of the framework against the experiment before introducing magnetic effects in Section 5.7. In Figure 5.4(a), we present the results for the dimensionless poking force, $\bar{P} = PL^2/EI$, versus the dimensionless mid-span displacement, $\bar{\xi} = \xi/L$. The initial buckled configuration was generated with an end-to-end shortening of $\epsilon = 0.014$. Then, $\bar{\xi}$ was gradually increased while measuring the poking force. The resulting $\bar{P}(\bar{\xi})$ force-displacement curve exhibits the classic N-shape representative of bistable mechanisms [241]. Points A and E are the two stable stages. The maximum normalized poking force, \bar{P}_{max} , occurs at point B. The unstable branch, with negative stiffness, occurs between points B and D, and plot C is the unstable equilibrium state. Excellent agreement is found between experiments, FEM, and the solution of Equation (5.13).

In Figure 5.4(b), we plot \bar{P}_{max} , as a function of ϵ , finding a sub-linear dependence. For small values of the end-to-end shortening ($\epsilon \lesssim 0.1$), the observed scaling $\bar{P}_{\text{max}} \sim \sqrt{\epsilon}$ (dot-dashed line in Figure 5.4b) is consistent with Equation (5.23) when $B^a = 0$, obtained from the linearized theory for small deformations. For $\epsilon \gtrsim 0.1$, the linearized theory no

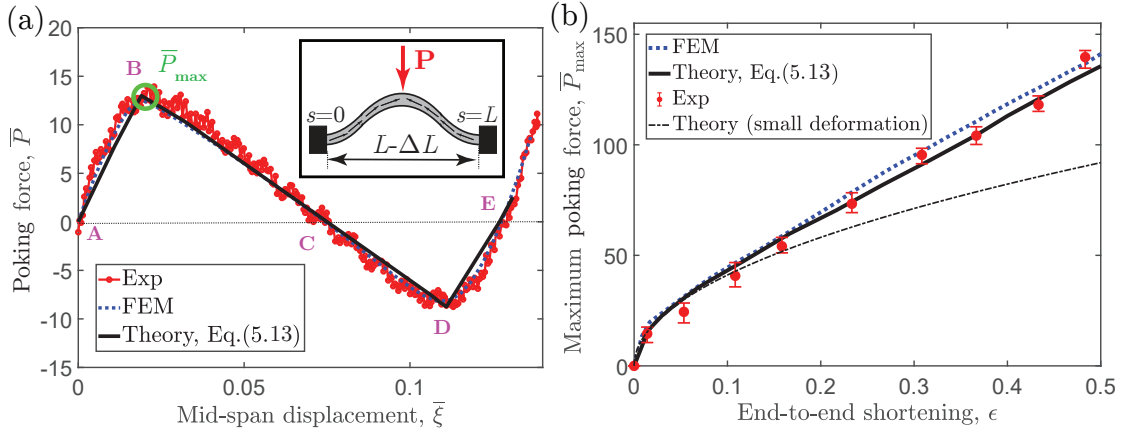


Figure 5.4: Snap buckling under poking force ($B^a = 0$). (a) Normalized poking force, \bar{P} , versus the mid-span displacement, $\bar{\xi}$, for the end-to-end shortening of $\epsilon = 0.014$. The maximum of the curve is defined as \bar{P}_{max} . (b) Normalized maximum poking force, \bar{P}_{max} , versus ϵ . The error bars correspond to the standard deviations of the experimental measurements for three identical specimens. (Inset) Schematic diagram of the loading configuration.

longer works, but the nonlinear theory of Equation (5.13) with $B^a = 0$ (solid line in Figure 5.4b) is in excellent agreement with the FEM and experiments, through the full range of explored ϵ . This agreement between the experiments, FEM, and the reduced-order beam model, even if within a classic setting, serves as a first step in validation.

5.7 Snapping under Magnetic Loading

We proceed by investigating the buckling of the bistable beam under an external magnetic field, this time with no poking force ($P = 0$), seeking to quantify how the critical magnetic field strength, B_{cr}^a , required for switching between the two stable states, depends on the end-to-end shortening, ϵ .

In Figure 5.5, making use of the dimensionless magneto-elastic parameter defined in Equation (5.24), we plot $\bar{B}_{cr}^a(\epsilon)$ curves obtained as predicted from FEM simulations, the 1D theory and the experiments. Naturally, increasingly deformed pre-configurations (increasing ϵ) require a higher value of B_{cr}^a for snapping. We find a good agreement between the FEM, the experimental data, and the solution of Equation (5.13). For small deformations ($\epsilon \lesssim 0.1$), the data follows the scaling $B_{cr}^a \sim \sqrt{\epsilon}$, consistently with Equation (5.23). For higher values of ϵ , the overall $B_{cr}^a(\epsilon)$ curves computed from FEM are captured by the solutions of Equation (5.13) with $P = 0$ reasonably well.

The Riks procedure in FEM (cf. Section 5.4.2) enables us to capture the unstable equilib-

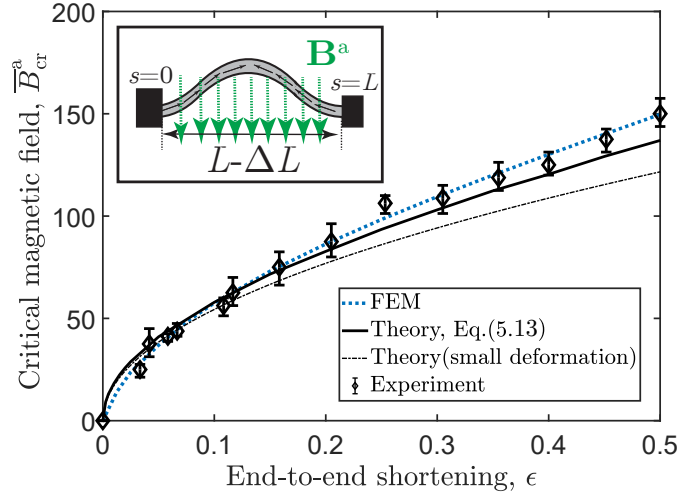


Figure 5.5: Snap buckling under magnetic actuation. Normalized critical strength of the uniform magnetic field required for beam snapping, \bar{B}_{cr}^a , as a function of end-to-end shortening, ϵ . The results were obtained from the nonlinear elastic theory in Equation (5.13) (solid line), small-deformations theory (dashed line), FEM (dotted line), and experiments (data points with error bars). The error bars of the experimental data correspond to the standard deviation of the measurements on three identical specimens. (Inset) Schematic of the bistable beam under magnetic loading.

rium path during snapping under actuation by a magnetic field between the first to the second stable configuration. In Figure 5.6(a), we plot the normalized magnetic load, \bar{B}^a , as a function of the normalized mid-span displacement of the beam, $\bar{\xi}$, for two representative values of the end-to-end shortening, $\epsilon = \{0.008, 0.014\}$. The FEM-computed results (dotted lines) are in quantitative agreement with the experimental data. For $\epsilon = 0.008$, the $\bar{B}^a(\bar{\xi})$ curve is non-monotonic, first increasing to a maximum, then decreasing to become negative until a minimum is reached, to then increase again. The case with $\epsilon = 0.014$ is more complex; the Riks method captures a force-displacement equilibrium path with a complex transition between the two stable states, with winding branches and multiple equilibrium solutions for the same $\bar{\xi}$. However, note that some of the winding-branch segments computed from FEM are not practically relevant; only the solutions with the lowest energy barrier are experimentally observable.

To gain further insight into the energetics of the load-displacement path discussed above, focusing on $\epsilon = 0.014$, we now use FEM to compute the total strain energy, U , as a function of $\bar{\xi}$ during the snapping process; the results are plotted in Figure 5.6(b). The points A, B, ..., and G labeled in the plot correspond to the computed configurations shown in Figure 5.6(c). During the transition path between the stable states A and G, U increases with $\bar{\xi}$ from a minimum (A) to a local maximum (C1) and decreases to another minimum (G). Hence, the corresponding energy barrier, ΔU_s , between this minimum

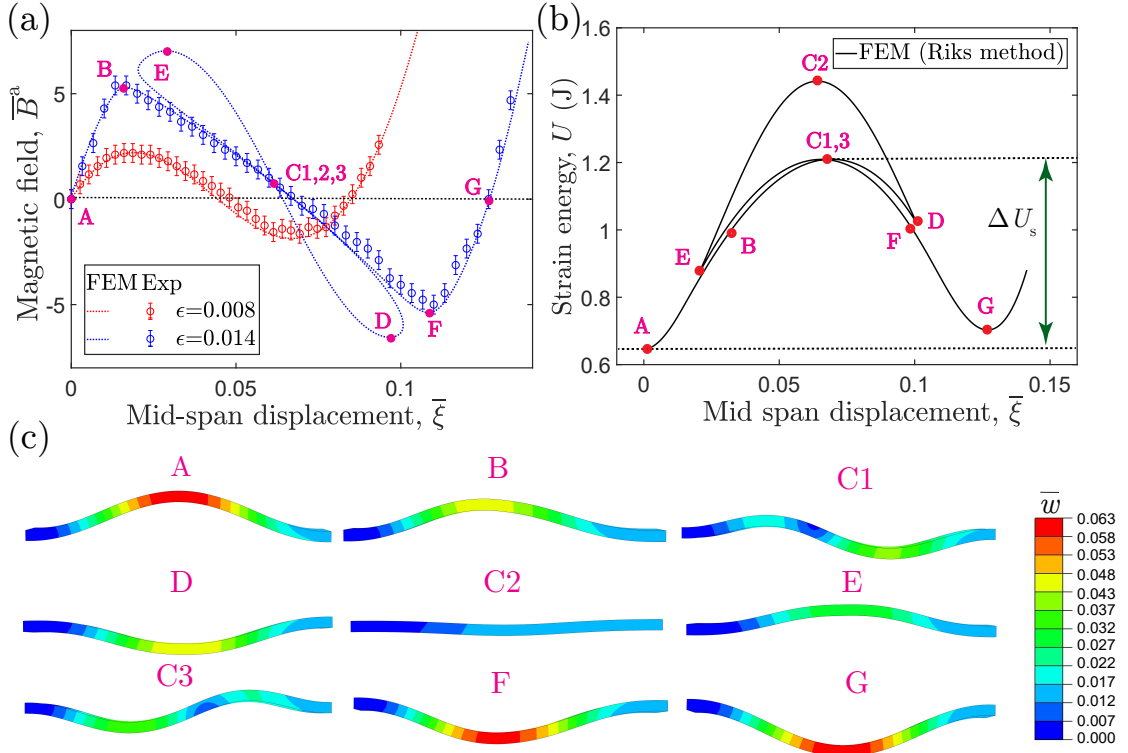


Figure 5.6: Bifurcation diagram for the snap-through of the bistable beam under magnetic actuation. (a) Normalized magnetic field, \bar{B}^a , versus the normalized mid-span displacement, $\bar{\xi}$: FEM simulations and experiments for two beams with $\epsilon = \{0.008, 0.014\}$. (b) FEM-computed strain energy, U , versus $\bar{\xi}$, for $\epsilon = 0.014$. The beam must overcome the energy barrier, ΔU_s (vertical double-arrow), to switch between the two stable states. (c) Representative FEM-computed configurations of the beam along the equilibrium solution path corresponding to the same points in the plots of panels (a) and (b). The color bar represents the normalized displacement of the beam \bar{w} .

and the local maximum must be overcome for snap-through. According to the principle of minimum potential energy, the lowest-energy path is the one observed in practice. Consequently, the higher energy configurations shown in Figure 5.6(c) for points D, C2, E, and C3 are not observed experimentally. Indeed, the experimentally observed path in Figure 5.6(a) is an excellent match with the latest-energy path of Figure 5.6(b), passing through the points A-B-C1-F-G.

5.8 Snapping under Combined Poking Force and Magnetic Loading

Finally, we turn to the combined case of simultaneously loading the bistable beams with mechanical poking and a magnetic field, each of which was tackled individually in the

previous Sections 5.6 and 5.7. We seek to quantify how magnetic loading modifies the load-bearing capacity of the bistable beam under poking force and characterize the critical conditions for snap buckling.

In Figure 5.7(a), we present the normalized poking force, \bar{P} , versus the beam's mid-span displacement, $\bar{\xi}$, at different levels of the uniform magnetic field, $\bar{B}^a \hat{\mathbf{e}}_y$, varied systematically in the range $-3.9 \leq \bar{B}^a \leq 46.9$ (see legend of the plot). We focus on the representative case with $\epsilon = 0.014$. To track the full equilibrium path, including its unstable portions, the indenter was glued to the beam at mid-span, as described in Section 5.3.5. At each value of \bar{B}^a , the signal-to-noise ratio of the measurements was enhanced by repeating three independent, but otherwise identical, experimental runs; their average is reported as the $\bar{P}(\bar{\xi})$ curves of Figure 5.7(a). Throughout, excellent agreement is found between experiments (solid lines) and the FEM (dotted lines).

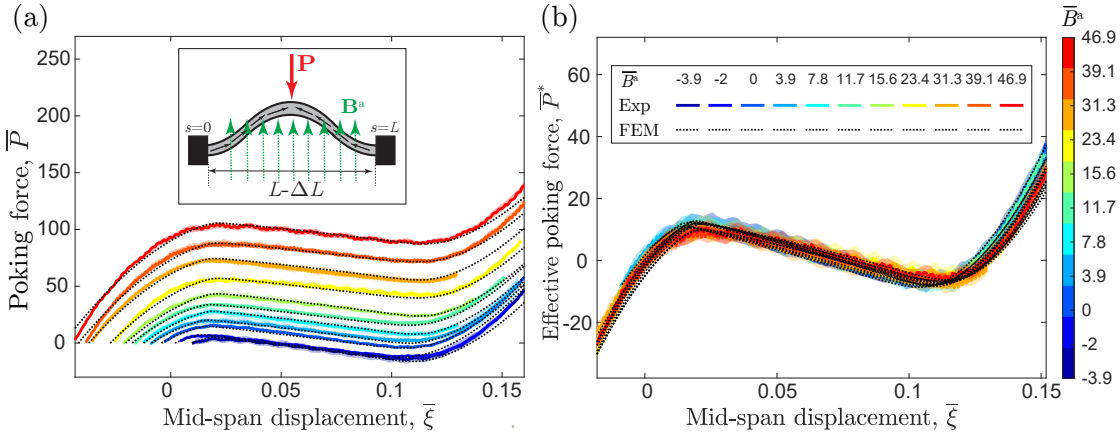


Figure 5.7: Load-displacement curves for the indented magnetic beam (with $\epsilon = 0.014$) in the presence of a uniform magnetic field. (a) The normalized poking force, \bar{P} , is plotted versus the normalized mid-span displacement, $\bar{\xi}$, at various levels of prescribed field strength, \bar{B}^a . (Inset) Schematic diagram of the bistable beam under combined magnetic and mechanical loading. (b) The normalized effective poking force, \bar{P}^* , as a function of the normalized mid-span displacement, $\bar{\xi}$, for the curves in (a), collapsing on a single curve. The experiments and FEM simulations are represented by solid lines and dotted lines, respectively. The shaded region of each curve represents the standard deviation of three identical measurements.

Under an external magnetic field, the poking force-displacement response of the hard-magnetic beam can be modified significantly with respect to the purely mechanical case ($\bar{B}^a = 0$ and results in Section 5.6). When the applied magnetic field is in the opposite direction of the poking force ($\bar{B}^a > 0$), the generated magnetic torques oppose the direction of the poking-induced beam rotation. Consequently, as the field strength is increased, the beam stiffens and becomes more resistant to snap buckling (the local maximum of \bar{P} increases). By contrast, when the magnetic load is applied in the same

direction to the poking ($\bar{B}^a < 0$), snap-through occurs at lower poking forces as the magnetic torques are in the same direction of the poking-induced rotation.

In Figure 5.7(b), to compare the elastic and magnetic loads, we plot the normalized effective poking force, \bar{P}^* , as a function of the normalized mid-span displacement, $\bar{\xi}$, for the corresponding curves in Figure 5.7(a). We find that the experimental and simulations data collapse into a single curve, indicating that the effect of magnetic load on the snap buckling of magnetic beams can be interpreted as a second poking force in addition to the mechanical load (see Section 5.5). Treatment of the effect of magnetic torques developed under a uniform magnetic field as an equivalent poking force acting at mid-span simplifies the calculation of the critical snap buckling load for a hard-magnetic beam under combined elastic and magnetic loading.

In Figure 5.8(a), we quantify the dimensionless relation between the maximum (critical) poking force, \bar{P}_{\max} , and the magnitude of the prescribed magnetic field \bar{B}^a , for four values of the end-to-end shortenings, $\epsilon = \{0.014, 0.053, 0.108, 0.158\}$. The experimental force-displacement signals were smoothed with a 50-point moving average filter to facilitate the extraction of \bar{P}_{\max} , the largest load that the beam can sustain prior to snapping. Again, an excellent agreement is observed between the experiments (data points), FEM (dotted lines), and the solution of Equation (5.13) (solid lines). We find the robust linear scaling $\bar{P}_{\max} \sim \bar{B}^a$, with a slope of 2. Increasing ϵ results in an increase of the offset at $\bar{B}^a = 0$ of the linear curves, as dictated by the purely mechanical poking case in Figure 5.4. Hence, increasing the end-to-end shortening results in a larger poking force required for snapping under a particular level of field strength, set by the offset of the linear behavior. The experimental and FEM data are in remarkable agreement with Equation (5.23), indicating that the largest value of end-to-end shortening explored in these experiments (and FEM simulations) still lies in the regime of validity, with small deformations ($|\theta| \ll 1$), of the linearized theory developed in Section 5.5.1.

In Figure 5.8b, making use of Equation (5.23), we now replot all the data in Figure 5.8a but with $\bar{P}_{\max} - 2C_0\sqrt{\epsilon}$ as a function of $2\bar{B}^a$. The purpose is to remove the effect of end-to-end shortening and characterize the magneto-elastic effect of the snapping beam. Again as predicted by the linearized theory, we find a striking collapse of all the data into a master curve of unit slope, passing through the origin. This collapse indicates that Equation (5.23), based on a linearized theory and combining the dimensionless groups of magnetic ($bhB^aB^rL^2/\mu_0EI$) and mechanical (PL^2/EI) load, serves as a high-fidelity description of the magneto-elastic behavior of our hard-magnetic bistable beams, with different end-to-end shortenings ($\epsilon \lesssim 0.1$), in the limit of small deformations ($\theta \ll 1$).

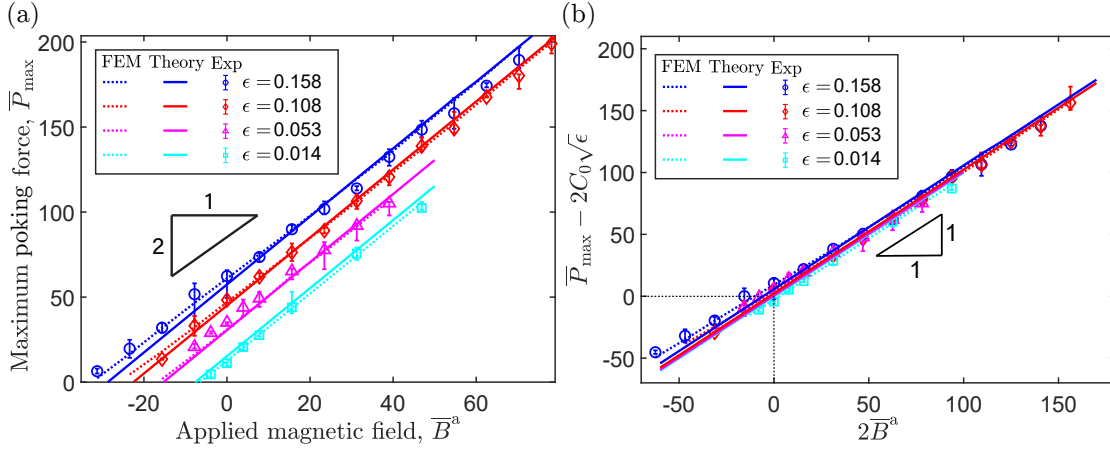


Figure 5.8: Critical poking force for snap-transition under magnetic actuation. (a) Normalized maximum poking force, \bar{P}_{\max} , versus the prescribed applied magnetic field, \bar{B}^a , at different end-to-end shortenings ($\epsilon = \{0.158, 0.108, 0.053, 0.014\}$): experiments (data points), theoretical predictions from Equation (5.13) (solid lines), and FEM (dotted lines). The line slope of 2, is consist of Equation (5.23). (b) Master curve for the experimental results, FEM simulations, and the theoretical predictions for the data in (a). The quantity, $\bar{P}_{\max} - 2C_0\sqrt{\epsilon}$ in Equation (5.23), is plotted as a function of $2\bar{B}^a$, yielding a collapse of all the data. The term $-2C_0\sqrt{\epsilon}$ removes the offset due to the end-to-end shortening.

5.9 Summary and Outlook

In this Chapter, we investigated the snapping behavior of bistable magneto-active beams under combined mechanical and magnetic actuation, incorporating experiments, FEM, and a reduced-order model. Considering a pre-compressed bistable beam with different levels of end-to-end shortening, we characterized the load-displacement response, the critical poking force, the field strength at the onset of snapping, and the effect of magnetic loading on snap buckling under poking force. The Riks method was employed in the 3D FEM simulations to analyze the snap transition. We also developed a beam theory to rationalize the observed magneto-elastic response. Precision experiments validated the theory and the FEM simulations.

More specifically, we studied the snap buckling of the beam under three different loading cases: (i) poking force only, (ii) magnetic field only, and (iii) combined magnetic and mechanical loading. Case (i), even if classic, served for pre-validation. In case (ii), we triggered snap buckling under a magnetic field for various end-to-end shortenings by designing the magnetization profile of the beam. For small deformations, the critical magnetic field increased with the square root of the end-to-end shortening. The Riks method was used to explore the equilibrium transition path, finding that increasing

the end-to-end shortening complicates the instability response, but the experimentally observable solution corresponds to the lowest energy level. Finally, in case (iii), we examined how magnetic loading affects the poking-induced snapping of the bistable beam. The critical poking force for snapping can be adjusted by the magnitude and direction of the magnetic field. Our magnetic beam model captures these results. In the small deformation limit, the critical poking force at the onset of snapping is linearly proportional to the applied magnetic field with a slope and offset that can be predicted. In this limit, a master curve is uncovered that collapses the experimental and FEM-computed data.

Our study provides insight into the nonlinear magneto-elastic coupling of bistable beams, which could be extended in several directions for future work. Fundamentally, the dynamics of multi-stable structures integrated with soft active materials remain relatively unexplored and deserve further attention. From a practical viewpoint, optimization and inverse design is an exciting direction: compact actuators could be designed using bistable beams while minimizing the total energy consumption during actuation. The magnetization profile chosen in Equation (5.1) may come across as *ad hoc*, even if we found that it is more effective in inducing snap buckling compared to uniform magnetization. Future work should explore other magnetization designs more systematically. Owing to the complex relationship between the design parameters and snap-through characteristics, modeling the deformation of bistable beams under other boundary conditions should be considered.

In closing, we believe that our comprehensive framework is a step forward toward the predictive design of bistable magneto-elastic beams. We hope that the snapping behavior and the stiffness-tuning capability of these components will be exploited for a variety of future applications, including actuators, robotics, MEMS, programmable devices, metamaterials, and energy harvesting devices.

6 Snapping of Bistable Magnetic Shells for Braille Reader Design

In this Chapter, a design concept is introduced for the building block, a *dot*, of programmable braille readers utilizing bistable shell buckling, magnetic actuation, and pneumatic loading. The design process is guided by Finite Element simulations, which are initially validated through precision experiments conducted on a scaled-up, single-shell model system. Then, the simulations are leveraged to systematically explore the design space, adhering to the standardized geometric and physical specifications of braille systems. The findings demonstrate the feasibility of selecting design parameters that satisfy both geometric requirements and blocking forces under moderate magnetic fields facilitated by pneumatic loading to switch between the two stable states. The advantages of the proposed design include the reversible bistability of the actuators and fast state-switching via a transient magnetic field. While the study is focused on experimentally validated numerical simulations, several manufacturing challenges that need to be resolved for future physical implementations are identified.

The text and figures in this Chapter are adapted from the unpublished manuscript submitted to the Journal of Advanced Materials Technologies in Ref. [323], which has just been accepted: Arefeh Abbasi, Tian Chen, Bastien F. G. Aymon, and Pedro M. Reis. **“Leveraging the snap buckling of bistable magnetic shells to design a refreshable braille dot.”** arXiv preprint arXiv:2307.10933 (2023).

The structure of this Chapter is as follows. The motivation of this study and a brief literature review on the state-of-the-art of refreshable braille displays and braille actuators are presented in Section 6.1. In Section 6.2, we define the braille reader design concept. We explain the experimental protocol for the experiments in the scaled-up braille system in Section 6.3. Then, we detail the finite element modeling (FEM) simulation performed to acquire the result in Section 6.4. In Section 6.5, we validate the FEM simulations against experiments in the scale-up systems. Following that, in Section 6.6, we provide the

design of braille dots at the real scale. In Section 6.7, we propose a design improvement of the braille dots using a pneumatic system. In Section 6.8, we discuss some potential challenges and limitations expected to be encountered during the real-scale fabrication. A solenoid coil design for the braille dots at a real scale was proposed in Section 6.9. Furthermore, in Section 6.10, we summarize our findings and provide a perspective for future work.

6.1 Literature Review and Motivation

Shallow shells, with their unique structural characteristics, can exhibit bistable behavior, meaning they possess two stable states [324]. With this ability to maintain stable states until triggered otherwise, bistable shells have found numerous engineering applications for switching [325, 24], locking [294], or actuation mechanisms [326, 327]. The fast transition between these two stable states, also known as *snap-through*, can be triggered in different ways, for example, through magnetic loading [246, 245], mechanical loading [283], or fluid flow [328].

Serving as a motivation for our study, we will consider the bistable behavior of hard-magnetic shells in the context of the potential application to braille displays [329]. Combining the inherent bistability of shells made of h-MREs with magnetic and mechanical actuation, our vision is that braille displays could be made refreshable through controlled state changes. While static embossed paper is the traditional medium for braille, modern assisting devices, such as refreshable braille displays (RBDs), enable dynamic reading and writing [329, 330]. RBDs provide access to written content using arrays of morphable physical dots, whose configuration adjusts dynamically to represent different sequences of braille symbols in accordance with international braille standards [331, 332, 333, 329].

In recent years, technological advancements have stimulated the development of RBD devices driven by a variety of actuation mechanisms, including piezoelectrics [334, 335, 336, 337], electromagnetics [338, 339, 340], or thermopneumatics [341]. These devices often use advanced materials such as electroactive polymers [342, 343, 344, 345], shape memory alloys [346, 347, 348], or dielectric elastomers [349, 350]. Piezoelectric actuators have been favored for commercial RBDs due to their fast refresh rates, low power consumption, and reliability, albeit at a relatively high cost [329, 334, 335]. Electromagnetic linear actuators tend to have a low ratio between output force and operating velocity, requiring complex packaging and a considerable force to hold a raised dot [69, 351]. RBD devices utilizing shape memory alloys require intricate heating and cooling processes, posing practical implementation challenges [336, 348, 346]. Dielectric elastomers have been gaining traction for lightweight tactile displays, offering high actuator density and a wide range

of motion, with performance comparable to previous technologies, but in a more compact form [349, 350]. However, their required large driving voltages can be impractical for some applications. Most technological solutions for braille readers cannot offer sufficiently high-quality performance, especially regarding the balance between fast shape-changing dynamics and low power consumption [352]. Additionally, the mainstream adoption of advanced tactile displays is hindered by the lack of compact, large-area actuator arrays that can stimulate multiple sensory receptors while adhering to high user-safety standards. Existing solutions tend to be costly and require complex manufacturing processes. Despite ongoing efforts [353], designing RBD devices that are simple, compact, low-cost, large-scale, user-friendly, and reliable remains a formidable challenge.

Here, we propose a novel design concept for braille dots, the building block of braille readers. Our design leverages the buckling and bistability of thin shells fabricated from hard magneto-rheological elastomers (h-MREs). Inspired by the popular ‘*pop it*’ toy [354], these shells can be reversibly set in a convex or concave state (Figure 6.1a). Each of these shells (dots) can then be arranged in a 3×2 matrix and programmed, on-demand, to form a braille symbol. The dots have independent writing and reading phases under magnetic and mechanical loading, respectively. During writing, a transient external magnetic field can induce snap-through buckling to transition the shell between its two stable states: from ON (bump) to OFF (dimple) or vice versa. For reading, shells in the ON state must sustain a blocking force in reaction to the finger indentation without snapping to the OFF state. Throughout, our mechanics-based design process is centered on Finite Element Method (FEM) simulations. We first validate these simulations against precision experiments on a scaled-up (centimeter-scale) physical model of a braille dot. Then, we study dots at their actual scale, ensuring adherence to standard braille specifications [333], with a special focus on their geometry, elastic response, and actuation. Although the primary driver of actuation is an external magnetic field, it is supplemented with a transient pneumatic loading to aid in widening the design space. Our numerical exploration of the design parameters allows us to identify the regions that meet the various design constraints, making a step toward a new class of programmable braille displays.

6.2 Problem Definition: Braille Reader Design Concept

Worldwide, 285 million people experience visual impairments, including 39 million living with blindness [355]. These impairments present challenges in navigating and interacting with the world, influencing various aspects of daily life, such as access to printed or digital content. Braille code, a tactile writing system, facilitates these interactions, mapping

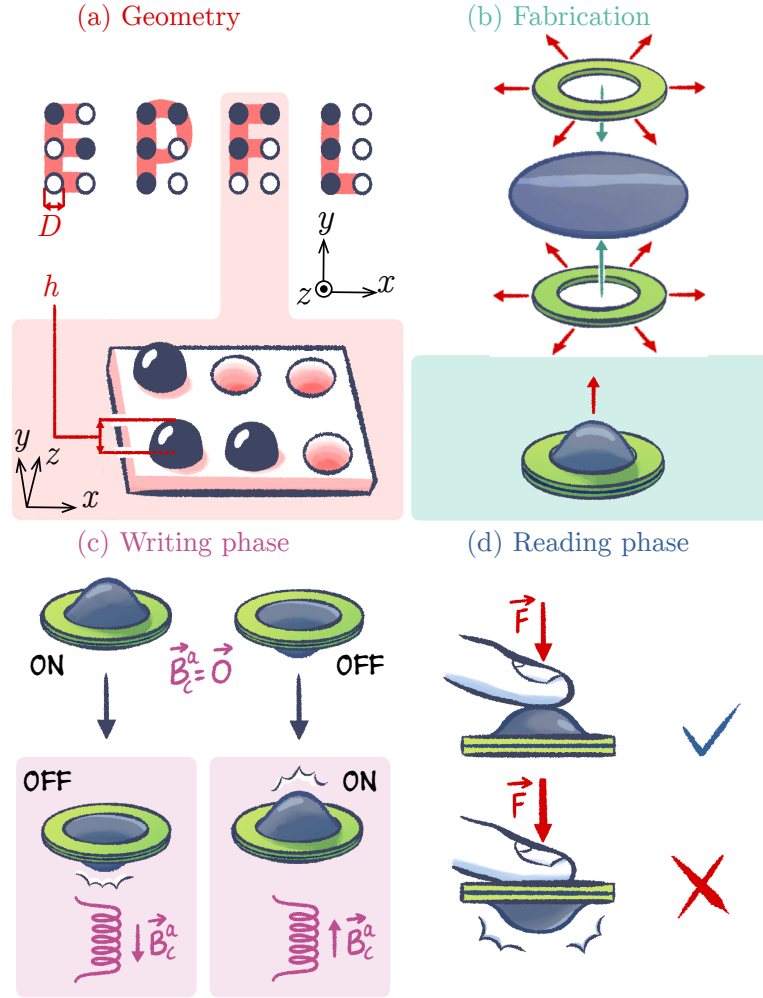


Figure 6.1: **Design, fabrication, and operation of a bistable Braille dot.** (a) *Geometry*: A word is formed by assembling a series of braille cells, each comprising 3×2 dots. “EPFL” is shown as an example. (b) *Fabrication*: A bistable shell is fabricated by sandwiching a circular h-MRE plate between two radially pre-stretched boundary annuli. This pre-stretch is then released to buckle the plate into a shell. (c) *Writing phase*: an external magnetic field, \mathbf{B}^a , sets each shell in one of its two stable states, either ON (bump) or OFF (dimple). (d) *Reading phase*: an index finger applies an indentation force, F on each dot.

symbols (*e.g.*, letters, numbers, and punctuation) into arrays of cells, each comprising a 3×2 matrix of dots. Each dot can independently be raised or flat, and words are then formed by assembling a series of such cells. Braille users typically read by tracing their fingertips across rows of these cells, whose dimensions are optimized to allow the index finger pad to cover the entire cell and discern each dot.

The specifications for braille cells and dots are standardized by the World Blind Union [333],

and the relevant parameters are required to lie within the following ranges: $\ell_d \in [2.3, 2.5]$ mm for the dot-to-dot spacing, $\ell_c \in [6, 7]$ mm for the distance between two distinct cells, and $\ell_l \in [10, 11]$ mm for the distance between two lines of words. Furthermore, each raised dot must feature a quasi-hemispherical cap with base diameter $D \in [1.4, 1.6]$ mm and height $h \in [0.4, 0.9]$ mm [356]. Finally, to sustain the normal indentation force applied by the index finger during reading, each dot must be able to withstand a minimum blocking force of $F > 50$ mN [333].

Our objective is to design a programmable braille dot that adheres to the aforementioned braille specification. We consider a bistable shell clamped at its base (Figure 6.1a, b). The analysis is segmented into two phases: “*Writing*” (Figure 6.1c) and “*Reading*” (Figure 6.1d). For writing, the ON-OFF switching is done via magnetic actuation. Concurrently with this phase, we temporarily depressurize the shell to lower the energy barrier required for buckling. By contrast, during the reading phase, the shell is pressurized to increase its rigidity. We seek to identify the key design variables and protocols required for the fabrication and operation of our system. Next, we describe the geometric considerations and the two operational phases.

The geometry of our model braille-dot (Figure 6.1a) comprises a shell of diameter $D=1.45$ mm and height $h=0.48$ mm, in accordance with braille standards. This shell is fabricated by the buckling of a radially compressed circular plate (thickness t) made of h-MRE [232] when the in-plane pre-stretch, λ , of two boundary annuli is released (Figure 6.1b), as detailed in Section 6.3. One first goal of the design is to select appropriate values of t and λ that, upon buckling of the plate, yield a shell with the target value of h , satisfying braille requirements.

For the writing phase (Figure 6.1c), we will characterize the snap buckling of the shells under loading by a uniform magnetic field, \mathbf{B}_c^a , to switch between their two stable states. We assume that each dot, which would eventually form the 3×2 cell, can be actuated independently. For the present study, we restrict our focus to the operation of a single dot. The goal of this design phase is to identify the critical magnetic field, B_c^a , required for snapping under the limitation set by upper-bound of the linear regime of the \mathbf{B} - \mathbf{H} hysteresis curve for the h-MRE material [32] (additional details are provided in Section 6.3). Subsequently, we aim to determine the corresponding geometric and fabrication parameters, t , and λ , that yield the desired snap-buckling characteristics.

For the reading phase (Figure 6.1d), the braille dots must be designed such that the user can tactilely discern the dots without altering their state. The challenge lies in ensuring that a dot in the ON state can sustain the indentation force mentioned above ($F \geq 50$ mN) without snapping to the OFF state, thereby inadvertently erasing the

braille pattern. This design phase targets the determination of optimal geometric and fabrication parameters for the dot, specifically its thickness t and pre-stretch λ , to meet this requirement.

The constraints associated with the fabrication protocol and the ensuing dot geometry, coupled with the requirements for the reading and writing phases, underscore the intricacies involved with designing our braille dot. We aim to identify the feasible design parameter space of the system (specifically, t and λ) that satisfies the constraints on h , F , and B_c^a . This design exploration will be performed solely using FEM simulations, which will be initially validated against experiments in a scaled-up system.

6.3 Experiments with the Scaled-up System

In this Section, we detail the fabrication protocol, geometric characterization, and testing (writing and reading phases) for the experiments on our scaled-up model system. The data obtained from these experiments serve to validate the FEM simulations in Section 6.5.

Fabrication: We have followed an established experimental procedure to prepare the h-MRE material used to fabricate our specimens [233, 283, 232]. First, we mixed Vinylpolysiloxane (VPS-32, Elite Double, Zhermack) with NdPrFeB particles (MQFP-15-7-20065-089, Magnequench), with volume fraction $c_v=18.7\%$. Then, an automated film applicator (ZAA 2300, Zehntner) spread the VPS-NdPrFeB mixture into a thin film, which, upon curing, yielded a thin elastic plate. By modulating the gap height of the film applicator, we fabricated 10 plates with thicknesses in the range $t=[0.180, 1.080]$ mm, measured using an optical microscope (VHX-950F, Keyence). Post-curing, we cut eight circular plates (Figure 6.2a) with diameters in the range $D_p=[25, 60]$ mm, in increments of 5 mm.

Magnetization: Various steps are involved in the magnetization of the magnetic plate, as illustrated in the schematic diagrams in Figure 6.2(a)-(d). The cut circular h-MRE plate of diameter D_p from the fabricated plate (Figure 6.2a) does not possess any magnetic properties. Therefore, to magnetize the plate, we folded it symmetrically into a semicircle along x -axis (Figure 6.2b) and then into a quarter-circle along y -axis (Figure 6.2c). Third, we placed the folded quarter-circle plate in the impulse magnetizer (IM-K-010020-A, flux density ≈ 4.4 T, Magnet-Physik Dr. Steingroever GmbH) at an angle of $\alpha = 45^\circ$ with respect to the positive y axis, aligned with the edge of the quarter circle (Figure 6.2d). The magnetizer generates a magnetic field of strength \mathbf{B} , inducing a permanent magnetic dipole in the NdPrFeB particles. Assuming a uniform particle dispersion within the polymer matrix, the magnetization magnitude computed from the volume average of

the total magnetic moment of the individual particles is $M = \mu_0^{-1} B^r = 134.4 \text{ kAm}^{-1}$, where B^r is the residual magnetic flux density and μ_0 the relative permeability of air. After unfolding, the magnetization pattern of the circular plate is four-fold symmetric (Figure 6.2e). In each of the plate's four quarters, $k = \{1, 2, 3, 4\}$, the magnetization is expected to be $\mathbf{M} \approx M \hat{\mathbf{n}}_k$, pointing along the unit vector:

$$\hat{\mathbf{n}}_k = -\cos(\alpha + (k-1)\pi/2) \hat{\mathbf{e}}_x - \sin(\alpha + (k-1)\pi/2) \hat{\mathbf{e}}_y, \quad (6.1)$$

where $\alpha = 45^\circ$ is the orientation of the folded plate in the magnetizer (see Figure 6.2d).

Empirically, we found that our chosen magnetization profile is more effective in inducing snap buckling than simpler patterns (*e.g.*, uniform magnetization parallel or perpendicular to the plate mid-surface). Our choice aligns with the anti-symmetric profile selected in recent snap-buckling studies of h-MRE beams [283, 243]. We also acknowledge that our choice of the magnetization profile is motivated by fabrication simplicity. However, we recognize the need to conduct a more systematic exploration of other profiles [357] in future research.

Having fabricated and magnetized the plates, we proceeded to produce shallow shells through radial compression of the said plates. First, we fabricated two VPS-32 annuli to act as the clamped boundary of the shell, each with inner and outer diameters of $D = D_p/2$ and $2D = D_p$, respectively (Figure 6.2f). Next, we stretched these annuli using two rigid cylinders of diameter $D + \lambda D$ (Figure 6.2g), resulting in the radial pre-stretch of $\lambda = \Delta D/D$ (Figure 6.2g). The plate was then sandwiched and bonded between the annuli using the same VPS material. After curing, the cylinders were removed, thereby relaxing the pre-stretched. Consequently, the plate buckled out-of-plane due to the in-plane (x - y) radial compression, yielding a shell, the braille dot (Figure 6.2h). The height, h , of this newly formed shell was measured using an optical profilometer (VR-3200, Keyence Corporation).

For the *writing experiments* (Figure 6.2i), the sample designated for testing was placed within the region of the uniform magnetic field produced by a set of Helmholtz coils [104, 233, 283]. The sample was clamped between two acrylic (rigid) plates. Gravitational effects were minimized by orienting the shell's snapping direction (along $\pm \hat{\mathbf{z}}$) perpendicularly to gravity ($-\mathbf{g}\hat{\mathbf{y}}$). We determined the critical magnetic field B_c^a needed for snap-buckling, thereby writing the desired state of the braille dot. To do so, we gradually increased the magnetic flux density by increasing the current I in the coils, in increments of 0.05 A over 20 s intervals, until snap-through occurred [283].

For the *reading experiments*, we used the apparatus shown in Figure 6.2(j). The specimen

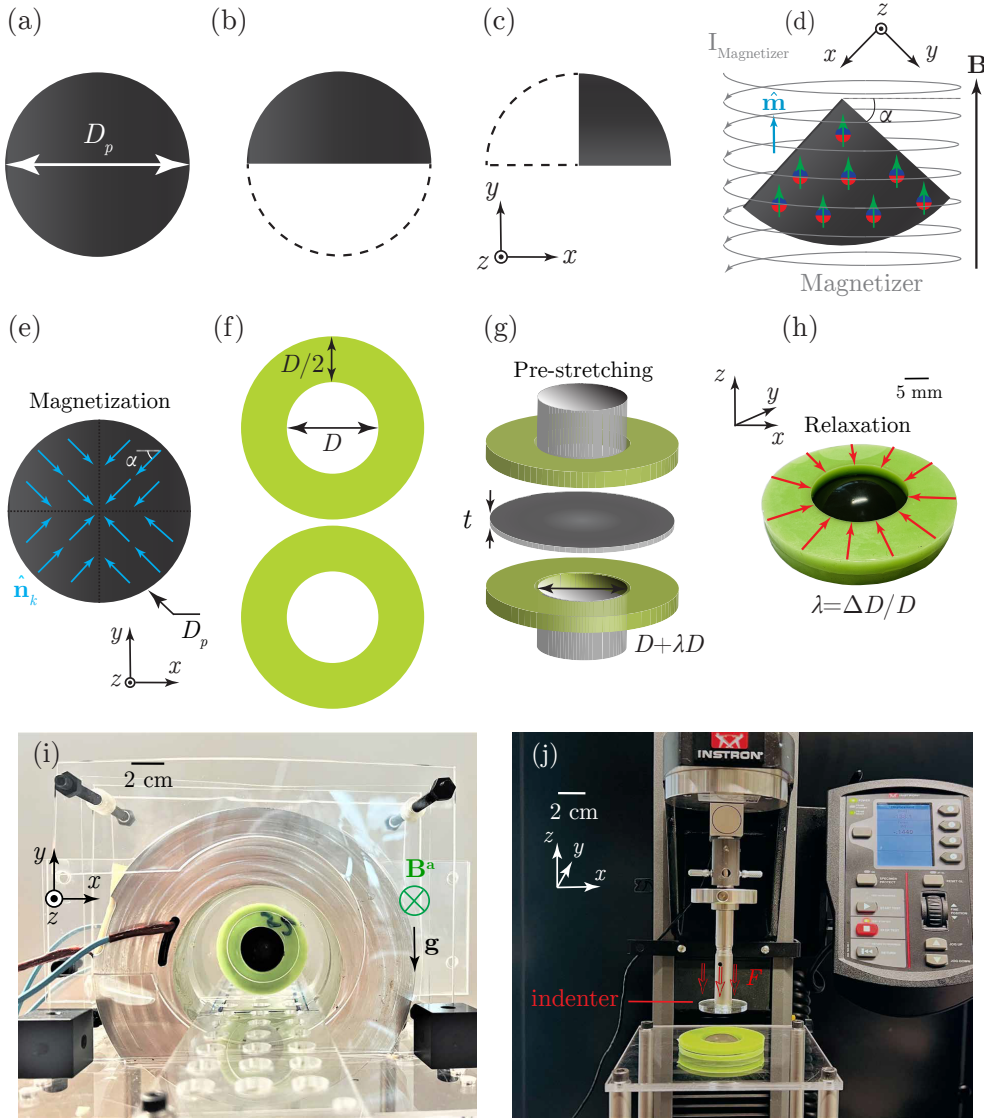


Figure 6.2: **Fabrication and experimental apparatus for the scaled-up model.** (a) A circular magnetic plate (diameter of D_p) is first (b) folded along the x -axis and then (c) along the y -axis to form a quarter-circle shape. (d) The folded plate is inserted into the pulse magnetizer at an angle $\alpha = 45^\circ$. The magnetizer generates a strong axial magnetic field, \mathbf{B} , which induces a magnetic moment, \mathbf{m} . (e) The circular h-MRE plate was magnetized while folded, yielding the magnetization profile described by Equation (6.1). (f) Two VPS annuli serve to constrain the plate boundary. (g) Cylinders pre-stretched the annuli, which sandwich the h-MRE plate. (h) Upon release of the pre-stretch, the plate buckles to form a shell. (i) Photograph of the apparatus for the *writing* experiments. The shell is placed between two Helmholtz coils and loaded by a uniform magnetic field along $\hat{\mathbf{z}}$. (j) Photograph of the apparatus for the *reading* experiments; a plate indents the shell, and the blocking force F is measured.

was mounted on an acrylic plate containing a hole to equalize the in-out differential pressure. The shell equator was clamped using its thick boundary annuli and mounted onto an acrylic plate using silicone glue. For the indenter, we used a rigid acrylic disk of diameter $D_{\text{ind}} = 0.8D$, smaller than the inner diameter (D) of the thick annular boundary to prevent contact with the perimeter during indentation. The indentation displacement was imposed at a constant velocity, 0.06 mm s^{-1} . The reaction force, f , exerted on the indenter was measured by a load cell (2530-5N, Instron). We define the *blocking force*, F , as the maximum of f , beyond which the shell undergoes snap-through buckling, altering the state of the dot.

6.4 Finite Element Modeling Simulations

We conducted the FEM simulations using the commercial package ABAQUS/Standard, undertaking two distinct series of simulations with the same protocol but different parameters. First, we worked with the same parameters as the scaled-up model system described in Section 6.3. The objective was to validate the FEM simulations against experiments. For the second series of simulations, we shifted to the realistic dimensions of the braille dots, which will be discussed in Section 6.6. In this case, the plate thickness was varied in the range $t=[0.025, 0.325] \text{ mm}$ (increments of 0.025 mm), and the fabrication pre-stretch of the magnetic plate in the range $\lambda = [0.05 - 0.2]$ (increments of 0.025).

The initially flat, circular magnetic plate was modeled as a three-dimensional solid body. Geometric nonlinearities were accounted for throughout the analysis. Similarly to the experiments, the plate was segmented into four quadrants, each with a magnetization oriented along \mathbf{n}_k (cf Section 6.3, Equation (6.1) and Figure 6.2e). The magnetic plate was discretized using the user-defined 8-node brick element proposed by Zhao *et al.* [32] for the modeling of hard-magnetic deformable solids under a uniform magnetic field. We conducted a convergence study to determine the appropriate level of mesh discretization, resulting in 6 elements in the thickness direction, 60 elements along the diameter, and 200 elements circumstantially. Mechanical loads, both contact (indentation) and distributed (pressure), were applied via a dummy mesh of C3D8R solid elements sharing the same nodes as the user elements. The material was assumed to be an incompressible ($\nu \approx 0.5$) Neo-Hookean solid with a bulk modulus 100 times higher than its shear modulus ($G = E/3$) and a Young's modulus of $E = 1.76 \text{ MPa}$.

In both the scaled-up and real-scale simulations, we explored various combinations of the parameters (t , D , λ) to investigate (1) geometry of the fabricated dot (Figure 6.1b), (2) writing phase (Figure 6.1c), and (3) reading phase (Figure 6.1d), as specified next.

(1) **Geometry:** To account for the possible emergence of higher-order modes during plate buckling, we simulated the entire magnetized plate without any symmetry assumptions (cf. Section 6.3). In order to break the symmetry on the $x - y$ plane and induce buckling, a small out-of-plane displacement ($0.01t$) was applied as an initial perturbation. Then, we specified the Dirichlet boundary condition on each boundary node and applied compression by imposing radially inward-directed displacements toward the center of the plate, a process that led to the formation of the shell. The extent of compression was set through λ .

(2) **Writing:** For the writing-phase simulations, having set the dot geometry in step (1), we subjected the raised dot (ON state) to a uniform external magnetic field, $B^a = 1$ T. The field was applied with a slight misalignment of 1° about the $-\hat{\mathbf{z}}$ direction to trigger asymmetrical buckling modes, thus providing a closer approximation of actual experimental conditions. The magnitude of the magnetic field was then increased linearly in the range of $[0, 1]$ T. The magnetic field magnitude, B_c^a , needed to snap the dot to the second stable state, was determined from the magnetic-field increment at which the displacement of the shell pole exhibited a sudden jump.

(3) **Reading:** For the reading-phase simulations, the indentation was simulated using a rigid circular plate indenter that exerted controlled displacements and discretized using rigid elements. The contact between the indenter and the shell was assumed to be hard and frictionless, thereby preventing surface penetration and sliding. To quantify the mechanical force needed to induce snapping, the dots were subjected to a downward indentation load (along $-\hat{\mathbf{z}}$) until reversal occurred, and the blocking (maximum) force, F , was recorded.

(4) **Pneumatic loading:** When simulating the real-scale braille dots, we also considered a constant pneumatic load, as will be discussed in Section 6.7. This pressure loading served to widen the design space by stiffening the dot against snapping during the reading phase (indentation) and reducing the energy barrier during the writing phase. For each dot geometry, we first measured the critical pressure, P_{cr} , required to snap the shell on its own, following the same procedure used to measure the critical magnetic field for snapping [104, 258]. A constant positive (or negative) pressure difference, within the range $|\Delta P| \in [0, P_{cr})$ (in increments of 1 kPa) was applied normally to the surface of the shell before initiating the reading (or writing) simulation steps, respectively. Steps (2) and (3) described above were repeated under this constant pneumatic loading. Finally, the blocking force, F , and the critical magnetic field amplitude, B_c^a , were recorded for each pair of parameters $(\Delta P, t)$. For these simulations, we set the fabrication pre-stretch to $\lambda = 0.15$.

6.5 Validation of the FEM Simulations Against Experiments

We first validate the FEM simulations (technical details are provided in Section 6.4) against experiments (see Section 6.3) on the scaled-up model system, considering the results from the geometry characterization of the fabricated shells, as well as from the reading and writing experiments.

During sample fabrication, the buckling of the plate, which yields a shell, may produce undesirable wrinkling patterns [358]. To act as braille dots, ideal shells should be smooth (*i.e.*, free of these wrinkles). Toward identifying the design space for these ideal shells, Figure 6.3(a) presents a phase diagram of the thickness-diameter parameter space (t , D) for representative shells fabricated with a pre-stretch of $\lambda = 0.1$ (see Section 6.3, and 6.4). There is excellent agreement between experiments (crosses) and FEM (circles), serving as a first step in validating the simulations. Wrinkling is observed for higher values of the slenderness ratio D/t . For the chosen pre-stretch ($\lambda = 0.1$), the empirical phase boundary between ideal and wrinkled shells is $t \approx 0.02D$ (dashed line). First, focusing on the geometry characterization, Figure 6.3(b) plots the normalized height, h/t , of the smooth shells (blue region in Figure 6.3a) versus D/t . The FEM simulations (lines) and experimental data (symbols) are obtained with a fabrication pre-stretch of $\lambda = 0.1$ and thickness in the range $t \in [0.18, 1.08]$ mm (see Section 6.3). The data collapses onto a single curve, with excellent agreement between experiments and FEM, thereby validating the FEM for the shell fabrication. Moreover, the inset of Figure 6.3(b) shows that the relation between h/t and D/t is a power-law with an exponent of $\approx 2/3$ [359, 1].

Toward validating the writing-phase simulations, in Figure 6.3(c), we plot the normalized magnetic field required for snapping, $B_c^a B^r / (E\mu_0)$, as a function of D/t , where E is Young's modulus, μ_0 is relative permeability of air, and B^r is the residual magnetic flux density. Naturally, increasingly slender shells require a lower magnetic field for snapping, and the data collapse into a single curve, exhibiting a power law with an exponent ≈ -1 . This scaling originates from the balance between magnetic and elastic energies investigated in our previous work [104, 247], which suggests $B_c^a B^r / (E\mu_0) \sim (D/t)^{-1}$; a prediction in agreement with our present data (inset of Figure 6.3c).

In Figure 6.3(d), we present the results for the reading, plotting the normalized blocking force, $FD/(Et^3)$ (required to snap the shell), as a function of D/t . Again the experiments (symbols) are in excellent agreement with the FEM (lines). The data is consistent with a power law with exponent ≈ 1.5 , which can be rationalized using well-established results for the indentation of a spherical shell by a flat plate, causing mirror buckling (to produce an inverted cap) of the shell [77, 266, 2, 360]. Balancing the stretching and bending energies of the shell, the dimensionless indentation force is expected to scale as

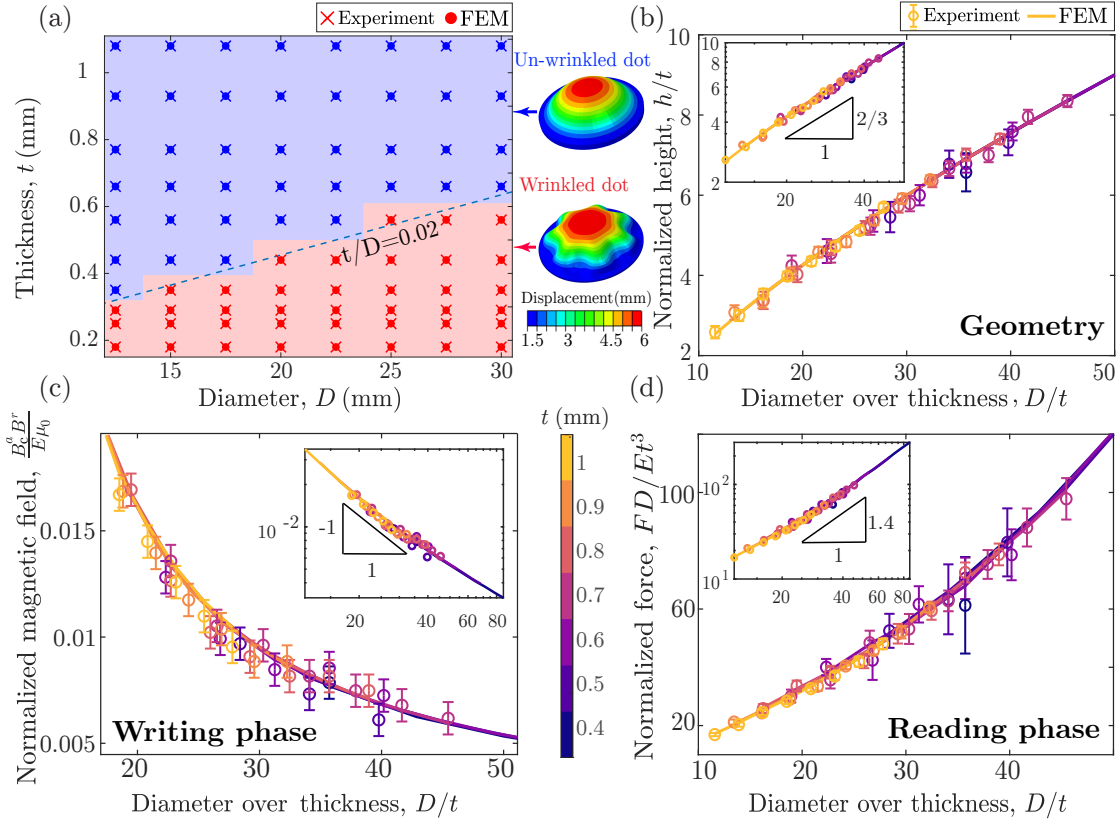


Figure 6.3: **Validation of FEM simulations against the scaled-up experiments.** (a) Phase diagram in the (t, D) parameter space. The experiments and simulations correspond to the cross and circle symbols, respectively. The smooth and wrinkled shells are represented by the blue and red symbols, respectively; the empirical phase boundary between the two is represented by the dashed line. The normalized (b) shell height, h/t , (c) critical magnetic field, $B_c^a B^r / (E \mu_0)$, and (d) blocking force, $FD / (Et^3)$ are plotted as functions of the normalized base diameter of the shell, D/t , for 10 different values of thickness, t . The error bars of the experimental data represent the standard deviation of 6 independent measurements on the same specimen. The different values of t are color-coded (see adjacent color bar). The solid lines and data symbols correspond to FEM and experiments, respectively. The insets show the log-log plots of the data. Throughout, the fabrication pre-stretch is $\lambda = 0.1$.

$FD / (Et^3) \sim (D/t)^{3/2}$, a prediction that is consistent in our data (inset of Figure 6.3d).

For completeness, we present the dimensional version of the data presented in Figure 6.3 for the geometry characterization (Figure 6.4a,d), and both the writing (Figure 6.4b,e) and reading (Figure 6.4c,f) operational phases of the scaled-up dots. In Figure 6.4(a, b, c), we plot the height h , the magnetic snapping load B_c^a , and the maximum indentation force, F as a function of the thickness t , respectively. In Figure 6.4(d, e, f), we plot the h , B_c^a , F as a function of the diameter of the dot D , respectively. The diameter and thickness

are color-coded in Figure 6.4(a, b, c), and Figure 6.4(d, e, f), respectively.

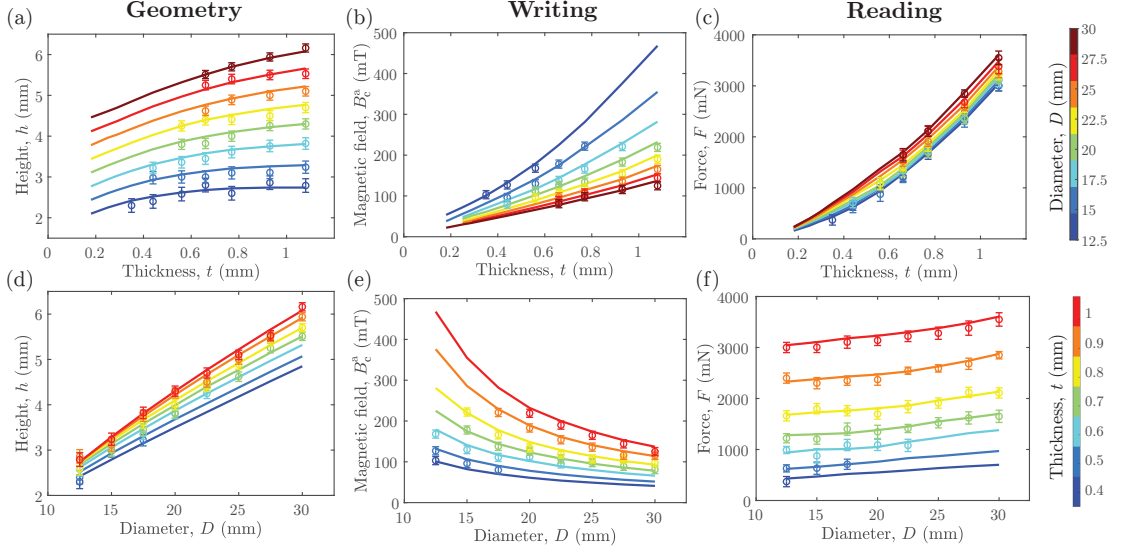


Figure 6.4: FEM versus experiments data (dimensional): (a) Dot height, h , (b) magnetic field, B_c^a , and (c) indentation force, F , as a function of the thickness, t , for the diameter range of $D \in [12.5, 30]$ mm in increments of 2.5 mm. (d) Dot height, h , (e) magnetic field, B_c^a , and (f) indentation force, F , as a function of the diameter, D , for the thickness range of $t = \{0.18, 0.25, 0.29, 0.35, 0.44, 0.56, 0.66, 0.77, 0.93, 1.08\}$ mm. The solid lines represent the FEM results, and the symbols correspond to the experimental data. The error bars of the experimental data correspond to the standard deviation of different measurements on the same specimen.

Figure 6.4(a) and (d) show the height of the dot as a function of thickness t and D , respectively. Increasing the thickness and diameter results in an increase in the dot height. When the diameter increases for a specific thickness value, the change in height becomes more significant compared to the increase in thickness. The FEM and experimental results are in good agreement, thus verifying the FEM framework for geometry.

In Figure 6.4(b), and (e), we plot the critical magnetic field for snapping, B_c^a , as a function of t , and D , respectively. We observed that as the thickness of the dot increases, so does the magnetic snapping load. However, increasing the diameter for each thickness has the opposite effect, as it leads to a decrease in the snapping load, which becomes more dominant in larger thicknesses. This is due to the fact that the slenderness ratio D/t decreases. The FEM and experimental data match in this operational phase of the design as well.

In Figure 6.4(c) and (f), which correspond to the reading phase, we plot the indentation force, F , is plotted as a function of t , and D , respectively. We find that increasing the

thickness has a significant impact on the increase in force, F . However, increasing the diameter only results in a slight increase in force. This is opposite to the relationship between D , t , and height. Again, the FEM and experiments are in excellent agreement.

Overall, we found excellent agreement between the experiments and the FEM simulations of the scaled-up model system for the shell-fabrication protocol and their geometric characterization, as well as for the reading and writing phases.

6.6 Design of Braille Dots at the Real Scale

We shift our attention from the scaled-up model system to investigate the design of the real-scale braille dots. Leveraging the FEM simulations validated above and following the protocol details in Section 6.4, we explore the design space for braille dots and determine their optimal fabrication and operational conditions. Each dot must conform to the specifications laid out in Section 6.6. Our objective is to determine the optimal ranges for the key geometrical parameters (thickness, t , and fabrication pre-stretch, λ) that simultaneously meet the acceptable design constraints for dot height (obtained from fabrication) and meet feasible operational conditions for the writing phase (critical magnetic field for actuation), and reading phase (blocking force). Finally, we will identify the intersecting region of these three design sub-spaces.

First, we characterize the geometry of the dots obtained from the fabrication step of the simulations. In Figure 6.5(a), we plot the dot height, h , versus thickness, t , for different levels of λ . The color map represents the various levels of λ , whose range is specified in Section 6.4. The resulting $h(t)$ curves exhibit a non-monotonic trend, with overall values (including the maximum of the curves) that increase with λ . This non-monotonic behavior arises because, for either very thick or thin plates, the pre-stretch release (compression) leads to planar (radial) contraction rather than increasing the out-of-plane deformation of the buckled plate (shell). The horizontal dashed line represents the minimum dot height, $h \geq 0.48 \text{ mm}$, required by braille specifications. Thus, to satisfy this requirement, we find that the feasible range for the fabrication pre-stretch is $\lambda \geq 0.15$, and the viable thickness range is $t \in [0.05, 0.325] \text{ mm}$.

Next, we consider the writing phase, which enables the braille dot (magnetic shell) to switch between its two stable stages. In Figure 6.5(b), we plot the critical amplitude of the magnetic field, B_c^a , required to snap the dot as a function of t , for different fabrication pre-stretches. We observe that, B_c^a increases with λ (and thus for taller dots; cf. Figure 6.5a), also with a non-monotonic dependence on t . To prevent the demagnetization of the shell due to high magnetic fields [32], we established the upper limit $B_c^a \leq 500 \text{ mT}$, represented

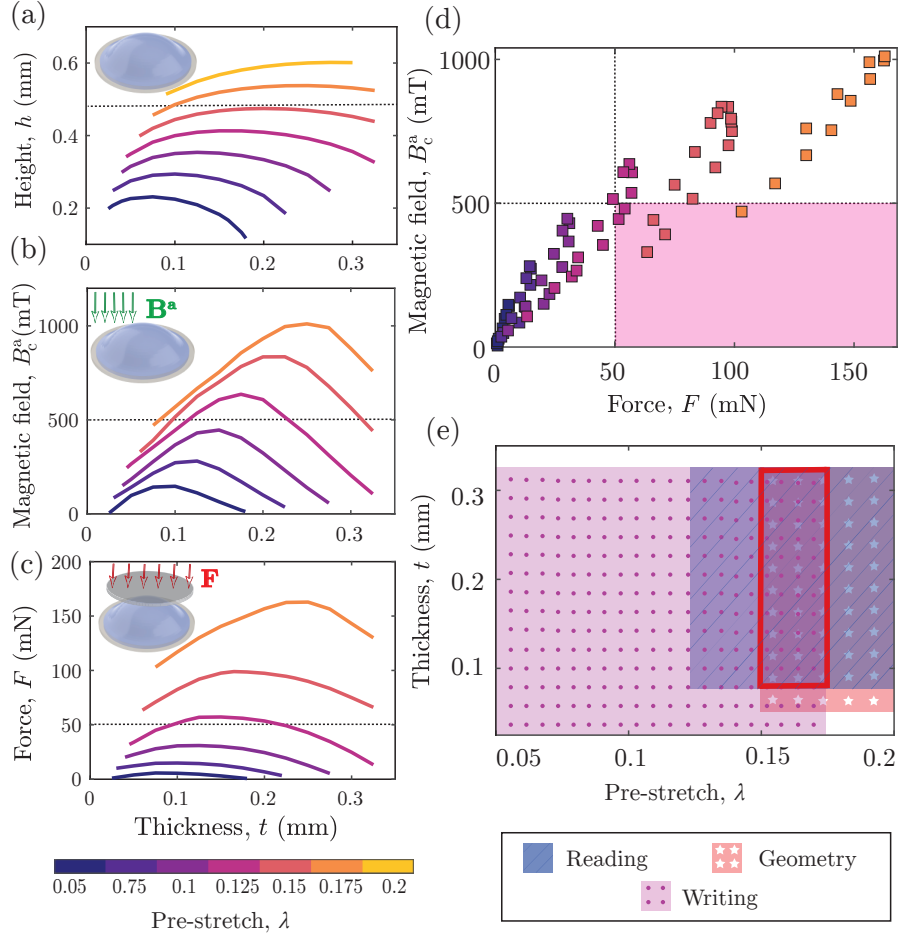


Figure 6.5: **Design of the real-scale braille dot.** The (a) dot height, h , (b) critical magnetic field, B_c^a , and (c) blocking force, F , are all plotted versus thickness, t , at different levels of pre-stretching, $\lambda=[0.05, 0.2]$ (increments of 0.05). The horizontal dashed lines represent the design constraints of the corresponding quantities. (d) The phase diagram in the (B_c^a, F) parameter space, with the desired shaded region. (e) The phase diagram in the (t, λ) parameter space for the geometry step and reading and writing phases, with the feasible design space indicated by the rectangle region. All results were obtained from FEM simulations.

by the horizontal dashed line in Figure 6.5b). Consequently, for actuation within this magnetic-field limit, the allowed parameters are in the ranges $t \in [0.025, 0.325]$ mm, and $\lambda \in [0.05, 0.175]$.

Finally, we turn our attention to the reading phase. In Figure 6.5(c), we plot the blocking force, F , as a function of t , using the same ranges of the other parameters which are specified in Section 6.4. Increasing λ leads to an overall increase of the $F(t)$ curves, much like the writing phase, which is also non-monotonic. Combining these results with the $h(t)$ data in Figure 6.5(a) implies that taller dots require a higher indentation force for

inversion, presumably due to their geometry-induced rigidity [41, 361]. According to braille specifications, the blocking force of the dot must be at least $F \geq 50$ mN (horizontal dashed line in Figure 6.5c), which is limited by the potential snapping of the shell due to the touch by a fingertip. Under this constraint, we determine that the ranges of feasible parameters for this reading phase are $t \in [0.075, 0.325]$ mm, and $\lambda \geq 0.125$.

Combining the above results for the viable ranges of the parameter space (t, λ) dictated by the geometry characterization, writing, and reading phases, we present the intersection of these three design phases in Figure 6.5(d). At each level of λ (colored symbols), we plot B_c^a as a function of F for all the thickness values. An overall correlation emerges between B_c^a and F . In the plot, the design constraints on B_c^a and F mentioned above are represented by the shaded region, which only intersects with a few of the explored designs ($\lambda \geq 0.125$). The design constraints require a sufficiently high blocking force while ensuring a sufficiently low magnetic field, a trade-off that is challenging to achieve in our system.

In Figure 6.5(e), we present an alternative version of the overlap of all of the design constraints explored above, now in the final target design parameter space (t, λ) . Each separate shaded/textured region relates to the individual viable bounds obtained above for the geometric characterization, writing, and reading phases. Meeting all the constraints and ensuring braille standards requires an overlap of these three regions; *i.e.*, the domain enclosed by the dashed rectangle with $t \in [0.1, 0.325]$ mm and $\lambda \in [0.15, 0.175]$.

6.7 Design Improvement Using a Pneumatic System

The feasible design space identified from the results in the previous section is rather limited, making a flexible fabrication process challenging. The design requires the shell to be able to snap during the writing phase yet remain resistant to snapping during the reading phase. To address these conflicting limitations without altering the geometry, we propose the incorporation of an additional pneumatic loading system. This pneumatic component modulates the energy barrier for buckling in both the reading and writing phases; the pressure difference, ΔP , between the inside and outside of the dot is positive for the reading phase and negative for the writing phase. The implementation details of this pneumatic loading in the FEM simulations are provided in Section 6.4. Hereon, we focus on shells fabricated with a pre-stretch of $\lambda = 0.15$, which was deemed practical from the parameter exploration presented above.

For the writing phase, the dot is depressurized to reduce the critical magnetic field B_c^a required for snapping, thereby facilitating the switching of the dot. In Figure 6.6(a), we

plot B_c^a versus ΔP , for different values of t . The results show that applying pneumatic loading substantially reduces the magnetic field B_c^a . The $B_c^a(\Delta P)$ curves are linear, with a slope that varies with t . For example, depending on t , a dot depressurized by $\Delta P \lesssim -60$ kPa can lower the critical magnetic field for snapping by as much as 50%, compared to the zero-pressure case. The horizontal dashed line represents the maximum acceptable magnetic field.

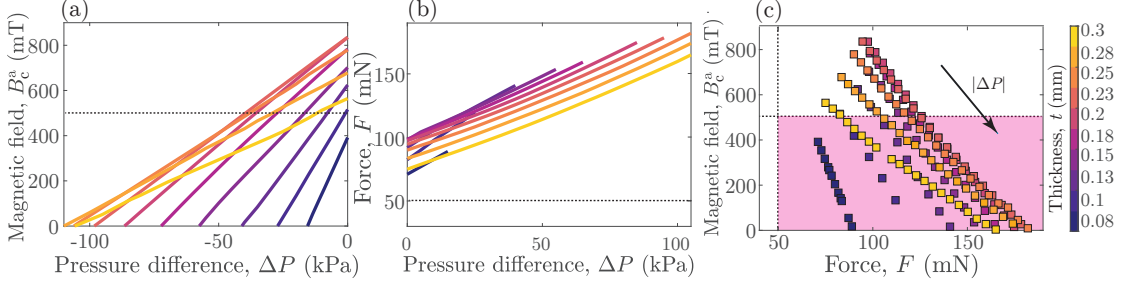


Figure 6.6: Improved design of real-scale braille dots with pneumatic system. (a) Blocking force, F , and (b) magnetic field, B_c^a , plotted as a function of the pressure difference, ΔP . The thickness was varied in the range $t = [0.075 - 0.3]$ mm (in increments of 0.025 mm) for a specific pre-stretch $\lambda = 0.15$. The horizontal dashed lines represent the limiting bounds imposed by the braille standards. (c) The phase diagram in the (B_c^a, F) parameter space with the desired regions of viable parameters (shaded region), for different levels of pressure difference, $0 < |\Delta P| < 120$ kPa. All results were obtained from FEM simulations.

For the reading phase, in contrast to the writing phase, the dot is pressurized to enhance the blocking force, F , and better resist indentation. The dot is first pressurized and then loaded at its pole. In Figure 6.6(b), we present the dependence of the blocking force F on the applied ΔP for different thickness values, t (see adjacent color bar). In the explored range of parameters, the $F(\Delta P)$ response is linear, as expected from previous work [41, 361], and no buckling occurs. For example, the resistance of the dot to indentation force can be increased by up to 100% (at $t = 0.2$ mm) compared to the zero-pressure case. We find that all curves are now well above the 50 mN limit imposed by braille standards.

Finally, in Figure 6.6(c), we combine data from both phases with pneumatic loading (Figure 6.6a and 6.6b) and plot B_c^a versus F . The shaded region indicates the viable range of parameter space; with a pneumatic load of $|\Delta P| \geq 40$ kPa, we achieve successful reading and writing operations across the full thickness range. The limit values of $|\Delta P|$ could be further tuned by varying the fabrication pre-stretch λ , but we leave a more systematic exploration for future work. Our results demonstrate that by using this additional pneumatic component, the design space of the system is significantly expanded compared to the zero-pressure case explored in Section 6.6.

6.8 Expected Challenges to Fabricate at-Scale Braille Dots

The focus of the present mechanics-based study is on proposing a design concept for a switchable braille dot and exploring its feasible parameter space using predictive computational tools. Still, in this section, we discuss some potential challenges and limitations expected to be encountered during the miniaturization and fabrication of at-scale dots for actual implementation in concrete applications.

Scaling down the proposed design concept, especially in terms of fabrication, should introduce a distinct set of challenges than those encountered in our model centimeter-scale experiments, whose purpose was to validate the FEM simulations. These expected challenges include the details of the actual fabrication processes, material properties, and actuation mechanisms within smaller dimensions. In terms of fabrication, achieving the level of precision desired for the dot fabrication, based on the release of stretch in the pre-stretched plate, may be difficult to implement at the sub-millimeter scale, and the miniaturized components may require specialized manufacturing processes. Furthermore, given that the size of the magnetic particle we used in the fabrication of the MRE material was $\approx 5\mu m$, achieving at-scale dots with homogeneous thickness may require the usage of magnetic nanoparticles.

In addition, generating the required magnetic field and enabling actuation of the braille dot at the real scale will call for the development of custom-designed electromagnetic coils. Even if, in practice, we believe that this will be a non-trivial task, in the next section, we demonstrate that, in principle, it is feasible. Specifically, we have performed simulations using COMSOL of the magnetic field generated by an electromagnet (solenoid) under the design constraints imposed by the actual scale of a braille dot. Our results show that it is reasonable to expect to generate magnetic fields of the magnitude of $B_{\max} \approx 200 \text{ mT}$, which is within the range required for the operation of the braille dot (cf. Figure 6.6). Actual practical implementations of our proposed design will likely have to tackle other concrete, practical challenges, including the potential heterogeneity of the magnetic field, that go beyond the scope of the present study.

6.9 Designing a Solenoid for a Braille Reader

In this section, we propose a solenoid design to generate the magnetic field during the *Writing* phase and optimize the magnetic field in the volume beneath each braille dot. We first specify the wiring of the solenoid, which determines the multi-turn solenoid density of the current. Next, we calculate the diameter of the electromagnet and the dimensions of the conducting section, which forms the solenoid core.

In Fig. 6.7(a), we show the schematic of a solenoid with a ferromagnetic core and the cross-sectional view of the coil outside. The cylindrical core has a diameter of d_i and a length of L . The coil has a diameter of d_o after winding N turns with wire of diameter ρ . The current I passes through the coil to generate the magnetic field.

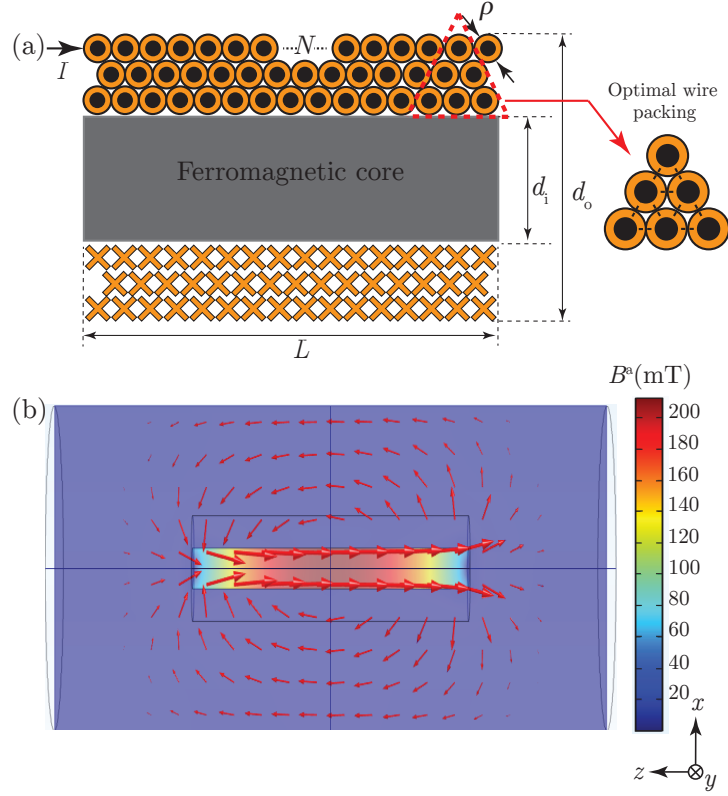


Figure 6.7: **Solenoid design** (a) Schematic diagram of a ferromagnetic-cored solenoid, composed of a multi-turn coil and a cylindrical ferromagnetic core with a diameter of d_i and a length of L . The core is wound with N turns of copper wire with a diameter of ρ , resulting in a solenoid with an outer diameter of d_o . (Inset) The wiring compacity is represented as a face-centered cubic in 2D. (b) The computed field displays the vector (arrow) and magnitude (color code) of the magnetic flux density B_c^a generated by the solenoid under a current of $I = 0.182$ A. Due to its symmetry, the field is depicted in the x - z plane ($y=0$).

To optimize the intensity and model the wiring geometry, the core is uniformly wired with a triangular lattice circle arrangement [362, 363]. Circle packing density is defined as the ratio of the cross-sectional area taken up the wires to the available space. The theoretical maximum packing density for the lattice arrangement of the wires, as shown in the inset of Fig. 6.7, is equal to $\Lambda = \pi/\sqrt{12}$, and the optimal number of turns is calculated as [362,

363]

$$N_{\text{opt}} = \frac{(d_o - d_i)LA}{s} \quad (6.2)$$

where $s = \pi\rho^2$ is the cross-section area of a wire.

We consider the outer diameter of the solenoid, d_o , to be the limiting design factor due to the miniature size of the braille dots and the necessary dot-dot distancing. Therefore, we set $d_o = 2.5$ mm at the beginning of our design process. Additionally, we limited the thickness of the device by setting the solenoid's length to $L = 10$ mm. The inner diameter of the solenoid, d_i , was also determined to be 1 mm to provide sufficient space for winding the ferromagnetic core. Finally, the trade-off between the wire cross-section and the maximum current capacity of the wire, as defined by the American Wire Gauge (AWG) [364] table, determines the maximum magnetic field that can be generated. For this proposal design, we considered AWG 29 wire, which has a maximum current capacity of $I = 0.182$ A. To simulate the Solenoid core in COMSOL, we used a built-in Mumetal material (an iron alloy with high relative permeability) due to its high relative permeability.

In Figure 6.7(b), we present a simulation of the magnetic flux generated by the solenoid while taking into account the design parameters mentioned earlier. These simulations were conducted using the magnetic field interface of COMSOL, based on Ampere's Law. The electromagnet functions as a magnetic dipole, and the amplitude of its flux is directly controlled by the current intensity. The polarity of the magnetic field is indicated by the direction of the red arrow, which represents the direction of the induced magnetic dipole. According to the Ampere theorem, the analytical expression for the maximum magnetic flux on the axis [363, 362] can be written as

$$\mathbf{B}_{\text{max}} = \mu_0 \frac{j(d_o - d_i)}{2} \left(\frac{L}{\sqrt{L^2 + \frac{(d_o + d_i)^2}{4}}} \right) \quad (6.3)$$

where $j = AI/s$ is the current density. According to the FEM simulations, the maximum magnetic field of $B_{\text{max}} = 213$ mT was generated with the current limit level of $I = 0.182$ A, which gives us a good range of magnetic field for the required range specified in Section 6.7. There is still room for optimization of the proposed design, which is beyond the scope of the current manuscript. The advantage of this electromagnet over the permanent magnet is that the magnetic field can be rapidly switched over a wide range of values by controlling the electric current I .

6.10 Summary and Outlook

We have proposed a new design concept for a reversibly switchable braille dot as a building block for refreshable braille displays. The proposed mechanism uses bistable magnetic shells that can be snapped on-demand under an external magnetic field (writing phase) while resisting buckling due to the indentation by a fingertip (reading phase). An additional pressure-loading component expands the available design space without modifying the dot geometry. First, we performed experiments on a scaled-up model system to validate FEM simulations. These simulations were then leveraged to systematically explore the design space at realistic scales while meeting braille standards (geometry and tactile sensitivity) with reasonable magnetic field strengths and temporary pneumatic loading. Our design boasts several advantages over existing solutions, including bistability for self-stabilization, as well as fast state-switching and pattern refreshment. This switching can be triggered by a transient magnetic field rather than a continuous energy input. Finally, a constant pneumatic input for the whole actuator enables the tuning of the power input of the system.

While our design introduces promising advances, it is not without potential limitations. Its complexity calls for advanced manufacturing and assembly techniques. Miniaturized solenoids to generate the required magnetic field under each dot would need to be developed. Furthermore, incorporating a hybrid magnetic and pneumatic system could pose challenges in terms of size and power, particularly for portable or battery-operated devices. Despite these potential obstacles, we anticipate that future research and physical implementation of this concept could make it possible to build a new class of compact, user-friendly, and cost-effective braille readers.

7 Conclusion and Perspectives

In this final chapter, we begin by presenting a summary of our main findings in Section 7.1. In Section 7.2, we outline several areas of ongoing research that build up from the research methods and results established in the present thesis, particularly those discussed in Chapter 4. Lastly, in Section 7.3, we highlight potential directions for future research.

7.1 Summary of Findings

In this thesis, we have studied a series of research problems on the mechanics of slender structures. Throughout, we combined experimental and numerical methods. As a starting point for the research, we revisited the mechanics of thin spherical shells toward identifying the key factors contributing to their imperfections-sensitive buckling instabilities. We also investigated a non-destructive method to anticipate the stability landscape of shell structures and critical loading conditions. We considered both simplified scenarios with a single defect and more realistic situations with a large distribution of random imperfections. In parallel to our study on the mechanics of shells, we also investigated magneto-active structures, focusing on bistable beams and shells made from magneto-rheological elastomers (MREs). The mechanical behavior of these slender magnetic structures was investigated through a combination of experimental, numerical, and analytical methods to gain insight into their response to various mechanical and magnetic loading conditions. Specifically, we examined the various deformation modes and (snap) buckling of slender magnetic beams and shells. Furthermore, we exploited the knowledge of the instability of slender structures combined with active MREs under magnetic field actuation for potential applications; we proposed the guidelines for designing a novel class of braille readers. In this final project, we followed a perspective of harvesting mechanical instabilities of shell structures as opportunities for functionality instead of the first route for failure.

In **Chapter 1**, in the first part, we introduced the motivation of the thesis and presented a literature review of the state-of-the-art theoretical, numerical, and experimental analysis of shell structures. First, we presented examples of shell structures found in nature and used in engineering, with length scales ranging from microns to several hundred meters. Then, we highlighted the importance of the imperfection sensitivity of shell buckling, causing the actual measurement of the buckling pressure to be lower than the classic theoretical predictions for the imperfection-free counterparts. We also presented an overview of the existing literature on the non-destructive probing technique for spherical and cylindrical shells. In practice, the imperfections are often unidentified and can be difficult to detect, which begs for an alternative approach to assessing the stability of shells and categorizing defects without destroying the structure. We saw that although, to date, there has been considerable research on the non-destructive testing of cylindrical shells, it has remained inconclusive whether probing techniques can serve as an effective way of assessing the stability of spherical shells in a way that parallels some reported successes for cylindrical shells. In the second part, we reviewed the literature on magneto-active structures made of magneto-rheological elastomers (MREs). We considered and compared several models of structures made of MREs. Further, we discussed the dimensional reduction from the 3D constitutive description of MREs to derive structural theories for beams, rods, plates, and shells and how these models can be used to design functionality in magneto-active slender structural elements. From all of this existing body of literature, we identified the timely and relevant research niche for our work to provide much-needed physical insight into the buckling instabilities of elastic and magneto-elastic beams and shell structures.

In **Chapter 2**, we used finite-element simulations to compare the buckling strength of imperfect shells containing either a dimpled or a bumpy imperfection. We considered defects with a standard Gaussian profile, enabling direct and detailed comparisons across two cases. Our results evidence that the role of bumps in reducing the buckling strength of the spherical shell is less dramatic than for dimples within the ranges of parameters we explored. The sensitivity of the knockdown factor to the detailed defect geometry is also less prominent in bumps. Overall, the knockdown factor of a bumpy shell is always greater than that of a dimpled one for the same magnitude of geometric parameters. In both cases, the knockdown factor is not always reduced when the defect is widened. We discussed the differences in knockdown factor between dimpled and bumpy shells using their mean and Gaussian curvature profiles. Our interpretation suggests that regions of the imperfect shell with minimal mean curvature serve as weak points for the onset of buckling. These minima occur at the defect core for dimpled shells and at the defect rim for bumpy shells. For the latter, the core appears to have a stiffening effect, which repels the post-buckling inverted caps, making the buckling mode asymmetric and potentially multi-lobed. Our results demonstrate that different types of defects, even if

characterized by similar geometric parameters can yield quantitatively and qualitatively different reductions of buckling strength.

In **Chapter 3**, we investigated the behavior of imperfect spherical shells subjected to a point indentation, with a focus on the effect of the indentation angle. We showed that when the indentation is applied at the center of the defect under imposed displacement conditions, the knockdown factor of the shell can be successfully identified by tracking the peak of the force-displacement curve with increasing prescribed pressure level and extrapolating to the point of maximum force reaching zero. In this case, the indentation can be used to probe the stability of the shell non-destructively. However, as the probe is moved away from the center of the defect beyond a critical angle, the probing test fails to identify the buckling point prior to the collapse of the shell. We found that the localized nature of indentation in spherical shells limits the interaction between the defect and the probe. The characteristic length is associated with the indentation's neighborhood in both the linear and nonlinear regimes. Our findings demonstrate that point-load probing can only be useful as a local strategy to assess the stability of spherical shells as long as the indentation is performed in the close neighborhood of the defect.

In **Chapter 4**, we presented preliminary findings from our ongoing research on a probabilistic investigation of the non-destructive poking method. We studied spherical shells with randomly distributed imperfections, where the size of defects was chosen based on a lognormal distribution. We explored two different scenarios: one involving the random selection of the defect size and shell configuration and the other randomizing the location of the indentation. In both cases, we analyzed statistics related to the knockdown factor obtained through extrapolation and compared it with actual knockdown factor data. We also looked into how the extrapolation method, defect size, and minimum separation angle between defects influenced the results. Our observations highlighted that the accuracy of the extrapolated results and the ability to predict the actual knockdown factor depended strongly on the chosen extrapolation technique. This is primarily due to the significant influence of various shell parameters and the uncertainties introduced by the extrapolation technique. At the end of this chapter, we also provided recommendations for further exploration of these results.

In **Chapter 5**, we turned to magneto-active systems, starting with an investigation of the snapping behavior of bistable magneto-elastic beams under combined mechanical and magnetic actuation. The study combined experiments, a reduced-order theoretical model, and FEM simulations. We considered a pre-compressed (clamped-clamped) bistable beam with different levels of end-to-end shortening. We started by characterizing the beam's load-displacement response, the critical poking force, the field strength at the onset of snapping, and the effect of magnetic loading on snap buckling under the poking

force. The Riks method was employed in the FEM simulations to analyze the snap transition. We also developed a beam theory to rationalize the observed magneto-elastic response. Precision experiments validated the theory and the FEM simulations. We studied the snap buckling of the beam under three different loading cases: poking force only, magnetic field only, and combined magnetic and mechanical loading. The first case served as a pre-validation of the FEM simulations. In the second case, we triggered snap buckling under a magnetic field for various end-to-end shortenings by designing the magnetization profile of the beam. For small deformations, we found that the critical magnetic field increased with the square root of the end-to-end shortening. The Riks method was used to explore the equilibrium transition path, finding that increasing the end-to-end shortening complicates the instability response, but the experimentally observable solution corresponds to the lowest energy level. Finally, in the third case, we examined how magnetic loading affects the poking-induced snapping of the bistable beam. The critical poking force for snapping could be adjusted by the magnitude and direction of the magnetic field, and our magnetic beam model captured these results. In the small deformation limit, the critical poking force at the onset of snapping was linearly proportional to the applied magnetic field with a slope and offset that we were able to predict. In this limit, a master curve was uncovered that collapses the experimental and FEM-computed data. Our study offers insight into the nonlinear magneto-elastic coupling of bistable beams, providing a predictive design approach by exploiting snapping behavior and stiffness-tuning capability.

In **Chapter 6**, we combined the mechanics of shells with magneto-elastic actuation explored in the preceding chapters to propose a new design concept for a reversibly switchable braille dot as a building block for refreshable braille displays. The proposed mechanism utilized bistable magnetic shells that could be snapped on-demand under an external magnetic field (writing phase) while resisting buckling due to the indentation by a fingertip (reading phase). An additional pressure-loading component was applied to expand the available design space without modifying the dot geometry. First, we performed experiments on a scaled-up model system to validate FEM simulations. These simulations were then leveraged to systematically explore the design space at realistic scales while meeting braille standards (geometry and tactile sensitivity) with reasonable magnetic field strengths and temporary pneumatic loading. Our design boasted several advantages over existing solutions, including bistability for self-stabilization, as well as fast state-switching and pattern refreshment. This switching could be triggered by a transient magnetic field rather than a continuous energy input. Finally, a constant pneumatic input for the whole actuator enabled the tuning of the power input of the system. While our design introduces promising advances, it is not without potential limitations.

7.2 Opportunities for Future Work

In the following, we provide an overview of ongoing collaborative research efforts related to the main topics of this thesis. Then, we highlight possible extensions of the present research, which the author is starting to explore in collaboration with other colleagues. Finally, we identify some possible directions for future work that the current research has opened up and are yet to be pursued.

Programming the buckling capacity: The study reported in Ref. [112] (see AppendixA) was performed in collaboration with the author of this thesis. In this project, we analyzed the impact of defect-defect interactions on the buckling behavior of pressurized hemispherical shells containing two dimpled imperfections. We found that, at a specific defect separation determined by the critical buckling wavelength, the knockdown factor of the shell with two defects reached its maximum level when compared to the case of shells with a single defect. These results have sparked further interest in leveraging defect-defect interactions to design spherical shells with programmable buckling capacity. By strategically arranging the defects on the shell in a packing scheme that maintains equal spacing, matching the critical buckling wavelength across the shell surface, we hypothesize that the shell's buckling capacity could be augmented. Additionally, the knockdown factor could be fine-tuned by tailoring the design of the imperfections.

Using machine-learning tools to predict the buckling capacity of shell structures: In Chapters 1 and 2, we delved into the challenge of predicting the critical buckling conditions of imperfect shells, a longstanding problem in the mechanics community. Over the years, researchers have persistently sought to establish definitive correlations between defect geometries, knockdown factors, and buckling capacities, employing theoretical, numerical, and experimental methodologies in the field of mechanics. With the recent resurgence of machine-learning (ML) tools and data-driven techniques, we anticipate that the task of predicting the buckling capacity of shell structures based on their geometry could be made more streamlined and efficient. While data acquired through FEM modeling may prove cumbersome in certain instances, we propose leveraging the Graph Neural Network (GNN) algorithm to study shell buckling. This approach enables us to simulate a range of scenarios, from single defect instances to those with multiple defects distributed randomly across the shell; each represented as a graph. Subsequently, we aim to establish a model that predicts the relationship between the test predictions (the anticipated outcomes) and the test ground truth (the actual data derived from the FEM simulations). In our pursuit, we have harnessed a substantial volume of data, including approximately 10,000 simulations of knockdown factors for shells containing one, two, and multiple random defects. We allocate 90% for the training of our model and reserve the

remaining 10% for proof testing. This research plan is presently underway in collaboration with the group of Prof. Miguel Bessa (Brown University).

Combing the non-destructive technique with machine learning tools: Following our investigations into the non-destructive probing technique for spherical shells containing either a single defect (cf. Chapter 3) or a random distribution of defects (cf. Chapter 4), we have concluded that the predictions for the onset of buckling are significantly influenced by the location of the indentation and the chosen extrapolation method. Therefore, these predictions are rather unreliable. To address this issue, we propose the utilization of ML techniques to effectively train the data for non-destructive prediction of the knockdown factor. We expect that this approach should enable us to make accurate estimates even beyond the range of the observed data. It is worth noting that extrapolation in ML methods poses a challenge, as these models are inherently constrained by the data on which they have been trained. These ML techniques may struggle to project accurately into regions of the feature space that significantly deviate from their training set. To overcome this limitation, we advocate for training our model using the complete set of maximum force-pressure signals up until the buckling point. This comprehensive dataset should empower our model to provide reliable predictions based on the indentation of shell structures. We are currently executing this research plan, also in collaboration with the group of Prof. Miguel Bessa (Brown University).

The effect of defect removal on the buckling of spherical shells with multiple imperfections: Building upon the groundwork laid by Derveni *et al.* [118] in their study of the probabilistic buckling of spherical shells with a range of imperfections, our current endeavor, led by Fani Derveni, Florian Choquart, Dong Yan, in collaboration with the author of this thesis, aims to systematically eliminate defects in order of severity within a spherical shell characterized by a distribution of imperfections. Our goal is to quantify how the knockdown factor is affected by this removal process and subsequently compare these findings with those of the classical hypothesis. Additionally, we seek to reevaluate and provide a rational interpretation of the seminal experiments conducted by Carlson *et al.* [88], which noted an increase in knockdown factors with the progressive elimination of severe defects.

7.3 Final Remarks

The study of the mechanics of slender structures has a rich and long history, from the foundational works of Euler, Bernoulli, Kirchhoff, von Kármán, and many other giants in the field. The recent decades have witnessed a resurgence of interest in this field across engineering and physics disciplines. Slender structures, characterized by

significantly smaller dimensions in one direction, exhibit distinct mechanical behaviors that are rooted in nonlinear geometries, encompassing diverse phenomena, including deformation, instability, and response to external loads. Notably, buckling, a sudden and catastrophic failure due to compressive loads, is a critical focus influenced by geometry, imperfections, material properties, and boundary conditions. Hence, comprehending these factors is essential for designing and optimizing performance and reliability, from nano-scale devices to large-scale engineering structures.

Within the vast and challenging umbrella of the research problematics described above, the work performed through this thesis has focused on studying the instabilities in elastic and magneto-elastic beams and shells, spanning from the buckling of imperfect shells to the computational design of a programmable Braille reader. Through rigorous analyses and experiments, we deepened our understanding of structural instabilities and proposed their practical applications in assistive technology. This research sought to connect fundamental concepts in mechanics with applied engineering, providing a basis for future work in functional structures and assistive technologies for the visually impaired. As we conclude this journey, it is our hope that these findings will inspire and spark future research efforts that will further bridge the gap between the foundations of mechanics and innovative engineering applications.

A Appendix: Defect-Defect Interactions in Spherical Shells

This appendix comprises the manuscript authored by Fani Derveni, in collaboration with the author of this thesis as cited in Ref.[112]: Fani Derveni, Arefeh Abbasi, and Pedro M. Reis. **"Defect-Defect Interactions in the Buckling of Imperfect Spherical Shells."** Journal of Applied Mechanics, 1-10 (2023). However, for the sake of brevity and to prevent redundancy, the introduction of the paper has been omitted (refer to Chapter 1, Section 1.2 for the relevant literature review).

We perform finite element simulations to study the impact of defect-defect interactions on the pressure-induced buckling of thin, elastic, spherical shells containing two dimpled imperfections. Throughout, we quantify the critical buckling pressure of these shells using their knockdown factor. We examine cases featuring either identical or different geometric defects and systematically explore the parameter space, including the angular separation between the defects, their widths and amplitudes, and the radius-to-thickness ratio of the shell. As the angular separation between the defects is increased, the buckling strength initially decreases, then increases before reaching a plateau. Our primary finding is that the onset of defect-defect interactions, as quantified by a characteristic length scale associated with the onset of the plateau, is set by the critical buckling wavelength reported in the classic shell-buckling literature. Beyond this threshold, within the plateau regime, the buckling behavior of the shell is dictated by the largest defect.

This Appendix is organized as follows. First, in Section A.1, we define the problem at hand and outline the research questions. Next, in Section A.2, we describe the FEM simulations employed in our study. In Section A.3, we present a first set of results on the influence of the radius-to-thickness ratio on the buckling behavior of shells containing two defects. More detailed results for shells with identical defects are provided in Section A.4 and with different defects in Section A.5. Finally, in Section A.6, we summarize the conclusions of our study and offer suggestions for future research directions.

A.1 Problem Definition

We aim to study the buckling of imperfect hemispherical shells containing two dimpled defects. The geometric properties of these two imperfections can be either identical or different. Methodologically, we conduct FEM simulations, which have been previously validated thoroughly against experiments [118]. First, we focus on how the angular separation between the two defects affects the knockdown factor, characterizing how the interaction regime is impacted by the width and amplitude of the imperfections. Then, we compare the threshold of the defect-defect separation for the onset of interactions to the theoretical prediction of the full wavelength of the classic critical buckling wavelength for a spherical shell [113]. Our main finding is that the arc length associated with the defect-defect interaction threshold depends directly on the radius-to-thickness ratio of the shell, scaling linearly with this critical buckling wavelength.

We consider a thin, elastic, and hemispherical shell of radius, R , and thickness, h , as illustrated in Figure A.1(a,b). The shell is clamped at the equator and contains *two* geometric imperfections. In their undeformed configuration, each defect is shaped as a Gaussian dimple, with the following radial deviation from the perfect spherical geometry:

$$\hat{w}_i(\alpha) = -\delta_i e^{-(\alpha/\alpha_i)^2}, \quad (\text{A.1})$$

where the indices $i = \{1, 2\}$ represent each of the two defects, α is the local angular distance corresponding to each defect (measured from their centers), α_i is the half-angular width of the i th defect, and δ_i is its amplitude (maximum radial deviation of the mid-surface of the shell). The global angular (zenith) coordinate, β , is defined from the pole ($\beta = 0$), where the first defect ($i = 1$) is always located. The other defect is at β_2 . Following conventional practice in shell-buckling studies [84, 257], the defect amplitude of each defect is normalized as $\bar{\delta}_i = \delta_i/h$, while the width is normalized as $\lambda_i = [12(1 - \nu^2)]^{1/4} (R/h)^{1/2} \alpha_i$. Here, ν is the Poisson's ratio of the material. The shell thickness, h , is kept constant throughout so that we focus only on geometric imperfections, unlike previous work on through-thickness defects [253] or elasto-plastic dents [256].

First, we will analyze shells containing two identical defects: $\lambda = \lambda_1 = \lambda_2$ and $\bar{\delta} = \bar{\delta}_1 = \bar{\delta}_2$. Subsequently, we will consider the scenario of two different defects; $\lambda_1 \neq \lambda_2$ and/or $\bar{\delta}_1 \neq \bar{\delta}_2$. Since the $i = 1$ defect is always positioned at the shell pole ($\beta = 0$) and the $i = 2$ defect is at β_2 , the angular separation (center-to-center) between the two defects is $\varphi_{(1,2)} = \beta_2$. To facilitate the discussion on defect-defect interactions later in this Appendix, it is important to define an alternative angular separation:

$$\varphi_{(1,2)}^* = \varphi_{(1,2)} - m \frac{\alpha_1 + \alpha_2}{\sqrt{2}}, \quad (\text{A.2})$$

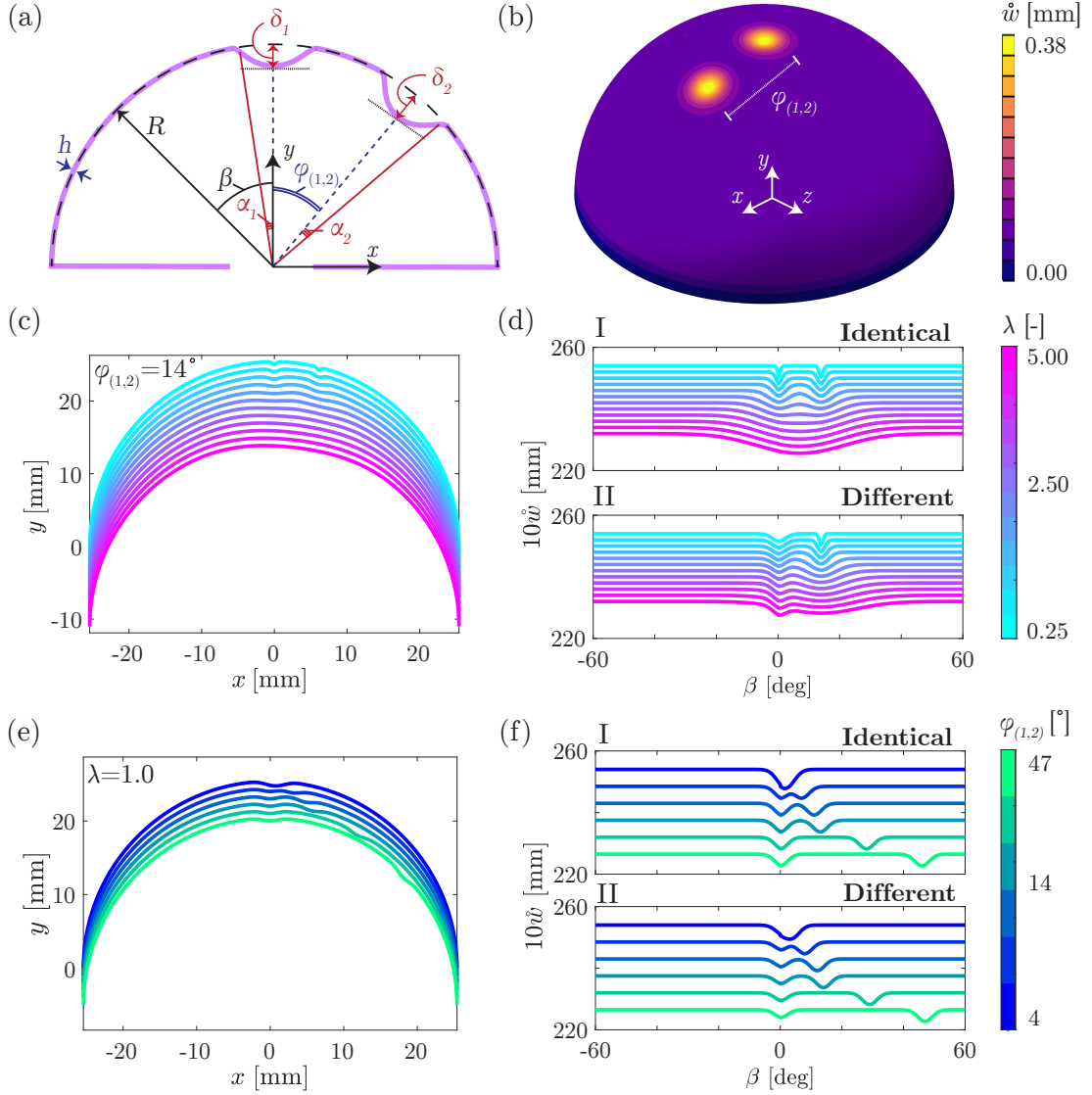


Figure A.1: **Reference geometry of the imperfect hemispherical shell with two dimpled defects.** (a) 2D schematic, defining all relevant geometric quantities. (b) 3D representation; the shade (see colorbar) represents the radial deviation \hat{w} from a perfect sphere. (c,e) Geometric profiles of identical-defect shells for (c) fixed $\bar{\delta} = 1.5$, $\varphi_{(1,2)} = 14^\circ$ and varying λ_i , and (e) fixed $\bar{\delta} = 1.5$, $\lambda_i = 1.0$ and varying $\varphi_{(1,2)}$. (d,f) Radial deflection, \hat{w} , versus zenith angle, β , for (d) constant $\varphi_{(1,2)} = 14^\circ$ between (dI) identical defects with various λ_i or (dII) different defects with various λ_2 . (f) Similar data, with constant $\lambda_i = 1$, for (fI) identical defects with various $\varphi_{(1,2)}$ or (fII) different defects with various $\varphi_{(1,2)}$. The representative cases for identical defects (dI, fI) have $\bar{\delta}_i = 1.5$, and the different-defects cases (dII, fII) have $\bar{\delta}_1 = 1$, $\bar{\delta}_2 = 1.5$ and $\lambda_1 = 1$. For clarity, all profiles are offset in panels (c,d) by 1 mm, in (e) by 2 mm, and in (f) by 5.5 mm downwards. Also, the \hat{w} profiles in panels (d) are shown with an amplification factor of 10.

where $m = \{1, 2, 3\}$ is an integer. The different values of m correspond to successively excluding wider portions from the core of the defects when considering their angular separation. A more comprehensive discussion on this point will be provided in Section A.4. Finally, recalling Equation (A.1), the combined profile of a shell with two dimples is

$$\hat{w}(\beta, \theta) = \hat{w}_1(0, 0) + \hat{w}_2(\varphi_{(1,2)}, \theta_2), \quad (\text{A.3})$$

where β and θ are the *global* zenith and azimuthal spherical (polar) coordinates, respectively.

Figures A.1(c-f) depict representative examples of the mid-surface profile of a shell with $R/h = 100$. These profiles are visualized within the great plane that intersects the shell and passes through the centers of the two imperfections. Note that, given the localized (dimpled) profile in Equation (A.3), the shells are *not* axisymmetric, and the profiles shown in Figure A.1 are solely for illustration purposes. Figures A.1(c,e) show the Cartesian profiles in the y - x great plane; for clarity, all profiles are offset vertically (see caption for details). As an alternative representation, the $\hat{w}(\beta)$ curves in Figures A.1(d,f) correspond to the radial deviation from a perfect hemisphere as a function of the global zenith angle, $\beta \in [-60, 60]^\circ$. These limiting angles are chosen as the maximum location of the defects to avoid interactions with the equator boundary [118]. When their widths, λ_i , are too large (Figures A.1c,d) or when their angular separation, $\varphi_{(1,2)}$, is too small (Figures A.1e,f), the two defects can merge to form a single defect.

Following a similar approach as in previous studies [89, 102, 253, 258, 118], we depressurize the clamped hemispherical shell until buckling occurs. Given the actual critical buckling pressure of the imperfect shell, p_{\max} , the knockdown factor is defined as $\kappa = p_{\max}/p_c$, where p_c is the classic prediction for the respective perfect shell geometry [82, 89]. Our goal is to characterize how κ for a shell with the two-defect geometry specified above depends on the following geometric parameters: $\bar{\delta}_i$, λ_i , $\varphi_{(1,2)}$, and R/h . We will give particular attention to identifying the regimes where the interactions between the two defects induce non-trivial changes in κ .

Our main contribution will be the definition of a threshold arc length for the separation between the two defects, beyond which their interactions become negligible. We will consider two versions of this separation-arclength threshold: $l_p = R\varphi_{p(1,2)}$, defined from center-to-center of the defect, and $l_p^* = R\varphi_{p(1,2)}^*$, adjusted to account for edge effects of the defects using $\varphi_{(1,2)}^*$ introduced in Equation (A.2). We provide evidence that this latter arclength, with $m = 1$, is set by

$$l_p^* \approx l_c = 2\pi[12(1 - \nu^2)]^{-1/4}\sqrt{Rh}, \quad (\text{A.4})$$

where l_c , computed in the seminal work by Hutchinson [113], is the theoretical critical buckling wavelength for a spherical shell. More technically, l_c is the full wavelength of the axisymmetric bifurcation mode at the equator of the shell.

In the previous work of Derveni *et al.* [118], we presented preliminary evidence for the result in Equation (A.4), but only with a single value of $R/h = 110$. Hence, we were unable to fully test Equation (A.4). In the present study, we will change this radius-to-thickness ratio within the range $R/h \in [100, 500]$ to examine how l_p^* relates to l_c . Furthermore, in Ref. [118], we reported evidence for the potential interactions between nearby defects and how they can lead to stronger or weaker shells in comparison to single-defect shells. However, the data in that study were limited to a few specific cases. In the present work, we will explore the various geometric parameters of the system systematically and seek to characterize how defect-defect interactions impact κ for spherical shells containing two imperfections.

A.2 Methodology: FEM Simulations

We performed full 3D simulations using the Finite Element Method (FEM) with the commercial software ABAQUS/Standard. In our prior work [118, 110], we validated this approach against precision experiments similar to the multi-defects geometry considered here. Each quarter of the hemispherical shell is discretized in the meridional and azimuthal using four-noded S4R shell elements: a total of 67500 elements for shells with $R/h \leq 300$ and 187500 elements for shells with $R/h \geq 400$. This level of discretization was deemed suitable after conducting a thorough mesh-convergence analysis. To set the initial geometry of the imperfect shell, we initiated with a perfect hemispherical mesh. Subsequently, we introduced nodal displacements according to the desired profiles of the two imperfections, following Equation (A.3), with varying values for the geometric parameters $(\bar{\delta}_i, \lambda_i, \varphi_{(1,2)})$. The shell thickness remained constant throughout the simulations.

The shells were subject to uniform live pressure on their outer surface, while their equator was set as a clamped boundary. We employed a Riks (static) solver with the following parameters for the shells with $R/h \leq 300$: an initial arc length increment of 0.1, a minimum increment of 10^{-5} , and a maximum increment of 0.5. For the thinnest shells with $R/h \geq 400$, the corresponding parameters of the Riks solver were 0.002, 10^{-10} , and 0.2, respectively. Geometric nonlinearities were considered throughout the analysis.

The hemispherical shells were modeled using the material properties of vinylpolysiloxane (VPS-32, Elite Double 32, Zhermack) as a neo-Hookean and incompressible solid; the material had a Poisson's ratio of $\nu \approx 0.5$ and Young's modulus of $E = 1.26$ MPa. These

material properties were chosen to match those of previous shell-buckling experiments [89, 102, 253, 258, 118] used to validate our FEM-simulation approach. The geometric parameters of the two-defect imperfect shells were varied in the following ranges: $\bar{\delta}_i \in [0.5, 3]$, $\lambda_i \in [0.25, 5]$, $R/h \in [100, 500]$ (constant $R = 25.4$ mm, varying h) and $\varphi_{(1,2)} \in [1, 60]^\circ$.

A.3 Hypothesis for the Defect-Defect Interaction Regime

We start our investigation by quantifying how the knockdown factor, κ , of the two-defects shells depends on the radius-to-thickness ratio, R/h . Throughout, we will focus on numerical experiments conducted using the FEM simulation approach described in the preceding section.

In Figure A.2, we plot κ versus the defect-defect angular separation, $\varphi_{(1,2)}$, for shells comprising either (a) two identical or (b) two different defects, at several values of R/h . For now, we set the amplitudes and widths of the defects as follows. For the case of identical defects (Figure A.2a), we fixed $\bar{\delta} = 1.5$ and $\lambda = 1$. For the case of different defects (Figure A.2b), we fixed $\bar{\delta}_1 = 1$, $\bar{\delta}_2 = 1.5$ and $\lambda_1 = \lambda_2 = 1$. All curves are non-monotonic as a function of $\varphi_{(1,2)}$: κ first decreases, reaching a minimum (κ_{\min}), then increases to a maximum (κ_{\max}), and subsequently decreases to a constant plateau value (κ_p). As suggested in Ref. [118], this non-monotonic behavior at small values of $\varphi_{(1,2)}$ arises from defect-defect interactions. By contrast, in the plateau region at large values of $\varphi_{(1,2)}$, the largest defect dominates. Note that the horizontal dashed lines in Figure A.2 correspond to κ values for a single-defect shell with $(\bar{\delta}, \lambda) = (1.5, 1)$ and $R/h = 100$, aligning with the plateaus of all the two-defects curves. The identical-defects shells (Figure A.2a) exhibit higher values of κ_{\max} than the different-defects shells (Figure A.2b), suggesting that defect-defect interactions are less pronounced in the latter case.

To help visualize the buckling process, the insets of Figure A.2 offer representative snapshots of the greater-plane (2D) profiles obtained from the FEM simulations for shells with $R/h = 100$ and various defect-defect angular separations. Near κ_{\min} (e.g., $\varphi_{(1,2)} = 8^\circ$), the two defects are almost superimposed, resulting in a reduced knockdown factor (cf. Equation A.3). For intermediate separations (e.g., $\varphi_{(1,2)} = 14^\circ$), near κ_{\max} , the region between the two defects acts as a constraint for buckling, leading to higher values of κ . When the two defects are sufficiently far apart (e.g., $\varphi_{(1,2)} = 29^\circ$), in the plateau region, the largest defect dominates the buckling.

All the plotted data sets in Figure A.2, with varying R/h values, exhibit the aforementioned non-monotonic behavior of $\kappa(\varphi_{(1,2)})$. However, as R/h increases, the interaction regions

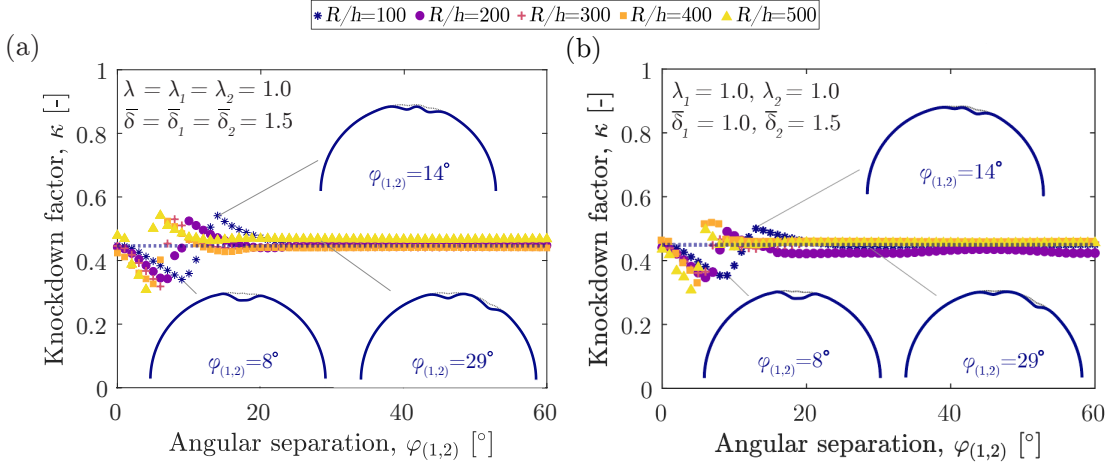


Figure A.2: **Knockdown factor versus angular separation.** Knockdown factor, κ , as a function of angular separation, $\varphi_{(1,2)}$, for (a) identical and (b) different defects. The respective values of λ_i and $\bar{\delta}_i$ are provided in the legend of each plot. Shells with varying radius-to-thickness ratios, R/h , are considered, as indicated in the top legend (common to both panels). Insets: Greater-plane profiles of imperfect shells with $R/h = 100$ and different values of $\varphi_{(1,2)}$ in their original configurations (dotted lines) and at the onset of buckling (solid lines). The radial deviation of the latter is amplified by a factor of 3 for visualization purposes. The horizontal dashed lines correspond to the κ values of a single-defect shell with $R/h = 100$ and $(\bar{\delta}, \lambda) = (1.5, 1)$.

(before the plateau is reached) progressively shift to lower values of $\varphi_{(1,2)}$. This observation highlights the influence of the radius and thickness of the shell on the defect-defect interactions. We hypothesize that the threshold angular separation, below which defects interact and above which the plateau begins, is directly related to \sqrt{Rh} ; the characteristic length scale associated with the balance between bending and stretching effects [258]. Consequently, we anticipate that the onset of the plateau in the $\kappa(\varphi_{(1,2)})$ curves is directly related to the critical buckling wavelength, $l_c \sim \sqrt{Rh}$, as expressed in Equation (A.4). The results in the next section will confirm this hypothesis.

A.4 Interactions between Two Identical Defects

In this section, we focus solely on imperfect shells with two *identical* defects. The angular separation between their centers, $\varphi_{(1,2)}$, can be recast as the defect-defect separation *arc length*, $l = R\varphi_{(1,2)}$. Our objective is to quantify the dependence of the FEM-computed knockdown factor, κ , for these shells on l , R/h , $\bar{\delta}$, and λ .

In Figure A.3, we present $\kappa(l)$ curves for a shell with $R/h = 100$: in panel (a) for fixed widths ($\lambda = 1$) while varying their amplitudes ($\bar{\delta} \in [0.5, 3]$), and, in (b), for fixed

defect amplitudes ($\bar{\delta} = 1.5$) while varying their widths ($\lambda \in [0.25, 5]$). In both plots, the vertical lines represent the critical buckling wavelength for a spherical shell, l_c , provided in Equation (A.4) [113], for this shell with $R/h = 100$. Note that l_c does not depend on any of the defect parameters. Figure A.3(a) and Figure A.3(b) both exhibit non-monotonic $\kappa(l)$, indicative of defect-defect interactions, which consistently occur for $l \lesssim l_c$ (shaded region). For $l \gtrsim l_c$, all curves reach a plateau. Naturally, the specific values of κ_{\min} , κ_{\max} , and κ_p depend on the actual defect geometry, as extensively investigated in previous studies for single-defect [89, 105, 110] and many-defects[118] scenarios.

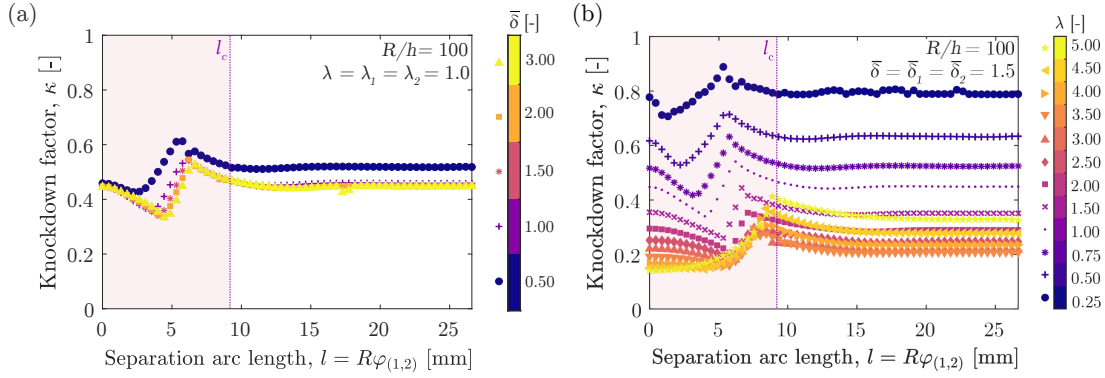


Figure A.3: **Knockdown factor versus separation arc length.** Knockdown factor, κ , for a shell with $R/h = 100$ as a function of the defect-defect arclength, l , for identical defects. Panel (a): fixed $\lambda = 1$, varying $\bar{\delta} \in [0.5, 3]$. Panel (b): fixed $\bar{\delta} = 1.5$, varying $\lambda \in [0.25, 5]$. Different markers and a color bar distinguish the various parameter values. The vertical dotted line presents the theoretical, critical buckling wavelength, l_c (cf. Equation A.4), for $R/h = 100$.

We now select some data from Figure A.3(a), for $\lambda = 1$ and $\bar{\delta} = \{0.5, 1.0, 1.5\}$, and from Figure A.3(b), for $\bar{\delta} = 1.5$ and $\lambda = \{0.5, 1.0, 3.0\}$, and present them in Figure A.4(a) and (b) as a function of the normalized arc length l/l_c . Additional simulation data for $R/h = 200$ and 500 are included. The shaded regions indicate small angular separations where the two defects overlap (cf. the corresponding 2D profiles in Figure A.1). It is remarkable that all the $\kappa(l/l_c)$ data collapse, with the emergence of their plateaus past $l/l_c \gtrsim 1$.

The aforementioned observation regarding the onset of the plateau underscores the importance of the critical buckling wavelength, l_c , in setting the threshold arc length separation for the defect-defect interaction regime. This finding represents an important step in confirming the hypothesis laid out in Section A.3. To quantify this threshold, we consider the maximum (κ_{\max}) and plateau (κ_p) values of the $\kappa(l)$ curves in Figures A.3 and A.4. The threshold separation is defined as the arc length corresponding to the 10%

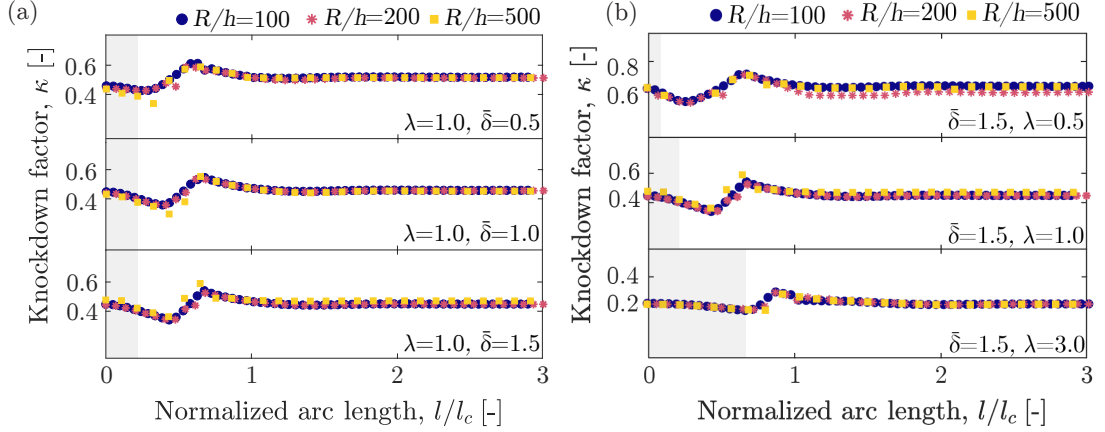


Figure A.4: **Knockdown factor versus normalized arc length.** Knockdown factor, κ , as a function of l/l_c , the defect-defect arc length normalized by the critical buckling wavelength defined in Equation (A.4). (a) Constant $\lambda = 1$, varying $\bar{\delta}$. (b) Constant $\bar{\delta} = 1.5$, varying λ . The different markers refer to various radius-to-thickness ratios, R/h . The shaded areas indicate the regions where the defects overlap, resulting in a single larger defect.

cut-off: $0.1(\kappa_{\max} - \kappa_p)$. An uncertainty of $\pm 0.05(\kappa_{\max} - \kappa_p)$ is assigned to each threshold value to account for the non-sharp onset of the plateau, consistently with the percentual definitions used in previous work [105]. As mentioned in Section A.1, there are two possible definitions for the defects separation arc length, l_p or l_p^* , depending on whether we consider the center-to-center ($\phi_{(1,2)}$) or the adjusted ($\phi_{(1,2)}^*$) angular separations, respectively. The latter excludes a portion from the core of the defects and was defined in Equation (A.2). Schematics illustrating these two definitions are provided in Figure A.5 (top).

At this point, it is important to revisit the Gaussian shape (cf. Equation A.1) of the dimpled imperfections we are considering. Note that, at the local angular coordinate of each defect $\alpha = m \alpha_i$, its deviation from the perfect sphere is $\hat{w}_i = -\delta_i e^{-m}$. Also, $\alpha_i/\sqrt{2}$ can be interpreted as the standard deviation of this Gaussian shape, $\hat{w}_i(\alpha)$. Therefore, l_p^* can be seen as excluding some portion of the core of each defect. Taking the values $m = 1, 2$, or 3 corresponds to excluding 68.3%, 95.6%, and 99.7% of the defect, respectively [365]. The choice of m determines the extent to which the core of the defect is excluded, with $m = 3$ effectively considering the edge-to-edge separation between defects. It is important to note that at $\alpha = \alpha_i/\sqrt{2}$, there is an inflection point in Equation (A.2) and $\hat{w}_i''(\alpha_i/\sqrt{2}) = 0$.

We have measured l_p or l_p^* as functions of l_c , for shells with $R/h \in [100, 500]$ and two identical defects with $(\bar{\delta}, \lambda) = (1.5, 1.0)$. It is worth noting that the different values of

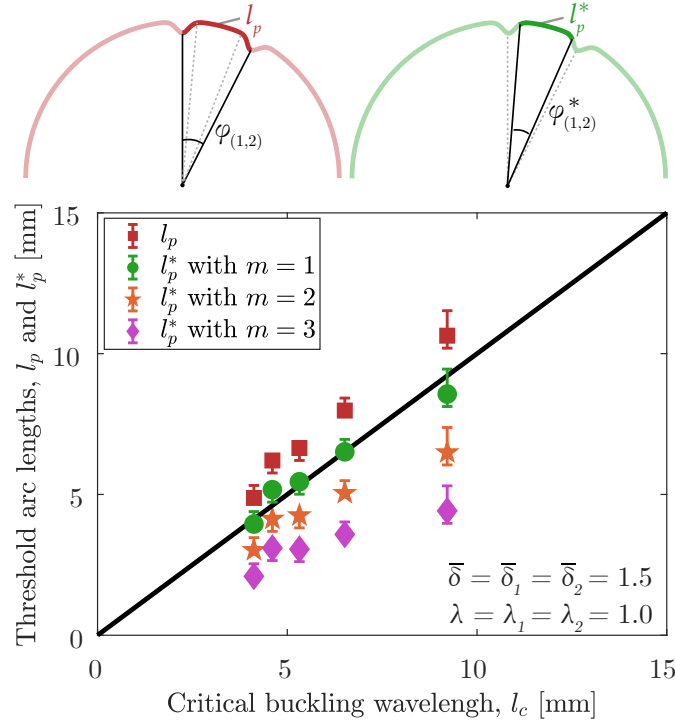


Figure A.5: **Threshold arc length versus the critical buckling wavelength.** Threshold arc length separations for the interaction regime, l_p and l_p^* , versus the critical buckling wavelength, l_c , for identical defects with $\bar{\delta} = 1.5$ and $\lambda = 1$. Both $l_p = R\varphi_{(1,2)}$ (squares) and $l_p^* = R\varphi_{(1,2)}^*$ (circles for $m = 1$, pentagams for $m = 2$, and diamonds for $m = 3$) threshold definitions are examined, as illustrated in the 2D schematics (top). The threshold values, l_p and l_p^* are computed as described in the text. The error bars represent $\pm 0.05|\kappa_{\max} - \kappa_p|$. The solid line represents $l_p = l_p^* = l_c$.

R/h yield different values of l_c according to Equation (A.4); specifically, l_c increases as R/h decreases. The results shown in Figure A.5 confirm the hypothesis presented in Section A.3: there is a clear *linear* scaling between l_p or l_p^* with varying m values (cf. Equation A.2) and l_c . What is more, when using the l_p^* definition with $m = 1$, the data lie on the line $l_p^* = l_c$. This remarkable result demonstrates that the threshold separation for defect-defect interactions is set by the critical buckling wavelength of the shell at the inflection point in the Gaussian profile, $\hat{w}(\alpha_i)$. Hence, for the remainder of our study, we will adopt the definition of l_p^* with $m = 1$.

Having examined the specific geometry for an imperfect shell with $(\bar{\delta}, \lambda) = (1.5, 1.0)$ (albeit with different R/h), we now explore the geometric parameter space more systematically. In Figure A.6(a), we plot l_p^*/l_c as a function of $\bar{\delta}$ (with fixed $\lambda = 1.0$), and in Figure A.6(b) λ (with fixed $\bar{\delta} = 1.5$), for different R/h values (see legend). Overall, the data consistently align closely with $l_p^*/l_c = 1$ (horizontal dashed line), especially

when $\bar{\delta} \geq 1$ (Figure A.6a) and $\lambda \leq 2.5$ (Figure A.6b). In Figure A.6(a), l_p^*/l_c remains approximately constant for all $\bar{\delta} \in [0.5, 3]$ and all $R/h \in [100, 500]$. As also highlighted in Figure A.3(a), the l_p^*/l_c data lie almost on top of the dashed line, deviating by at most 20% within the entire range of $\bar{\delta}$ that we explored. More quantitatively, in Figure A.6(b), for shells with $\lambda \leq 2.5$, the FEM-measured l_p^* is in excellent agreement with the analytical result for l_c , within a 16% difference. For wider defects with $\lambda \geq 2.5$, l_p^* deviates by up to $\approx 50\%$ from l_c . Note that in these shells with wide defects (large λ values), the two defects tend to be nearly juxtaposed, as seen in the profiles in Figure A.1(c) and (d), as well as the shaded region in Figure A.6b (for shells with $R/h = 100$). We attribute the larger deviations of l_p^*/l_c from unity for shells with wide defects to their overlap, which leads to a distorted, imperfect shell geometry.

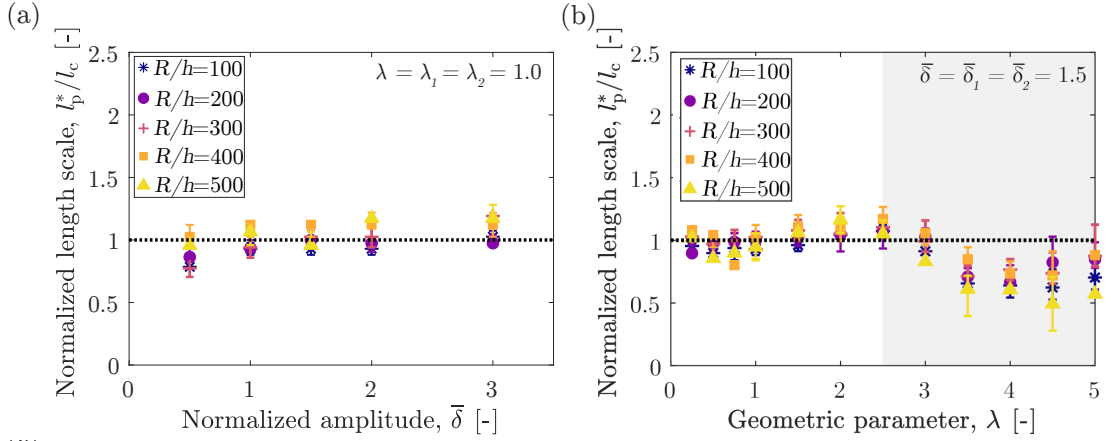


Figure A.6: **Normalized length scale versus defect geometry** Normalized threshold defect-defect arclength, l_p^*/l_c , versus (a) normalized amplitude, $\bar{\delta}$, and (b) normalized width, λ , for various values of $R/h \in [100, 500]$. In panel (a), $\lambda = 1$ is kept fixed, and in panel (b), $\bar{\delta} = 1.5$ is fixed. Each marker represents a different value of $R/h \in [100, 500]$, and the horizontal dashed lines correspond to $l_p^* = l_c$. The shaded area in panel (b) highlights the region where defects tend to overlap, forming a single larger defect.

A.5 Interactions between Two Different Defects

In the previous section, we examined shells with two identical defects. Now, we shift our focus to the case of different defects ($\bar{\delta}_1 \neq \bar{\delta}_2$ or $\lambda_1 \neq \lambda_2$). We will fix the geometry of the $i = 1$ defect at the pole with $(\lambda_1, \bar{\delta}_1) = (1.0, 1.0)$, and vary the width (λ_2) and amplitude ($\bar{\delta}_2$) of the second defect.

In Figure A.7(a), we plot the knockdown factor, κ , as a function of defect-defect arc length separation, l , for shells with fixed $R/h = 100$ and $\lambda_2 = 1.0$, while varying $\bar{\delta}_2 \in [0.5, 3]$.

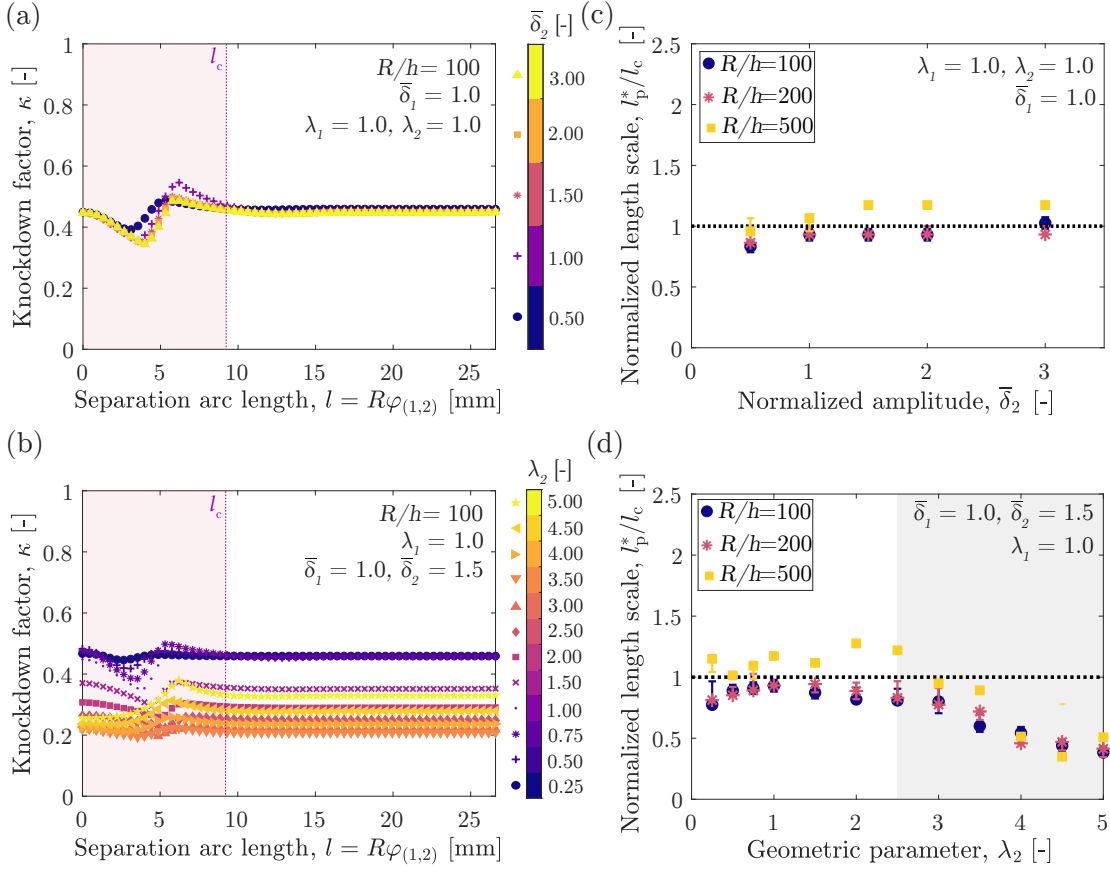


Figure A.7: **Knockdown factor, κ , versus arc length, l , for shells with $R/h = 100$.** (a) Fixed $\lambda_1 = \lambda_2 = 1$, $\bar{\delta}_1 = 1$ and varying $\bar{\delta}_2 \in [0.5, 3]$. (b) Fixed $\bar{\delta}_1 = 1$, $\bar{\delta}_2 = 1.5$, $\lambda_1 = 1$ and varying $\lambda_2 \in [0.25, 5]$. Normalized arclength, l_p^*/l_c , versus (c) $\bar{\delta}_2$, and (d) λ_2 for $R/h \in [100, 500]$. Different markers and colors are used to represent different (a) $\bar{\delta}_2$, (b) λ_2 , and (c,d) R/h . The vertical dashed lines in panels (a,b) refer to the theoretical prediction of l_c for shells with $R/h = 100$, while the horizontal dashed lines in panels (c,d) represent $l_p^* = l_c$. The shaded region in panel (d) indicates the region where defects overlap, forming a single larger defect (shown for $R/h = 100$, as a representative example).

These $\kappa(l)$ curves are similar to those for the identical-defects case discussed in Section A.4: κ initially decreases to κ_{\min} , then increases κ_{\max} , before settling to a plateau (κ_p). The exact values of κ_{\min} , κ_{\max} , and κ_p are slightly influenced by the amplitude of the $i = 2$ defect, particularly for $\bar{\delta}_2 = \{0.5, 1.0\}$, but not for $\bar{\delta}_2 > 1.0$, consistent with the known sensitivity of shell buckling to imperfections [89].

In Figure A.7(b), we present $\kappa(l)$ curves for shells with a fixed $R/h = 100$ and $\bar{\delta}_2 = 1.5$, while varying $\lambda_2 \in [0.25, 5]$. The response of these shells is qualitatively different from the behavior described in the previous paragraph, exhibiting three distinct regimes. In the first, when $\lambda_2 \leq 1$, the $\kappa(l)$ curves show the same minimum-maximum-plateau dependence

described above and in Section A.4. Since $\lambda_2 > \lambda_1$, the plateau is dictated by the largest ($i = 2$) defect. In the second regime, for $1.5 \leq \lambda_2 \leq 3$, the $\kappa(l)$ curves shift, as a whole, to lower values. While a clear minimum is still observed, the maximum becomes less prominent, tending towards $\kappa_{\max} \rightarrow \kappa_p$. In this regime, the buckling is still dictated by the largest $i = 2$ defect. In the third regime, for $\lambda \geq 3.5$, the $\kappa(l)$ curves shift upwards.

In Figure A.7(a,b), the vertical dotted lines represent the critical buckling wavelength, l_c , defined in Equation (A.4), with $R/h = 100$. Similarly to the case of identical defects, we observe that the region (shaded) of interaction for these shells with two different defects lies within $l < l_c$. As in Section A.4, we also compute the normalized threshold for defect-defect interactions (onset of the plateau of the $\kappa(l)$ curves), l_p^*/l_c , for the present case of different defects. These results are presented in Figure A.7(c,d).

In Figure A.7(c), when fixing $\bar{\delta}_1$, λ_1 , and λ_2 , we observe that $l_p^*/l_c \approx 1$ (within 17%) across the whole range of $\bar{\delta}_2$. This finding reinforces that $\bar{\delta}$ is not critical in determining the onset of defect interactions, consistently with the identical-defects case (Figure A.6a). The behavior becomes less straightforward when varying λ_2 while fixing $\bar{\delta}_1$, λ_1 , and $\bar{\delta}_2$, (see Figure A.7d). Here, l_p^*/l_c remains near unity for $\lambda_2 \leq 3$, with a deviation of around 22% for $\lambda_2 \in [0.25, 1]$ and 28% for $\lambda_2 \in [1.5, 3]$. However, when $\lambda_2 \geq 3.5$, l_p^*/l_c progressively drops below unity, reaching approximately 0.4. Recalling the profiles in Figure A.1(d), we note that the edges of the narrow $i = 1$ defect overlap with the wider $i = 2$ defect for larger values of λ_2 . Thus, the shell geometry deviates substantially from a perfect sphere, and the critical buckling wavelength in Equation (A.4) no longer sets the edge of the interaction region. This complex behavior, arising from the increasing overlap of the defects and the nontrivial shell geometries, falls beyond the scope of the present work and warrants further investigation.

Note that, in Figure A.7(c,d), while l_p^*/l_c remains close to unity for intermediate values of λ_2 , the thinnest shells with $R/h = 500$ exhibit notable discrepancies compared to the $R/h = \{100, 200\}$ shells (the results for these two are almost overlapping). We have conducted comprehensive mesh-convergence tests, and it appears that the discrepancies are not due to the discretization. Instead, we attribute these deviations to the higher fluctuations observed in the measured $\kappa(l)$ curves, especially in the plateau region, which in turn affects the measurement of l_p^* using the 10% criterion introduced in Section A.4.

A.6 Summary and Outlook

Using experimentally validated FEM simulations, we investigated the effect of defect-defect interactions on the buckling of pressurized hemispherical shells containing two

dimpled imperfections. We examined cases of identical and different defects, varying their geometric parameters (amplitude, $\bar{\delta}_i$, and width, λ_i) and their relative separation. We measured the knockdown factor (the normalized critical buckling pressure), κ , for these imperfect shells as a function of the angular separation, $\varphi_{(1,2)}$, between their two defects. We then used $\varphi_{(1,2)}$ to define an arc length separation $l = R\varphi_{(1,2)}$. Our findings revealed significant defect-defect interactions when the two defects are in close proximity, leading to non-monotonic behavior in $\kappa(l)$, below a threshold in l . We modified the definition of this interaction threshold, denoted as l_p^* , which corresponds to the inflection point of the Gaussian profile. Beyond l_p^* , the $\kappa(l)$ curves reached a plateau, indicating diminished interactions and the dominance of the largest defect in dictating the knockdown factor.

The main contribution of our study lies in establishing that the onset of defect-defect interactions is determined by the critical buckling wavelength [113], as $l_p^* \approx l_c$ (cf. Equation A.4). This result is valid for defects with $\lambda_i < 3$, regardless of whether they are identical or different. However, for wider defects, the dimples tend to overlap, and the shell geometry becomes increasingly distorted. The defect amplitude, $\bar{\delta}_i$, plays a negligible role in setting l_p^* . It is important to note that l_c depends only on the radius, R , and thickness, h , of the shell (other than the Poisson ratio, which was fixed to $\nu = 0.5$ throughout our study).

We hope that our results will stimulate further interest in harnessing defect-defect interactions to enhance the buckling response of spherical shells or inspire the development of novel functional mechanisms derived from these interactions.

Bibliography

- [1] SP Timoshenko and JM Gere. *Theory of Elastic Stability McGraw-Hill, 1961*. Dover reprint of 2nd edition, 2009.
- [2] Basile Audoly and Yves Pomeau. *Elasticity and geometry: from hair curls to the non-linear response of shells*. Oxford University Press, 2010.
- [3] Gemma Ibarz, Lars Dähne, Edwin Donath, and Helmut Möhwald. “Smart micro- and nanocontainers for storage, transport, and release”. *Advanced Materials* 13.17 (2001), pp. 1324–1327.
- [4] K Tsuji. “Microencapsulation of pesticides and their improved handling safety”. *Journal of microencapsulation* 18.2 (2001), pp. 137–147.
- [5] Mary Ann Augustin and Yacine Hemar. “Nano- and micro-structured assemblies for encapsulation of food ingredients”. *Chemical society reviews* 38.4 (2009), pp. 902–912.
- [6] P. Terndrup Pedersen and J. Juncher Jensen. “Buckling behaviour of imperfect spherical shells subjected to different load conditions”. *Thin-Walled Structures. Buckling Strength of Imperfection-sensitive Shells* 23.1 (1995), pp. 41–55.
- [7] James Marston Fitch and Daniel P Branch. “Primitive architecture and climate”. *Scientific American* 203.6 (1960), pp. 134–145.
- [8] William A Nash. *Hydrostatically Loaded Structures: The Structural Mechanics, Analysis and Design of Powered Submersibles*. Elsevier, 1995.
- [9] Edward N Brown, CA Friehe, and DH Lenschow. “The use of pressure fluctuations on the nose of an aircraft for measuring air motion”. *Journal of Applied Meteorology and Climatology* 22.1 (1983), pp. 171–180.
- [10] Pedro M Reis, Fabian Brau, and Pascal Damman. “The mechanics of slender structures”. *Nature Physics* 14.12 (2018), pp. 1150–1151.
- [11] Warner Tjardus Koiter. “Over de stabiliteit van het elastisch evenwicht”. Ph.D. thesis, Delft University of Technology, Delft, The Netherlands (1945).

- [12] Walter Wunderlich and Ursula Albertin. “Buckling behaviour of imperfect spherical shells”. *International Journal of Non-Linear Mechanics* 37.4-5 (2002), pp. 589–604.
- [13] URL: <chrome-extension://efaidnbmnnnnibpcajpcgclefindmkaj/https://condivisionext.rfi.it/Documenti%20condivisi/La%20Stabilit%C3%A0%20del%20binario%20-%2012%20ottobre%202017/Godart%20TEG-LTR.pdf>.
- [14] URL: <https://www.istockphoto.com/de/fotos/dead-leaves-on-white>.
- [15] URL: <https://www.pinterest.ch/pin/179862578850383598/>.
- [16] Eduard Ventsel and Theodor Krauthammer. *Thin Plates and Shells: Theory, Analysis, and Applications*. CRC Press, 2001.
- [17] Chris R Calladine. *Theory of shell structures*. Cambridge university press, 1983.
- [18] Junuthula Narasimha Reddy. *Theory and analysis of elastic plates and shells*. CRC press, 1999.
- [19] Weihua Li, Kosta Kostidis, Xianzhou Zhang, and Yang Zhou. “Development of a force sensor working with MR elastomers”. *2009 IEEE/ASME International Conference on Advanced Intelligent Mechatronics*. Singapore: IEEE, 2009, pp. 233–238.
- [20] Luis Dorfmann and Ray W. Ogden. *Nonlinear Theory of Electroelastic and Magnetoelastic Interactions*. Springer US, 2014.
- [21] Pedro M. Reis. “A Perspective on the Revival of Structural (In)Stability With Novel Opportunities for Function: From Buckliphobia to Buckliphilia”. *Journal of Applied Mechanics* 82.11 (2015).
- [22] Michael Gomez, Derek E Moulton, and Dominic Vella. “Critical slowing down in purely elastic ‘snap-through’ instabilities”. *Nature Physics* 13.2 (2017), pp. 142–145.
- [23] Michael Gomez, Derek E Moulton, and Dominic Vella. “Passive control of viscous flow via elastic snap-through”. *Physical review letters* 119.14 (2017), p. 144502.
- [24] Philipp Rothmund, Alar Ainla, Lee Belding, Daniel J Preston, Sarah Kurihara, Zhigang Suo, and George M Whitesides. “A soft, bistable valve for autonomous control of soft actuators”. *Science Robotics* 3.16 (2018), eaar7986.
- [25] Johannes TB Overvelde, Tamara Kloek, Jonas JA D’haen, and Katia Bertoldi. “Amplifying the response of soft actuators by harnessing snap-through instabilities”. *Proceedings of the National Academy of Sciences* 112.35 (2015), pp. 10863–10868.
- [26] Yancheng Li, Jianchun Li, Weihua Li, and Haiping Du. “A state-of-the-art review on magnetorheological elastomer devices”. *Smart materials and structures* 23.12 (2014), p. 123001.

- [27] Bonnie L Gray. “A review of magnetic composite polymers applied to microfluidic devices”. *Journal of The Electrochemical Society* 161.2 (2014), B3173.
- [28] Lindsey Hines, Kirstin Petersen, Guo Zhan Lum, and Metin Sitti. “Soft actuators for small-scale robotics”. *Advanced materials* 29.13 (2017), p. 1603483.
- [29] Shuai Wu, Wenqi Hu, Qiji Ze, Metin Sitti, and Ruike Zhao. “Multifunctional magnetic soft composites: A review”. *Multifunctional materials* 3.4 (2020), p. 042003.
- [30] Seppe Terryn, Jakob Langenbach, Ellen Roels, Joost Brancart, Camille Bakkali-Hassani, Quentin-Arthur Poutrel, Antonia Georgopoulou, Thomas George Thuruethel, Ali Safaei, Pasquale Ferrentino, et al. “A review on self-healing polymers for soft robotics”. *Materials Today* 47 (2021), pp. 187–205.
- [31] Zhongyi Nie, Jean Won Kwak, Mengdi Han, and John A Rogers. “Mechanically Active Materials and Devices for Bio-Interfaced Pressure Sensors—A Review”. *Advanced Materials* (2022), p. 2205609.
- [32] Ruike Zhao, Yoonho Kim, Shawn A Chester, Pradeep Sharma, and Xuanhe Zhao. “Mechanics of hard-magnetic soft materials”. *Journal of the Mechanics and Physics of Solids* 124 (2019), pp. 244–263.
- [33] Liu Wang, Yoonho Kim, Chuan Fei Guo, and Xuanhe Zhao. “Hard-magnetic elastica”. *Journal of the Mechanics and Physics of Solids* 142 (2020), p. 104045.
- [34] Guo Zhan Lum, Zhou Ye, Xiaoguang Dong, Hamid Marvi, Onder Erin, Wenqi Hu, and Metin Sitti. “Shape-programmable magnetic soft matter”. *Proceedings of the National Academy of Sciences* 113.41 (2016), E6007–E6015.
- [35] A. Dorfmann and R. W. Ogden. “Magnetoelastic modelling of elastomers”. *European Journal of Mechanics-A/Solids* 22 (2003), pp. 497–507.
- [36] Wenqi Hu, Guo Zhan Lum, Massimo Mastrangeli, and Metin Sitti. “Small-scale soft-bodied robot with multimodal locomotion”. *Nature* 554.7690 (2018), pp. 81–85.
- [37] Hongri Gu, Quentin Boehler, Haoyang Cui, Eleonora Secchi, Giovanni Savorana, Carmela De Marco, Simone Gervasoni, Quentin Peyron, Tian-Yun Huang, Salvador Pane, Ann M. Hirt, Daniel Ahmed, and Bradley J. Nelson. “Magnetic cilia carpets with programmable metachronal waves”. *Nature Communications* 11 (2020), p. 2637.
- [38] Yunus Alapan, Alp C Karacakol, Seyda N Guzelhan, Irem Isik, and Metin Sitti. “Reprogrammable shape morphing of magnetic soft machines”. *Science advances* 6.38 (2020), eabc6414.
- [39] Yoonho Kim, German A. Parada, Shengduo Liu, and Xuanhe Zhao. “Ferromagnetic soft continuum robots”. *Science Robotics* 4.33 (2019), eaax7329.

- [40] Olek C Zienkiewicz and Robert L Taylor. *The finite element method for solid and structural mechanics*. Elsevier, 2005.
- [41] A. Lazarus, H. C. B. Florijn, and P. M. Reis. “Geometry-Induced Rigidity in Nonspherical Pressurized Elastic Shells”. *Physical Review Letters* 109 (14 2012), p. 144301.
- [42] Miroslava Nadkova Petrova and Dobrina Zheleva-Martins. “Shells as a Universal Structural Type in Nature and Design”. *Structural Shells [Working Title]*. IntechOpen, 2022.
- [43] Eleni Katifori, Silas Alben, Enrique Cerda, David R. Nelson, and Dumais Jacques. “Foldable structures and the natural design of pollen grains”. *Proceedings of the National Academy of Sciences USA* 107.17 (2010), pp. 7635–7639.
- [44] Mark Hilburger. “Developing the next generation shell buckling design factors and technologies”. *53rd AIAA/ASME/ASCE/AHS/ASC Structures, Structural Dynamics and Materials Conference 20th AIAA/ASME/AHS Adaptive Structures Conference 14th AIAA*. 2012, p. 1686.
- [45] URL: <https://news.utk.edu/2019/02/12/nature-prefers-asymmetrical-pollen-grains-study-finds/>.
- [46] URL: <https://www.pinterest.ch/pin/art-design--724938871251632024/>.
- [47] URL: https://commons.wikimedia.org/wiki/File:T%C3%A9l%C3%A9phone_Crane_Profil_Droit.jpg.
- [48] URL: <https://www.irishtimes.com/business/retail-and-services/galway-egg-firm-entitled-to-injunction-against-competitor-1.3766727>.
- [49] URL: <https://materialdistrict.com/article/coconut-world-coconut-day/>.
- [50] URL: <https://www.beiberia.com/top-5-best-beaches-of-portugal/>.
- [51] URL: <https://pharmaceuticalmanufacturer.media/pharmaceutical-industry-insights/the-hard-line/>.
- [52] URL: <https://www.usaeop.com/blog/ceramics-what-creates-the-basis-for-our-daily-objects/>.
- [53] URL: <https://www.actionnews5.com/2019/04/19/breakdown-science-behind-how-airplanes-fly-sky/>.
- [54] URL: <https://www.futurethink.com.sg/leadershipstylequestionnaire/can-learn-1986-challenger-disaster-2/>.
- [55] URL: <https://www.digitimes.com/news/a20230103VL206/gps-satellite-south-korea.html>.

- [56] Florent Savine, François-Xavier Irisarri, Cédric Julien, Angela Vincenti, and Yannick Guerin. “A component-based method for the optimization of stiffener layout on large cylindrical rib-stiffened shell structures”. *Structural and Multidisciplinary Optimization* 64.4 (2021), pp. 1843–1861.
- [57] Davide Ferretto, Oscar Gori, Roberta Fusaro, and Nicole Viola. “Integrated Flight Control System Characterization Approach for Civil High-Speed Vehicles in Conceptual Design”. *Aerospace* 10.6 (2023), p. 495.
- [58] João Paulo Eguea, Gabriel Pereira Gouveia da Silva, and Fernando Martini Catalano. “Fuel efficiency improvement on a business jet using a camber morphing winglet concept”. *Aerospace Science and Technology* 96 (2020), p. 105542.
- [59] Michael Nemeth, James Starnes Jr, Michael Nemeth, and James Starnes Jr. “The NASA monographs on shell stability design recommendations-A review and suggested improvements”. *38th Structures, Structural Dynamics, and Materials Conference*. 1997, p. 1302.
- [60] Joshua P Davis, John P Mayberry, and Jay P Penn. “On-orbit servicing: Inspection repair refuel upgrade and assembly of satellites in space”. The Aerospace Corporation, report (2019), p. 25.
- [61] Robert Millard Jones. *Buckling of bars, plates, and shells*. Bull Ridge Corporation, 2006.
- [62] Russell C Hibbeler and Gary Nolan. *Structural analysis*. Prentice Hall Upper Saddle River^ eNew Jersey New Jersey, 1997.
- [63] Eric W Weisstein. “Solid of revolution”. <https://mathworld.wolfram.com/> (2006).
- [64] Earl William Swokowski. *Calculus with analytic geometry*. Taylor & Francis, 1979.
- [65] Robert Merton. “A History Of Mechanical Inventions By Abbott Payson Usher” (1935).
- [66] Allison Lee Palmer. *Leonardo da Vinci: A reference guide to his life and works*. Rowman & Littlefield, 2018.
- [67] Morris H Shamos. *Great experiments in physics: firsthand accounts from Galileo to Einstein*. Courier Corporation, 1987.
- [68] JE Marquina, ML Marquina, V Marquina, and JJ Hernández-Gómez. “Leonhard Euler and the mechanics of rigid bodies”. *European Journal of Physics* 38.1 (2016), p. 015001.
- [69] Dimitar N Karastoyanov, Lyubka A Doukovska, and Vassia K Atanassova. “Electromagnetic linear micro drives for Braille screen: characteristics, control and optimization”. *Proc. of the Third International Conference on Telecommunications and Remote Sensing-ICTRS’*. Vol. 14. 2014, pp. 88–93.

- [70] Carl Friedrich Gauss. *Theoria combinationis observationum erroribus minimis obnoxiae*. Vol. 3. Dieterich, 1828.
- [71] Augustus Edward Hough Love. “XVI. The small free vibrations and deformation of a thin elastic shell”. *Philosophical Transactions of the Royal Society of London*.(A.) 179 (1888), pp. 491–546.
- [72] Raymond David Mindlin and Jiashi Yang. *An introduction to the mathematical theory of vibrations of elastic plates*. World Scientific, 2006.
- [73] GJ Hutchins and AI Soler. “Approximate elasticity solution for moderately thick shells of revolution” (1973).
- [74] Eric Reissner. “On axisymmetrical deformations of thin shells of revolution”. *Proceedings of Symposia in Applied Mathematics*. Vol. 3. 1. 1950, pp. 27–52.
- [75] J Lyell Sanders Jr. “Nonlinear theories for thin shells”. *Quarterly of Applied Mathematics* 21.1 (1963), pp. 21–36.
- [76] Bernard Budiansky. “On the best first-order linear shell theory”. *The Prager Anniversary Volume-Progress in Applied Mechanics* (1963).
- [77] Lev Davidovich Landau, Evgenij M Lifšic, Evgenii Mikhailovich Lifshitz, Arnold Markovich Kosevich, and Lev Petrovich Pitaevskii. *Theory of elasticity: volume 7*. Vol. 7. Elsevier, 1986.
- [78] C. D. Babcock. “Shell stability”. *Journal of Applied Mechanics* 50.4b (1983), pp. 935–940.
- [79] L. A. Samuelson and S. Eggwertz. *Shell Stability Handbook*. London: Elsevier Applied Science, 1992.
- [80] I. Elishakoff. *Resolution of the Twentieth Century Conundrum in Elastic Stability*. Singapore: World Scientific Publishing, 2014.
- [81] Sujit S. Datta, Alireza Abbaspourrad, Esther Amstad, Jing Fan, Shin-Hyun Kim, Mark Romanowsky, Ho Cheung Shum, Bingjie Sun, Andrew S. Utada, and Maike Windbergs. “25th anniversary article: Double emulsion templated solid microcapsules: Mechanics and controlled release”. *Advanced Materials* 26.14 (2014), pp. 2205–2218.
- [82] R. Zoelly. “Ueber ein knickungsproblem an der kugelschale”. Ph.D. thesis, ETH Zürich, Zürich, Switzerland (1915).
- [83] H.-S. Tsien. “A theory for the buckling of thin shells”. *Journal of the Aeronautical Sciences* 9.10 (1942), pp. 373–384.
- [84] A. Kaplan and Y. C. Fung. *A nonlinear theory of bending and buckling of thin elastic shallow spherical shells*. Technical Note 3212. Washington, DC: National Advisory Committee for Aeronautics, 1954.

- [85] R. H. Homewood, A. C. Brine, and Aldie E. Johnson. “Experimental investigation of the buckling instability of monocoque shells”. *Experimental Mechanics* 1.3 (1961), pp. 88–96.
- [86] L. Seaman. “The nature of buckling in thin spherical shells”. Ph.D. thesis. Cambridge, MA: Massachusetts Institute of Technology, 1962.
- [87] M. A. Krenzke and T. J. Kiernan. “Elastic stability of near-perfect shallow spherical shells”. *AIAA Journal* 1.12 (1963), pp. 2855–2857.
- [88] R. L. Carlson, R. L. Sendelbeck, and N. J. Hoff. “Experimental studies of the buckling of complete spherical shells”. *Experimental Mechanics* 7.7 (1967), pp. 281–288.
- [89] Anna Lee, Francisco López Jiménez, Joel Marthelot, John W Hutchinson, and Pedro M Reis. “The geometric role of precisely engineered imperfections on the critical buckling load of spherical elastic shells”. *Journal of Applied Mechanics* 83.11 (2016), p. 111005.
- [90] J. W. Hutchinson, D. B. Muggeridge, and R. C. Tennyson. “Effect of a local axisymmetric imperfection on the buckling behavior of a circular cylindrical shell under axial compression”. *AIAA Journal* 9.1 (1971), pp. 48–52.
- [91] B. Budiansky and J. W. Hutchinson. “Buckling of circular cylindrical shells under axial compression”. *Contributions to the Theory of Aircraft Structures*. The Netherlands: Delft University Press, 1972, pp. 239–259.
- [92] Th. von Kármán and H.-S. Tsien. “The buckling of spherical shells by external pressure”. *Journal of the Aeronautical Sciences* 7.2 (1939), pp. 43–50.
- [93] Th von Karman. “The influence of curvature on the buckling characteristics of structures”. *Journal of the Aeronautical Sciences* 7.7 (1940), pp. 276–289.
- [94] Theodore von Karman. “The buckling of thin cylindrical shells under axial compression”. *Journal of the Aeronautical Sciences* 8.8 (1941), pp. 303–312.
- [95] P. P. Bijlaard and R. H. Gallagher. “Elastic instability of a cylindrical shell under arbitrary circumferential variation of axial stress”. *Journal of the Aerospace Sciences* 27.11 (1960), pp. 854–858.
- [96] Bo O Almroth. “Influence of edge conditions on the stability of axially compressed cylindrical shells.” *AIAA Journal* 4.1 (1966), pp. 134–140.
- [97] Shigeo Kobayashi. “The influence of the boundary conditions on the buckling load of cylindrical shells under axial compression”. *The Journal of the Japan Society of Aeronautical Engineering* 16.170 (1968), pp. 74–82.

- [98] W. L. Chen. “Effect of geometrical imperfection on the elastic buckling of thin shallow spherical shells”. Ph.D. thesis. Cambridge, MA: Massachusetts Institute of Technology, 1959.
- [99] Mark W Hilburger, Michael P Nemeth, and James H Starnes Jr. “Shell buckling design criteria based on manufacturing imperfection signatures”. *AIAA J.* 44.3 (2006), pp. 654–663.
- [100] JMT Thompson. “Making of thin metal shells for model stress analysis”. *Journal of Mechanical Engineering Science* 2.2 (1960), pp. 105–108.
- [101] A. Lee, P.-T. Brun, J. Marthelot, G. Balestra, F. Gallaire, and P. M. Reis. “Fabrication of slender elastic shells by the coating of curved surfaces”. *Nature Communications* 7 (2016), p. 11155.
- [102] Joel Marthelot, Francisco López Jiménez, Anna Lee, John W. Hutchinson, and Pedro M. Reis. “Buckling of a Pressurized Hemispherical Shell Subjected to a Probing Force”. *Journal of Applied Mechanics* 84.12 (2017), p. 121005.
- [103] Anna Lee, Dong Yan, Matteo Pezzulla, Douglas P Holmes, and Pedro M Reis. “Evolution of critical buckling conditions in imperfect bilayer shells through residual swelling”. *Soft Matter* 15.30 (2019), pp. 6134–6144.
- [104] Dong Yan, Matteo Pezzulla, Lilian Cruveiller, Arefeh Abbasi, and Pedro M Reis. “Magneto-active elastic shells with tunable buckling strength”. *Nature communications* 12.1 (2021), p. 2831.
- [105] Francisco López Jiménez, Joel Marthelot, Anna Lee, John W. Hutchinson, and Pedro M. Reis. “Technical brief: knockdown factor for the buckling of spherical shells containing large-amplitude geometric defects”. *Journal of Applied Mechanics* 84 (2017), p. 034501.
- [106] John W. Hutchinson. “Buckling of spherical shells revisited”. *Proceeding of the Royal Society A: Mathematical, Physical and Engineering Sciences* 472.2195 (2016), p. 20160577.
- [107] Hutchinson John W. and Thompson J. Michael T. “Nonlinear buckling behaviour of spherical shells: barriers and symmetry-breaking dimples”. *Philosophical Transactions of the Royal Society A: Mathematical, Physical and Engineering Sciences* 375.2093 (2017), p. 20160154.
- [108] John W. Hutchinson and J. Michael T. Thompson. “Nonlinear buckling interaction for spherical shells subject to pressure and probing forces”. *Journal of Applied Mechanics* 84.6 (2017), p. 061001.

- [109] John W. Hutchinson and J. Michael T Thompson. “Imperfections and energy barriers in shell buckling”. *Int. J. Solids Struct. Special Issue Dedicated to the Memory of George Simitses* 148-149 (2018), pp. 157–168.
- [110] Arefeh Abbasi, Fani Derveni, and Pedro M. Reis. “Comparing the Buckling Strength of Spherical Shells With Dimpled Versus Bumpy Defects”. *Journal of Applied Mechanics* 90.6 (2023), p. 061008.
- [111] Luc Wullschlegler. “Numerical investigation of the buckling behaviour of axially compressed circular cylinders having parametric initial dimple imperfections”. PhD thesis. ETH Zurich, 2006.
- [112] Fani Derveni, Arefeh Abbasi, and Pedro Reis. “Defect-Defect Interactions in the Buckling of Imperfect Spherical Shells”. *Journal of Applied Mechanics* (2023), pp. 1–10.
- [113] J. W. Hutchinson. “Imperfection Sensitivity of Externally Pressurized Spherical Shells”. *Journal of Applied Mechanics* 34 (1967), pp. 49–55.
- [114] John C Amazigo. “Buckling under axial compression of long cylindrical shells with random axisymmetric imperfections”. *Quarterly of Applied Mathematics* 26.4 (1969), pp. 537–566.
- [115] Isaac Elishakoff and Johann Arbocz. “Reliability of axially compressed cylindrical shells with random axisymmetric imperfections”. *International Journal of Solids and Structures* 18.7 (1982), pp. 563–585.
- [116] Isaac Elishakoff and Johann Arbocz. “Reliability of axially compressed cylindrical shells with general nonsymmetric imperfections” (1985).
- [117] Isaac Elishakoff. “Probabilistic resolution of the twentieth century conundrum in elastic stability”. *Thin-Walled Structures* 59 (2012), pp. 35–57.
- [118] Fani Derveni, William Gueissaz, Dong Yan, and Pedro M Reis. “Probabilistic buckling of imperfect hemispherical shells containing a distribution of defects”. *Philosophical Transactions of the Royal Society A* 381.2244 (2023), p. 20220298.
- [119] Ronald Aylmer Fisher and Leonard Henry Caleb Tippett. “Limiting forms of the frequency distribution of the largest or smallest member of a sample”. *Mathematical proceedings of the Cambridge philosophical society*. Vol. 24. 2. 1928, pp. 180–190.
- [120] Waloddi Weibull. “The phenomenon of rupture in solids”. *IVA Handlingar* 153 (1939).
- [121] Waloddi Weibull. “A statistical distribution function of wide applicability”. *Journal of Applied Mechanics* (1951).
- [122] A. De S. Jayatilaka and K. Trustrum. “Statistical approach to brittle fracture”. *Journal of Materials Science* 12.7 (1977), pp. 1426–1430.

- [123] Zdeněk P Bažant, Jia-Liang Le, and Martin Z Bazant. “Scaling of strength and lifetime probability distributions of quasibrittle structures based on atomistic fracture mechanics”. *Proceedings of the National Academy of Sciences* 106.28 (2009), pp. 11484–11489.
- [124] Jia-Liang Le, Roberto Ballarini, and Zhiren Zhu. “Modeling of probabilistic failure of polycrystalline silicon MEMS structures”. *Journal of the American Ceramic Society* 98.6 (2015), pp. 1685–1697.
- [125] J. Michael T. Thompson and Jan Sieber. “Shock-sensitivity in shell-like structures: with simulations of spherical shell buckling”. *International Journal of Bifurcation and Chaos* 26.2 (2016), p. 1630003.
- [126] J Michael T Thompson, John W Hutchinson, and Jan Sieber. “Probing shells against buckling: a nondestructive technique for laboratory testing”. *International Journal of Bifurcation and Chaos* 27.14 (2017), p. 1730048.
- [127] Emmanuel Viot, Tobias Kreilos, Tobias M. Schneider, and Shmuel M. Rubinstein. “Stability landscape of shell buckling”. *Physical Review Letters* 119.22 (2017), p. 224101.
- [128] Maria Esslinger and Bodo Geier. *Calculated post-buckling loads as lower limit of experimental axial buckling loads of circular cylinders*. German Research and Testing Institute for Aerospace, 1972.
- [129] Jiří Horák, Gabriel J Lord, and Mark A Peletier. “Cylinder buckling: the mountain pass as an organizing center”. *SIAM Journal on Applied Mathematics* 66.5 (2006), pp. 1793–1824.
- [130] J. Michael T. Thompson. “Advances in shell buckling: theory and experiments”. *International Journal of Bifurcation and Chaos* 25.1 (2015), p. 1530001.
- [131] J Michael T Thompson and Jan Sieber. “Shock-sensitivity in shell-like structures: with simulations of spherical shell buckling”. *International Journal of Bifurcation and Chaos* 26.02 (2016), p. 1630003.
- [132] Lorenz Baumgarten and Jan Kierfeld. “Shallow shell theory of the buckling energy barrier: From the Pogorelov state to softening and imperfection sensitivity close to the buckling pressure”. *Physical Review E* 99 (2019), p. 022803.
- [133] Tobias Kreilos and Tobias M. Schneider. “Fully localized post-buckling states of cylindrical shells under axial compression”. *Proceedings of the Royal Society A: Mathematical, Physical and Engineering Sciences* 473.2205 (2017), p. 20170177.
- [134] Don O Brush, Bo O Almroth, and JW Hutchinson. “Buckling of bars, plates, and shells” (1975).

- [135] Haigui Fan. “Critical buckling load prediction of axially compressed cylindrical shell based on non-destructive probing method”. *Thin-Walled Structures* 139 (2019), pp. 91–104.
- [136] Kshitij Kumar Yadav and Simos Gerasimidis. “A nondestructive method to find the buckling capacity for thin shells”. *Proceedings of the Annual Stability Conference*. Proceedings of the Annual Stability Conference. Atlanta, GA: Structural Stability Research Council, 2020.
- [137] Kshitij Kumar Yadav, Nicholas L. Cuccia, Emmanuel Viot, Shmuel M. Rubinstein, and Simos Gerasimidis. “A Nondestructive Technique for the Evaluation of Thin Cylindrical Shells’ Axial Buckling Capacity”. *Journal of Applied Mechanics* 88.5 (2021), p. 051003.
- [138] Anaïs Abramian, Emmanuel Viot, Emilio Lozano, Shmuel M. Rubinstein, and Tobias M. Schneider. “Nondestructive Prediction of the Buckling Load of Imperfect Shells”. *Physical Review Letters* 125.22 (2020), p. 225504.
- [139] Suhas Ankalkhope and Sandeep Jose. “Non-destructive prediction of buckling load of axially compressed cylindrical shells using Least Resistance Path to Probing”. *Thin-Walled Structures* 170 (2022), p. 108497.
- [140] Rainer MJ Groh and Alberto Pirrera. “Spatial chaos as a governing factor for imperfection sensitivity in shell buckling”. *Physical Review E* 100.3 (2019), p. 032205.
- [141] Jiajia Shen, RMJ Groh, Mark Schenk, and Alberto Pirrera. “Experimental path-following of equilibria using Newton’s method. Part II: applications and outlook”. *International Journal of Solids and Structures* 213 (2021), pp. 25–40.
- [142] Nicholas L Cuccia, Kshitij Kumar Yadav, Marec Serlin, Emmanuel Viot, Simos Gerasimidis, and Shmuel M Rubinstein. “Hitting the mark: probing at the initiation site allows for accurate prediction of a thin shell’s buckling load”. *Philosophical Transactions of the Royal Society A* 381.2244 (2023), p. 20220036.
- [143] Hamid Souri, Hritwick Banerjee, Ardian Jusufi, Norbert Radacsi, Adam A Stokes, Inkyu Park, Metin Sitti, and Morteza Amjadi. “Wearable and stretchable strain sensors: materials, sensing mechanisms, and applications”. *Advanced Intelligent Systems* 2.8 (2020), p. 2000039.
- [144] Tingting Ye, Jiacheng Wang, Yiding Jiao, Luhe Li, Er He, Lie Wang, Yiran Li, Yanjing Yun, Dan Li, Jiang Lu, et al. “A tissue-like soft all-hydrogel battery”. *Advanced Materials* 34.4 (2022), p. 2105120.
- [145] Yoonho Kim and Xuanhe Zhao. “Magnetic soft materials and robots”. *Chemical reviews* 122.5 (2022), pp. 5317–5364.

- [146] Yuchen Wang, Jiaqi Liu, and Shu Yang. “Multi-functional liquid crystal elastomer composites”. *Applied Physics Reviews* 9.1 (2022), p. 011301.
- [147] Andreas Lendlein, Hongyan Jiang, Oliver Jünger, and Robert Langer. “Light-induced shape-memory polymers”. *Nature* 434.7035 (2005), pp. 879–882.
- [148] Timothy F Scott, Andrew D Schneider, Wayne D Cook, and Christopher N Bowman. “Photoinduced plasticity in cross-linked polymers”. *Science* 308.5728 (2005), pp. 1615–1617.
- [149] Marc Behl and Andreas Lendlein. “Shape-memory polymers”. *Materials today* 10.4 (2007), pp. 20–28.
- [150] Yiping Liu, Ken Gall, Martin L Dunn, Alan R Greenberg, and Julie Diani. “Thermomechanics of shape memory polymers: uniaxial experiments and constitutive modeling”. *International Journal of Plasticity* 22.2 (2006), pp. 279–313.
- [151] Yoonho Kim, Hyunwoo Yuk, Ruike Zhao, Shawn A Chester, and Xuanhe Zhao. “Printing ferromagnetic domains for untethered fast-transforming soft materials”. *Nature* 558.7709 (2018), pp. 274–279.
- [152] Alan Wineman and Je-Hong Min. “Time dependent scission and cross-linking in an elastomeric cylinder undergoing circular shear and heat conduction”. *International Journal of Non-Linear Mechanics* 38.7 (2003), pp. 969–983.
- [153] Dana R Rottach, John G Curro, Joanne Budzien, Gary S Grest, Carsten Svaneborg, and Ralf Everaers. “Molecular dynamics simulations of polymer networks undergoing sequential cross-linking and scission reactions”. *Macromolecules* 40.1 (2007), pp. 131–139.
- [154] J David Carlson and Mark R Jolly. “MR fluid, foam and elastomer devices”. *mechatronics* 10.4-5 (2000), pp. 555–569.
- [155] Kostas Danas, SV Kankanala, and Nicolas Triantafyllidis. “Experiments and modeling of iron-particle-filled magnetorheological elastomers”. *Journal of the Mechanics and Physics of Solids* 60.1 (2012), pp. 120–138.
- [156] Ioan Bica, Eugen M Anitas, Madalin Bunoiu, Boris Vatzulik, and Iulius Juganaru. “Hybrid magnetorheological elastomer: Influence of magnetic field and compression pressure on its electrical conductivity”. *Journal of Industrial and Engineering Chemistry* 20.6 (2014), pp. 3994–3999.
- [157] Tian Chen, Mark Pauly, and Pedro M Reis. “A reprogrammable mechanical metamaterial with stable memory”. *Nature* 589.7842 (2021), pp. 386–390.
- [158] Liu Wang, Dongchang Zheng, Pablo Harker, Aman B Patel, Chuan Fei Guo, and Xuanhe Zhao. “Evolutionary design of magnetic soft continuum robots”. *Proceedings of the National Academy of Sciences* 118.21 (2021), e2021922118.

- [159] Ziyu Ren, Wenqi Hu, Xiaoguang Dong, and Metin Sitti. “Multi-functional soft-bodied jellyfish-like swimming”. *Nature Communications* 10.1 (2019), p. 2703.
- [160] Sandhya Rani Gouda, Immihan Ceren Yasa, Xinghao Hu, Hakan Ceylan, Wenqi Hu, and Metin Sitti. “Biodegradable untethered magnetic hydrogel Milli-Grippers”. *Advanced Functional Materials* 30.50 (2020), p. 2004975.
- [161] Holger Böse, Raman Rabindranath, and Johannes Ehrlich. “Soft magnetorheological elastomers as new actuators for valves”. *Journal of Intelligent Material Systems and Structures* 23.9 (2012), pp. 989–994.
- [162] Hen-Wei Huang, Mahmut Selman Sakar, Andrew J Petruska, Salvador Pané, and Bradley J Nelson. “Soft micromachines with programmable motility and morphology”. *Nature communications* 7.1 (2016), p. 12263.
- [163] Jiachen Zhang and Eric Diller. “Untethered miniature soft robots: Modeling and design of a millimeter-scale swimming magnetic sheet”. *Soft robotics* 5.6 (2018), pp. 761–776.
- [164] Eric Diller, Jiang Zhuang, Guo Zhan Lum, Matthew R Edwards, and Metin Sitti. “Continuously distributed magnetization profile for millimeter-scale elastomeric undulatory swimming”. *Applied Physics Letters* 104.17 (2014).
- [165] T Xu, J Zhang, M Salehizadeh, O Onaizah, and E Diller. *Millimeter-scale flexible robots with programmable three-dimensional magnetization and motions. Sci. Robot.* 4, eaav4494. 2019.
- [166] Yu Huang, Jian Zhao, and Shutian Liu. “Design optimization of segment-reinforced bistable mechanisms exhibiting adjustable snapping behavior”. *Sensors and Actuators A: Physical* 252 (2016), pp. 7–15.
- [167] Laliphat Manamanchaiyaporn, Tiantian Xu, and Xinyu Wu. “Magnetic Soft Robot With the Triangular Head–Tail Morphology Inspired By Lateral Undulation”. *IEEE/ASME Transactions on Mechatronics* 25.6 (2020), pp. 2688–2699.
- [168] Xuanhe Zhao and Yoonho Kim. *Soft microbots programmed by nanomagnets*. 2019.
- [169] Jizhai Cui, Tian-Yun Huang, Zhaochu Luo, Paolo Testa, Hongri Gu, Xiang-Zhong Chen, Bradley J Nelson, and Laura J Heyderman. “Nanomagnetic encoding of shape-morphing micromachines”. *Nature* 575.7781 (2019), pp. 164–168.
- [170] Brett Cowan and Paris R Von Lockette. “Fabrication, characterization, and heuristic trade space exploration of magnetically actuated Miura-Ori origami structures”. *Smart Materials and Structures* 26.4 (2017), p. 045015.
- [171] Larissa S Novelino, Qiji Ze, Shuai Wu, Glaucio H Paulino, and Ruike Zhao. “Untethered control of functional origami microrobots with distributed actuation”. *Proceedings of the National Academy of Sciences* 117.39 (2020), pp. 24096–24101.

- [172] S. Macrae Montgomery, Shuai Wu, Xiao Kuang, Connor D. Armstrong, Cole Zemelka, Qiji Ze, Rundong Zhang, Ruike Zhao, and H. Jerry Qi. “Magneto-mechanical metamaterials with widely tunable mechanical properties and acoustic bandgaps”. *Advanced Functional Materials* 31 (2021), p. 2005319.
- [173] S Macrae Montgomery, Shuai Wu, Xiao Kuang, Connor D Armstrong, Cole Zemelka, Qiji Ze, Rundong Zhang, Ruike Zhao, and H Jerry Qi. “Magneto-mechanical meta-materials with widely tunable mechanical properties and acoustic bandgaps”. *Advanced Functional Materials* 31.3 (2021), p. 2005319.
- [174] Yucai Lin, Ziyang Hu, Miaoxin Zhang, Ting Xu, Shile Feng, Lei Jiang, and Yongmei Zheng. “Magnetically Induced Low Adhesive Direction of Nano/Micropillar Arrays for Microdroplet Transport”. *Advanced Functional Materials* 28.49 (2018), p. 1800163.
- [175] Zhengzhi Wang, Kun Wang, Deshan Liang, Linhai Yan, Ke Ni, Houbing Huang, Bei Li, Zhiwei Guo, Junsheng Wang, Xingqiao Ma, et al. “Hybrid magnetic micropillar arrays for programmable actuation”. *Advanced Materials* 32.25 (2020), p. 2001879.
- [176] Dirk-M Drotlef, Peter Blümner, Periklis Papadopoulos, and Aránzazu Del Campo. “Magnetically actuated micropatterns for switchable wettability”. *ACS applied materials and interfaces* 6.11 (2014), pp. 8702–8707.
- [177] Zining Yang, Jun Kyu Park, and Seok Kim. “Magnetically responsive elastomer–silicon hybrid surfaces for fluid and light manipulation”. *Small* 14.2 (2018), p. 1702839.
- [178] Jisoo Jeon, Jeong Eun Park, Sei Jin Park, Sukyoung Won, Hangbo Zhao, Sanha Kim, Bong Sup Shim, Augustine Urbas, A John Hart, Zahyun Ku, et al. “Shape-programmed fabrication and actuation of magnetically active micropost arrays”. *ACS applied materials and interfaces* 12.14 (2020), pp. 17113–17120.
- [179] Shaojun Jiang, Yanlei Hu, Hao Wu, Yachao Zhang, Yiyuan Zhang, Yulong Wang, Yinghui Zhang, Wulin Zhu, Jiawen Li, Dong Wu, et al. “Multifunctional Janus microplates arrays actuated by magnetic fields for water/light switches and bio-inspired assimilatory coloration”. *Advanced Materials* 31.15 (2019), p. 1807507.
- [180] Yangying Zhu, Dion S Antao, Rong Xiao, and Evelyn N Wang. “Real-time manipulation with magnetically tunable structures”. *Advanced Materials* 26.37 (2014), pp. 6442–6446.
- [181] Xiaoguang Dong, Guo Zhan Lum, Wenqi Hu, Rongjing Zhang, Ziyu Ren, Patrick R Onck, and Metin Sitti. “Bioinspired cilia arrays with programmable nonreciprocal motion and metachronal coordination”. *Science advances* 6.45 (2020), eabc9323.

- [182] SN Khaderi, JMJ Den Toonder, and PR Onck. “Microfluidic propulsion by the metachronal beating of magnetic artificial cilia: a numerical analysis”. *Journal of fluid mechanics* 688 (2011), pp. 44–65.
- [183] Zhijie Qi, Mingxing Zhou, Ya Li, Zhiqiang Xia, Wenxing Huo, and Xian Huang. “Reconfigurable flexible electronics driven by origami magnetic membranes”. *Advanced Materials Technologies* 6.4 (2021), p. 2001124.
- [184] Takumi Kawasetsu, Takato Horii, Hisashi Ishihara, and Minoru Asada. “Mexican-hat-like response in a flexible tactile sensor using a magnetorheological elastomer”. *Sensors* 18.2 (2018), p. 587.
- [185] Youcan Yan, Zhe Hu, Zhengbao Yang, Wenzhen Yuan, Chaoyang Song, Jia Pan, and Yajing Shen. “Soft magnetic skin for super-resolution tactile sensing with force self-decoupling”. *Science Robotics* 6.51 (2021), eabc8801.
- [186] Yuanzhao Wu, Yiwei Liu, and Youlin Zhou. “Qikui Man, Chao Hu, Waqas Asghar, Fali Li, Zhe Yu, Jie Shang, Gang Liu, Meiyong Liao, and Run-Wei Li. A skin-inspired tactile sensor for smart prosthetics”. *Science Robotics* 3.9 (2018).
- [187] Tess Hellebrekers, Oliver Kroemer, and Carmel Majidi. “Soft magnetic skin for continuous deformation sensing”. *Advanced Intelligent Systems* 1.4 (2019), p. 1900025.
- [188] Sungwoong Jeon, Sangwon Kim, Shinwon Ha, Seungmin Lee, Eunhee Kim, So Yeun Kim, Sun Hwa Park, Jung Ho Jeon, Sung Won Kim, Cheil Moon, Bradley J. Nelson, Jin-young Kim, Seong-Woon Yu, and Hongsoo Choi. “Magnetically actuated microrobots as a platform for stem cell transplantation”. *Science Robotics* 4.30 (2019), eaav4317.
- [189] Xuanhe Zhao, Jaeyun Kim, Christine A Cezar, Nathaniel Huebsch, Kangwon Lee, Kamal Bouhadir, and David J Mooney. “Active scaffolds for on-demand drug and cell delivery”. *Proceedings of the National Academy of Sciences* 108.1 (2011), pp. 67–72.
- [190] Christine A Cezar, Stephen M Kennedy, Manav Mehta, James C Weaver, Luo Gu, Herman Vandenburgh, and David J Mooney. “Biphasic ferrogels for triggered drug and cell delivery”. *Advanced healthcare materials* 3.11 (2014), pp. 1869–1876.
- [191] Xinyue Liu, Yueying Yang, Maria Eugenia Inda, Shaoting Lin, Jingjing Wu, Yoonho Kim, Xiaoyu Chen, Dacheng Ma, Timothy K Lu, and Xuanhe Zhao. “Magnetic living hydrogels for intestinal localization, retention, and diagnosis”. *Advanced functional materials* 31.27 (2021), p. 2010918.

- [192] Yoonho Kim, Emily Genevriere, Pablo Harker, Jaehun Choe, Marcin Balicki, Robert W Regenhardt, Justin E Vranic, Adam A Dmytriw, Aman B Patel, and Xuanhe Zhao. “Telerobotic neurovascular interventions with magnetic manipulation”. *Science Robotics* 7.65 (2022), eabg9907.
- [193] Terunobu Miyazaki and Hanmin Jin. *The physics of ferromagnetism*. Vol. 158. Springer Science & Business Media, 2012.
- [194] JM Ginder, SM Clark, WF Schlotter, and ME Nichols. “Magnetostrictive phenomena in magnetorheological elastomers”. *International Journal of Modern Physics B* 16.17n18 (2002), pp. 2412–2418.
- [195] Zvi Rigbi and Leif Jilken. “The response of an elastomer filled with soft ferrite to mechanical and magnetic influences”. *Journal of magnetism and magnetic materials* 37.3 (1983), pp. 267–276.
- [196] John M Ginder, Mark E Nichols, Larry D Elie, and Janice L Tardiff. “Magnetorheological elastomers: properties and applications”. *Smart Structures and Materials 1999: Smart Materials Technologies*. Vol. 3675. International Society for Optics and Photonics. 1999, pp. 131–138.
- [197] K. Danas, S. V. Kankanala, and N. Triantafyllidis. “Experiments and modeling of iron-particle-filled magnetorheological elastomers”. *Journal of the Mechanics and Physics of Solids* 60.1 (Jan. 1, 2012), pp. 120–138.
- [198] John M. Ginder, William F. Schlotter, and Mark E. Nichols. “Magnetorheological elastomers in tunable vibration absorbers”. *Proc. SPIE 4331, Smart Structures and Materials 2001: Damping and Isolation*. Newport Beach, CA, United States: Society of Photo-Optical Instrumentation Engineers, 2001, pp. 103–110.
- [199] Hua-xia Deng, Xing-long Gong, and Lian-hua Wang. “Development of an adaptive tuned vibration absorber with magnetorheological elastomer”. *Smart Materials and Structures* 15.5 (2006), N111–N116.
- [200] Hyun Kee Kim, Hye Shin Kim, and Young-Keun Kim. “Stiffness control of magnetorheological gels for adaptive tunable vibration absorber”. *Smart Materials and Structures* 26.1 (2017), p. 015016.
- [201] Jonathan J. Nagel, George Mikhail, Hongseok Noh, and Jeonghoi Koo. “Magnetically actuated micropumps using an Fe-PDMS composite membrane”. *Smart Structures and Materials 2006: Smart Electronics, MEMS, BioMEMS, and Nanotechnology*. Ed. by Vijay K. Varadan. Vol. 6172. International Society for Optics and Photonics. SPIE, 2006, pp. 288–296.

- [202] Shi-Yang Tang, Xuchun Zhang, Shuaishuai Sun, Dan Yuan, Qianbin Zhao, Sheng Yan, Lei Deng, Guolin Yun, Jun Zhang, Shiwu Zhang, and Weihua Li. “Versatile Microfluidic Platforms Enabled by Novel Magnetorheological Elastomer Microactuators”. *Advanced Functional Materials* 28.8 (2018), p. 1705484.
- [203] Tao Hu, Shouhu Xuan, Li Ding, and Xinglong Gong. “Stretchable and magneto-sensitive strain sensor based on silver nanowire-polyurethane sponge enhanced magnetorheological elastomer”. *Materials & Design* 156 (2018), pp. 528–537.
- [204] Shunta Kashima, Fumikazu Miyasaka, and Katsuhiro Hirata. “Novel Soft Actuator Using Magnetorheological Elastomer”. *IEEE Transactions on Magnetics* 48.4 (2012), pp. 1649–1652.
- [205] Jacopo Ciambella and Giuseppe Tomassetti. “A form-finding strategy for magneto-elastic actuators”. *International Journal of Non-Linear Mechanics* 119 (2020), p. 103297.
- [206] Wei Chen, Zhi Yan, and Lin Wang. “Complex transformations of hard-magnetic soft beams by designing residual magnetic flux density”. *Soft matter* 16.27 (2020), pp. 6379–6388.
- [207] Wei Chen, Zhi Yan, and Lin Wang. “On mechanics of functionally graded hard-magnetic soft beams”. *International Journal of Engineering Science* 157 (2020), p. 103391.
- [208] Lucio Pancaldi, Pietro Dirix, Adele Fanelli, Augusto Martins Lima, Nikolaos Stergiopulos, Pascal John Mosimann, Diego Ghezzi, and Mahmut Selman Sakar. “Flow driven robotic navigation of microengineered endovascular probes”. *Nature Communications* 11 (2020), p. 6356.
- [209] Clifford Truesdell and Richard Toupin. *The classical field theories*. Springer, 1960.
- [210] William Fuller Brown. *Magnetoelastic interactions*. Vol. 9. Springer, 1966.
- [211] Pao Yih-Hsing and Yeh Chau-Shiung. “A linear theory for soft ferromagnetic elastic solids”. *International Journal of Engineering Science* 11.4 (1973), pp. 415–436.
- [212] Y-H Pao. “Electromagnetic forces in deformable continua”. In: *Mechanics today*. Volume 4.(A78-35706 14-70) New York 4 (1978), pp. 209–305.
- [213] Mark R. Jolly, J. David Carlson, Beth C. Muñoz, and Todd A. Bullions. “The magnetoviscoelastic response of elastomer composites consisting of ferrous particles embedded in a polymer matrix”. *Journal of Intelligent Material Systems and Structures* 7.6 (1996), pp. 613–622.
- [214] A Dorfmann and RW1064 Ogden. “Nonlinear magnetoelastic deformations of elastomers”. *Acta Mechanica* 167 (2004), pp. 13–28.

- [215] A Dorfmann and RW21853031071 Ogden. “Some problems in nonlinear magnetoelectricity”. *Zeitschrift für angewandte Mathematik und Physik ZAMP* 56 (2005), pp. 718–745.
- [216] SV Kankanala and N20998281115 Triantafyllidis. “On finitely strained magnetorheological elastomers”. *Journal of the Mechanics and Physics of Solids* 52.12 (2004), pp. 2869–2908.
- [217] Dipayan Mukherjee, Laurence Bodelot, and Kostas Danas. “Microstructurally-guided explicit continuum models for isotropic magnetorheological elastomers with iron particles”. *International Journal of Non-Linear Mechanics* 120 (2020), p. 103380.
- [218] M Rambašek, D Mukherjee, and Kostas Danas. “A computational framework for magnetically hard and soft viscoelastic magnetorheological elastomers”. *Computer Methods in Applied Mechanics and Engineering* 391 (2022), p. 114500.
- [219] Dipayan Mukherjee, Matthias Rambašek, and Kostas Danas. “An explicit dissipative model for isotropic hard magnetorheological elastomers”. *Journal of the Mechanics and Physics of Solids* 151 (2021), p. 104361.
- [220] Jean-Pierre Voropaieff, Laurence Bodelot, Kostas Danas, and Nicolas Triantafyllidis. “Modeling and Identification of the constitutive behavior of magneto-rheological elastomers”. 2017.
- [221] G. Bertotti. *Hysteresis in Magnetism: For Physicists, Materials Scientists, and Engineers*. Electromagnetism. Elsevier Science, 1998.
- [222] Xiao Kuang, Shuai Wu, Qiji Ze, Liang Yue, Yi Jin, S Macrae Montgomery, Fengyuan Yang, H Jerry Qi, and Ruike Zhao. “Magnetic dynamic polymers for modular assembling and reconfigurable morphing architectures”. *Advanced materials* 33.30 (2021), p. 2102113.
- [223] Daniel Garcia-Gonzalez. “Magneto-visco-hyperelasticity for hard-magnetic soft materials: theory and numerical applications”. *Smart Materials and Structures* 28.8 (2019), p. 085020.
- [224] Rundong Zhang, Shuai Wu, Qiji Ze, and Ruike Zhao. “Micromechanics Study on Actuation Efficiency of Hard-Magnetic Soft Active Materials”. *Journal of Applied Mechanics* 87 (2020), p. 091008.
- [225] Dipayan Mukherjee, Laurence Bodelot, and Kostas Danas. “Microstructurally-guided explicit continuum models for isotropic magnetorheological elastomers with iron particles”. *International Journal of Non-Linear Mechanics* (Dec. 12, 2019), p. 103380.

- [226] Daniel Garcia-Gonzalez and Mokarram Hossain. “Microstructural modelling of hard-magnetic soft materials: Dipole–dipole interactions versus Zeeman effect”. *Extreme Mechanics Letters* 48 (2021), p. 101382.
- [227] M. V. Vaganov, D. Yu. Borin, S. Odenbach, and Yu. L. Raikher. “Effect of local elasticity of the matrix on magnetization loops of hybrid magnetic elastomers”. *Journal of Magnetism and Magnetic Materials. The selected papers of Seventh Moscow International Symposium on Magnetism (MISM-2017)* 459 (2018), pp. 92–97.
- [228] M. V. Vaganov, D. Yu. Borin, S. Odenbach, and Yu. L. Raikher. “Training effect in magnetoactive elastomers due to undermagnetization of magnetically hard filler”. *Physica B: Condensed Matter* 578 (2020), p. 411866.
- [229] M Schümann, D Yu Borin, J Morich, and S Odenbach. “Reversible and non-reversible motion of NdFeB-particles in magnetorheological elastomers”. *Journal of Intelligent Material Systems and Structures* 32 (2021), pp. 3–15.
- [230] E. Psarra, L. Bodelot, and K. Danas. “Wrinkling to crinkling transitions and curvature localization in a magnetoelastic film bonded to a non-magnetic substrate”. *Journal of Mechanics and Physics of Solids* 133 (2019), p. 103734.
- [231] Tomohiko G Sano. “Reduced theory for hard magnetic rods with dipole–dipole interactions”. *Journal of Physics A: Mathematical and Theoretical* 55 (10 2022), p. 104002.
- [232] Dong Yan, Bastien FG Aymon, and Pedro M Reis. “A reduced-order, rotation-based model for thin hard-magnetic plates”. *Journal of the Mechanics and Physics of Solids* 170 (2023), p. 105095.
- [233] Dong Yan, Arefeh Abbasi, and Pedro M Reis. “A comprehensive framework for hard-magnetic beams: reduced-order theory, 3D simulations, and experiments”. *International Journal of Solids and Structures* (2021), p. 111319.
- [234] Tomohiko G. Sano, Matteo Pezzulla, and Pedro M. Reis. “A Kirchhoff-like theory for hard magnetic rods under geometrically nonlinear deformation in three dimensions”. *Journal of the Mechanics and Physics of Solids* 160 (2022), p. 104739.
- [235] Wei Chen and Lin Wang. “Theoretical modeling and exact solution for extreme bending deformation of hard-magnetic soft beams”. *Journal of Applied Mechanics* 87.4 (2020), p. 041002.
- [236] Wei Chen, Lin Wang, Zhi Yan, and Bo Luo. “Three-dimensional large-deformation model of hard-magnetic soft beams”. *Composite Structures* 266 (2021), p. 113822.
- [237] Amir Mehdi Dehrouyeh-Semnani. “On bifurcation behavior of hard magnetic soft cantilevers”. *International Journal of Non-Linear Mechanics* 134 (2021), p. 103746.

- [238] Riccardo Durastanti, Lorenzo Giacomelli, and Giuseppe Tomassetti. “Shape programming of a magnetic elastica”. *Mathematical Models and Methods in Applied Sciences* 31.04 (2021), pp. 675–710.
- [239] AB Pippard. “The elastic arch and its modes of instability”. *European Journal of Physics* 11.6 (1990), p. 359.
- [240] P Patricio, M Adda-Bedia, and M Ben Amar. “An elastica problem: instabilities of an elastic arch”. *Physica D: Nonlinear Phenomena* 124.1-3 (1998), pp. 285–295.
- [241] Mattias Vangbo and Ylva Bäcklund. “A lateral symmetrically bistable buckled beam”. *Journal of Micromechanics and Microengineering* 8.1 (1998), p. 29.
- [242] Mattias Vangbo. “An analytical analysis of a compressed bistable buckled beam”. *Sensors and Actuators A: Physical* 69.3 (1998), pp. 212–216.
- [243] Kai Tan, Lingling Chen, Shengyou Yang, and Qian Deng. “Dynamic snap-through instability and damped oscillation of a flat arch of hard magneto-active elastomers”. *International Journal of Mechanical Sciences* 230 (2022), p. 107523.
- [244] Eric M. Stewart and Lallit Anand. “Magneto-viscoelasticity of hard-magnetic soft-elastomers: Application to modeling the dynamic snap-through behavior of a bistable arch”. *Journal of the Mechanics and Physics of Solids* 179 (2023), p. 105366.
- [245] Keith A Seffen and Stefano Vidoli. “Eversion of bistable shells under magnetic actuation: a model of nonlinear shapes”. *Smart Materials and Structures* 25.6 (2016), p. 065010.
- [246] EG Loukaides, SK Smoukov, and KA Seffen. “Magnetic actuation and transition shapes of a bistable spherical cap”. *International Journal of Smart and Nano Materials* 5.4 (2014), pp. 270–282.
- [247] Matteo Pezzulla, Dong Yan, and Pedro M Reis. “A geometrically exact model for thin magneto-elastic shells”. *Journal of the Mechanics and Physics of Solids* 166 (2022), p. 104916.
- [248] W. T. Koiter. “The nonlinear buckling behavior of a complete spherical shell under uniform external pressure, Parts I, II, III & IV”. *Proceedings of the Koninklijke Nederlandse Akedemie van Wetenschappen Series B-Physical Sciences* B72 (1969), pp. 40–123.
- [249] F.I. Niordson. *Shell Theory*. North-Holland Series in Applied Mathematics and Mechanics. Elsevier Science, Amsterdam, 1985. ISBN: 9780444599094.
- [250] Th Von Karman and Hsue-Shen Tsien. “The buckling of spherical shells by external pressure”. *Journal of the Aeronautical Sciences* 7.2 (1939), pp. 43–50.

- [251] Th Von Karman, Louis G Dunn, and Hsue-Shen Tsien. “The influence of curvature on the buckling characteristics of structures”. *J. Aeronaut. Sci.* 7.7 (1940), pp. 276–289.
- [252] JW Hutchinson, WT Koiter, et al. “Postbuckling theory”. *Applied Mechanics Reviews* 23.12 (1970), pp. 1353–1366.
- [253] Dong Yan, Matteo Pezzulla, and Pedro M Reis. “Buckling of pressurized spherical shells containing a through-thickness defect”. *Journal of Mechanics and Physics of Solids* 138 (2020), p. 103923.
- [254] S. Gerasimidis, E. Viot, J. W. Hutchinson, and S. M. Rubinstein. “On Establishing Buckling Knockdowns for Imperfection-Sensitive Shell Structures”. *Journal of Applied Mechanics* 85.9 (2018), p. 091010.
- [255] Jayson Paulose and David R Nelson. “Buckling pathways in spherical shells with soft spots”. *Soft Matter* 9.34 (2013), pp. 8227–8245.
- [256] Simos Gerasimidis and JW Hutchinson. “Dent imperfections in shell buckling: The role of geometry, residual stress, and plasticity”. *Journal of Applied Mechanics* 88.3 (2021).
- [257] Tatsuzo Koga and Nicholas J Hoff. “The axisymmetric buckling of initially imperfect complete spherical shells”. *International Journal of Solids and Structures* 5.7 (1969), pp. 679–697.
- [258] Arefeh Abbasi, Dong Yan, and Pedro M Reis. “Probing the buckling of pressurized spherical shells”. *Journal of the Mechanics and Physics of Solids* 155 (2021), p. 104545.
- [259] Eduard Riks. “An incremental approach to the solution of snapping and buckling problems”. *International Journal of Solids and Structures* 15.7 (1979), pp. 529–551.
- [260] Daniel Claxton. “Surface Curvature, MATLAB Central File Exchange. Retrieved December 9, 2022” (2022). www.mathworks.com/matlabcentral/fileexchange/11168-surface-curvature.
- [261] S. Cohn-Vossen. “Unstarre geschlossene Flächen”. *Mathematische Annalen* 102 (1929), p. 10.
- [262] Saullo GP Castro, Rolf Zimmermann, Mariano A Arbelo, Regina Khakimova, Mark W Hilburger, and Richard Degenhardt. “Geometric imperfections and lower-bound methods used to calculate knock-down factors for axially compressed composite cylindrical shells”. *Thin-Walled Struct.* 74 (2014), pp. 118–132.
- [263] Jan Sieber, John W Hutchinson, and J Michael T Thompson. “Buckling thresholds for pre-loaded spherical shells subject to localized blasts”. *Journal of Applied Mechanics* 87.3 (2020).

- [264] Eric Reissner. “Stresses and Small Displacements of Shallow Spherical Shells. I”. *Journal of Mathematics and Physics* 25.1-4 (1946), pp. 279–300.
- [265] Eric Reissner. “Stresses and Small Displacements of Shallow Spherical Shells. II”. *Journal of Mathematics and Physics* 25.1-4 (1946), pp. 80–85.
- [266] Alekse_ Vasil_ evich Pogorelov. *Bendings of Surfaces and Stability of Shells (Translations of Mathematical Monographs)*. Vol. 72. American Mathematical Society, 1988.
- [267] Matteo Pezzulla and Pedro M. Reis. “A weak form implementation of nonlinear axisymmetric shell equations with examples”. *Journal of Applied Mechanics* 84.3 (2019), p. 034501.
- [268] CA Schenk and GI1173 Schuëller. “Buckling analysis of cylindrical shells with cutouts including random boundary and geometric imperfections”. *Computer methods in applied mechanics and engineering* 196.35-36 (2007), pp. 3424–3434.
- [269] Vissarion Papadopoulos and Manolis Papadrakakis. “The effect of material and thickness variability on the buckling load of shells with random initial imperfections”. *Computer Methods in Applied Mechanics and Engineering* 194.12-16 (2005), pp. 1405–1426.
- [270] Christian A Schenk and Gerhart I Schuëller. “Buckling analysis of cylindrical shells with random geometric imperfections”. *International journal of non-linear mechanics* 38.7 (2003), pp. 1119–1132.
- [271] MK Chryssanthopoulos and Carlo Poggi. “Stochastic imperfection modelling in shell buckling studies”. *Thin-walled structures* 23.1-4 (1995), pp. 179–200.
- [272] Vissarion Papadopoulos and Pavlos Iglelis. “The effect of non-uniformity of axial loading on the buckling behaviour of shells with random imperfections”. *International Journal of Solids and Structures* 44.18-19 (2007), pp. 6299–6317.
- [273] Zhixin Xiong, Zhiquan Huang, and Xiaochuan Yu. “Application of random geometric imperfection method to nonlinear buckling analysis of spherical shell”. *Journal of Marine Science and Technology* 27.1 (2019), p. 4.
- [274] S Surendran, Tiku T Tanyimboh, and Massoud Tabesh. “Peaking demand factor-based reliability analysis of water distribution systems”. *Advances in Engineering Software* 36.11-12 (2005), pp. 789–796.
- [275] Ying Min Low. “A new distribution for fitting four moments and its applications to reliability analysis”. *Structural Safety* 42 (2013), pp. 12–25.
- [276] Jia-Liang Le and Zdeněk P Bažant. “Failure probability of concrete specimens of uncertain mean strength in large database”. *Journal of Engineering Mechanics* 146.6 (2020), p. 04020039.

- [277] Oscar Lopez-Pamies, Taha Goudarzi, and Kostas Danas. “The nonlinear elastic response of suspensions of rigid inclusions in rubber: II—a simple explicit approximation for finite-concentration suspensions”. *Journal of the Mechanics and Physics of Solids* 61.1 (2013), pp. 19–37.
- [278] Bhavesh Shrimali, Victor Lefèvre, and Oscar Lopez-Pamies. “A simple explicit homogenization solution for the macroscopic elastic response of isotropic porous elastomers”. *Journal of the Mechanics and Physics of Solids* 122 (2019), pp. 364–380.
- [279] Victor Lefèvre and Oscar Lopez-Pamies. “Nonlinear electroelastic deformations of dielectric elastomer composites: II—Non-Gaussian elastic dielectrics”. *Journal of the Mechanics and Physics of Solids* 99 (2017), pp. 438–470.
- [280] URL: https://scikit-learn.org/stable/modules/gaussian_process.html.
- [281] A.M. Johansen. “Markov Chain Monte Carlo”. *International Encyclopedia of Education (Third Edition)*. Ed. by Penelope Peterson, Eva Baker, and Barry McGaw. Third Edition. Oxford: Elsevier, 2010, pp. 245–252.
- [282] Michael A Stephens. “EDF statistics for goodness of fit and some comparisons”. *Journal of the American statistical Association* 69.347 (1974), pp. 730–737.
- [283] Arefeh Abbasi, Tomohiko G Sano, Dong Yan, and Pedro M Reis. “Snap buckling of bistable beams under combined mechanical and magnetic loading”. *Philosophical Transactions of the Royal Society A* 381.2244 (2023), p. 20220029.
- [284] Yunteng Cao, Masoud Derakhshani, Yuhui Fang, Guoliang Huang, and Changyong Cao. “Bistable structures for advanced functional systems”. *Advanced Functional Materials* 31.45 (2021), p. 2106231.
- [285] Kon-Well Wang and Ryan L Harne. *Harnessing bistable structural dynamics: for vibration control, energy harvesting and sensing*. John Wiley & Sons, 2017.
- [286] Anirban Ghosh, Gertjan Koster, and Guus Rijnders. “Multistability in bistable ferroelectric materials toward adaptive applications”. *Advanced functional materials* 26.31 (2016), pp. 5748–5756.
- [287] Ryan L Harne and KW Wang. “A review of the recent research on vibration energy harvesting via bistable systems”. *Smart materials and structures* 22.2 (2013), p. 023001.
- [288] Xianbo Sun, Yahui Zhang, and David Kennedy. “On stochastic dynamic analysis and assessment of bistable structures”. *Nonlinear Dynamics* 95.4 (2019), pp. 3205–3218.
- [289] M. Taher A. Saif. “On a tunable bistable MEMS-theory and experiment”. *Journal of microelectromechanical systems* 9.2 (2000), pp. 157–170.

- [290] Tian Chen, Osama R. Bilal, Kristina Shea, and Chiara Daraio. “Harnessing bistability for directional propulsion of soft, untethered robots”. *Proceedings of the National Academy of Sciences* 115.22 (2018), pp. 5698–5702.
- [291] Samuel C. Stanton, Clark C. McGehee, and Brian P. Mann. “Nonlinear dynamics for broadband energy harvesting: Investigation of a bistable piezoelectric inertial generator”. *Physica D: Nonlinear Phenomena* 239.10 (2010), pp. 640–653.
- [292] Dan J. Clingman and Jack Thiesen. “The development of two broadband vibration energy harvesters (BVEH) with adaptive conversion electronics”. *Industrial and Commercial Applications of Smart Structures Technologies 2017*. Vol. 10166. International Society for Optics and Photonics, 2017, pp. 68–86.
- [293] Adrienne Crivaro, Robert Sheridan, Mary Frecker, Timothy W. Simpson, and Paris Von Lockette. “Bistable compliant mechanism using magneto active elastomer actuation”. *Journal of Intelligent Material Systems and Structures* 27.15 (2016), pp. 2049–2061.
- [294] Xue Hou, Yin Liu, Guangchao Wan, Zhe Xu, Chunsheng Wen, Hui Yu, John XJ Zhang, Jianbao Li, and Zi Chen. “Magneto-sensitive bistable soft actuators: Experiments, simulations, and applications”. *Applied Physics Letters* 113.22 (2018), p. 221902.
- [295] Benjamin Trembl, Andrew Gillman, Philip Buskohl, and Richard Vaia. “Origami mechanologic”. *Proceedings of the National Academy of Sciences* 115.27 (2018), pp. 6916–6921.
- [296] Jakob A. Faber, Andres F. Arrieta, and André R. Studart. “Bioinspired spring origami”. *Science* 359.6382 (2018), pp. 1386–1391.
- [297] Tian Chen, Jochen Mueller, and Kristina Shea. “Integrated design and simulation of tunable, multi-state structures fabricated monolithically with multi-material 3D printing”. *Scientific reports* 7.1 (2017).
- [298] X Liu, F Lamarque, E Doré, and P Pouille. “Multistable wireless micro-actuator based on antagonistic pre-shaped double beams”. *Smart Materials and Structures* 24.7 (2015), p. 075028.
- [299] Weileun Fang and JA Wickert. “Post buckling of micromachined beams”. *Journal of Micromechanics and Microengineering* 4.3 (1994), p. 116.
- [300] Jin-Han Jeon, Tai-Hong Cheng, and Il-Kwon Oh. “Snap-through dynamics of buckled IPMC actuator”. *Sensors and Actuators A: Physical* 158.2 (2010), pp. 300–305.

- [301] Jonathon Cleary and Hai-Jun Su. “Modeling and experimental validation of actuating a bistable buckled beam via moment input”. *Journal of Applied Mechanics* 82.5 (2015), p. 051005.
- [302] Wenzhong Yan, Yunchen Yu, and Ankur Mehta. “Analytical modeling for rapid design of bistable buckled beams”. *Theoretical and Applied Mechanics Letters* 9.4 (2019), pp. 264–272.
- [303] Jian Zhao, Jianyuan Jia, Xiaoping He, and Hongxi Wang. “Post-buckling and snap-through behavior of inclined slender beams”. *Journal of Applied Mechanics* 75.4 (2008), p. 041020.
- [304] Paul Cazottes, Amâncio Fernandes, Joël Pouget, and Moustapha Hafez. “Bistable buckled beam: modeling of actuating force and experimental validations”. *Journal of Mechanical Design* 131.10 (2009), pp. 1001001–1001011.
- [305] B Camescasse, A Fernandes, and Jean Pouget. “Bistable buckled beam: Elastica modeling and analysis of static actuation”. *International Journal of Solids and Structures* 50.19 (2013), pp. 2881–2893.
- [306] B Camescasse, A Fernandes, and Jean Pouget. “Bistable buckled beam and force actuation: Experimental validations”. *International Journal of Solids and Structures* 51.9 (2014), pp. 1750–1757.
- [307] PS Harvey Jr and LN Virgin. “Coexisting equilibria and stability of a shallow arch: Unilateral displacement-control experiments and theory”. *International Journal of Solids and Structures* 54 (2015), pp. 1–11.
- [308] Alessandro Cazzolli and Francesco Dal Corso. “Snapping of elastic strips with controlled ends”. *International Journal of Solids and Structures* 162 (2019), pp. 285–303.
- [309] Yingchao Zhang, Yang Jiao, Jian Wu, Yinji Ma, and Xue Feng. “Configurations evolution of a buckled ribbon in response to out-of-plane loading”. *Extreme Mechanics Letters* 34 (2020), p. 100604.
- [310] Guangchao Wan, Yin Liu, Zhe Xu, Congran Jin, Lin Dong, Xiaomin Han, John XJ Zhang, and Zi Chen. “Tunable bistability of a clamped elastic beam”. *Extreme Mechanics Letters* 34 (2020), p. 100603.
- [311] Raymond H Plaut. “Snap-through of arches and buckled beams under unilateral displacement control”. *International Journal of Solids and Structures* 63 (2015), pp. 109–113.
- [312] Slava Krylov, Bojan R Ilic, and Stella Lulinsky. “Bistability of curved microbeams actuated by fringing electrostatic fields”. *Nonlinear Dynamics* 66.3 (2011), pp. 403–426.

- [313] Lior Medina, Rivka Gilat, and Slava Krylov. “Bistability criterion for electrostatically actuated initially curved micro plates”. *International Journal of Engineering Science* 130 (2018), pp. 75–92.
- [314] Corrado Maurini, Joel Pouget, and Stefano Vidoli. “Distributed piezoelectric actuation of a bistable buckled beam”. *European Journal of Mechanics-A/Solids* 26.5 (2007), pp. 837–853.
- [315] Vivek Ramachandran, Michael D Bartlett, James Wissman, and Carmel Majidi. “Elastic instabilities of a ferroelastomer beam for soft reconfigurable electronics”. *Extreme Mechanics Letters* 9 (2016), pp. 282–290.
- [316] A Amor, A Fernandes, and J Pouget. “Snap-through of elastic bistable beam under contactless magnetic actuation”. *International Journal of Non-Linear Mechanics* 119 (2020), p. 103358.
- [317] K. Das and R. C. Batra. “Pull-in and snap-through instabilities in transient deformations of microelectromechanical systems”. *Journal of Micromechanics and Microengineering* 19.3 (2009), p. 035008.
- [318] A Pandey, D E Moulton, D Vella, and D P Holmes. “Dynamics of snapping beams and jumping poppers”. *Europhysics Letters* 105.2 (2014), p. 24001.
- [319] Tomohiko G Sano and Hirofumi Wada. “Snap-buckling in asymmetrically constrained elastic strips”. *Physical Review E* 97.1 (2018), p. 013002.
- [320] Mark Alger. *Polymer Science Dictionary*. Springer Science & Business Media, 1996. ISBN: 978-0-412-60870-4.
- [321] Michael Gomez, Derek E Moulton, and Dominic Vella. “Dynamics of viscoelastic snap-through”. *Journal of the Mechanics and Physics of Solids* 124 (2019), pp. 781–813.
- [322] Oliver M O’Reilly. “Kirchhoff’s rod theory”. *Modeling Nonlinear Problems in the Mechanics of Strings and Rods*. Springer, 2017, pp. 187–268.
- [323] Arefeh Abbasi, Tian Chen, Bastien FG Aymon, and Pedro M Reis. “Designing a braille reader using the snap buckling of bistable magnetic shells”. *arXiv preprint arXiv:2307.10933* (2023).
- [324] Matteo Taffetani, Xin Jiang, Douglas P Holmes, and Dominic Vella. “Static bistability of spherical caps”. *Proceedings of the Royal Society A: Mathematical, Physical and Engineering Sciences* 474.2213 (2018), p. 20170910.
- [325] M Taher A Saif. “On a tunable bistable MEMS-theory and experiment”. *Journal of microelectromechanical systems* 9.2 (2000), pp. 157–170.
- [326] Ryan L Harne and Kon-Well Wang. *Harnessing bistable structural dynamics: for vibration control, energy harvesting and sensing*. John Wiley & Sons, 2017.

- [327] Tian Chen, Osama R Bilal, Kristina Shea, and Chiara Daraio. “Harnessing bistability for directional propulsion of soft, untethered robots”. *Proceedings of the National Academy of Sciences* 115.22 (2018), pp. 5698–5702.
- [328] Gaetano Arena, Rainer MJ Groh, Alex Brinkmeyer, Raf Theunissen, Paul M. Weaver, and Alberto Pirrera. “Adaptive compliant structures for flow regulation”. *Proceedings of the Royal Society A: Mathematical, Physical and Engineering Sciences* 473.2204 (2017), p. 20170334.
- [329] Daniele Leonardis, Loconsole Claudio, and Antonio Frisoli. “A survey on innovative refreshable braille display technologies”. *International Conference on Applied Human Factors and Ergonomics*. Springer. 2017, pp. 488–498.
- [330] Javier Jiménez, Jesús Olea, Jesús Torres, Inmaculada Alonso, Dirk Harder, and Konstanze Fischer. “Biography of louis braille and invention of the braille alphabet”. *Survey of Ophthalmology* 54.1 (2009), pp. 142–149.
- [331] Jun Su Lee and Stepan Lucyszyn. “A micromachined refreshable Braille cell”. *Journal of Microelectromechanical Systems* 14.4 (2005), pp. 673–682.
- [332] Xiaosong Wu, Haihong Zhu, Seong-Hyok Kim, and Mark G Allen. “A portable pneumatically-actuated refreshable braille cell”. *TRANSDUCERS 2007-2007 International Solid-State Sensors, Actuators and Microsystems Conference*. IEEE. 2007, pp. 1409–1412.
- [333] Noel H Runyan and Federico Carpi. “Seeking the ‘holy Braille’ display: might electromechanically active polymers be the solution?” *Expert Review of Medical Devices* 8.5 (2011), pp. 529–532.
- [334] Pruittikorn Smithmaitrie. “Analysis and design of piezoelectric braille display”. *Rehabilitation Engineering*. IntechOpen, 2009.
- [335] Pruittikorn Smithmaitrie, Jinda Kanjantoe, and Pichaya Tandayya. “Touching force response of the piezoelectric Braille cell”. *Proceedings of the 1st international convention on Rehabilitation engineering & assistive technology: in conjunction with 1st Tan Tock Seng Hospital Neurorehabilitation Meeting*. 2007, pp. 174–178.
- [336] Ramiro Velazquez, Edwige E Pissaloux, Moustapha Hafez, and Jérôme Szewczyk. “Tactile rendering with shape-memory-alloy pin-matrix”. *IEEE Transactions on Instrumentation and Measurement* 57.5 (2008), pp. 1051–1057.
- [337] Hermes Hernandez, Enrique Preza, and Ramiro Velazquez. “Characterization of a piezoelectric ultrasonic linear motor for Braille displays”. *2009 Electronics, Robotics and Automotive Mechanics Conference (CERMA)*. IEEE. 2009, pp. 402–407.
- [338] Stanislav Simeonov and Neli Simeonova. “Graphical interface for visually impaired people based on bi-stable solenoids”. *arXiv preprint arXiv:1401.5289* (2014).

- [339] Gemma Carolina Bettelani, Giuseppe Averta, Manuel Giuseppe Catalano, Barbara Leporini, and Matteo Bianchi. “Design and validation of the readable device: a single-cell electromagnetic refreshable braille display”. *IEEE Transactions on Haptics* 13.1 (2020), pp. 239–245.
- [340] Iosko Balabozov, Ivan Yatchev, and Krastyo Hinov. “Computer modeling and experimental verification of dynamic characteristics of permanent magnet linear actuator for braille screen”. *2014 International Conference on Applied and Theoretical Electricity (ICATE)*. IEEE. 2014, pp. 1–4.
- [341] Fernando Vidal-Verdú, Manuel J Madueno, and Rafael Navas. “Thermopneumatic actuator for tactile displays and smart actuation circuitry”. *Smart Sensors, Actuators, and MEMS II*. Vol. 5836. SPIE. 2005, pp. 484–492.
- [342] P Chakraborti, HA Karahan Toprakci, P Yang, N Di Spigna, P Franzon, and T Ghosh. “A compact dielectric elastomer tubular actuator for refreshable Braille displays”. *Sensors and Actuators A: Physical* 179 (2012), pp. 151–157.
- [343] Zhi Ren, Xiaofan Niu, Dustin Chen, Wei Hu, and Qibing Pei. “A new bistable electroactive polymer for prolonged cycle lifetime of refreshable Braille displays”. *Electroactive Polymer Actuators and Devices (EAPAD) 2014*. Vol. 9056. SPIE. 2014, pp. 511–519.
- [344] Gabriele Frediani, James Busfield, and Federico Carpi. “Enabling portable multiple-line refreshable Braille displays with electroactive elastomers”. *Medical Engineering & Physics* 60 (2018), pp. 86–93.
- [345] Yu Qiu, Zhiyun Lu, and Qibing Pei. “Refreshable tactile display based on a bistable electroactive polymer and a stretchable serpentine Joule heating electrode”. *ACS Applied Materials & Interfaces* 10.29 (2018), pp. 24807–24815.
- [346] W Makishi, K Iwami, Y Haga, and M Esashi. “Batch fabrication of SMA actuated pin display for blind aid”. *Technical Digest of the Sensor Symposium*. Vol. 18. 2001, pp. 137–142.
- [347] R Velázquez, EE Pissaloux, M Hafez, and J Szewczyk. “Toward low-cost highly portable tactile displays with shape memory alloys”. *Applied Bionics and Biomechanics* 4.2 (2007), pp. 57–70.
- [348] Nadine Besse, Samuel Rosset, Juan Jose Zarate, and Herbert Shea. “Flexible active skin: large reconfigurable arrays of individually addressed shape memory polymer actuators”. *Advanced Materials Technologies* 2.10 (2017), p. 1700102.
- [349] Ig Mo Koo, Kwangmok Jung, Ja Choon Koo, Jae-Do Nam, Young Kwan Lee, and Hyouk Ryeol Choi. “Development of soft-actuator-based wearable tactile display”. *IEEE Transactions on Robotics* 24.3 (2008), pp. 549–558.

- [350] Marc Matysek, Peter Lotz, Thomas Winterstein, and Helmut F Schlaak. “Dielectric elastomer actuators for tactile displays”. *World Haptics 2009-Third Joint Euro-Haptics conference and Symposium on Haptic Interfaces for Virtual Environment and Teleoperator Systems*. IEEE. 2009, pp. 290–295.
- [351] Ivan Yatchev, Krastio Hinov, Iosko Balabozov, and Kristina Krasteva. “Static force characteristics of electromagnetic actuators for Braille screen”. *Facta Universitatis-Series: Electronics and Energetics* 24.2 (2011), pp. 157–167.
- [352] H Hawkeye King, Regina Donlin, and Blake Hannaford. “Perceptual thresholds for single vs. multi-finger haptic interaction”. *2010 IEEE Haptics Symposium*. IEEE. 2010, pp. 95–99.
- [353] Hiroki Ishizuka and Norihisa Miki. “MEMS-based tactile displays”. *Displays* 37 (2015), pp. 25–32.
- [354] Haley Velasco. *How Pop Its, the TikTok Sensation, Became the Toy of the Pandemic*. 2021.
- [355] Donatella Pascolini and Silvio Paolo Mariotti. “Global estimates of visual impairment: 2010”. *British Journal of Ophthalmology* 96.5 (2012), pp. 614–618.
- [356] Robert Norton, John Brown, Michael Katzmann, and Karen Keninger. “Braille Book and Pamphlets; Specification 800:2014”. Library of Congress, USA (1994).
- [357] Zhi Zhao and Xiaojia Shelly Zhang. “Topology optimization of hard-magnetic soft materials”. *Journal of the Mechanics and Physics of Solids* 158 (2022), p. 104628.
- [358] Benny Davidovitch, Robert D Schroll, Dominic Vella, Mokhtar Adda-Bedia, and Enrique A Cerda. “Prototypical model for tensional wrinkling in thin sheets”. *Proceedings of the National Academy of Sciences* 108.45 (2011), pp. 18227–18232.
- [359] Stephen Timoshenko, Sergius Woinowsky-Krieger, et al. *Theory of plates and shells*. Vol. 2. McGraw-hill New York, 1959.
- [360] Ashkan Vaziri. “Mechanics of highly deformed elastic shells”. *Thin-Walled Structures* 47.6-7 (2009), pp. 692–700.
- [361] Dominic Vella, Amin Ajdari, Ashkan Vaziri, and Arezki Boudaoud. “Indentation of Ellipsoidal and Cylindrical Elastic Shells”. *Phys. Rev. Lett.* 109 (14 2012), p. 144302.
- [362] Paul H Schimpf. “A detailed explanation of solenoid force”. *International Journal on Recent Trends in Engineering & Technology* 8.2 (2013), p. 7.
- [363] Hugo Salmon. “Mobile magnetic microrobots control and study in microfluidic environment: New tools for biomedical applications”. PhD thesis. Paris 11, 2014.

- [364] Wikipedia. *American Wire Gauge*. 2023. URL: https://en.wikipedia.org/wiki/American_wire_gauge.
- [365] William Feller. “An introduction to probability theory and its applications”. 81 (1968), 174–182, Vol. 81, John Wiley & Sons.



Arefeh Abbasi

Curriculum Vitae

Address: Ecole Polytechnique Fédérale de Lausanne
EPFL STI IGM FLEXLAB, MED 0 1526
Station 9, 1015 Lausanne, Switzerland

Phone: +41 (21) 69-38 249
Email: arefeh.abbasi@epfl.ch

Google Scholar ID: <https://scholar.google.com/citations?user=4orB1OAAAAAJ&hl=en>

I am a Ph.D. student in mechanical engineering at EPFL. I conduct research utilizing experimental, numerical, and analytical methods to investigate the mechanics of structures in coupled multi-physical fields and to provide insights for functional design. My current research involves aspects of mechanical (in)stability of slender structures and magneto-active materials and structures. My interdisciplinary work spans across solid mechanics, soft materials, and multi-physics coupling, and I am keenly interested in leveraging the principles of mechanics and materials to inform the design of devices across the length scales. As a postdoc researcher, I am eager to develop my knowledge and skills further and pursue a rewarding career in academia.

Education

- | | |
|--|--------------|
| Ph.D. in Mechanics , Ecole Polytechnique Fédérale de Lausanne (EPFL), Switzerland | 2019–Present |
| Supervisor: Prof. Pedro M. Reis | |
| Topic: Probing the mechanics of slender structures: from buckling to functionality | |
| MS in Mechanical Engineering , Shiraz University of Technology, Iran | 2014–2017 |
| Supervisor: Prof. Jafar Rouzegar | |
| Topic: Finite element formulation for static and dynamic analysis of composite plates integrated with piezoelectric layers using refined plate theory | |
| BS in Mechanical Engineering , Shiraz University, Iran | 2010–2014 |
| Topic: Investigating various techniques for measuring residual stresses | |

Research projects

- ❖ **Shell Buckling:** We revisited the mechanics of thin spherical shells by identifying the key factors contributing to their buckling instability and rationalizing their imperfection sensitivity using numerical and experimental methods [6, 8]. We investigated a non-destructive method to anticipate shell structures' stability landscape and critical loading conditions, considering both simplified scenarios with a single defect [4] and more realistic situations with random imperfection distributions [10]. Finally, we harvested the mechanical instabilities of shell structures as opportunities for functionality instead of the first route for failure [9].
- ❖ **Soft Magnetic Materials:** Our research was centered on the mechanics of magneto-active structures produced from magneto-rheological elastomers (MREs). The mechanical behavior of slender magnetic structures was investigated through a combination of experimental, numerical, and analytical methods to gain insight into their response to various loading conditions. Specifically, we examined the various modes of deformation [5] and (snap) buckling [7, 9] of slender magnetic structures, as well as the mechanics of magnetic shells with adjustable buckling properties [3]. Furthermore, we exploited the knowledge of the instability of slender structures combined with active MREs under magnetic field actuation for potential applications; we proposed the guidelines for designing a novel class of braille reader [9].
- ❖ **Smart Composite Structures:** We performed the static (bending) and dynamic (free and forced vibration) analyses of laminated [2] and FGM [1] composite plates integrated with piezoelectric layers. In our investigation, finite element formulation and plate theory were combined to improve the performance of smart structures.

Publications

- [10] **Abbasi, A.**, Lin, Y. L., Derveni, F., and Reis, P. M., “Probing of the buckling statistics of spherical shells with a distribution of imperfections,” *In preparation*.
- [9] **Abbasi, A.**, Chen, T., Aymon, F. G., and Reis, P. M., “Leveraging the snap buckling of bistable magnetic shells to design a refreshable braille dot,” *Advanced Materials Technologies*, Accepted (2023).
- [8] Derveni, F., **Abbasi, A.**, and Reis, P. M., “Defect-Defect Interactions in the Buckling of Imperfect Spherical Shells,” *Journal of Applied Mechanics*, 1-10 (2023).
- [7] **Abbasi, A.**, Sano, T. G., Yan, D., and Reis, P. M., “Snap buckling of bistable beams under combined mechanical and magnetic loading,” *Philosophical Transactions of the Royal Society A*, **381**(2244), 20220029 (2023).
- [6] **Abbasi, A.**, Derveni, F., and Reis, P. M., “Comparing the buckling strength of spherical shells with dimpled versus bumpy defects,” *Journal of Applied Mechanics*, **90**(6), 061008 (2023).
- [5] Yan, D., **Abbasi, A.**, and Reis, P. M., “A comprehensive framework for hard-magnetic beams: Reduced-order theory, 3D simulations, and experiments,” *International Journal of Solids and Structures*, **257**, 111319 (2022).
- [4] **Abbasi, A.**, Yan, D., and Reis, P. M., “Probing the buckling of pressurized spherical shells,” *Journal of the Mechanics and Physics of Solids*, **155**, 104545 (2021).
- [3] Yan, D., Pezzulla, M., Cruveiller, L., **Abbasi, A.**, and Reis, P. M., “Magneto-active elastic shells with tunable buckling strength,” *Nature communications*, **12**(1), 2831 (2021).
- [2] Rouzegar, J., and **Abbasi, A.**, “A refined finite element method for bending analysis of laminated plates integrated with piezoelectric fiber-reinforced composite actuators,” *Acta Mechanica Sinica*, **34**, 689-705 (2018).
- [1] Rouzegar, J., and **Abbasi, A.**, “A refined finite element method for bending of smart functionally graded plates,” *Thin-walled structures*, **120**, 386-396 (2017).

Presentations and outreach

- **American Physical Society (APS) March Meeting**, Las Vegas, USA 2023
Probing of the buckling of spherical shells with a distribution of imperfections
- **11th European Solid Mechanics Conference (ESMC)**, Galway, Ireland 2022
Snap buckling of magneto-active shallow shells for Braille readers
- **Flexible Structures Laboratory Invited Virtual Lab Tour**, South China University of Technology–China, Tel Aviv University–Israel, CU Boulder–USA, UIUC–USA, Brown University–USA, University of Houston–USA, Postech–South Korea, Swiss Mech Seminar–Switzerland, Freiburg University–Germany 2021-2022
Mechanics of magneto-active structures; one of the FleXLab team presenters
- **Presentation of the Flexible Structures Laboratory’s research activities**, EPFL, Switzerland 2020, 2022
Journées des Gymnasiens (High school students’ open days)
- **Mechanics Gathering Seminar**, EPFL, Switzerland 2021
Snap buckling of bistable beams under combined mechanical and magnetic loading
- **American Physical Society (APS) March Meeting**, Virtual 2021
Snap buckling of active bistable beams under magnetic actuation
- **Society of Engineering Sciences (SES)**, Virtual technical meeting 2020
Probing the buckling of spherical shells
- **American Physical Society (APS) March Meeting**, Virtual meeting 2020
Probing the buckling of spherical shells

Teaching and Supervision

- ❖ **Introduction to Structural Mechanics** (1st year undergrad) Springs 2020, 2021, 2022, 2023
Professor: Pedro M. Reis (ref. EPFL—ME-104)
60 hours of exercise preparation and session, Exam preparation
- ❖ **Mechanics of Slender Structures** (Master's degree) Falls 2019, 2020, 2021
Professor: Pedro M. Reis (ref. EPFL—ME-411)
30 hours of exercise preparation and session, Exam preparation
- ❖ **Mechanics of Structures** (2nd year undergrad) Falls 2022
Professor: Alain Preneloup (ref. EPFL—ME-232)
30 hours of exercise session
- ❖ **Mechanics of Materials Laboratory** (3rd year undergrad) Spring 2014
(ref. Shiraz University)
15 hours of Experiments demonstrations
- ❖ **Co-Supervision of Master research internship** —Manon Thbaut (EPFL) Spring 2022
Topic: Isotropic hard magnetorheological elastomers with bending-twisting-coupled actuation
- ❖ **Supervision of student research project**—Bastien Aymon (EPFL) Fall and Spring 2021
Topic: Design and fabrication of a bistable magnetic shell as an actuator

Academic Honors

- ❖ **Swiss Government Excellence Scholarship**, Grant no. 2019.0619 2019-2022
Issued by Federal Commission for Scholarships for Foreign Students (FCS)
- ❖ **Ranked 3rd based on overall GPA** 2017
Shiraz University of Technology
- ❖ **German Academic Exchange Service (DAAD) Scholarship** 2015
German-Iranian-Jordanian cooperation, CICTI, Furtwangen University, Germany
- ❖ **Ranked among top 4%** 2014
Nationwide university entrance exam, Shiraz University of Technology
- ❖ **Ranked among top 0.3%** 2010
National University Entrance Exam, Shiraz University

Summer Schools

- **Electro- and Magneto Mechanics of soft Solids: Experiments, Modeling, and Instability**, CISM Summer School, Udine, Italy Summer 2022
- **Soft Solids and Complex Fluids**, UMass Amherst, USA, Virtual Summer 2021

Skills

- **Programming Language:** Matlab, Python, HTML
- **Engineering Software:** ABAQUS, ANSYS, Catia V5, Solid Works, AutoCAD, COMSOL, LabView, Rhino
- **Experimental Skills:** Mechanical testing, Rapid prototyping, 3D printing, Electro-magnetic experiments and coils designing, Polymer synthesis, Fast imaging techniques, X-Ray tomography, Laser cutting, Milling, Lathing
- **Languages:** Farsi (Persian)-Native speaker, English-Fluent, French-B1, German-A1

Community Involvement

- Organizer of Weekly Group Meeting 2020-present
- Website Manager (<https://www.epfl.ch/labs/flexlab/>) 2022-present

Journal Reviewing

- Journal of Applied Mechanics
- Nature Communications
- International Journal of Solids and Structures
- Thin-Walled Structures

Professional Membership

- American Physical Society (APS) 2020-present
- Society of Engineering sciences (SES) 2020-present

References

- **Prof. Pedro M. Reis** (FleXLab, Ecole polytechnique fédérale de Lausanne, Switzerland)
pedro.reis@epfl.ch
- **Prof. Tian Chen** (Architected Intelligent Matter Laboratory, University of Houston, USA)
tianchen@uh.edu
- **Prof. Jafar Rouzegar** (Shiraz University of Technology, Iran)
rouzegar@sutech.ac.ir